Julian Camilo Restrepo Lozano

Theoretical and experimental study of carbon dioxide content removal from dry air by supersonic gas separation technique

São Paulo

2022

Julian Camilo Restrepo Lozano

Avaliação teórica e experimental da remoção de dióxido de carbono de ar seco pela técnica de separação supersônica

Thesis submitted in partial fulfillment of the requirements for the Degree of Doctor in Science of Mechanical Engineering (Energy and Fluids) at the Escola Politécnica da Universidade de São Paulo
Supervisor: Prof. Dr. José Roberto Simões-Moreira

Universidade de São Paulo – USP

Escola Politécnica

Revised version

São Paulo

2022

Este exemplar foi revisado e corrigido em relação à versão original, sob responsabilidade única do autor e com a anuência de seu orientador.

São Paulo, _____ de _____ de _____

Assinatura do autor: _____

Assinatura do orientador: _____

Catalogação-na-publicação

Restrepo Lozano, Julian Camilo

Avaliação teórica e experimental da remoção de dióxido de carbono de ar seco pela técnica de separação supersônica / J. C. Restrepo Lozano -- versão corr. -- São Paulo, 2022.

215 p.

Tese (Doutorado) - Escola Politécnica da Universidade de São Paulo. Departamento de Engenharia Mecânica.

1.Escoamento supersônico de gás real 2.Termodinâmica de misturas de gas real 3.CCS 4.Choque de condensação 5.MOC I.Universidade de São Paulo. Escola Politécnica. Departamento de Engenharia Mecânica II.t.

Acknowledgements

First of all, I want to thank my family and spouse. This work was only possible due to their support and inspiration. Also, I want to thank my undergrad professors, their motivation and lessons open a new world of opportunities and knowledge.

I would like to express my gratitude to my supervisor Prof. Dr José Roberto Simões-Moreira, due to his introduction to the real gas compressible flow phenomena. And the advice, freedom, means and trust gave by him for developing a new laboratory in the SISEA. Also, I want to thank the SISEA laboratory technicians (Thyago and Gustavo) because their excellent work was indispensable for achieving a perfectly operating test rig. I would like to especially thank some SISEA members: Larissa due to their true friendship, Andrés due to their companionship and outstanding work at the data acquisition system implementation, Claudio for helping me with the optical parts buying process and the optical tables assembling, Diego for their advice and relaxation moments, and Wellorzzon, Eliane and Lina for their tips and chats. Last but not least important Adrienne for their help.

I wish to express my appreciation to the RCGI. This research centre is an excellent example of industry-science integration. I learned a lot from them, especially from the technical discussion at the group meetings of the Project-39 team. I want to acknowledge Luciana excellent work in helping me with the buying and contracting process. And I gratefully acknowledge the support of the RCGI – Research Centre for Gas Innovation, hosted by the University of São Paulo (USP) and sponsored by FAPESP – São Paulo Research Foundation (2014/50279-4) and Shell Brasil, and the strategic importance of the support given by ANP (Brazil's National Oil, Natural Gas and Biofuels Agency) through the R&D levy regulation. Finally, I would like to thank FUSP for the scholarship from April 2022.

Abstract

Restrepo Lozano, Julian Camilo. **Theoretical and experimental study of carbon dioxide content removal from dry air by supersonic gas separation technique** 2022. 215 p. Thesis (Doctorate program) - Mechanical Engineering Program: Energy and fluids, Universidade de São Paulo, São Paulo, 2022.

In recent times, a remarkable acceleration in the research and development of new technologies to achieve a reliable energy transition took place. In such a context, carbon capture and sequestration (CCS) technologies have emerged as a transitory option. However, in some cases, such as Brazilian pre-salt reservoirs, carbon dioxide separation technologies could increase process efficiency and profitability, while at the same time reducing the carbon dioxide emissions. In this context, the utilization of a supersonic gas separator becomes relevant, because it allows separating high contents of carbon dioxide with low energy consumption and low maintenance. However, to improve the technology readiness level of (TRL), further theoretical and experimental work must be performed. Therefore, this thesis studies the more relevant gas dynamic phenomena inside the separator such as the viscous supersonic flow deployment and the condensation shock, in addition, this work also provided analytical tools for the device designing, as the implementation of the method of characteristics for real gas mixture supersonic flow. In addition, a unique experimental test-rig was designed, constructed, and commissioned for a dry air-carbon dioxide mixture. Such a test-rig allows the operation under different stagnation conditions (Pressure, temperature and carbon dioxide molar fraction). Also, high accuracy pressure transducers were used to ensure a quality quantitative insight about the phenomena, and direct and schlieren optical techniques were used for a qualitative experimental evaluation after using a high-speed camera. The supersonic nozzle was designed through the method of characteristic to ensure a shock-free flow, and to study the interaction between the phase change and the wave cancellation phenomena which produced three condensation shock topologies (classical, transition, and Mach wave). Finally, the validity of the proposed condensation shock model was discussed.

Keywords: Supersonic real gas flow. Real gas mixture thermodynamics. CCS. Condensation shock. MOC.

Resumo

Restrepo Lozano, Julian Camilo. **Avaliação teórica e experimental da remoção de dióxido de carbono de ar seco pela técnica de separação supersônica** 2022. 215 f. Tese (Programa de doutorado) - Programa de Pós-Graduação em Engenharia Mecânica: Energia e fluidos, Universidade de São Paulo, São Paulo, 2022.

Recentemente, tem acontecido uma notável aceleração na pesquisa e desenvolvimento de novas tecnologias para alcançar uma transição energética confiável. Nesse contexto, as tecnologias de captura e sequestro de carbono (CCS) surgiram como uma opção transitória. No entanto, em alguns casos, como os reservatórios brasileiros do pré-sal, as tecnologias de separação de dióxido de carbono poderiam aumentar a eficiência e a rentabilidade dos processos, ao mesmo tempo em que reduziam as emissões de dióxido de carbono. Nesse contexto, a utilização de um separador de gás supersônico torna-se relevante, pois permite separar alto teor de dióxido de carbono com baixo consumo de energia e baixa manutenção. No entanto, para melhorar o Nível de Maturidade Tecnológica (NMT), mais trabalhos teóricos e experimentais devem ser realizados. Portanto, essa tese estuda os fenômenos de escoamento compressível mais relevantes dentro do separador, como o escoamento supersônico viscoso e o choque de condensação. Além disso, este trabalho também forneceu ferramentas analíticas para a concepção do dispositivo, como a implementação do método de características para o escoamento supersônico da mistura de gases reais. Adicionalmente, uma bancada experimental foi projetada, construída e comissionada para uma mistura de dióxido de carbono com ar seco. Tal bancada de teste permite a operação em diferentes condições de estagnação (pressão, temperatura e fração molar de dióxido de carbono). Além disso, transdutores de alta precisão de pressão foram usados para garantir uma análise quantitativa sobre os fenômenos, e técnicas ópticas direta e schlieren foram usadas para uma avaliação experimental qualitativa após o uso de uma câmera de alta velocidade. O bocal supersônico foi projetado através do método de característica para garantir um escoamento livre de choque, e para estudar a interação entre a mudança de fase e os fenômenos de cancelamento de ondas que produziram três topologias de choque de condensação (clássica, transição e onda Mach). Finalmente, discute-se a validade do modelo de choque de condensação proposto.

Palavras-chave: Escoamento supersônico de gás real. Termodinâmica de misturas de gas real. CCS. Choque de condensação. MOC.

List of Figures

Figure 1.1 – CO_2 composition in Brazilian Pre-Salt fields. Adapted from (d'Almeida et al., 2018). 22
Figure 1.2 – Carbon dioxide separation technologies for off-shore platforms. 22
Figure 1.3 – Supersonic Separator typical design (Meneghini et al., Brazil patent, BR 20 2020 017289 7 U2, August 2020). 24
Figure 1.4 – Real gas effects, a) Compressibility factor for a methane and carbon dioxide mixture (50% CO_2), b) deviation on the speed-of-sound calculation for a methane and carbon dioxide mixture (30% mole CO_2 at 250 K) using different EOS, experimental data from (Younglove et al., 1993). 25
Figure 2.1 – Garret supersonic gas separator design. Adapted from (Garret et al., 1968). 31
Figure 2.2 – Bier et al. (1990b) experimental test-rig for supersonic carbon dioxide condensation evaluation. Adapted from (Bier et al., 1990b). 31
Figure 2.3 – Imaev et al. (2014) experimental test-rig for evaluation of supersonic gas separators. Adapted from (Imaev et al., 2014) 33
Figure 3.1 – GERG-2008, 210 binary pairs for 20 components (Kunz; Wagner, 2012a). 40
Figure 3.2 – Pure methane isotherms at 175 K, for several EOS: GERG-2008 (solid blue), PC-SAFT (dashed green), PR (dash-dot red) and extended CSP (dotted cyan) (Aursand et al., 2017). 45
Figure 3.3 – Reconstructed CO_2 isothermal loop at 295 K. 46
Figure 3.4 – Metastable and unstable regions for a pure substance. 47
Figure 3.5 – Spinodal line CO_2. 48
Figure 3.6 – Spinodal line for a molar binary mixture of 50 % CO_2 + CH_4. 49
Figure 3.7 – Droplet work of formation. 50
Figure 3.8 – Homogeneous nucleation kinetics, Adapted from (Luijten, 1998a). . . . 55
Figure 3.9 – Real gas flow chart for supersonic gas separators computation. 59
Figure 4.1 – Real gas compressible flow application for real gases a) Quasi-one dimensional viscous compressible flow, b) Continuous condensation shock in real gases c) Method of characteristics. 60
Figure 4.2 – Viscous potential for a respective sonic point displacement dashed line corresponds to the unphysical solution. 67
Figure 4.3 – Grüneisen parameter variation for superheated and supercritical vapour of a) Oxygen and b) Isobutane. 68
Figure 4.4 – Numerical solution procedure for supersonic viscous flow. 70
Figure 4.5 – Fourth-order Runge-Kutta. 71
Figure 4.6 – Shock wave capture using Brent scalar minimization. 73

Figure 4.7 – Ferrari (2021b) analytical and numerical results comparison, a) subsonic and b) supersonic solution. 74
Figure 4.8 – Experimental results used for validation, a) Pressure profile and b) Mach profile MDM, c) Pressure profile for steam d) Pressure profile for 75 % CO_2-Air mixture; the black continuous line represents the numerical solution and the black solid points, the experimental data and dashed line the throat position. 75
Figure 4.9 – Pressure distribution Arina's nozzle, ($P_0 = 100$ kPa, $T_0 = 288$ K), for dry air, dash-dotted line presents the throat position. 76
Figure 4.10–Prandtl-Mayer expansion wave. Adapted from (Hodge; Koenig, 1995). . 77
Figure 4.11–Real gas effects on Prandtl-Meyer angle in function of total velocity (a), and Mach number (b) for Toluene. 78
Figure 4.12–Droplet growth graphical representation. Adapted from (Peeters et al., 2004a). 80
Figure 4.13–Hugoniot curve (solid) and Rayleigh line (dashed) solution for a discontinuous condensation shock. 83
Figure 4.14–Typical pressure profile for a condensation shock. 84
Figure 4.15–Condensation shock control volume. 85
Figure 4.16–Specific entropy profile in a condensation shock. 91
Figure 4.17–Continuous condensation shock numerical solution. 92
Figure 4.18–Solution proceedure for the condensation shock thickness, discontinuous solution (dashed-dotted line), initial solutions (dashed lines) and the correct solution (continuous line). 92
Figure 4.19–Numerical results for Bakhtar & Zidi (1989) experiment a) Results for Rankine-Hugoniot maximum entropy production, b) Real gas weak shock approximation, (Water, $P_0 = 35.5$ bar, $T_0 = 548.6$ K). 93
Figure 4.20–Numerical results for Bier et al. (1990b) carbon dioxide condensation experiment a) and c) Results for Rankine-Hugoniot maximum entropy production, b) and d) Real gas weak shock approximation, for two stagnations temperature conditions $T_0 = 300.1$ K Figs. a and b, $T_0 = 304.1$ K Figs. c and d, respectively. 94
Figure 4.21–Numerical results for Bier et al. (1990a) carbon dioxide - dry air condensation experiment a) and c) Results for Rankine-Hugoniot maximum entropy production, b) and d) Real gas weak shock approximation, for two stagnations conditions i = ($P_0 = 9.98$ bar, $T_0 = 249.4$ K, CO_2 $\bar{x}_0 = 0.75$), and ii ($P_0 = 16.73$ bar, $T_0 = 243.3$ K, CO_2 $\bar{x}_0 = 0.5$). 95
Figure 4.22–Streamline, characteristic lines and interior operator. 98
Figure 4.23–Wall construction for axisymmetric nozzles. 101
Figure 4.24–Planar wall shape construction. 102

Figure 4.25–Inverse Prandtl-Meyer angle algorithm solver. 103
Figure 4.26–Flow diagram of MOC implementation for short axisymmetric and planar nozzles. 105
Figure 4.27–Mach, pressure and temperature surfaces for planar (left) and axisymmetric (right) nozzles, for Carbon dioxide. 106
Figure 4.28–Mach, pressure and temperature surfaces for planar (left) and axisymmetric (right) nozzles, for R1234yf under supercritical stagnation conditions. 106
Figure 4.29–Mach, pressure and temperature surfaces for planar (left) and axisymmetric (right) nozzles, for a carbon dioxide (50% mass fraction) methane mixture under high pressure stagnation conditions 107
Figure 4.30–Viscous simulation for carbon dioxide a) axisymmetric, b) planar and R1234yf c) axisymmetric d) planar nozzles. 108
Figure 4.31–Mach profile at nozzle outlet for different fluids and configurations. . . 109
Figure 4.32–Supersonic nozzle with central body, for CH_4-CO_2 50% mass mixture. . 110
Figure 5.1 – Phenomena involved in the supersonic separation operation. a) Real gas compressible flow of multiphase species, b) Shock waves formation and photographic documentation, c) Phase change formation, d) multiphase supersonic flow. 111
Figure 5.2 – Operation region test rig for a carbon dioxide - nitrogen mixture, coloured lines represent the binodal line for several CO_2 molar fractions, $\bar{x}$. 112
Figure 5.3 – Tank discharge time. 113
Figure 5.4 – Test-rig P&ID. 115
Figure 5.5 – Gas preparation section design. 116
Figure 5.6 – Laboratory refinishing a) Year 2018 b) Year 2022. 116
Figure 5.7 – Supersonic nozzle test-rig. 117
Figure 5.8 – Pressure regulation valve. 118
Figure 5.9 – K-Lab NOVA flow conditioner a) Part after machining b) installed in piping. 119
Figure 5.10–Termocouple installation in the stagnation chamber. 120
Figure 5.11–3D adaptor construction a) super-ellipses and profiles b) mechanical construction. 121
Figure 5.12–Finite element analysis of the supersonic nozzle, a) Von Misses stress results, b) Displacement. 122
Figure 5.13–Characteristic lines network for the nozzle supersonic part construction. 122
Figure 5.14–Wall profile construction for different carbon dioxide molar compositions. 124
Figure 5.15–O'ring groove and tap hole detail, units in mm. 124
Figure 5.16–Nozzle parts after machining a) Nozzle support, profiles, windows and cover, b) Nozzle profiles. 125

Figure 5.17–Supersonic nozzle and downstream section. 126
Figure 5.18–Optical tables alignment. 127
Figure 5.19–Direct optical arrangement, a) Lamp and light tunnel configuration, b) High-speed camera location. 128
Figure 5.20–Schlieren arrengment, ① Light source, ② optical fibre, ③ condensing lens, ④ flat mirror, ⑤ parabolic mirror, ⑥ direct still picture camera, ⑦ parabolic mirror, ⑧ flat mirror, ⑨ knife edge, ⑩ high-speed camera. 129
Figure 5.21–Typical test, tank pressure and stagnation temperature and pressure behaviour during a test. 130
Figure 5.22–First tests pressure profile nozzle 1, dry air $P_0 = 6$ bar, $T_0 = 293.5$. . . 131
Figure 5.23–First tests pressure profile nozzle 2, dry air $P_0 = 6$ bar, $T_0 = 295.3$. . . 131
Figure 6.1 – Supersonic flow regimes evaluated. 135
Figure 6.2 – Test 38 results a) Supersonic channel schlieren still picture, b) Nozzle pressure profile for a $t = 0$ s, c) Stagnation P_0, throat P_{th}, exit pressure P_e and stagnation temperature T_0 test evolution. 138
Figure 6.3 – Droplet separation on the transition regime. 139
Figure 6.4 – Test 21 results, a) Supersonic channel schlieren still picture b) Nozzle centreline grey pixel intensity, c) Nozzle pressure profile for a $t = 0$ s, d) Stagnation P_0, throat P_{th}, exit pressure P_e and stagnation temperature T_0 test evolution. 140
Figure 6.5 – Test 31 results, left $t = 0$ s and right $t = 4.5$ s. a and b) Supersonic channel schlieren still picture, c and d) Nozzle centreline grey pixel intensity, e and f) Nozzle pressure profile and g) Stagnation P_0, throat P_{th}, exit pressure P_e and stagnation temperature T_0 test evolution. . . 141
Figure 6.6 – Test 26 results, a) Supersonic channel schlieren still picture b) Nozzle centreline grey pixel intensity, c) Nozzle pressure profile for a $t = 0$ s, d) Stagnation P_0, throat P_{th}, exit pressure P_e and stagnation temperature T_0 test evolution. 142
Figure 6.7 – Test 30 results, a) Supersonic channel schlieren still picture, b) Nozzle pressure profile for a $t = 0$ s, c) Stagnation P_0, throat P_{th}, exit pressure P_e and stagnation temperature T_0 test evolution. 143
Figure 6.8 – Condensation shock starting position for $J_{crt} = 1 \times 10^{10}$ m^{-3}s^{-1}. 144
Figure 6.9 – Continuous condensation shock theory comparison, a) Test 31 A, b) Test 31 B and c) Test 38 A. 146
Figure A.1 – Droplet in a supersonic separator. 162
Figure A.2 – Axes and signs convention. 165
Figure A.3 – Thermodynamic potential 4D hypercube. 165
Figure F.1 – Flow rectifier technical drawing according to K-lab nova design established in ABNT NBR ISO 5167-1 181

Figure F.2 – Planar nozzle body technical drawing . . . 182
Figure F.3 – Nozzle profile 1A technical drawing. . . . 183
Figure F.4 – Nozzle profile 1B technical drawing. . . . 184
Figure F.5 – Nozzle profile 2A technical drawing. . . . 185
Figure F.6 – Nozzle profile 2B technical drawing. . . . 186
Figure F.7 – Window cover technical drawing. . . . 187
Figure F.8 – Optical windows technical drawing. . . . 188
Figure F.9 – Discharge welded assembly 1. . . . 189
Figure F.10– Discharge welded assembly 2. . . . 190
Figure F.11– Discharge threaded assembly 3. . . . 191
Figure G.1 – Compressor Reavell 5211 layout . . . 194
Figure H.1 – Temperature dry block calibrator and reference. . . . 196
Figure H.2 – Pressure calibrator connection to test-rig. . . . 198
Figure I.1 – Test 21 results, a) Supersonic channel schlieren still picture b) Nozzle centreline grey pixel intensity, c) Nozzle pressure profile for a $t = 0$ s, d) Stagnation P_0, throat P_{th}, exit pressure P_e and stagnation temperature T_0 test evolution. . . . 200
Figure I.2 – Test 22 results, left $t = 0$ s and right $t = 4$ s. a and b) Supersonic channel direct still picture, c and d) Nozzle centreline grey pixel intensity, e and f) Nozzle pressure profile and g) Stagnation P_0, throat P_{th}, exit pressure P_e and stagnation temperature T_0 test evolution. . . . 201
Figure I.3 – Test 23 results, left $t = 0$ s and right $t = 6$ s. a and b) Supersonic channel direct still picture, c and d) Nozzle centreline grey pixel intensity, e and f) Nozzle pressure profile and g) Stagnation P_0, throat P_{th}, exit pressure P_e and stagnation temperature T_0 test evolution. . . . 202
Figure I.4 – Test 24 results, left $t = 0.5$ s and right $t = 4.5$ s. a and b) Supersonic channel schlieren still picture, c and d) Nozzle centreline grey pixel intensity, e and f) Nozzle pressure profile and g) Stagnation P_0, throat P_{th}, exit pressure P_e and stagnation temperature T_0 test evolution. . . . 203
Figure I.5 – Test 25 results, left $t = 0$ s and right $t = 3$ s. a and b) Supersonic channel direct still picture, c and d) Nozzle centreline grey pixel intensity, e and f) Nozzle pressure profile and g) Stagnation P_0, throat P_{th}, exit pressure P_e and stagnation temperature T_0 test evolution. . . . 204
Figure I.6 – Test 26 results, a) Supersonic channel schlieren still picture b) Nozzle centreline grey pixel intensity, c) Nozzle pressure profile for a $t = 0$ s, d) Stagnation P_0, throat P_{th}, exit pressure P_e and stagnation temperature T_0 test evolution. . . . 205

Figure I.7 – Test 27 results, a) Supersonic channel schlieren still picture b) Nozzle centreline grey pixel intensity, c) Nozzle pressure profile for a $t = 0$ s, d) Stagnation P_0, throat P_{th}, exit pressure P_e and stagnation temperature T_0 test evolution. 206
Figure I.8 – Test 28 results, a) Supersonic channel direct still picture b) Nozzle centreline grey pixel intensity, c) Nozzle pressure profile for a $t = 0$ s, d) Stagnation P_0, throat P_{th}, exit pressure P_e and stagnation temperature T_0 test evolution. 207
Figure I.9 – Test 30 results, a) Supersonic channel schlieren still picture, b) Nozzle pressure profile for a $t = 0$ s, c) Stagnation P_0, throat P_{th}, exit pressure P_e and stagnation temperature T_0 test evolution. 208
Figure I.10–Test 31 results, left $t = 0$ s and right $t = 4.5$ s. a and b) Supersonic channel schlieren still picture, c and d) Nozzle centreline grey pixel intensity, e and f) Nozzle pressure profile and g) Stagnation P_0, throat P_{th}, exit pressure P_e and stagnation temperature T_0 test evolution. . . 209
Figure I.11–Test 32 results, a) Supersonic channel direct still picture, b) Nozzle pressure profile for a $t = 0$ s, c) Stagnation P_0, throat P_{th}, exit pressure P_e and stagnation temperature T_0 test evolution. 210
Figure I.12–Test 33 results, a) Supersonic channel direct still picture, b) Nozzle pressure profile for a $t = 0$ s, c) Stagnation P_0, throat P_{th}, exit pressure P_e and stagnation temperature T_0 test evolution. 211
Figure I.13–Test 34 results, a) Supersonic channel schlieren still picture, b) Nozzle pressure profile for a $t = 0$ s, c) Stagnation P_0, throat P_{th}, exit pressure P_e and stagnation temperature T_0 test evolution. 212
Figure I.14–Test 36 results a) Supersonic channel direct still picture, b) Nozzle pressure profile for a $t = 0$ s, c) Stagnation P_0, throat P_{th}, exit pressure P_e and stagnation temperature T_0 test evolution. 213
Figure I.15–Test 38 results a) Supersonic channel schlieren still picture, b) Nozzle pressure profile for a $t = 0$ s, c) Stagnation P_0, throat P_{th}, exit pressure P_e and stagnation temperature T_0 test evolution. 214

List of Tables

Table 2.1 – Supersonic separation Nozzles. 36
Table 4.1 – Stagnation points, and experimental data used for validation. 74
Table 5.1 – Springs used in the pressure regulation valve, data from manufacturer. . 118
Table 6.1 – Supersonic condensation tests 136
Table 6.2 – Mach numbers and temperatures at the condensation shock start. 145
Table A.1 – Conjugates of the fundamental equation 163
Table A.2 – Legendre transforms 164
Table A.3 – Thermodynamic potentials 167
Table A.4 – Maxwell Relations 167
Table E.1 – Preasure tap position nozzle 1. 177
Table E.2 – Preasure tap position nozzle 2. 177
Table E.3 – Nozzle channel profile 1, nozzle width 40 mm. 178
Table E.4 – Nozzle channel profile 2, nozzle width 40 mm. 179
Table H.1 – Stagnation thermocouple calibration and uncertainty assessment 197
Table H.2 – 17 bar kulites calibration and uncertainty assessment 197
Table H.3 – 35 bar kulites calibration and uncertainty assessment 198

List of abbreviations and acronyms

CCS	Carbon capture and storage
CFD	Computational fluid dynamics
EOS	Equation-of-state
MPEOS	Multi-parameter equation-of-state
MOC	Method of characteristics
MUSCL	Monotonic Upstream-centered Scheme for Conservation Laws
ORC	Organic Rankine Cycle
PREOS	Peng–Robinson Equation-of-state
SSL	Straight Sonic Line
SRKEOS	Soave-Redlich-Kwong equation of state
TRL	Technology readiness level
UN	United nations
VdWEOS	Van der Waals Equation-of-state

List of symbols

Latin symbols:

a	Polynomial adjust coefficients
A	Area m^2
c	Speed-of-sound ms^{-1}
C	Conjugate variable
C_P	Specific heat at constant pressure ($Jkg^{-1}K^{-1}$)
C_v	Specific heat at constant volume ($Jkg^{-1}K^{-1}$)
đ	Inexact differential
D_h	Hydraulic diameter (m)
D_m	Molecular diffusion coefficient (m^2s^{-1})
$error$	Instrument measurement error
ƒ	Specific Helmholtz free energy (Jkg^{-1})
f	Fanning friction factor
F	Helmholtz free energy (J)
$\mathscr{F}$	Legendre transform
$\mathcal{F}$	Fugacity (Pa)
g	Specific Gibbs free energy (Jkg^{-1})
Gr	Grüneisen paramenter

G	Gibbs free energy (J)
h	Specific enthalpy (Jkg^{-1})
$\dot{H}$	Heat time rate (W)
J	Homogeneous nucleation ratio ($\mathrm{s}^{-1}\mathrm{m}^{-3}$)
J	Mass flux ($\mathrm{kgs}^{-1}\mathrm{m}^{-2}$)
k	Isothermal compressibility (Pa^{-1})
k_B	Boltzmann constant $1.380649 \times 10^{-23}(\mathrm{m}^2\mathrm{kgK}^{-1}\mathrm{s}^{-2})$
K_n	Knudsen number
K	Integration constant method of characteristics
$\hat{l}$	Mean free path characteristic length (m)
$\mathfrak{m}$	Vapour molecular mass (kg)
$\dot{M}$	Mass flow rate (kgs^{-1})
$\mathcal{M}$	Any thermodynamic property
M	Mach number
N	Number of moles (mol)
P	Pressure (Pa)
q	Specific heat transfer (Jkg^{-1})
r	Radius (m)
$\mathcal{R}$	Universal gas constant ($\mathrm{Jmol}^{-1}\mathrm{K}^{-1}$)
Re	Reynolds number
s	Specific entropy ($\mathrm{Jkg}^{-1}\mathrm{K}^{-1}$)
$\mathcal{S}$	Supersaturation ratio
S	Entropy (JK^{-1})
SEE	Standard error of estimate
t	Time (s)
T	Temperature (K)

$\mathfrak{u}$	Specific internal energy (Jkg^{-1})
U	Instrument uncertainty
v	Specific volume ($\mathrm{m}^3\mathrm{kg}^{-1}$)
V	Total velocity (ms^{-1})
V	Volume (m^3)
w	Specific work (Jkg^{-1})
$\bar{x}$	molar fraction
x	Axial space coordinate (m)
X	Independent variable
y	orthogonal axis coordinate (m)
y	Liquid mass fraction ratio
Z	Compressibility factor

Superscripts:

$*$	Critical cluster condition
eq	State in thermodynamic equilibrium
r	Ideal part
$\circ$	Residual part

Subscripts:

0	Stagnation or reference condition
c	Critical fluid's condition
e	Nozzle exit
l	Relative to the liquid phase
g	Relative to the gas phase
r	Reference state for real gas mixtures
s	Relative to the surface interphase
s	Relative to the sonic point

th	Relative to the nozzle throat

Greek symbols:

α	Non-dimensional Helmholtz free energy
γ_{PV}	Real gas isentropic exponent
Γ	Fundamental derivative of gas dynamics
δ	Non-dimensional density
$\Delta\varphi$	Critical cluster formation free energy (J)
ϵ	Channel surface roughness height (m)
ζ	Zeldovich factor
η	Dynamic viscosity (Pa s)
$\bar{\theta}$	Non-dimensional surface tension
θ	Streamline angle
Λ	Viscous potential (m^{-1})
$\bar{\mu}$	Chemical potential (Jmol^{-1})
μ	Mach angle
ν	Prandtl-Meyer angle
Π	Non-dimensional pressure jump.
ρ	Density (kgm^{-3})
σ	Surface tension (Nm^{-1})
τ	Non-dimensional temperature
$\hat{\tau}$	Relaxation time
τ_w	Wall friction shear stress (Pa)
ϕ	Velocity potential
$\bar{\phi}$	Fugacity coefficient
Φ	Specific entropy source term ($\mathrm{JkgK}^{-1}\mathrm{m}^{-1}$)

Contents

1 INTRODUCTION . . . 21
1.1 Motivation and Scientific Contribution . . . 24
1.2 Thesis objective . . . 26
1.3 Thesis outline . . . 26
1.4 Thesis achievements . . . 27
1.5 Journal papers . . . 28
1.6 Conference proceedings . . . 29
1.7 Patent . . . 29

2 STATE OF THE ART OF SUPERSONIC GAS SEPARATION EXPERIMENTAL FACILITIES . . . 30

3 REAL GAS MIXTURE THERMODYNAMICS . . . 37
3.1 Multiparameter equation-of-state . . . 37
3.1.1 Pure substance . . . 38
3.1.2 Multicomponent . . . 40
3.2 Isothermal reconstruction . . . 44
3.3 Phase stability . . . 46
3.3.1 Phase stability for a pure substance . . . 47
3.3.2 Phase stability for a binary mixture . . . 48
3.4 Droplet work of formation. . . . 50
3.4.1 General expression of droplet work for a pure substance. . . . 52
3.5 Homogeneous nucleation . . . 53
3.5.1 Homogeneous nucleation kinetics . . . 55

4 REAL GAS COMPRESSIBLE FLUID DYNAMICS . . . 60
4.1 Quasi-one dimensional compressible viscous flow . . . 61
4.1.1 Compressible viscous real gas governing equations . . . 62
4.1.2 Sonic point . . . 66
4.1.3 Sonic point displacement . . . 66
4.1.4 Rankine-Hugoniot relations . . . 68
4.1.5 Friction factor . . . 69
4.1.6 Numerical solution . . . 69
4.1.6.1 Fourth-order Runge-Kutta . . . 71
4.1.6.2 Sonic point and shock wave capture . . . 72
4.1.7 Perfect viscous gas flow verification . . . 73

4.1.8 Real viscous gas flow validation . . . 73
4.1.9 Shock wave position verification . . . 76
4.2 Prandtl-Meyer expansion waves . . . 76
4.3 Condensation shock . . . 78
4.3.1 Droplet growth phenomena . . . 79
4.3.2 Single fluid model . . . 82
4.3.3 Discontinuity shock . . . 82
4.3.4 Continuous condensation shock . . . 84
4.3.5 Maximum entropy jump for a real gas weak shock . . . 87
4.3.6 Chapman-Jouguet point . . . 89
4.3.7 Numerical solution . . . 91
4.3.8 Condensation shock results . . . 93
4.3.8.1 Pure substance . . . 93
4.3.8.2 Mixture . . . 95
4.4 Method of characteristics . . . 96
4.4.1 Method of characteristics theory . . . 98
4.4.2 Numerical implementation . . . 99
4.4.2.1 Axisymmetric flow Solution . . . 99
4.4.2.2 Planar flow solution . . . 102
4.4.3 Real gas isentropic solver . . . 103
4.4.4 Results . . . 104
4.4.5 Wall shape verification . . . 107
4.4.6 Supersonic gas separator design . . . 109

5 EXPERIMENTAL TEST-RIG . . . 111
5.1 Gas preparation section . . . 114
5.2 Test section . . . 114
5.2.1 Pressure regulation valve . . . 117
5.2.2 Flow rectifier . . . 118
5.2.3 Stagnation chamber and 3D adapter . . . 119
5.2.4 Supersonic planar nozzle . . . 120
5.2.4.1 Mechanical design . . . 120
5.2.4.2 Supersonic channel design . . . 122
5.3 Downstream section . . . 125
5.4 Optical methods . . . 126
5.4.1 Direct optical arrangement . . . 127
5.4.2 Schlieren optical method . . . 127
5.5 First tests results . . . 129
5.6 Test rig Operation checklist . . . 132

6 EXPERIMENTAL RESULTS AND ANALYSIS 134
6.1 Classical condensation shock 135
6.2 Transition condensation shock 137
6.3 Mach wave condensation shock 139
6.4 Condensation shock theory validation 143
6.4.1 Critical nucleation rate criteria 143
6.4.2 Continuous condensation shock theory 145

7 CONCLUSIONS AND FUTURE WORKS 147

BIBLIOGRAPHY 150

APPENDIX 161

A – DROPLET THERMODYNAMICS 162

B – DEVELOPMENT OF COMPABILITY AND CHARACTERISTIC EQUATIONS 170
B.1 Characteristic Equation 171
B.2 Compatibility Equation 172

C – TWO-PHASE THERMODYNAMIC PROPERTIES 173

D – DISCHARGE TIME ANALYTICAL EXPRESSION 175

E – NOZZLES PROFILES AND PRESSURE TAPS LOCATIONS . 177

F – TECHNICAL DRAWINGS TEST RIG 180

G – TANK AND COMPRESSOR 192

H – CALIBRATION AND UNCERTAINTY ANALYSIS 195
H.1 Stagnation temperature calibration 195
H.2 Nozzle pressure transducer calibration 196

I – EXPERIMENTAL RESULTS 199

1 Introduction

In recent years, a remarkable acceleration in the research and development of new technologies to achieve a reliable energy transition has occurred. That has been lead by industrial companies, universities and research institutes around the world. Several efforts have been performed in order to achieve feasible energy growth to fulfil the sustainable development goals established by the United Nations (UN), specially the number seven related to affordable and clean energy. Numerous approaches are on the way, being carbon capture and sequestration (CCS) one of the more relevant options, because this technology becomes a key player in the energy transition towards cleaner energy vectors such as hydrogen or ammonia. In addition, it allows the use of existing infrastructure in which carbon dioxide can be used to add value to the processes, such as synthetic fuels production or their use as raw material by the chemical industry.

Also, CCS technologies could become an important tool to improve processes efficiency and production cost reductions, such as the pre-salt natural gas extraction process in the Brazilian coast. This is a critical subject for Brazilian energy independence, due to the pre-salt reservoir relevance in Brazilian oil production, making up to 56% (Oddone, 2018) of the total oil reserves in 2018. Nevertheless, the Brazilian oil and gas industry faces several challenges, including, among others, the oil extraction at ultra-deep water (Beltrao et al., 2009) and natural gas mixtures with high CO_2 concentrations (up to 80% in molar basis) (Nunes; Peinemann, 2006; d'Almeida et al., 2018), as shown in fig. 1.1. Therefore, from the oil and gas extraction economical point of view, such companies require new technologies that allow them to achieve low operational carbon dioxide extraction costs at a reduced platform space. The extraction process can be summarized in the following operational requirements:

- Reliable separation at high CO_2 concentrations;
- Low energy consumption;
- Low maintenance;

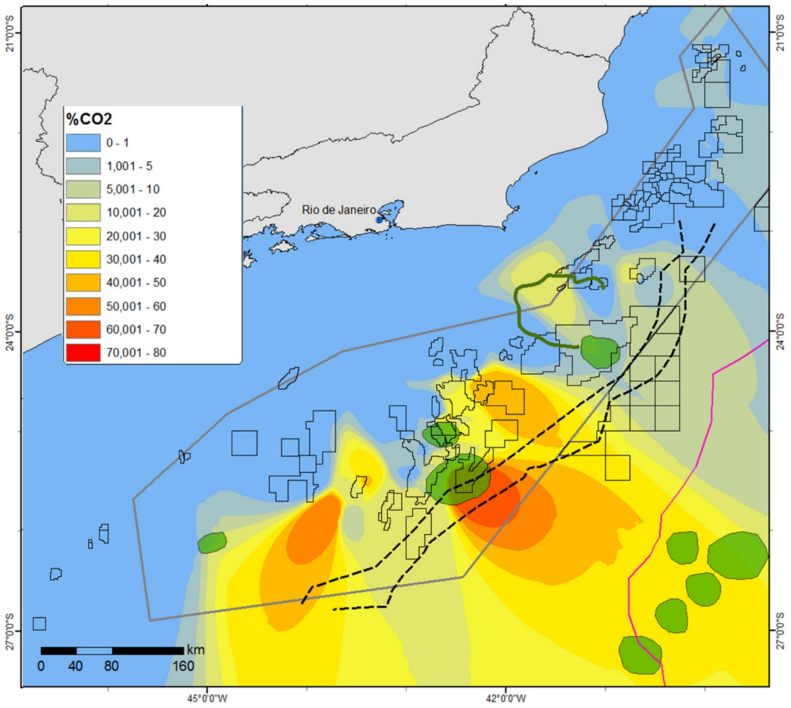

Figure 1.1 – CO_2 composition in Brazilian Pre-Salt fields. Adapted from (d'Almeida et al., 2018).

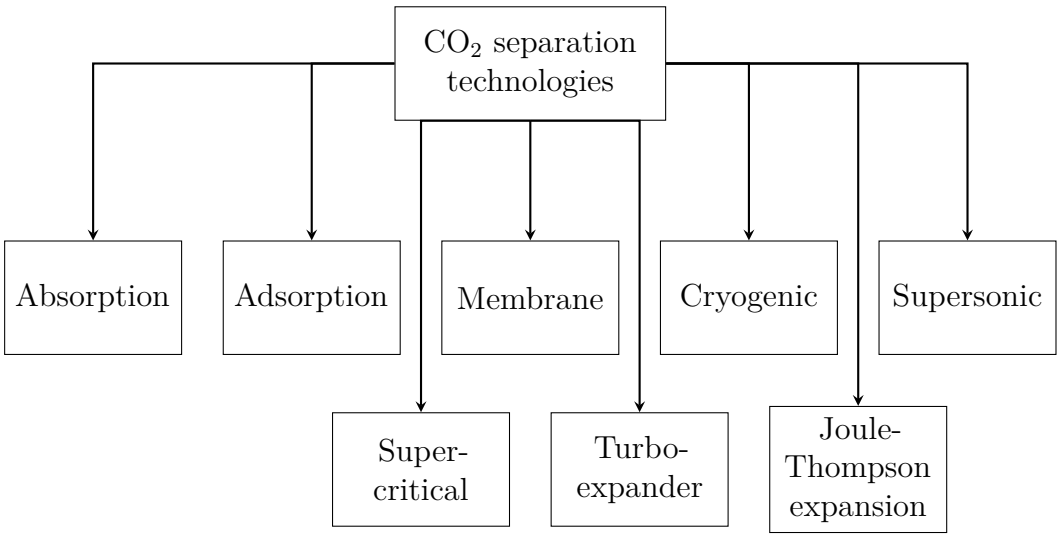

Figure 1.2 – Carbon dioxide separation technologies for off-shore platforms.

- Low Footprint.

Fig. 1.2 presents the current market options for the off-shore CO_2 separation. Each one has different working principles, however, one can divide them into three major groups. Firstly, absorption and adsorption technologies based their working principle on a surface or volumetric mass transfer from the carbon dioxide rich stream to a solute or adsorption material. In this same category one can find membrane separation, this technology uses permeable materials to separate different compounds from a rich carbon dioxide stream,

thanks to the membrane selectivity and the mass transfer area. All of these technologies have in common the requirement of high separation areas for elevated flow rates and carbon dioxide concentrations, which constrains their application potential in reduced space areas as the case of offshore platforms. Secondly, there is the cryogenic separation option. This alternative consists of the carbon dioxide rich stream refrigeration until the two-phase region achievement, resulting in carbon dioxide and other volatile compounds condensation from natural gas. Hence, this separation option requires auxiliary equipment and an external energy source for the refrigeration process, being both undesirable for an offshore extraction platform. Also, as stated by Goulart et al. (2020) the use of natural gas storage at supercritical conditions (high pressures and low temperatures) in salt caverns, could be used as carbon dioxide separation procedure. Because, due to the carbon dioxide's high molecular weight there is a gravimetric separation inside the cavern, leading to a lower concentration fraction at the cavern top.

Finally, there is a fourth category, which consists of a fluid strong expansion until achieving the two-phase change region. In this category, one can find the supersonic gas separation, turbo-expander and Joule-Thompson valve utilization. The last two technologies present high expansion irreversibilities leading to a significant loss in the stagnation pressure, resulting in the necessity of auxiliary compression equipment.

The aforementioned technologies require higher platform space for their utilization compared to supersonic gas separation and additional energy consumption. This scenario gives supersonic carbon dioxide separation a competitive advantage for the initial treatment of high carbon dioxide content flows, due to supersonic regime formation inside the device, leading to high mass flows rate achievement in a low off-shore platform area. In addition, this device can work without an electric energy supply, and can also operate with natural gas mixtures at high stagnation pressures and carbon dioxide concentrations. These technical advantages result in lower operating costs, as concluded by Machado et al. (2012). Therefore, due to this technology's relevance for the Brazilian oil and gas industry, the supersonic gas separation process should be studied and improved in order to increase the oil and gas extraction competitiveness of the Brazilian pre-salt reservoirs.

The working principle of a supersonic separator is based on a gas mixture supersonic expansion. That expansion leads to a sudden decrease of the flow temperature and pressure, and eventually under proper conditions the non-equilibrium condensation will be reached. After that, the condensed carbon dioxide could be removed by mechanical means, as the use of a swirling mechanism resulting in the contaminant separation by the mechanical removal of the droplets, allowing to achieve CO_2 concentrations up to 2% (Imaev et al., 2014). Fig. 1.3 exposes the more important parts of a supersonic separator, listed below:

- Gas Inlet: Inlet of CO_2 rich stream (1);

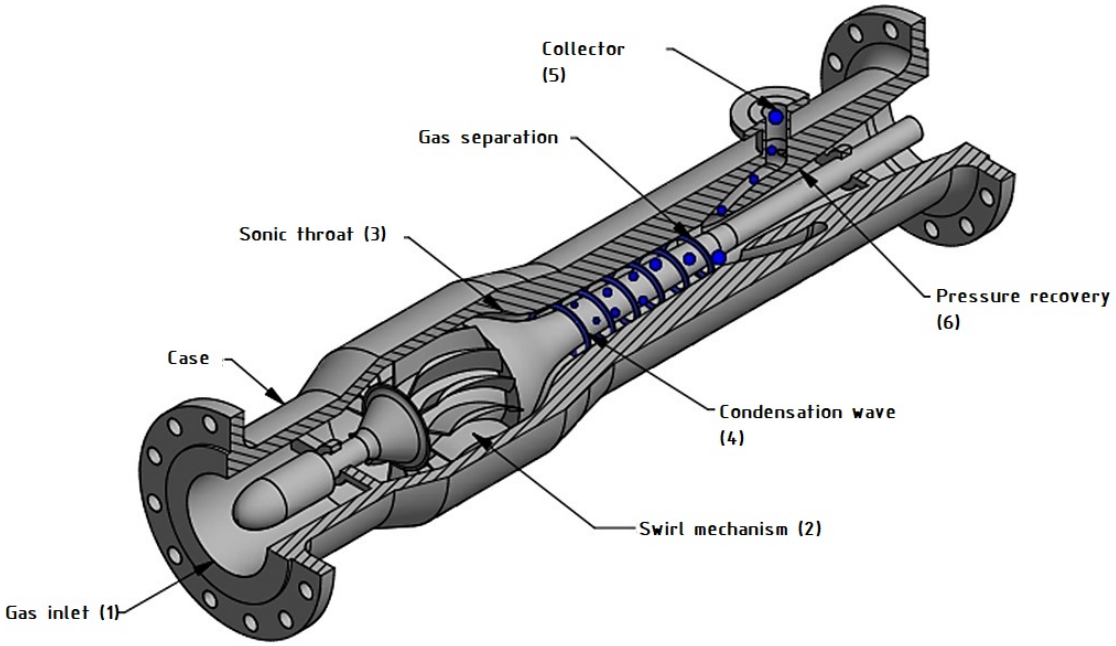

Figure 1.3 – Supersonic Separator typical design (Meneghini et al., Brazil patent, BR 20 2020 017289 7 U2, August 2020).

- Swirl mechanism: Mechanism used to mechanically separate the flow (e.g, vanes or elbow) (2);
- Sonic throat: Minimum flow area (3);
- Condensation Wave: Start of CO_2 condensation (4);
- Collector: Chamber used for CO_2 Collection (5);
- Pressure recovery: Supersonic diffuser used to recover the pressure on the flow (6).

1.1 Motivation and Scientific Contribution

As presented in the last section, supersonic gas separation technology is vital for some processes, especially for Brazilian off-shore natural gas production. Despite the supersonic gas separator's simple construction (see Fig. 1.3), this device presents complex underlying phenomena due to the combined effects of compressible flow, supersonic regime, real gas effects and non-equilibrium condensation. Therefore, further research must be performed in order to increase the Technology readiness level (TRL) of this device.

Thereby, two approaches must be performed to ensure this technology deployment. The first one is related to a theoretical framework formation, because there is a theoretical gap in real gas mixtures supersonic flows analysis. Hence, this work studies and applies the classic gas dynamics theory in order to reach an improved device analysis. This is

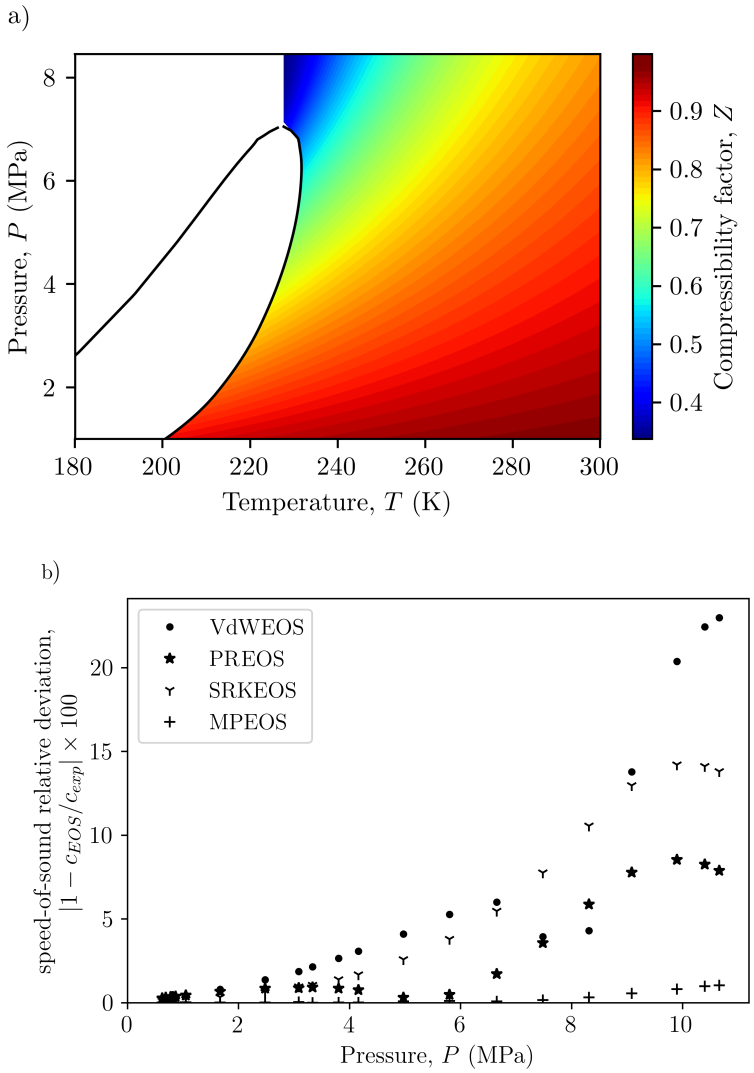

Figure 1.4 – Real gas effects, a) Compressibility factor for a methane and carbon dioxide mixture (50% CO_2), b) deviation on the speed-of-sound calculation for a methane and carbon dioxide mixture (30% mole CO_2 at 250 K) using different EOS, experimental data from (Younglove et al., 1993).

important since at high pressures the compressibility factor Z for methane - carbon dioxide mixture returns values close to 0.3 as presented in Fig. 1.4a, which makes the perfect gas approach not feasible for this application. Therefore, a precise device analysis requires robust equation-of-state (EOS) in their performance calculation. Nevertheless, not all EOS will give the desired outcomes precision, because as presented on Fig. 1.4b, the EOS selection influences the speed-of-sound computation deviation. For this evaluation was selected the more popular cubic EOSs, namely: Van der Waals EOS (VdWEOS), Soave-Redlich-Kwong EOS (SRKEOS) and Peng-Robinson EOS (PREOS) and a state-of-the-art EOS called Multi-Parameter EOS (MPEOS), and later compared them against experimental data collected by Younglove et al. (1993). The Fig. 1.4b outcomes show better MPEOS performance compared to cubic EOS, specially at high pressures, and these speed-of-sound deviations impact the compressible flow solution as presented by Restrepo

et al. (2022). In conclusion, real gas effects have to be considered for the device designing and analysis, and also the EOS selection has an important effect on the device evaluation and, for this reason a MPEOS will be used in this thesis.

Additional to a new theoretical framework for the study of the real gas mixture supersonic flows, this thesis also presents the design and construction of a state-of-the-art test-rig for the experimental evaluation of supersonic gas separators. This test-rig is devoted to operating at high CO_2 fractions to study the combined effects of pressure, concentration and temperature on the device stagnation conditions, and in the separator performance. Also, special care has been dedicated to obtaining a robust design and flexibility to testing different supersonic gas separators geometries and arrangements.

1.2 Thesis objective

This thesis carries out a theoretical framework for the analysis and design of supersonic gas separators; such a framework allows to consider the viscous, real, and bidimensional flow effects on the real gas compressible flows computation. In addition, this thesis presents the design and construction process of a unique test rig for evaluating such devices. This test rig assesses the stagnation conditions variations namely: pressure, temperature, and concentration on the condensation shock formation. Both approaches are devoted to accelerating the development of supersonic gas separation technologies and increasing their competitiveness and efficiency.

1.3 Thesis outline

To fulfil the thesis objective, this work is separated in several chapters,as explained as follows:

- Chapter 1 shows the work introduction.
- Chapter 2 presents the experimental evaluation of supersonic separators state-of-the-art.
- Chapter 3 shows the theoretical concepts related to the real gas thermodynamics required for the supersonic separator evaluation, and the spinodal line formation and the homogeneous condensation phenomena in a real gas mixture.
- Chapter 4 focuses on the derivation of a real gas compressible fluid dynamics theory for supersonic gas separators; this chapter is divided into two sections: the first one explores the gas dynamics theory for real gas mixtures (e.g., quasi-one-dimensional viscous flow; normal shock waves; expansion and condensation waves), and the

second one, apply these concepts on the supersonic gas separator construction (through the method of characteristics). This chapter shows the new theoretical developments achieved in this thesis, such as a new formulation for real gas viscous flows computation proposal, the application of the method of characteristics for real gas mixtures, and new approaches for the solution of condensation waves on real gases.

- Chapter 5 describes the designing and construction process of the developed test-rig, it is important to highlight that the theory developed in chapter 4, allows the test-rig designing.
- Chapter 6 presents and discusses the experimental outcomes obtained in the new test-rig.
- Chapter 7 collects the conclusions of the entire work and also suggests the next activities to be performed in this research line.

1.4 Thesis achievements

The new theoretical framework and experimental test-rig construction lead to the following achievements classified by their contribution:

Theoretical achievements:

- It was presented a thermodynamic framework for the evaluation of supersonic gas separators.
- It was developed a new theory for the analysis of real gas viscous flows in supersonic nozzles.
- It was developed a robust solver for the computation of the Prandtl-Meyer angle for real gas mixtures.
- It was developed a new approach for solving condensation shocks in real gas mixtures.
- It was developed new mathematical expressions for the maximum non-dimensional pressure jump and specific entropy jump computation for a real gas weak shock.
- The method of characteristics was implemented for the first time in the open literature for real gas mixtures in planar and axisymmetric short nozzles.
- A patent for a variable area supersonic gas separator was registered.

Experimental achievements:

- It was designed and constructed a unique experimental infrastructure for the evaluation of supersonic gas separators.
- It was constructed a test-rig with the state-of-the-art design guidelines. It was included a flow rectifier and a three-dimensional adapter constructed by additive manufacturing.
- It was designed and constructed a planar nozzle frame, which allows the use of interchangeable nozzles at high pressures without high deformations and leaks.
- It was designed and constructed a set of supersonic nozzles using the method of characteristic for real gases mixtures.
- It was implemented two optical evaluation techniques for the supersonic flow analysis.
- It was designed and constructed a high precision rail system to allow the axial displacement of the discharge section, allowing the testing of supersonic separators of different geometries and sizes.
- It was proposed and implemented a routine for the test-rig operation.

Such achievements resulted in the following publications in international journals, conference proceedings and in a patent deposit:

1.5 Journal papers

- Short nozzles design for real gas supersonic flow using the method of characteristics. **Applied Thermal Engineering**., 207, 118063. Restrepo, J. C., Bolaños-Acosta, A. F., & Simões-Moreira, J. R. (2022).
  doi: 10.1016/j.applthermaleng.2022.118063 .
- Two semi-analytical approaches for solving condensation shocks in supersonic nozzle flows. **Int. J. Heat Mass Transfer**, 173, 121212. Bolaños-Acosta, A. F., Restrepo, J. C., & Simões-Moreira, J. R. (2021).
  doi: 10.1016/j.ijheatmasstransfer.2021.121212 .
- Viscous effects on real gases in quasi-one-dimensional supersonic convergent-divergent nozzle flows. **Journal of Fluid Mechanics** . Restrepo, J. C. & Simões-Moreira, J. R. doi: https://doi.org/10.1017/jfm.2022.853.

1.6 Conference proceedings

- Numerical study and development of an experimental test-rig configuration of a supersonic nozzle for gas separation. In: **26th International Congress of Mechanical Engineering, 2021, Florianopolis**
- Theoretical analysis of supersonic phase change for carbon dioxide in a de Laval nozzle. **25th IIR International Congress of Refrigeration, 2019, Montreal**
- Operational Behaviour of Supersonic Separators for Real Gas Mixtures of Methane and Carbon Dioxide, From the Homogeneous Nucleation Point of View. In: **ASME 2019 38th International Conference on Ocean, Offshore and Arctic Engineering, 2019, Glasgow.**
- Real gas analysis of weak oblique shockwaves for carbon dioxide. In: XIV **Congresso Ibero-Americano Em Engenharia Mecânica CIBEM 2019, 2019, Cartagena.**
- Comparison between numerical approaches to simulate a supersonic nozzle. In: **13th World Congress in Computational Mechanics - WCCM2018, 2018, New York**

1.7 Patent

- Natural gas separation system from gas components, through a supersonic convergent-divergent nozzle with variable area. (In portuguese), Number: PI20170039, Deposited: 24/08/20

2 State of the art of supersonic gas separation experimental facilities

In this chapter, it will be discussed the more relevant experimental works on carbon dioxide supersonic phase change by supersonic methods and will be along with operating conditions and the supersonic separation process efficiency.

Fig. 2.1 presents the concept of a supersonic separator, which starts with the work of Garret et al. (1968), pioneers in the concept of the supersonic separation technique. Their work considered several issues related to this kind of technology, as the phase change in supersonic flow with normal and oblique shocks waves. The length of the nozzle allows the formation of droplets, which later goes towards the collection chamber, through a porous media, achieving the condensate separation. The main challenge in the design of this kind of supersonic separator consists in the adequate elbow geometry design, because, if there is not an appropriate coupling between the convergent section and the separation process, high pressure losses could occur inside the nozzle.

Bier et al. (1990b) presented the first work for evaluating carbon dioxide supersonic condensation. This research evaluated the CO_2 spontaneous condensation in a convergent-divergent nozzle for several stagnation pressures, the experimental evaluation of the condensation shocks effects on the supersonic flow were shown. Fig. 2.2 presents the experimental arrangement used by this work, which consisted in using a closed loop circuit for stagnation pressures higher than 20 bar, otherwise the nozzle discharge to atmosphere. This test-rig did not have an optical access, the experimental evaluation was done through several wall pressure measurements using an sliding plate along the nozzle axis. As a continuation of the previous research, Bier et al. (1990a) provided new insights on the carbon dioxide condensation in dry air mixtures. This work evaluated the CO_2 concentration effects on the carbon dioxide condensation and also provided a new formulation for the nucleation rate calculation.

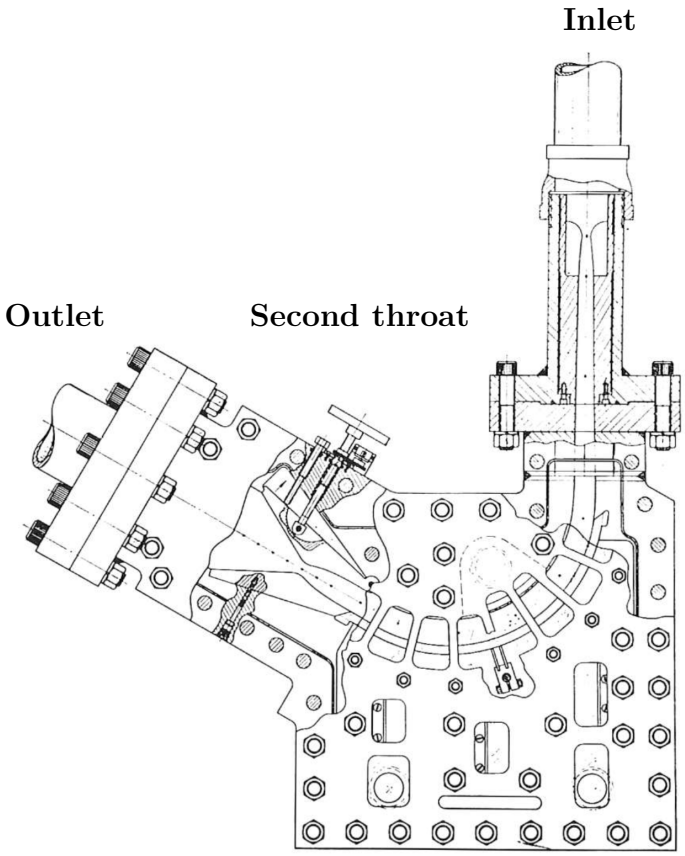

Figure 2.1 – Garret supersonic gas separator design. Adapted from (Garret et al., 1968).

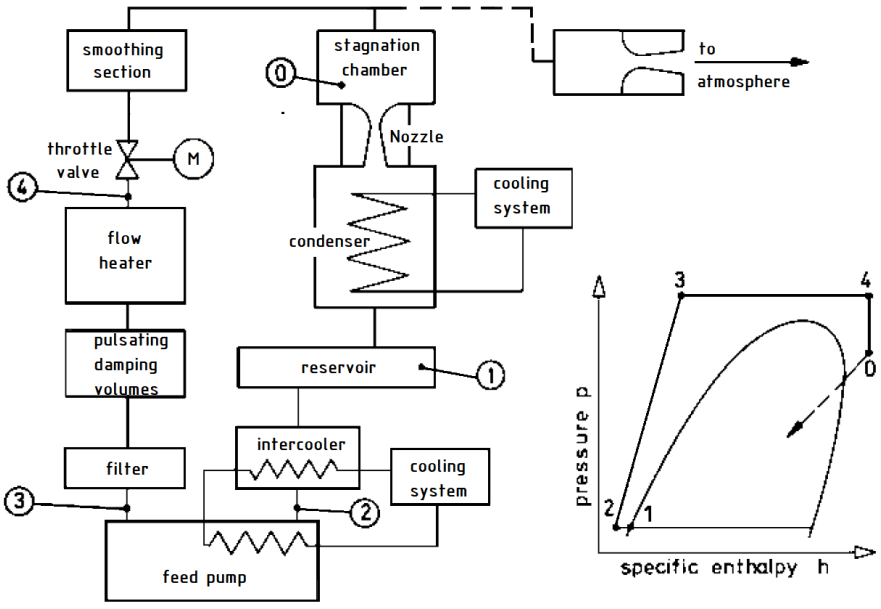

Figure 2.2 – Bier et al. (1990b) experimental test-rig for supersonic carbon dioxide condensation evaluation. Adapted from (Bier et al., 1990b).

Wyslouzil et al. (2000) carried out several tests with water, propanol and ethanol binary mixtures. This work was important due to their rigorous experimental procedure, for the evaluation of the supersonic phase change point for each one of the mixtures tested.

A convergent-divergent Laval nozzle was employed, without any flow separation mechanism. In the design of the convergent part a cubic spline was used for the wall profile variation. In the divergent part the authors employed a design criterion that the composite curve should be continuous through the second derivative, therefore, decreasing the presence of weak shocks in the divergent section. One important conclusion of their work was that the process was repeatable across different external conditions, thus ensuring confidence about the reliability of a supersonic phase change.

Liu et al. (2005) proposed the use of a supersonic swirl to intensify the separation process after the nozzle throat. Wet air was used as working fluid, with a maximum working pressure of 1 MPa and a flow rate of 600 m^3h^{-1}. A humidifier was placed downstream from the compressor. The main focus of this work, was to retrieve the stagnation temperature profile inside the nozzle, obtaining a maximum ΔT of 20 K.

Prast et al. (2006) reported an experimental and numerical evaluation Twister^{TM} separator and their operation in field. They found a good experimental recovery efficiency (68%) with a good pressure recovery ratio (73%). However, the authors did not reported the experimental setup nor the measurements used.

Haghighi (2010) designed an U-Shaped convergent-divergent nozzle, and claimed it was possible to obtain a higher centrifugal acceleration than in previous works. Nevertheless, their experimental arrangement just allowed to measure stagnation temperatures and pressures, and they did not evaluate the phase change in the nozzle or the separation efficiency.

Wen et al. (2011) built a supersonic separator for wet air, using swirl vanes to improve the supersonic separation. These vanes were located at the nozzle inlet. The experimental setup was composed of a screw compressor with a maximum pressure of 1.3 MPa and a flow rate of 360 m^3h^-1. Humidity/temperature transducers were placed at the nozzle inlet and outlet. The goal of that study was to find a relationship between mass flow and swirl strength.

Ding et al. (2014), estimated the non-equilibrium condensation of wet air in a supersonic nozzle. The work started evaluating the different conservation equations for supersonic flow with phase change, and also used an analytical expression to estimate the phase change position. With this information, they refined the mesh in this section in order to improve the accuracy of the prediction of the phase change. The main objective of the paper was to estimate the effect of water condensation in the mass flow rate and the pressure disturbances caused due the unsteady condensation. The experimental facility was composed of a screw compressor with maximum pressure of 0.9 MPa and a flow rate of 600 m^3h^{-1}. The convergent-divergent nozzle had a throat height of 5 mm, with optical access. MEMS pressure transducers were employed to track the pressure oscillations. The frequency of these oscillations was compared to simulation results, showing good

agreement.

Samawe et al. (2014) evaluated a commercial supersonic separator in a closed loop, and compared the experimental pressure profile against a CFD model simulation. A good agreement was found. However, they did not measure the separator efficiency.

Imaev et al. (2014) performed several tests on a commercial 3S separation unit. Their setup is schematically shown in Fig. 2.3. The main focus of the study was to control the temperature inside the nozzle, and subsequently guarantee the particle coagulation before the flow reached the solidification temperature. The experimental facility employed a liquid N_2 tank for methane cooling, and a CO_2 tank and disperser for the mixture preparation. Besides that, there were several measurement instruments as pressure transducers and thermocouples. The main result of this research was the observation of the influence of inlet temperature in the separation efficiency. For temperatures bellow than 213 K, the efficiency of the supersonic separator decreased as the temperature fell, because there was no droplet coalescence and therefore, it was difficult to start the crystallization.

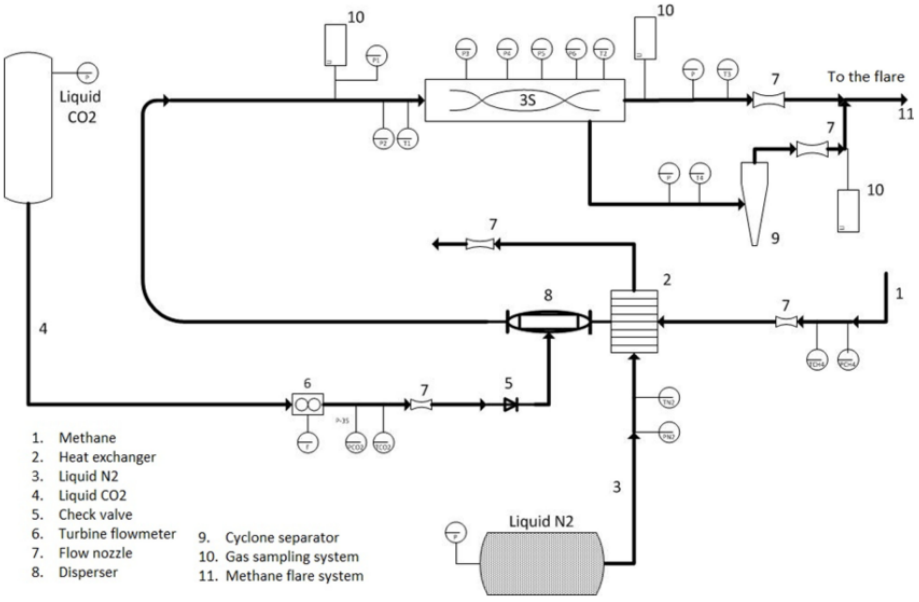

Figure 2.3 – Imaev et al. (2014) experimental test-rig for evaluation of supersonic gas separators. Adapted from (Imaev et al., 2014)

Cao & Yang (2015) tested a supersonic separator with swirl vanes for wet air separation. The process started with the compression of atmospheric air and its storage in a surge tank. A high pressure pump with a micro mist humidifier was placed in parallel. Finally, the air and water vapour were mixed in a humidifying tank. This mixture then went through the supersonic separator. It became evident that a high pressure recovery ratio would decrease the ΔT and therefore the water condensation. According to the authors, that was the most important variable of their study. In their analysis the inlet temperature varied from 284 K to 309 K and the pressure from 0.7 MPa to 0.9 MPa.

Chang & Bai (2017) analysed natural gas evaporation using a convergent-divergent nozzle. The main achievement of this research was to measure particle diameter and distribution. The authors used a laser diffraction system and founded a mean particle diameter of 50 µm at the nozzle outlet.

Lettieri et al. (2017) calculated and tested the rapid expansion and subsequent condensation of CO_2 flowing at supersonic velocities in a convergent-divergent supersonic nozzle. They employed a shearing interferometer arrangement to visualize the density field inside the nozzle. The system was composed by a liquid CO_2 tank, a pump, a high pressure and high temperature tank. A square section nozzle with a cross-section area of 20 mm^2 was designed. This small area was selected to decrease the mass flow and increase the tank blow time. The images captured by the shearing interferometer arrangement were used to measure the metastable phase density. The images clearly represented this point as a "fog" zone in the nozzle. This visualization corresponded to a pressure recovery measured by the pressure transducers, indicating the starting of nucleation.

Niknam et al. (2018), developed their own asymmetric supersonic separator model, produced using CNC machining. The experimental set-up employed an oil-free compressor with a flow rate of 14.4 Nm^3h^{-1}, and a moisture injection station. The supersonic separator had several points of measurement of static pressure and temperature. The authors measured the water removal efficiency of the device, finding maximum values of 27.5% with an inlet pressure of 0.8 MPa and a pressure recovery ratio of 60%. They concluded that the pressure recovery ratio and inlet temperature had low influence in the process, and the most important parameter was the inlet pressure.

Vlasenko et al. (2018) presented an experimental study of a combined supersonic separator, tested at a maximum stagnation pressure of 0.4 MPa, atmospheric air was compressed and dried, later it was used a fluidized water bed for the mist air preparation. An axisymmetric supersonic separator was designed and constructed after using a hybrid design of a vortex tube. Maximum separation efficiency of 40% was achieved.

Majidi & Farhadi (2020) presented an experimental and theoretical approach for the development of a supersonic separator dehumidification performance, at low stagnation pressures 0.4 MPa. It was used an ultrasonic humidifier for the moist air preparation, it was achieved a maximum separation efficiency of 75 %.

The main information contained in the last works, was summarized in the Table 2.1, where was studied the following subjects:

1. Work Focus: In this part was established the main proposal of the paper, being classified as follows:
    - Separation: Supersonic separation of a condensible at high speeds.

- Dehydratation: Condensation and separation of several natural gas components.
- Condensation: Condensation inside a supersonic nozzle, without separation.

2. Optical Method: Optical method used to evaluate qualitative or quantitative the phenomena.
   - Direct: Direct visualization of the phenomena, without any optical arrangement.
   - Schlieren: Use of the schlieren technique to find density gradients inside the flow.
   - Interferometer: Use of an interferometer, to find density fields inside the flow.
   - Laser: Use of laser to measure the mean particle diameter.
3. Nozzle Geometry: Arrangement of the different nozzle sections.
   - C: Convergent
   - D: Divergent
4. η : Separator efficiency, Is the ratio between the dry gas mass rate and the inlet mass rate $\dot{m}_{Dry}/\dot{m}_{Inlet}$.
5. SM : Separation mechanism.
   - E: Elbow.
   - S : Swirl.
   - SS : Supersonic Swirl.

For all the subjects without relevant data was used the NA acronym.

As summarized in Table 2.1, there are few works dealing with carbon dioxide supersonic condensation or separation, most of the previous works have been focused on the humid air supersonic separation or carbon dioxide as a pure substance. Few works evaluate CO_2 mixtures and allows an optical insight of the process. Bearing this in mind, this thesis developed a new test-rig design which gives the possibility to testing carbon dioxide - dry air mixtures, at medium stagnation pressures $P < 5$ MPa with optical access, to ensure a precise quantitative and qualitative process description.

Table 2.1 – Supersonic separation Nozzles.

Reference	Work Focus	Working Fluid	Optical Method	P_0 [MPa]	P_1/P_0 [%]	T_0 [K]	Nozzle Geometry	Mach [-]	η [%]	SM
(Garret et al., 1968)	Separation	NG	Direct	12,4	23	305	C-D-C	2,2	50	E
(Bier et al., 1990b)	Condensation	CO_2	NA	4,5	NA	300-325	C-D	NA	NA	NA
(Bier et al., 1990a)	Condensation	CO_2 + dry air	NA	3	NA	230-270	C-D	NA	NA	NA
(Wyslouzil et al., 2000)	Condensation	HC + Water	NA	0,059	NA	288	C-D	NA	NA	NA
(Liu et al., 2005)	Separation	Wet air	NA	0,71	80	301	C-D	NA	NA	SS
(Prast et al., 2006)	Separation	NG	NA	3	73	295	C-D	NA	68	S
(Haghighi, 2010)	Separation	Air	NA	0,34	40	NA	C-D	NA	NA	E
(Wen et al., 2011)	Separation	Wet Air	NA	1,3	NA	NA	C-D	NA	NA	S
(Samawe et al., 2014)	Separation	CO_2 + CH_4	NA	3	60	NA	C-D	NA	NA	S
(Imaev et al., 2014)	Separation	CO_2 + CH_4	NA	6	42	318	C-D-C	NA	70	S
(Ding et al., 2014)	Condensation	Wet air	Direct	0,8	NA	294	C-D	NA	NA	NA
(Cao; Yang, 2015)	Separation	Wet air	NA	0,6	30	303	C-D	1,4	NA	S
(Chang; Bai, 2017)	Condensation	NG + Water	Laser	0,5	20	300	C-D	6,52	NA	NA
(Lettieri et al., 2017)	Condensation	CO_2	Interferometry	8,6 - 5,7	40	310	C-D	NA	NA	NA
(Niknam et al., 2018)	Separation	Wet air	NA	0,5	80	300	C-D	1,5	20	S.
Vlasenko et al. (2018)	Separation	Wet air	NA	0,4	NA	NA	CD	NA	40	NA
(Majidi; Farhadi, 2020)	Separation	Wet air	NA	0,4	70	293	CD	NA	75	NA

3 Real gas mixture thermodynamics

3.1 Multiparameter equation-of-state

An equation-of-state (EOS) is a mathematical expression developed to describe and quantify the thermodynamic behaviour of a pure substance or mixture. In addition, an EOS allows the substance phase identification and evaluation for a defined thermodynamic state.

Several EOS have been proposed throughout history, such as the ideal gas equation, and the cubic equation-of-state, among others. Nevertheless, their reliability is not good enough for modern applications, such as carbon, capture and storage (Gernert, 2013), renewable energy or for an efficient energy use (Goodwin et al., 2010).

In this context, a new type of equation-of-state was proposed, called multiparameter Equation-of-state MPEOS, this EOS is formulated in terms of specific Helmholtz free energy, and it was calibrated through experimental data fitted using optimization algorithms (Span, 2000). The classical definition of specific Helmholtz free energy $\mathfrak{f}$ for a single component is

$$d\mathfrak{f} = -sdT - Pdv, \tag{3.1}$$

where s denotes the specific entropy, T the absolute temperature, P the pressure and v the specific volume. This definition was derived from Table A.3 (See Appendix A) for a single component without surface tension work. If the temperature and volume of the substance is known, it is possible to identify other thermodynamic properties as pressure

$$P = -\left(\frac{\partial \mathfrak{f}}{\partial v}\right)_T, \tag{3.2}$$

or specific entropy

$$s = -\left(\frac{\partial \mathfrak{f}}{\partial T}\right)_v. \tag{3.3}$$

A MPEOS is based in the non-dimensional Helmholtz free energy α

$$\alpha = \frac{\mathfrak{f}}{\mathcal{R}T}, \tag{3.4}$$

where $\mathcal{R}$ is the universal gas constant, α can be expressed as the sum of their ideal α° and residual parts α^r

$$\alpha = \alpha^\circ + \alpha^r. \tag{3.5}$$

As a consequence of their non dimensional formulation, the temperature must be expressed in a non-dimensional form

$$\tau = \frac{T_c}{T}, \tag{3.6}$$

and in the same fashion for volume or density

$$\delta = \frac{\rho}{\rho_c} = \frac{v_c}{v}. \tag{3.7}$$

After introducing these definitions, one can now describe the pressure and entropy as a function of the non-dimensional Helmholtz free energy, for example pressure

$$\frac{P}{\mathcal{R}T} = -\rho\delta \left(\frac{\partial\alpha}{\partial\delta}\right)_\tau, \tag{3.8}$$

specific entropy

$$\frac{s}{\mathcal{R}} = \left(\frac{\partial\tau\alpha}{\partial\tau}\right)_\delta, \tag{3.9}$$

and compressibility factor

$$Z = \frac{P}{\mathcal{R}\rho T} = -\delta \left(\frac{\partial\alpha}{\partial\delta}\right)_\tau. \tag{3.10}$$

Some thermodynamic properties were previously explained as a function of non-dimensional Helmholtz free energy and their derivatives, this arrangement is the same for modelling a pure substance or mixture. Nevertheless, for the formulation of an ideal and residual non-dimensional Helmholtz free energy, it is required a different approach for each case.

3.1.1 Pure substance

For a pure substance the notation of Span (2000) will be used, for the ideal non-dimensional Helmholtz free energy:

$$\alpha^0 = \ln\delta + a_1 \ln\tau + a_2 + a_3\tau + a_4\tau^{-1} + a_5\tau^{-2} + a_6\tau^{-3} + a_7 \ln[1 - e^{(-a_8\tau)}], \tag{3.11}$$

where a_i are fitting parameters, which depend on each substance. One can note that Eq. 3.11 is a function of the temperature and density. Temperature is used for the polynomial part and the density is used in the first term. Although the ideal formulation should be just a function of the temperature, the density term is used to stablish a reference state required for the entropy estimation. The residual part can be expressed as:

$$\alpha^r = \underbrace{\sum N_k \delta^{i_k} \tau^{j_k}}_{\text{Polinomial terms}} + \underbrace{\sum N_k \delta^{i_k} \tau^{j_k} \exp\left(-\delta^{l_k}\right)}_{\text{Exponential terms}} + \underbrace{\sum N_k \delta^{i_k} \tau^{j_k} \exp\left(-\phi_k(\delta-1)^2 - \beta_k(\tau-\gamma_k)^2\right)}_{\text{Gaussian bell Shaped terms}}, \tag{3.12}$$

where N_k, ϕ, β and γ are fitting parameters which depend on each substance. Eq. 3.12 represents the non-ideal behaviour of the MPEOS, therefore it should be represented by all the fitting data used to elaborate the EOS. Span (2000) classifies the residual terms in two categories, listed bellow:

- Polynomial and exponential terms: They represent the molecular interaction of the substance.
- Gaussian bell shaped terms: They represent the highly non-linear substance behaviour near to critical point.

After defining the ideal and residual part of the Helmholtz free energy for a pure substance, their derivatives computation are required. Nevertheless, the only derivative that is constant for any substance and state is the derivative of the ideal part in reduced density terms

$$\left(\frac{\partial\alpha^\circ}{\partial\delta}\right)_\tau = \frac{1}{\delta}. \tag{3.13}$$

Other derivatives must be evaluated for a specific substance and state, according to the following notation:

$$\alpha^{\mathrm{r}}_\delta = \left(\frac{\partial\alpha^{\mathrm{r}}}{\partial\delta}\right)_\tau, \quad \alpha^{\mathrm{o}}_\delta = \left(\frac{\partial\alpha^{\mathrm{o}}}{\partial\delta}\right)_\tau, \tag{3.14}$$

$$\alpha^{\mathrm{r}}_{\delta\delta} = \left(\frac{\partial^2\alpha^{\mathrm{r}}}{\partial\delta^2}\right)_\tau, \quad \alpha^{\mathrm{o}}_{\delta\delta} = \left(\frac{\partial^2\alpha^{\mathrm{o}}}{\partial\delta^2}\right)_\tau, \tag{3.15}$$

$$\alpha^{\mathrm{r}}_{\tau} = \left(\frac{\partial \alpha^{\mathrm{r}}}{\partial \tau}\right)_{\delta}, \qquad \alpha^{\mathrm{o}}_{\tau} = \left(\frac{\partial \alpha^{\mathrm{o}}}{\partial \tau}\right)_{\delta}, \tag{3.16}$$

$$\alpha^{\mathrm{r}}_{\tau\tau} = \left(\frac{\partial^2 \alpha^{\mathrm{r}}}{\partial \tau^2}\right)_{\delta}, \quad \alpha^{\mathrm{o}}_{\tau\tau} = \left(\frac{\partial^2 \alpha^{\mathrm{o}}}{\partial \tau^2}\right)_{\delta}, \tag{3.17}$$

$$\alpha^{\mathrm{r}}_{\delta\tau} = \left(\frac{\partial^2 \alpha^{\mathrm{r}}}{\partial \delta \partial \tau}\right), \quad \alpha^{\mathrm{r}}_{\delta\tau\tau} = \left(\frac{\partial^3 \alpha^{\mathrm{r}}}{\partial \delta \partial \tau^2}\right). \tag{3.18}$$

3.1.2 Multicomponent

The non-dimensional Helmholtz free energy definition for a multicomponent system should be modified in comparison to a pure substance, because it has to consider the molar fraction of the component, excess properties and the reference temperature and density. By contrast of the pure substance case, for a real gas mixture it is difficult to estimate the critical point and even it is possible the existence of two or more points (Bell; Jäger, 2017). Instead, it is used a reference temperature and density as a function of the corresponding interaction parameters of the mixture. This work uses the GERG - 2008 EOS (Kunz; Wagner, 2012a), due to the good performance and reliability for natural gas mixtures (Baladao, 2015). Fig. 3.1 shows the components available for this EOS and the methods used in the interaction parameters formulation.

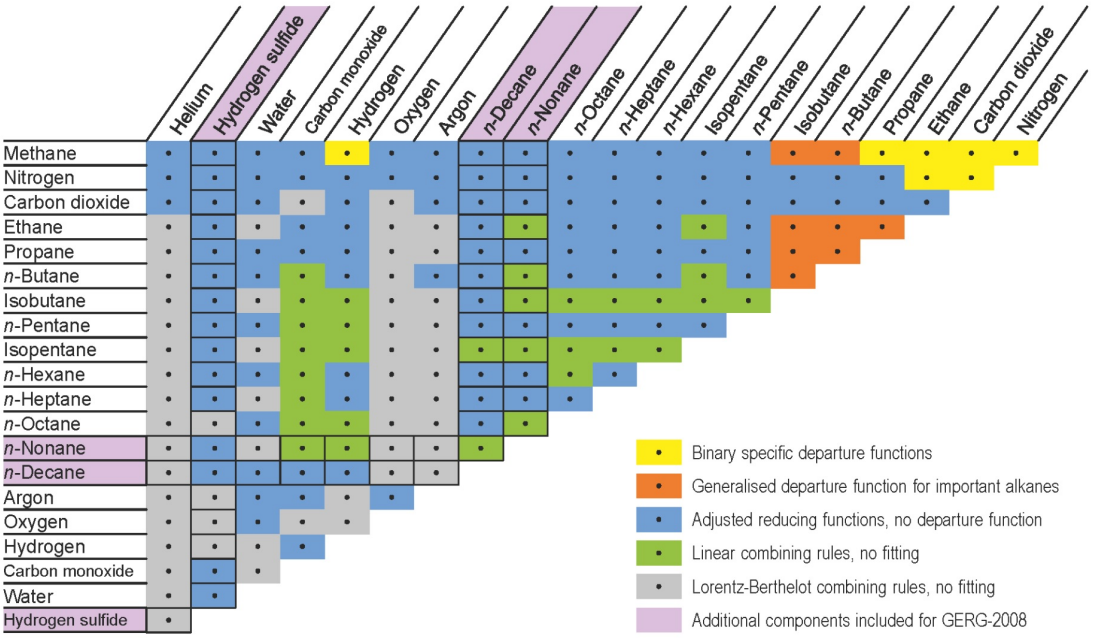

Figure 3.1 – GERG-2008, 210 binary pairs for 20 components (Kunz; Wagner, 2012a).

The reference temperature is

$$T_r(\bar{x}) = \sum_{i=1}^{N} \bar{x}_i^2 T_{c,i} + \sum_{i=1}^{N-1} \sum_{j=i+1}^{N} 2\bar{x}_i \bar{x}_j \beta_{T,ij} \gamma_{T,ij} \frac{\bar{x}_i + \bar{x}_j}{\beta_{T,ij}^2 \bar{x}_i + \bar{x}_j} (T_{c,i} T_{c,j})^{0.5}, \tag{3.19}$$

where x denotes the molar fraction. The reference density is:

$$\frac{1}{\rho_r(\bar{x})} = v_r(\bar{x}) = \sum_{i=1}^{N} \bar{x}_i^2 \frac{1}{\rho_{c,i}} + \sum_{i=1}^{N-1} \sum_{j=i+1}^{N} 2\bar{x}_i \bar{x}_j \beta_{v,ij} \gamma_{v,ij} \frac{\bar{x}_i + \bar{x}_j}{\beta_{v,ij}^2 \bar{x}_i + \bar{x}_j} \frac{1}{8} \left(\frac{1}{\rho_{c,i}^{1/3}} + \frac{1}{\rho_{c,j}^{1/3}} \right)^3. \tag{3.20}$$

The ideal non-dimensional Helmholtz free energy is

$$\alpha^{\circ}(\rho, T, \bar{x}) = \sum_{i=1}^{N} \bar{x}_i \left[\alpha_{oi}^{\circ}(\rho, T) + \ln \bar{x}_i \right], \tag{3.21}$$

and the reduced part

$$\alpha^{r}(\delta, \tau, \bar{x}) = \underbrace{\sum_{i=1}^{N} \bar{x}_i \alpha_{\circ i}^{\mathrm{r}}(\delta, \tau)}_{\text{departure function}} + \underbrace{\sum_{i=1}^{N-1} \sum_{j=i+1}^{N} \bar{x}_i \bar{x}_j F_{ij} \alpha_{ij}^{r}(\delta, \tau)}_{\text{Excess terms}}, \tag{3.22}$$

where α_{oi}° and $\alpha_{\circ i}^{\mathrm{r}}$ are ancillary functions which deals with the ideal and residual part for each component. After define the ideal and residual part of the Helmholtz free energy for a real gas mixture, it is required to formulate their derivatives as a function of the composition and density, as presented bellow:

Ideal gas part:

$$\left(\frac{\partial \alpha^{\circ}}{\partial \delta} \right)_{\tau,\bar{x}} = \sum_{i=1}^{N} \bar{x}_i \frac{\rho_{\mathrm{r}}}{\rho_{\mathrm{c},i}} \left(\frac{\rho_c i}{\rho} \right), \tag{3.23}$$

$$\left(\frac{\partial \alpha^{\circ}}{\partial \delta} \right)_{\tau,\bar{x}} = -\sum_{i=1}^{N} x_i \left(\frac{\rho_r}{\rho_c i} \right)^2 \left(\frac{\rho_c i}{\rho} \right)^2, \tag{3.24}$$

$$\left(\frac{\partial^2 \alpha^{\circ}}{\partial \delta \partial \bar{x}} \right)_{\tau} = \sum_{i=1}^{N} \frac{\rho_{\mathrm{r}}}{\rho_{\mathrm{c},i}} \left(\frac{\partial \alpha_{oi}^{\mathrm{o}}}{\partial \left(\rho / \rho_{\mathrm{c},i} \right)} \right)_{T}, \tag{3.25}$$

$$\left(\frac{\partial^2 \alpha^{\circ}}{\partial \bar{x}^2} \right)_{\tau,\delta} = \sum_{i=1}^{N} \frac{1}{\bar{x}_i}. \tag{3.26}$$

Residual part:

$$\left(\frac{\partial \alpha^{r}}{\partial \delta} \right)_{\tau,\bar{x}} = \sum_{i=1}^{N} \bar{x}_i \left(\frac{\partial \alpha_{\mathrm{oi}}^{\mathrm{r}}}{\partial \delta} \right)_{\tau} + \sum_{i=1}^{N-1} \sum_{j=i+1}^{N} \bar{x}_i \bar{x}_j F_{ij} \left(\frac{\partial \alpha_{ij}^{\mathrm{r}}}{\partial \delta} \right)_{\tau}, \tag{3.27}$$

$$\left(\frac{\partial^2 \alpha^{r}}{\partial \delta^2} \right)_{\tau,\bar{x}} = \sum_{i=1}^{N} \bar{x}_i \left(\frac{\partial^2 \alpha_{\mathrm{oi}}^{\mathrm{r}}}{\partial \delta^2} \right)_{\tau} + \sum_{i=1}^{N-1} \sum_{j=i+1}^{N} \bar{x}_i \bar{x}_j F_{ij} \left(\frac{\partial^2 \alpha_{ij}^{\mathrm{r}}}{\partial \delta^2} \right)_{\tau}, \tag{3.28}$$

$$\left(\frac{\partial^2 \alpha^r}{\partial\delta\partial\bar{x}}\right)_\tau = \left(\frac{\partial \alpha^{\mathrm{r}}_{\mathrm{o}i}}{\partial\delta}\right)_\tau + \sum_{\substack{k=1 \\ k\neq i}}^{N} \bar{x}_k F_{\mathrm{ik}} \left(\frac{\partial \alpha^{\mathrm{r}}_{ik}}{\partial\delta}\right)_\tau . \tag{3.29}$$

After defining residual and ideal non dimensional Helmholtz free energy for a pure substance and a real gas mixture, it is possible to show the definition of the most common thermodynamic properties as a function of the partial derivatives of the non dimensional Helmholtz free energy.

Returning to the definition of pressure in Eq. 3.8, pressure can be expressed in ideal and residual terms

$$\frac{P}{\mathcal{R}T} = \rho\delta\left[\left(\frac{\partial \alpha^\circ}{\partial\delta}\right)_\tau + \left(\frac{\partial \alpha^r}{\partial\delta}\right)_\tau\right], \tag{3.30}$$

after substituting Eq. 3.13 in Eq. 3.30, one obtains the expression to calculate pressure in function of the ideal and residual non-dimensional Helmholtz free energy

$$P = \mathcal{R}\rho T(1 + \delta\alpha^r_\delta). \tag{3.31}$$

Similarly, is possible to define the specific entropy from the Eq. 3.9, resulting in:

$$\frac{s}{\mathcal{R}} = -\alpha^\circ - \alpha^r + \tau(\alpha^\circ_\tau + \alpha^r_\tau). \tag{3.32}$$

Using the Helmholtz free energy definition it is possible to calculate all the other thermodynamic potentials , such as internal energy $u = Ts + f$, which becomes:

$$\frac{\mathfrak{u}}{\mathcal{R}T} = \cancel{-\alpha^\circ - \alpha^r} + \tau(\alpha^\circ_\tau + \alpha^r_\tau) + \cancel{\alpha^\circ + \alpha^r}, \tag{3.33}$$

resulting in:

$$\frac{\mathfrak{u}}{\mathcal{R}T} = \tau(\alpha^\circ_\tau + \alpha^r_\tau). \tag{3.34}$$

And enthalpy $h = \mathfrak{u} + P/\rho$:

$$\frac{h}{\mathcal{R}T} = \tau(\alpha^\circ_\tau + \alpha^r_\tau) + 1 + \delta\alpha^r_\delta. \tag{3.35}$$

Also, the Gibbs free energy can be calculated $g = h - Ts$:

$$\frac{g}{\mathcal{R}T} = \cancel{\tau(\alpha^\circ_\tau + \alpha^r_\tau)} + 1 + \delta\alpha^r_\delta + \alpha^\circ + \alpha^r - \cancel{\tau(\alpha^\circ_\tau + \alpha^r_\tau)}, \tag{3.36}$$

resulting in:

$$\frac{g}{\mathcal{R}T} = 1 + \delta\alpha^r_\delta + \alpha^\circ + \alpha^r. \tag{3.37}$$

In addition, it is necessary to define some important partial derivatives as expressed in Eq. 3.39, Eq. 3.41 and 3.44.

$$\left(\frac{\partial P}{\partial \rho}\right)_T = \mathcal{R}T\left(\frac{\partial(\delta(1+\delta\alpha_\delta^r))}{\partial\delta}\right)_\tau, \tag{3.38}$$

$$\left(\frac{\partial P}{\partial \rho}\right)_T = \mathcal{R}T\left(1+2\delta\alpha_\delta^{\mathrm{r}}+\delta^2\alpha_{\delta\delta}^{\mathrm{r}}\right), \tag{3.39}$$

$$\left(\frac{\partial P}{\partial T}\right)_\rho = \mathcal{R}\rho\left(\frac{\partial(-\tau(1+\delta\alpha_\delta^r))}{\partial\tau}\right)_\delta, \tag{3.40}$$

$$\left(\frac{\partial P}{\partial T}\right)_\rho = \mathcal{R}\rho\left(1+\delta\alpha_\delta^{\mathrm{r}}-\delta\tau\alpha_{\delta\tau}^{\mathrm{r}}\right), \tag{3.41}$$

$$\left(\frac{\partial v}{\partial T}\right)_P = -\frac{1}{\rho^2}\left(\frac{\partial \rho}{\partial T}\right)_P, \tag{3.42}$$

,

$$\left(\frac{\partial v}{\partial T}\right)_P = \frac{1}{\rho^2}\frac{\left(\frac{\partial p}{\partial T}\right)_\rho}{\left(\frac{\partial p}{\partial \rho}\right)_T}, \tag{3.43}$$

$$\left(\frac{\partial v}{\partial T}\right)_P = \frac{1}{\rho T}\frac{(1+\delta\alpha_\delta^{\mathrm{r}}-\delta\tau\alpha_{\delta\tau}^{\mathrm{r}})}{(1+2\delta\alpha_\delta^{\mathrm{r}}+\delta^2\alpha_{\delta\delta}^{\mathrm{r}})}. \tag{3.44}$$

Now it just remains to calculate the specific heat at constant volume and at constant pressure, the definition of specific heat at constant volume is:

$$C_v = \left(\frac{\partial \mathfrak{u}}{\partial T}\right)_v, \tag{3.45}$$

after converting it into a non-dimensional expression, one obtains:

$$\frac{C_v}{\mathcal{R}} = -\tau^2(\alpha_{\tau\tau}^\circ + \alpha_{\tau\tau}^r). \tag{3.46}$$

For the specific heat at constant pressure will be used the arrangement proposed by Pratt (2001):

$$C_P = C_v + T\left(\frac{\partial P}{\partial T}\right)_v\left(\frac{\partial v}{\partial T}\right)_P, \tag{3.47}$$

after substituting Eqs. 3.46, 3.41 and 3.44 into Eq. 3.47, one obtains:

$$\frac{C_P}{\mathcal{R}} = -\tau^2(\alpha_{\tau\tau}^\circ + \alpha_{\tau\tau}^r) + \frac{(1+\delta\alpha_\delta^{\mathrm{r}}-\delta\tau\alpha_{\delta\tau}^{\mathrm{r}})^2}{(1+2\delta\alpha_\delta^{\mathrm{r}}+\delta^2\alpha_{\delta\delta}^{\mathrm{r}})}. \tag{3.48}$$

The speed-of-sound definition is:

$$c^2 = \left(\frac{\partial P}{\partial \rho}\right)_s = \frac{1}{\rho^2}\left(-\frac{C_P}{C_v}\left(\frac{\partial P}{\partial v}\right)_T\right), \tag{3.49}$$

after substituting Eqs. 3.39, 3.46 and 3.48, it is obtained:

$$\frac{c^2}{\mathcal{R}T} = 1 + 2\delta\alpha^r_\delta + \delta^2\alpha^r_{\delta\delta} - \frac{\left(1 + \delta\alpha^r_\delta - \delta\tau\alpha^r_{\delta\tau}\right)^2}{\tau^2\left(\alpha^\circ_{\tau\tau} + \alpha^r_{\tau\tau}\right)}. \tag{3.50}$$

A last thermodynamic parameter will be required in the next chapters, named as the Grüneisen parameter:

$$Gr = \left(\frac{\partial \ln T}{\partial \ln \rho}\right)_s = \frac{\rho}{T}\left(\frac{\partial T}{\partial \rho}\right)_s, \tag{3.51}$$

after some algebraic manipulations and thermodynamics definitions use, it can be expressed in non-dimensional Helmholtz free energy terms, resulting in:

$$Gr = -\frac{\frac{1+\delta\alpha^r_\delta-\delta\tau\alpha^r_{\delta\tau}}{1+2\delta\alpha^r_\delta+\delta^2\alpha^r_{\delta\delta}}\left(\frac{(1+\delta\alpha^r_\delta-\delta\tau\alpha^r_{\delta\tau})^2}{\tau^2(\alpha^\circ_{\tau\tau}+\alpha^r_{\tau\tau})} - 1 - 2\delta\alpha^r_\delta - \delta^2\alpha^r_{\delta\delta}\right)}{\frac{\left(1+\delta\alpha^r_\delta-\delta\tau\alpha^r_{\delta\tau}\right)^2}{1+2\delta\alpha^r_\delta+\delta^2\alpha^r_{\delta\delta}} - \tau^2\left(\alpha^\circ_{\tau\tau} + \alpha^r_{\tau\tau}\right)}. \tag{3.52}$$

All these properties can be calculated for a pure substance or for a real gas mixture, because their difference lies in the non-dimensional Helmholtz free energy formulation.

This work uses CoolProp open source library (Bell et al., 2014) for the calculation and manipulation of the non-dimensional Helmholtz free energy terms, and for the binodal line computation of pure substances and real gas mixtures.

3.2 Isothermal reconstruction

There exist disadvantages of using a MPEOS because of their unusual behaviour for isothermal lines inside the two-phase region as addressed by Aursand et al. (2017). They performed several comparisons between different EOS for an isothermal line inside the two-phase region. It was found an awkward behaviour for a MPEOS (GERG - 2008) as depicted in Fig. 3.2, other EOS presented a behaviour similar to the expected (Maxwell loop) in the two-phase region, the main reason for this behaviour in the GERG-2008 is the absence of data and posterior calibration for these terms in the unstable and metastable regions.

This is an important issue for the calculation of the Spinodal line and the supersaturation ratio as presented in the next sections. To solve this, this work uses the approach of Matthis Thorade (2014) which is based on the work of Boltachev & Baidakov (2006). This

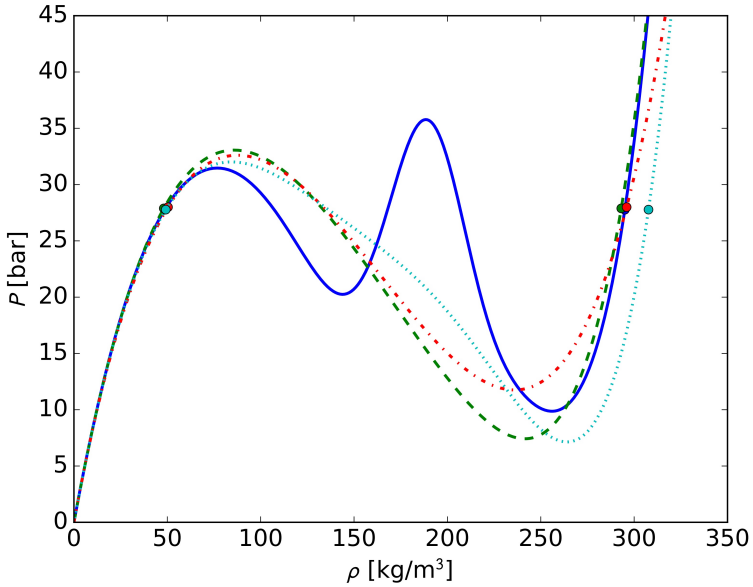

Figure 3.2 – Pure methane isotherms at 175 K, for several EOS: GERG-2008 (solid blue), PC-SAFT (dashed green), PR (dash-dot red) and extended CSP (dotted cyan) (Aursand et al., 2017).

approach consists in the isothermal loop reconstruction, towards the classical definition of Maxwell loop, for this will be used a series of coefficients $\overline{a}_i$ to reconstruct the non-dimensional Helmholtz free energy Eq. 3.53 and the pressure Eq. 3.54. The reconstructed values should fulfil the constraints established in the Eq. 3.55, Eq. 3.56 and Eq. 3.57.

$$\alpha = \overline{a}_0 - \frac{\overline{a}_1}{\delta} + \frac{\overline{a}_2}{\tau}\ln\delta + \frac{\overline{a}_3}{\tau}\delta + \frac{\overline{a}_4\delta^2}{\tau} + \frac{\overline{a}_5}{\tau}\frac{\delta^3}{3} + \frac{\overline{a}_6}{\tau}\frac{\delta^4}{4} + \frac{\overline{a}_7}{\tau}\frac{\delta^5}{5} \tag{3.53}$$

$$\frac{P}{\mathcal{R}\rho_c T_c} = \overline{a}_1\tau + \overline{a}_2\delta + \overline{a}_3\delta^2 + \overline{a}_4\delta^3 + \overline{a}_5\delta^4 + \overline{a}_6\delta^5 + \overline{a}_7\delta^6 \tag{3.54}$$

$$\left(\frac{\partial P}{\partial \rho}\right)_T\Bigg|_{\rho=\rho_l} \;\&\; \left(\frac{\partial P}{\partial \rho}\right)_T\Bigg|_{\rho=\rho_v} \tag{3.55}$$

$$\left(\frac{\partial^2 P}{\partial \rho^2}\right)_T\Bigg|_{\rho=\rho_l} \;\&\; \left(\frac{\partial^2 P}{\partial \rho^2}\right)_T\Bigg|_{\rho=\rho_v} \tag{3.56}$$

$$\int_{\rho_v}^{\rho_v} \frac{P}{\rho^2} d\rho = P_s\left(\frac{1}{\rho_v} - \frac{1}{\rho_l}\right) \tag{3.57}$$

After solving the system of equations, the isothermal loop was reconstructed as shown in Fig. 3.3, for reduced pressure and specific volume coordinates, it is possible to see the coincidence of both isothermal for the vapour and liquid region, however, for the two-phase region the isothermal line have an unrealistic behaviour because the pressure values exceed the critical pressure. Instead, the metastable Maxwell loop have a smooth behaviour as expected for an EOS in this region.

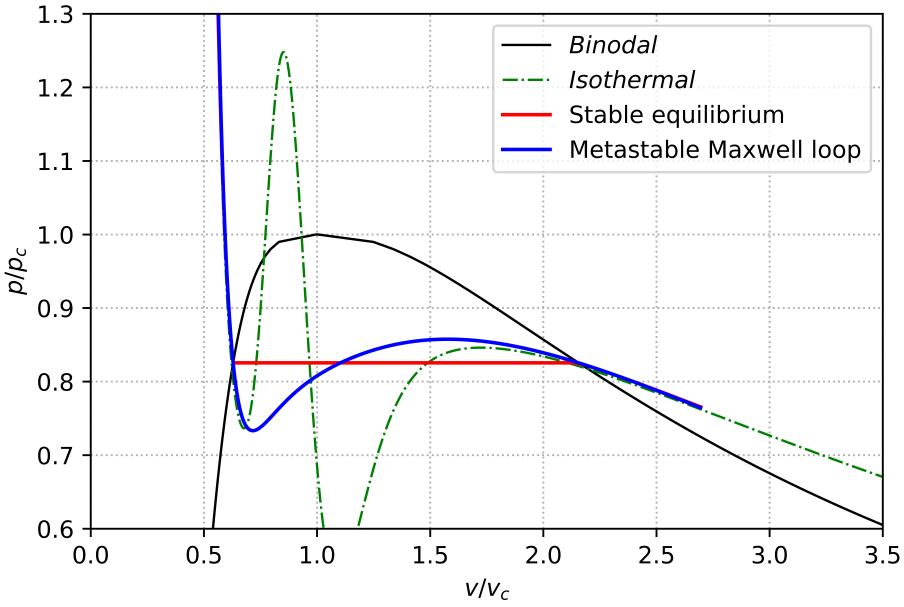

Figure 3.3 – Reconstructed CO_2 isothermal loop at 295 K.

3.3 Phase stability

In the real gas flow inside a supersonic separator, condensation is expected to occur at high speeds, however, at this condition the condensation process is beyond the equilibrium considerations (Emmons, 1958), therefore, the thermodynamic limits of phase change should be studied from the phase stability point of view. Fig. 3.4 exposes the stability regions corresponding to the two-phase region, being unstable, liquid-metastable and vapour-metastable regions. Both are constrained by the binodal and spinodal lines, explained bellow:

- Binodal line: It shows the phase change behaviour for systems in equilibrium, also known as saturation line.
- Spinodal line: It shows the ultimate phase stability limit of a pure substance or mixture.

In the metastable vapour region is possible the coexistence of vapour and two-phase mixtures in function of their energetic state. The region located further than the spinodal line is known as the unstable region, and from a thermodynamic point view is impossible the existence of a single vapour phase, and as sudden expansion achieves the spinodal line, the substance will be split into two phases and this process is known as spinodal decomposition (Debenedetti, 1996).

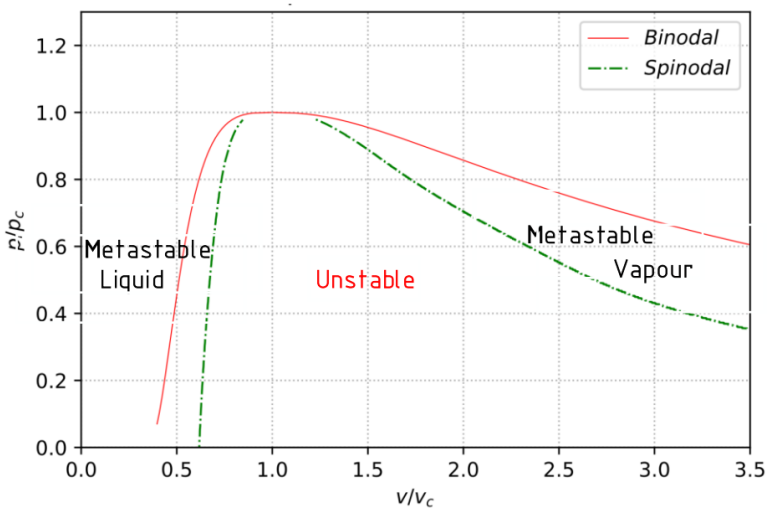

Figure 3.4 – Metastable and unstable regions for a pure substance.

The phase stability concept was defined by Beegle et al. (1974) and expanded by Tester & Modell (1997). The phase stability analysis consists in the isolated system evaluation under a small perturbation, as described:

$$\Delta U = \underbrace{\text{đ}U}_{\text{At equilibrium } =0} + \overbrace{\text{đ}^2U}^{\text{Stable}\geq 0} + \ldots \geq 0. \tag{3.58}$$

In this analysis was evaluated the internal energy change, as it is expanded in Taylor series. For an equilibrium system always the first derivative must be equal to zero, nevertheless if the system is unstable the second derivative will be less than zero. Therefore, the stability criterion is based on finding the conditions where the second derivative of a thermodynamic potential becomes zero in function of their natural independent variables. As MPEOS is expressed in non-dimensional Helmholtz free energy terms, this thermodynamic potential is used for the phase stability analysis, hence, from the Table A.3 will be simplified the Helmholtz free energy for a system without surface tension work, leading to:

$$dF = -SdT - Pd\mathsf{V} + \sum_i \mu_i dN_i. \tag{3.59}$$

As the number of variables involved are different for a pure substance or a binary mixture, it will be presented both approaches in the next section.

3.3.1 Phase stability for a pure substance

According to Debenedetti (1996) the spinodal line for a pure substance is located inside the two-phase region and must fulfil the following restriction

$$\left(\frac{\partial C_2}{\partial X_2}\right)_{C_1,X_3} = 0, \tag{3.60}$$

as a function of their conjugate C and the natural independent variables X (for a further explanation see Appendix A). In the case of Helmholtz free energy thermodynamic potential, Eq. 3.60 could be rewritten as:

$$\left(\frac{\partial P}{\partial \mathsf{V}}\right)_{T,N} = 0, \tag{3.61}$$

where V is the volume, and Eq. 3.61 is known as mechanical equilibrium. Nevertheless, applying this equation for an isothermal line obtained from a MPEOS is inadequate due the several maxima and minima points in this EOS as seen in the Fig. 3.2. For this reason the isothermal line is reconstructed and later for this line will be calculated their maximum and minimum points through numeric methods for each line resulting in the spinodal line computation as plotted in Fig. 3.5.

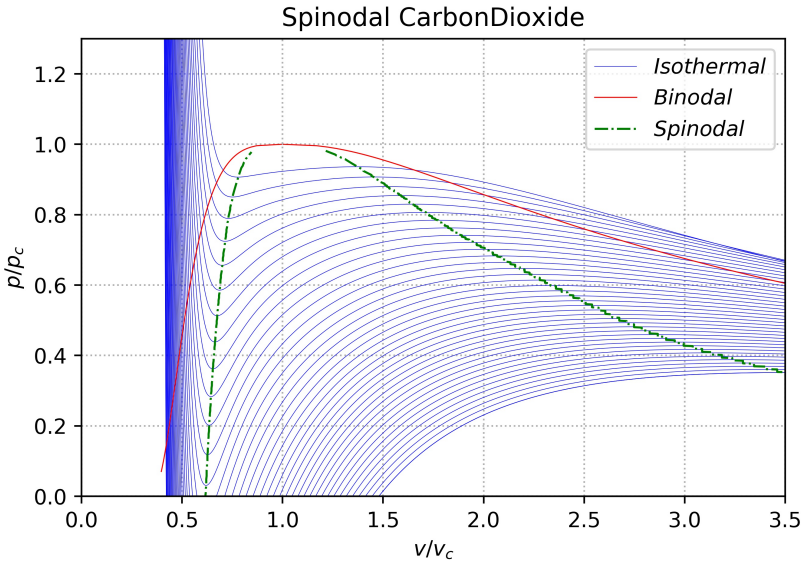

Figure 3.5 – Spinodal line CO_2.

3.3.2 Phase stability for a binary mixture

The expression shown in Eq. 3.60 should be modified to be applied to a real gas mixture, Debenedetti (1996) proposes the following restriction

$$\left(\frac{\partial C_{n+1}}{\partial X_{n+1}}\right)_{C_1,C_2,\ldots,C_n,X_{n+2}} = 0, \tag{3.62}$$

where n represents the number of components, which must be fulfilled simultaneously. Nevertheless, Beegle et al. (1974) suggest the use a hessian matrix formulation for the Helmholtz free energy resulting in:

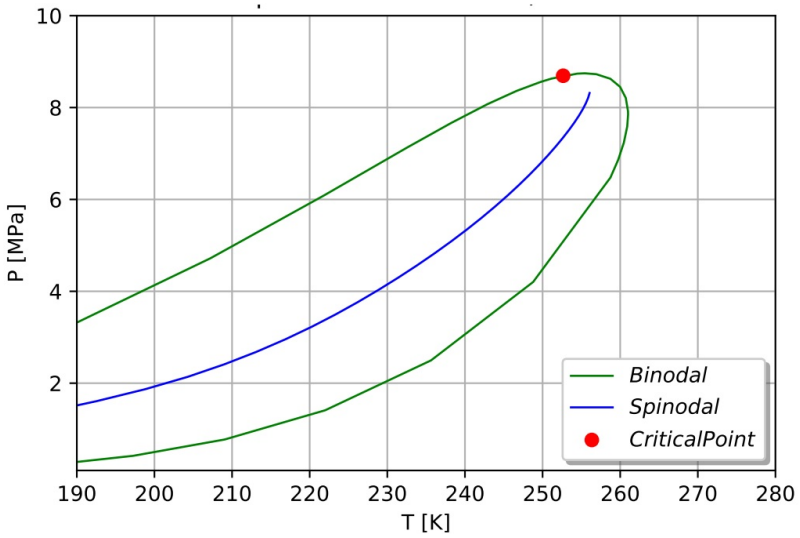

Figure 3.6 – Spinodal line for a molar binary mixture of 50 % CO_2 + CH_4.

$$L = \begin{bmatrix} \left(\frac{\partial^2 F}{\partial \mathsf{V}^2}\right)_{T,N_A,N_B} & \left(\frac{\partial^2 F}{\partial \mathsf{V} \partial N_A}\right)_{T,N_B} \\ \left(\frac{\partial^2 F}{\partial \mathsf{V} \partial N_A}\right)_{T,N_B} & \left(\frac{\partial^2 F}{\partial N_A^2}\right)_{T,\mathsf{V},N_B} \end{bmatrix} \tag{3.63}$$

And after considering this matrix, Bell & Jäger (2017) suggest that the spinodal line will be found where the determinant of the Eq. 3.63 becomes zero, therefore the spinodal line is located where:

$$\left(\frac{\partial^2 F}{\partial \mathsf{V}^2}\right)_{T,N_A,N_B} \left(\frac{\partial^2 F}{\partial N_A^2}\right)_{T,\mathsf{V},N_B} - \left(\frac{\partial^2 F}{\partial \mathsf{V} \partial N_A}\right)^2_{T,N_B} = 0. \tag{3.64}$$

After using the thermodynamic potentials defintions in Table A.3 for the pressure and the chemical potential μ. Eq. 3.64 can be expressed as:

$$\rho^2 \left(\frac{\partial P}{\partial \rho}\right)_{T,\bar{x}_A,\bar{x}_b} \left(\frac{\partial \mu_A}{\partial \bar{x}_A}\right)_{T,\rho,x_B} = \left(\frac{\partial P}{\partial \bar{x}_A}\right)^2_{T,\rho,\bar{x}_B}, \tag{3.65}$$

after employing the isothermal compressibility definition:

$$k = \frac{1}{\rho}\left(\frac{\partial \rho}{\partial P}\right)_{T,\bar{x}_A,\bar{x}_B}, \tag{3.66}$$

Eq. 3.65 becomes:

$$\frac{\rho}{k}\left(\frac{\partial \mu_A}{\partial \bar{x}_A}\right)_{T,\rho,\bar{x}_B} = \left(\frac{\partial P}{\partial \bar{x}_A}\right)^2_{T,\rho,\bar{x}_B}. \tag{3.67}$$

The spinodal computation was done using an isobaric marching algorithm, who marches through temperature changes until finding the thermodynamic conditions where

Eq. 3.67 is satisfied. The partial derivatives described on Eq. 3.67 were computed using centred finite differences as suggested by Kunz O & Jaeschke (2007). Fig. 3.6 presents the spinodal line computation results for an equimolar binary methane - carbon dioxide mixture.

3.4 Droplet work of formation.

As explained in the last subsection, the phase stability criteria allow one to know whether the system is unstable, metastable or stable. For a substance in a metastable condition, the phase change depends on the available work. Therefore, if the free energy is high enough for the critical radius formation, the phase change will start for this state as depicted in Fig. 3.7.

In order to calculate the work required for the droplet formation, the internal energy of a metastable phase within a bath (See Fig. 3.7 left) must be computed, this can be performed employing Eq. A.5, for an initial state without surface work.

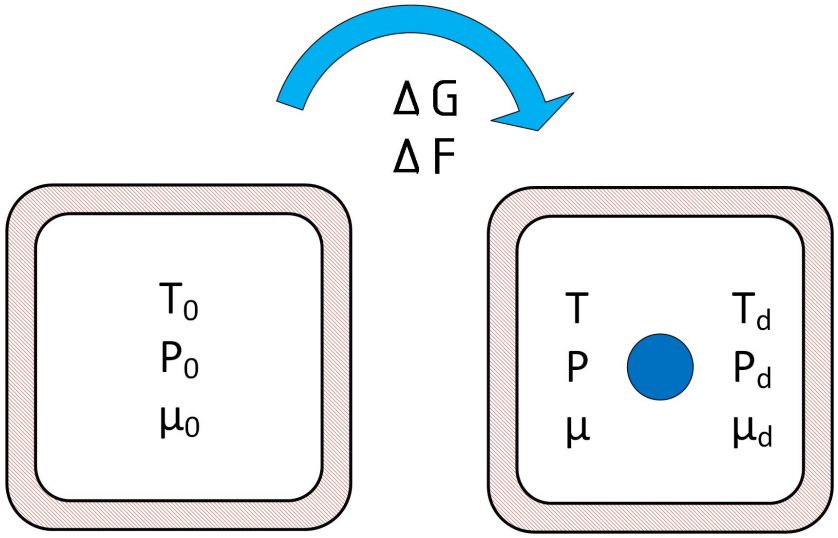

Figure 3.7 – Droplet work of formation.

$$U_0 = T_0 S_0 - P_0 V_0 + \sum \bar{\mu}^0_{i,g} N^0_{i,g}, \tag{3.68}$$

Analogously, one can analyse a system which considers the droplet formed (See Fig. 3.7 right), in this case Eq. A.5 (See Appendix A) becomes:

$$U = T_0 S - P_g \mathsf{V}_g - P_l \mathsf{V}_l + \sigma A + \sum \bar{\mu}_{i,g} N_{i,g} + \sum \bar{\mu}_{i,l} N_{i,l} + \sum \bar{\mu}_{i,s} N_{i,s}. \tag{3.69}$$

where subscripts 0, g and, l represents the initial state, gas and liquid phases, and s the surface interface for a droplet d. Now, the Helmholtz and Gibbs free energy of the system

before the droplet formation need to be calculated. After using the Helmholtz free energy definitions established on Table A.2, resulting in:

$$F_0 = U_0 - T_0 S_0 \tag{3.70}$$

and in an analogous manner for the Gibbs free energy:

$$G_0 = U_0 - T_0 S_0 + P_0 \mathsf{V}_0, \tag{3.71}$$

such equations could be simplified, after substituting Eq. 3.68 into Eqs. 3.70 and 3.71, resulting in

$$F_0 = -P_0 \mathsf{V}_0 + \sum \bar{\mu}^0_{i,g} N^0_{i,g} \tag{3.72}$$

and

$$G_0 = \sum \bar{\mu}^0_{i,g} N^0_{i,g}. \tag{3.73}$$

And the final state for Helmholtz and Gibbs free energy, Eq. 3.74 and Eq. 3.75 respectively.

$$F = U - T_0 S \tag{3.74}$$

$$G = U - T_0 S + P_0 (V_g + V_L) \tag{3.75}$$

After replacing Eq. 3.69 into Eq. 3.74 and 3.75, and subtracting the final state and the initial state it is obtained the work of formation in terms of Helmholtz free energy

$$\begin{aligned} \Delta F = (P_0 - P_l)\,\mathsf{V}_l + (P_0 - P_g)\,\mathsf{V}_g + \sigma A + \sum \left(\bar{\mu}_{i,g} - \bar{\mu}^0_{i,g}\right) N_{i,g} \\ + \sum \left(\bar{\mu}_{i,l} - \bar{\mu}^0_{i,g}\right) N_{i,l} + \sum \left(\bar{\mu}_{i,s} - \bar{\mu}^0_{i,g}\right) N_{i,s}, \end{aligned} \tag{3.76}$$

and Gibbs free energy

$$\Delta G = (P_0 - P_l)\,\mathsf{V}_l + \sigma A + \sum \bar{\mu}_{i,g} N_{i,g} + \sum \bar{\mu}_{i,l} N_{i,l} + \sum \bar{\mu}_{i,s} N_{i,s} - \sum \bar{\mu}^0_{i,g} N^0_{i,g} \tag{3.77}$$

If it is assumed a constant volume, number of moles, and no influence in the system pressure by the droplet formation and no chemical potential change in the vapour phase (see Eq. A.23) we could reduce the Eq. 3.76 to Eq. 3.78 for the Helmholtz free energy potential:

$$\Delta F = (P_0 - P_l)\,\mathsf{V}_l + \sigma A + \sum(\bar{\mu}_{i,l} - \bar{\mu}^{\circ}_{i,g})N_{i,l} + \sum(\bar{\mu}_{i,s} - \bar{\mu}^{\circ}_{i,g})N_{i,s} \tag{3.78}$$

In an analogous way, it is possible simplify the formation work in terms of the Gibbs free energy potential

$$\Delta G = (P_0 - P_l)\,\mathsf{V}_l + \sigma A + \sum(\bar{\mu}_{i,l} - \bar{\mu}^{\circ}_{i,g})N_{i,l} + \sum(\bar{\mu}_{i,s} - \bar{\mu}^{\circ}_{i,g})N_{i,s}. \tag{3.79}$$

After comparing Eq. 3.78 and Eq. 3.79, one can note that the work of formation is the same for both approaches and if we consider a system in equilibrium where all the chemical potential are equal (vapour, liquid and surface) we could obtain an expression for the critical cluster formation free energy, as expressed in:

$$\Delta\varphi = (P_v - P_l)\,\mathsf{V}_l + \sigma A. \tag{3.80}$$

For a spherical droplet, the Young-Laplace equation Eq. A.20 must be used in order to simplify Eq. 3.80 resulting in:

$$\Delta\varphi^* = \frac{-8\pi\sigma r^{3*}}{3r^*} + 4\pi\sigma^* r^{*2} \tag{3.81}$$

$$\Delta\varphi^* = \frac{4\pi\sigma r^{2*}}{3}. \tag{3.82}$$

3.4.1 General expression of droplet work for a pure substance.

Eq. 3.82 described the definition of formation work in a critical droplet cluster, nevertheless, in some cases must be required a more general expression in order to evaluate the particle growth as explained by Vehkamaki Hanna. (2006). Therefore, after starting from Eq. 3.78, one can obtain:

$$\Delta\varphi = (P_0 - P_l)\,\mathsf{V}_l + \sigma A + \sum(\mu_{i,l} - \mu^{\circ}_{i,g})N_{i,l} + \sum(\mu_{i,s} - \mu^{\circ}_{i,g})N_{i,s}. \tag{3.83}$$

After integrating Eq. A.23 for the interface between the droplet and the vapour, it was obtained

$$\mu_{i,l}\,(P_l) - \mu_{i,l}\,(P_0) = \mathsf{V}_{i,l}\,(P_l - P_0) \tag{3.84}$$

And subsequently, joining Eq. 3.83 and Eq.3.84, it is obtained Eq. 3.85 which allows estimating the formation work for a mixture even for a non-critical situation.

$$\Delta\varphi = \sum \Delta\mu_{i,l} N_{i,l} + \sigma A + \sum \left(\mu_{i,s} - \mu^0_{i,g}\right) N_{i,s} \tag{3.85}$$

3.5 Homogeneous nucleation

As expressed in section 3.3 the phase change of metastable vapour is limited by the spinodal line. Nevertheless, inside the metastable region phase change could occur depending on the nature of the flow and the phase change formation kinetics, basically, this could be divided in two different categories:

- Homogeneous nucleation: It is based on the kinetic formation of the particle due to energy fluctuations, when such fluctuation becomes high enough for the production of critical size embryos, phase change starts (Debenedetti, 1996).
- Heterogeneous nucleation: It is based on the droplet kinetic formation due to their interaction with a pre-existing surface, such as a particle or a wall.

Both analyses are suitable for the supersonic separator phase change evaluation, and it depends on the inlet conditions of the flow, if the flow is clean and free of any particle or droplet, the phase change will be driven by the homogeneous nucleation. And this is well known in the oil and gas industry, specially during the fast expansion of natural gas, and the subsequent mist formation (Muitjens et al., 1994).

A key parameter in the homogeneous nucleation theory is the nucleation rate, this parameter shows the nucleus formation per unit of volume and time, and it can adopt several formulations, nevertheless almost all of them have this structure:

$$J = K \exp\left(-\frac{\Delta\varphi}{k_b T}\right) \tag{3.86}$$

Being:

- K = Pre-exponential factor, it considers the surface tension, molecular diameter, molecular mass, and cluster density distribution effects on the new droplet distribution formation.
- $\Delta\varphi$ = Droplet formation work (See section 3.4).
- k_B = Boltzmann constant $1.380649 \times 10^{-23} \mathrm{m^2 kg K^{-1} s^{-2}}$.

Another important parameter, is the supersaturation ratio, which parameter shows the sub-cooling degree of a supersonic expansion into the metastable phase, in other

words the supersaturation ratio shows "how far" is the metastable phase compared to the equilibrium. From a general point of view the supersaturation ratio can be defined as (Campagna et al., 2020):

$$\mathcal{S} = \frac{\mathcal{F}}{\mathcal{F}_{eq}}, \tag{3.87}$$

where $\mathcal{F}$ is the fugacity, therefore, Eq. 3.87 compares the metastable fugacity against the equilibrium vapour phase for the same thermodynamic state. Eq.3.87 can be defined in chemical equilibrium terms, first, one can calculate the chemical equilibrium of the metastable vapour phase:

$$\bar{\mu} = \bar{\mu}_0 + k_b T \ln\left(\frac{\mathcal{F}}{\mathcal{F}_0}\right), \tag{3.88}$$

and for the equilibrium vapour:

$$\bar{\mu}_{eq} = \bar{\mu}_0 + k_b T \ln\left(\frac{\mathcal{F}_{eq}}{\mathcal{F}_0}\right), \tag{3.89}$$

where $\mathcal{F}_0$ and $\bar{\mu}_0$ are values for an arbitrary reference point. After substituting Eqs. 3.88 and 3.89 into 3.87, one obtains:

$$S = \exp\left(\frac{\bar{\mu} - \bar{\mu}_{eq}}{k_b T}\right). \tag{3.90}$$

Also, one can express the fugacity in terms of their partial pressure and the fugacity coefficient ϕ

$$\mathcal{F} = \bar{x} P \bar{\phi}, \tag{3.91}$$

so, Eq. 3.91 can be replaced into Eq. 3.87 for the metastable and equilibrium vapour, obtaining:

$$\mathcal{S} = \frac{\bar{\phi}\bar{x}P}{\bar{\phi}_{eq}\bar{x}_{eq}P}. \tag{3.92}$$

If one considers that carrier gas is not condensible and didn't take part in the nucleation, one can affirm that $\bar{\phi} \simeq \bar{\phi}_{eq}$. Therefore, Eq. 3.92 becomes:

$$\mathcal{S} = \frac{\bar{x}}{\bar{x}_{eq}}. \tag{3.93}$$

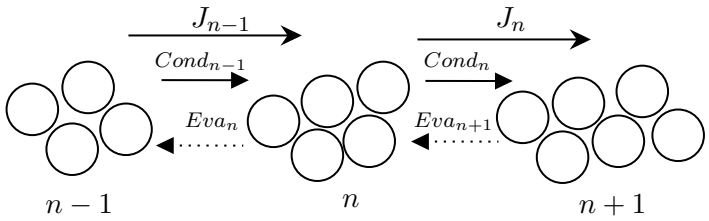

Figure 3.8 – Homogeneous nucleation kinetics, Adapted from (Luijten, 1998a).

3.5.1 Homogeneous nucleation kinetics

This work uses the theory development proposed by Luijten (1998a) due to their work on the high pressure nucleation of mixtures containing carrier gases. Let us start with homogeneous nucleation kinetics as illustrated in Fig. 3.8. This figure presents J on the nucleation clusters growth as reported by the $Cond$ variable driven by the supersaturation ratio. Nevertheless, if the supersaturation ratio starts to decrease, such a nucleus could to start to evaporate as presented by Eva. The rate of change of the clusters' density can be expressed by:

$$\frac{d\rho_n}{dt} = J_{n-1} - J_n, \tag{3.94}$$

where the nucleation rate can be expressed in terms of the clusters density evaporation and condensation resulting in:

$$J_n = Cond_n\rho_n - Eva_{n+1}\rho_{n+1}, \tag{3.95}$$

After evaluating Eq. 3.94 one can conclude that there are two cases when this derivative vanishes, the first one occurs if the equilibrium is reached, in this case Eq. 3.95 becomes:

$$Cond_n^{eq}\rho_n^{eq} = Eva_{n+1}^{eq}\rho_{n+1}^{eq}. \tag{3.96}$$

The second condition occurs when the nucleation evaluation time exceeds the nucleus formation time $t < 1\mu s$ (Feder et al., 1966; Abraham, 1974). In such a case the nucleation rate achieves a steady solution. Therefore, in this case, one can divide Eq. 3.95 by $Cond_n^{eq}\rho_n^{eq}$, achieving:

$$\frac{J_n}{Cond_n^{eq}\rho_n^{eq}} = \frac{Cond_n\rho_n}{Cond_n^{eq}\rho_n^{eq}} - \frac{Eva_{n+1}\rho_{n+1}}{Cond_n^{eq}\rho_n^{eq}}, \tag{3.97}$$

after replacing Eq. 3.96 into 3.97, one achieves:

$$\frac{J_n}{Cond_n^{eq}\rho_n^{eq}} = \frac{Cond_n\rho_n}{Cond_n^{eq}\rho_n^{eq}} - \frac{\rho_{n+1}}{\rho_{n+1}^{eq}}. \tag{3.98}$$

Also, one can have auxiliary definitions for the supersaturation ratio (Luijten, 1998a)

$$\mathcal{S} = \frac{Cond_n}{Cond_n^{eq}} = \frac{\bar{x}_v}{\bar{x}_v^{eq}} \simeq \frac{\rho_n}{\rho_n^{eq}}. \tag{3.99}$$

Hence, after substituting Eq. 3.99 into 3.98 one achieves:

$$\frac{J_n}{Cond_n^{eq}\rho_n^{eq}} = 1 - \frac{\rho_{n+1}}{\rho_{n+1}^{eq} S_{N+1}}. \tag{3.100}$$

And after considering all the nucleus being formed:

$$J\sum_{n=1}^{N}\left(\frac{1}{Cond_n^{eq}\rho_n^{eq}S_n}\right) = 1 - \frac{\rho_{N+1}}{\rho_{N+1}^{eq}S_{N+1}}, \tag{3.101}$$

the last sum can be expressed in a more general fashion as an integral:

$$J = \left[\int_1^{\infty} \frac{1}{C_n\rho_n^{eq}S_n} dn\right]^{-1}. \tag{3.102}$$

In order to evaluate the integral, the distribution of C_n,ρ_n^{eq} and S_n variables must be known. So let us define the ρ_n^{eq}, where from a thermodynamic point of view achieves the following form:

$$\rho_n^{\varepsilon q} = \rho_1^{eq} \exp\left(-\frac{\Delta\varphi_n^{eq}}{k_B T}\right) \tag{3.103}$$

For the internal consistent classical theory (ICCT) the cluster formation energy is :

$$\frac{\Delta\varphi_n^{eq}}{k_B T} = \bar{\theta}\left(n^{2/3} - 1\right) \tag{3.104}$$

where $\bar{\theta}$ is the dimensionless surface tension, which is defined as:

$$\bar{\theta} = \frac{\sigma a_0}{k_B T}, \tag{3.105}$$

the variable a_0 represents the molecular surface area, and after considering the cluster as a sphere, one obtains:

$$a_0 = (36\pi v_l^2)^{\frac{1}{3}}. \tag{3.106}$$

Now we have to calculate the μ difference between the metastable state and the equilibrium (Luijten, 1998a):

$$\Delta\mu \simeq v^l \Delta P - \Delta\mu_S, \tag{3.107}$$

where $\bar{\mu}_S$ is the chemical potential difference due to the vapour supersaturation (Luijten, 1998a)

$$\Delta\bar{\mu}_S = k_B T \ln(\mathcal{S}). \tag{3.108}$$

One can replace Eqs. 3.108, and 3.107 into Eq.3.85 in order to achieve an expression of the free energy required by the cluster formation:

$$\Delta\varphi_n = -nk_B T \ln(\mathcal{S}) + \sigma A, \tag{3.109}$$

where the product σA can be rewritten in terms of the molecular surface, therefore Eq. 3.109, becomes:

$$\Delta\varphi_n = -nk_B T \ln(\mathcal{S}) + \sigma a_0 n^{2/3}, \tag{3.110}$$

also, the density distribution of the cluster at the superheated state can be modelled as a distribution function of the cluster formation free energy.

$$\rho_n = \rho_1 \exp\left(n \ln \mathcal{S} - \bar{\theta} n^{2/3}\right). \tag{3.111}$$

For computing the critical cluster size, one has to find the saddle point in the free energy and number of monomers surface, resulting in:

$$\left(\frac{\partial \Delta\varphi_n}{\partial n}\right)_{n^*} = \left(\frac{\partial(-nk_B T \ln(\mathcal{S}) + \sigma a_0 n^{2/3})}{\partial n}\right)_{n^*} = 0, \tag{3.112}$$

$$n^* = \left(\frac{2\bar{\theta}}{3 \ln S}\right)^3, \tag{3.113}$$

Now, one must compute the critical cluster radius:

$$r^* = \left(\frac{3}{4\pi} v^l n^*\right)^{\frac{1}{3}}, \tag{3.114}$$

after substituting Eq. 3.114 into 3.82 one can calculate the cluster formation energy:

$$\frac{\Delta\varphi^*}{k_B T} = \frac{4\pi\sigma}{3k_B T} (r^*)^2 = \frac{4}{27} \frac{\bar{\theta}^3}{(\ln \mathcal{S})^2}. \tag{3.115}$$

For the Eq. 3.102 solution, one could express Eq. 3.104 in an alternative form, after multiplying by S_n:

$$S_n \rho_n^{\varepsilon q} = \rho_1^{eq} \exp\left(n \ln S_n - \bar{\theta}\left(n^{2/3} - 1\right)\right) = \rho_1^{eq} \exp\left(\frac{-\Delta\varphi_n}{k_B T} + \bar{\theta}\right) \tag{3.116}$$

Now, in order to compute the non-equilibrium energy of formation, one can use Taylor series in the region near to n^*, resulting in:

$$\Delta\varphi_n \simeq \Delta\varphi^* + \left(\frac{\partial^2 \Delta\varphi_n}{\partial n^2}\right)_{n=n^*} (n - n^*)^2 , \tag{3.117}$$

where the Zeldovich factor definition is:

$$\zeta = \left[\frac{-1}{2\pi k_B T}\left(\frac{\partial^2 \Delta\varphi_n}{\partial n^2}\right)_{n=n^*}\right]^{1/2} , \tag{3.118}$$

after substituting Eq. 3.118 into 3.117, it is obtained:

$$\Delta\varphi_n \simeq \Delta\varphi^* - \zeta^2 \pi k_B T \left(n - n^*\right)^2 \tag{3.119}$$

so, after substituting Eqs. 3.116 and 3.119 into Eq. 3.119, one obtains:

$$J = Cond_{n^*} \rho_1^{eq} \exp\left(-\frac{\Delta\varphi^*}{k_B T}\right) \left[\int_1^\infty \exp\left[-\zeta^2 \pi \left(n - n^*\right)^2\right] dn\right]^{-1} , \tag{3.120}$$

where:

$$Cond_{n^*} = a_0 n^{*2/3} \rho_1 \left(\frac{k_B T}{2\pi \mathfrak{m}}\right)^{1/2} , \tag{3.121}$$

being: $\mathfrak{m}$ is the vapour molecule mass.

Therefore, the nucleation rate equation is obtained after replacing Eq. 3.121 into 3.120 and performing the integral, resulting in:

$$J = \rho_1 \rho_1^{eq} v^l \left(\frac{2\sigma}{\pi m}\right)^{1/2} \exp\left[\bar{\theta} - \frac{4}{27}\frac{\bar{\theta}^3}{(\ln \mathcal{S})^2}\right] \tag{3.122}$$

Eq. 3.122 allows us to calculate the nucleation rate of a component in a supercritical carrier gas, as the case of methane and dry air mixtures, with carbon dioxide. The validity of such a expression is constrained by (Luijten, 1998a):

$$\bar{x}_2^{eq} \ll \ln \mathcal{S} \tag{3.123}$$

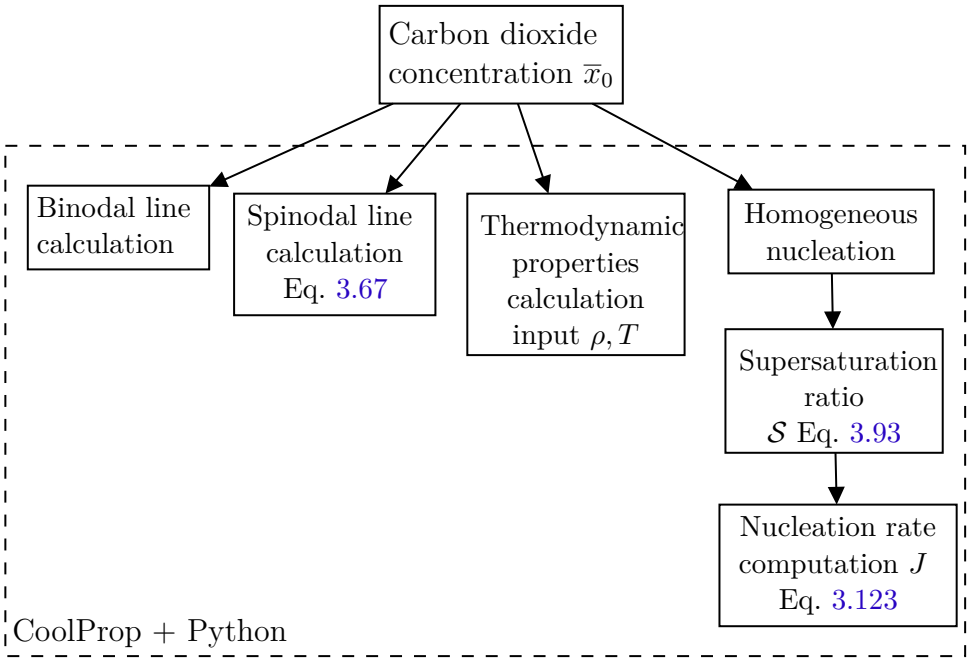

Figure 3.9 – Real gas flow chart for supersonic gas separators computation.

so, the use of Eq. 3.123 is valid as long as the methane, nitrogen or oxygen liquid molar fraction keep low compared to the $\ln S$ term in the new cluster formation.

Finally, Fig. 3.9 presents a flow diagram which considers the more important procedures developed in this chapter, all developed in Python coupled with CoolProp library. The carbon dioxide molar fraction is the input data, and with this value, the binodal and spinodal lines can be computed. Later, if the thermodynamic state is defined ρ and T, one could calculate any thermodynamic property. Finally, Fig. Fig. 3.9 presents the equations required for the homogeneous nucleation rate computation.

4 Real gas compressible fluid dynamics

As shown in previous chapters, the supersonic gas separator evaluation requires an accurate thermodynamic model employment to ensure reliable analysis and design. In this chapter, this analysis will be extended to include the real gas effects on the pure substance and mixture compressible flow in internal channels, and it is divided into three sections as presented in Fig. 4.1.

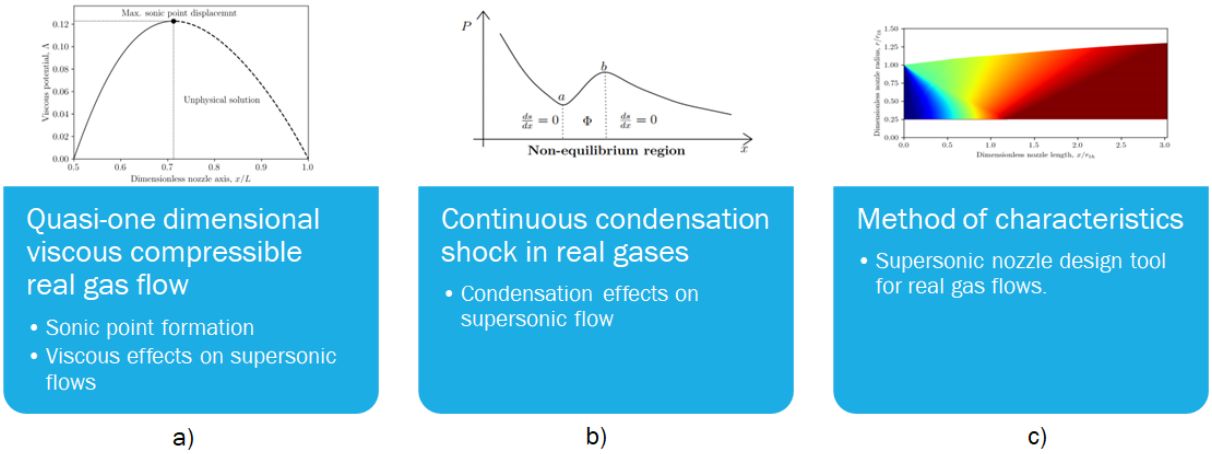

Figure 4.1 – Real gas compressible flow application for real gases a) Quasi-one dimensional viscous compressible flow, b) Continuous condensation shock in real gases c) Method of characteristics.

The quasi-one dimensional viscous compressible flow analysis is devoted for estimating the viscous effects on the sonic point and normal shock wave formation inside the nozzle further details about it implementation are presented in Fig. 4.4. Additionally, it was developed a theory for the computation of condensation shock in real gases and mixtures. Fig 4.17 presents the steps required for its implementation. Finally, the method of characteristics was implemented and used for designing short nozzles for planar and axisymmetric geometries, the algorithm used for its numerical solution is presented in Fig. 4.26.

4.1 Quasi-one dimensional compressible viscous flow

The quasi-one-dimensional analysis is a useful approach for simulating compressible flows inside internal channels. Because it can capture the sonic point and shock wave formation. The most typical application of this approach is the calculation of the supersonic convergent-divergent nozzle flow calculation. Therefore, the quasi-one-dimensional analysis will be devoted to this application. Different from other approaches, this work shows the viscous effects on real gas flow in supersonic convergent-divergent nozzles, to ensure a more realistic simulation.

Convergent-divergent or de Laval nozzles are intensely studied devices because of their widespread application in industrial and aerospace industries. They are also used currently in several other processes such as carbon capture and storage (CCS) (Gernert; Span, 2016) and the renewable energy field (Goodwin et al., 2010). Real gas effects become more relevant within these applications, and using accurate equations-of-state (EOS) become a fundamental tool for a precise and realistic flow calculation. Besides, current analysis is moving towards studying real gas mixtures in novel applications, such as Organic Rankine Cycles (ORC) (Invernizzi et al., 2019), supersonic ejectors (Aidoun et al., 2019), and supersonic gas separators (Cao; Bian, 2019).

In addition to the real gas effects, viscous effects may also be critical in some cases, especially for micro-nozzles (Louisos; Hitt, 2012) or nozzles manufactured by alternative production methods (e.g additive manufacturing) due to their inherent high surface roughness, leading to higher friction factors and consequently nozzle flow deviation from the isentropic behaviour.

As a general rule, a quasi-one-dimensional model is inaccurate for evaluating complex geometries or three-dimensional phenomena. It is, however, a powerful tool to obtain a fast and surprisingly accurate insight into the problem as well as to identify the essential flow parameters. In addition, that model enables robust EOS implementation due to its lower computational cost, which explains the reason for its widespread use. Arina (2004) suggests a real gas model for a cubic EOS, including the well-known Van der Walls and Redlich–Kwong EOS for solving the dense vapour region including the near to critical state. A shock-wave capturing algorithm was implemented. Guardone & Vimercati (2016) present a new formulation for the analytical solution of the convergent-divergent nozzle flow for a class of fluids known as Bethe–Zel'dovich–Thompson (BZT) fluids for several reservoir conditions in order to identify different operational regimes and at various shock waves conditions. Raman & Kim (2018) present a numerical solver for a convergent-divergent nozzle for carbon dioxide flow at supercritical conditions for different EOSs. Vimercati & Guardone (2018) show a steady-state evaluation for real gas in nozzles and a shock-wave capturing scheme for non-classical fluids with a high molecular complexity (BZT), using the Van der Waals EOS. Some authors devised accurate EOS simplifications

for real gases applications, such as Sirignano (2018), who presented a new approach by introducing a linearisation procedure to a cubic EOS to extend its application to several gas dynamic problems, such as the convergent-divergent nozzle. In addition, Yeom & Choi (2019) propose a novel approach using a stiffened gas EOS, in which the real gas equation of state was simplified, being validated for perfect gas and liquid flows in nozzles, Tosto et al. (2021) present a rigorous analysis for dense-vapours in compressible internal flows, such as inviscid real gas nozzle and a real gas Fanno flow.

There exist several approaches for the solution and analysis of steady-state real gas compressible flow in nozzles as shown above. Nevertheless, the open literature lacks work that evaluates the combination of viscous effects and real gas behaviour. Most of previous works have focused on perfect gases flow, such as Hoffman (1969), who evaluates viscous effects on the nozzle performance (Mach number at throat, discharge coefficient and nozzle efficiency), and the work presented by Beans (1970), whereby he proposes a methodology for solving generalized one-dimensional flow. Also, Buresti & Casarosa (1989) analyse the one-dimensional adiabatic viscous flow of gas-particle equilibrium streams. Recently, Ferrari (2021a) presents analytical solutions for diabatic viscous one-dimensional flow and Ferrari (2021b) calculates the exact solution for the perfect gas compressible viscous flow for subsonic or supersonic conical nozzles. In a similar study Yeddula et al. (2022), present an approach to solving the unsteady nozzle compressible flow with heat transfer using the Magnus expansion method.

Building up from previous analyses, this work presents a real gas formulation of compressible viscous flow and proposes a set of governing differential equations, which reveals the relationship between the real gas (through the Grüneisen parameter) and the friction factor. Furthermore, it is shown that at extreme operating conditions, namely high values of wall surface roughness and Grüneisen parameter in combination with small hydraulic diameter and low area ratio, the nozzle divergent part cannot achieve the supersonic regime for any pressure ratio.

4.1.1 Compressible viscous real gas governing equations

Euler's equations for compressible flow were modified by introducing the wall viscous terms in the momentum equation according to Ferrari's formulation (Ferrari, 2021b). Following the same approach, the conservation equations of mass, momentum, and energy for a quasi-one-dimensional adiabatic control volume are respectively:

$$\frac{\partial(\rho A)}{\partial t} + \frac{\partial(\rho A V)}{\partial x} = 0, \tag{4.1}$$

$$\frac{\partial(\rho V A)}{\partial t} + \frac{\partial\left(PA + \rho V^2 A\right)}{\partial x} = -\pi \tau_w D_h + P\frac{\partial A}{\partial x}, \tag{4.2}$$

$$\frac{\partial}{\partial t}\left[\rho\left(\mathfrak{u}+\frac{V^2}{2}\right)A\right]+\frac{\partial}{\partial x}\left[\rho\left(\mathfrak{u}+\frac{V^2}{2}\right)VA\right]+\frac{\partial(PVA)}{\partial x}=0. \tag{4.3}$$

Where t is the time, x is the nozzle axis, A is the cross-section area, V is the flow velocity, P is pressure, τ_w is the wall friction shear stress, D_h is the hydraulic diameter, $\mathfrak{u}$ is the specific internal energy, and ρ is the density.

The Fanning friction factor f is defined by

$$f=\frac{\tau_w}{\frac{1}{2}\rho V^2}. \tag{4.4}$$

Introducing f in the momentum equation 4.2, and after evaluating equations 4.1 - 4.3 in a steady state analysis a non-conservative form are achieved, where h denotes the specific enthalpy:

$$\frac{1}{\rho}\frac{d\rho}{dx}+\frac{1}{V}\frac{dV}{dx}+\frac{1}{A}\frac{dA}{dx}=0, \tag{4.5}$$

$$\frac{dP}{dx}+\rho V\frac{dV}{dx}=-\frac{2\rho V^2 f}{D_h}, \tag{4.6}$$

$$\frac{dh}{dx}+V\frac{dV}{dx}=0. \tag{4.7}$$

Also, after considering the Gibbs' relation

$$\frac{dh}{dx}=T\frac{ds}{dx}+\frac{1}{\rho}\frac{dP}{dx}+\sum_i \mu_i\frac{dN_i}{dx}, \tag{4.8}$$

where T, μ and s denote the temperature, chemical potential and specific entropy, respectively. After assuming a pure substance or a constant composition mixture $dN_i/dx=0$ and substituting Eq. 4.8 into Eq. A.1 and rearranging it, the energy equation becomes

$$T\frac{ds}{dx}+\frac{1}{\rho}\frac{dP}{dx}+V\frac{dV}{dx}=0. \tag{4.9}$$

Finally, a system of ordinary differential equations 4.5, 4.6, and 4.9 is obtained, which governs the viscous compressible real gas flow. The solution of that system of equations requires their formulation in an explicit form.

To obtain that, let first the pressure $P(\rho,s)$, be formulated as an exact derivative

$$\frac{dP}{dx}=\left(\frac{\partial P}{\partial \rho}\right)_s\frac{d\rho}{dx}+\left(\frac{\partial P}{\partial s}\right)_\rho\frac{ds}{dx}. \tag{4.10}$$

Next, the Maxwell relations is introduced along with the definition of the Grüneisen parameter

$$\frac{d\rho}{dx} = \frac{1}{c^2}\left(\frac{dP}{dx} - Gr\rho T\frac{ds}{dx}\right), \tag{4.11}$$

where c is the speed-of sound, after substituting the above equation 4.11 and Eq. 4.6 into Eq. 4.5, it is obtained

$$\frac{1}{V}\frac{dV}{dx} + \frac{1}{A}\frac{dA}{dx} + \frac{1}{c^2}\left(-\frac{2V^2 f}{D_h} - V\frac{dV}{dx} - GrT\frac{ds}{dx}\right) = 0, \tag{4.12}$$

in order to solve Eq. 4.12, the specific entropy increase rate in the nozzle has to be calculated; this is achieved after replacing Eq. 4.6 in Eq. 4.9 and rearrange it

$$\frac{ds}{dx} = \frac{2V^2 f}{TD_h}. \tag{4.13}$$

After substituting Eq. 4.13 into Eq. 4.12 and some algebraic manipulation the velocity area relation is obtained for a real gas viscous compressible flow

$$\frac{dV}{dx} = \frac{\left(\frac{2f}{D_h}M^2(Gr+1) - \frac{1}{A}\frac{dA}{dx}\right)V}{(1-M^2)}. \tag{4.14}$$

where M is the Mach number

$$M = \frac{V}{c}. \tag{4.15}$$

By analysing (4.14) one can notice that Gr in association with the normalized friction factor f/D_h, strongly affect the flow behaviour as it is analysed in detail further. Both contribution results in a new definition named viscous potential, Λ given by

$$\Lambda = \frac{2f}{D_h}(Gr+1), \tag{4.16}$$

which accounts for the departure from the isentropic flow formulation.

The Mach number variation inside the nozzle can be computed from Eq. 4.14 and by the Mach number definition Eq. 4.15 and its differentiation, one achieves:

$$\frac{1}{M}\frac{dM}{dx} = \frac{\Lambda M^2 - \frac{1}{A}\frac{dA}{dx} - \frac{1}{c}\frac{dc}{dx}(1-M^2)}{(1-M^2)}. \tag{4.17}$$

The speed-of-sound derivative can be explicitly expressed as a function of pressure and specific entropy $c(P,s)$, which yields:

$$\frac{dc}{dx} = \left(\frac{\partial c}{\partial P}\right)_s \frac{dP}{dx} + \left(\frac{\partial c}{\partial s}\right)_P \frac{ds}{dx}. \tag{4.18}$$

where, according to (Thompson, 1971) the speed-of-sound partial derivatives can be formulated as follows:

$$\left(\frac{\partial c}{\partial P}\right)_s = \frac{\Gamma - 1}{\rho c} \tag{4.19}$$

where Γ is the fundamental derivative of gas dynamics. And it can be formulated as Colonna et al. (2009):

$$\Gamma = 1 + \frac{\rho}{c}\left(\frac{\partial c}{\partial \rho}\right)_s \tag{4.20}$$

and,

$$\left(\frac{\partial c}{\partial s}\right)_P = \rho c \left(\frac{\partial T}{\partial P}\right)_s + \frac{c^3 \rho^2}{2}\left(\frac{\partial^2 T}{\partial P^2}\right)_s, \tag{4.21}$$

After several algebraic operations and thermodynamic definitions use, one can achieve:

$$\left(\frac{\partial c}{\partial s}\right)_P = \frac{GrT}{c} + \frac{GrTc\rho}{2}\left(\left(\frac{\partial Gr}{\partial P}\right)_s \frac{1}{Gr} + \frac{Gr - 2\Gamma + 1}{\rho c^2}\right), \tag{4.22}$$

finally after substituting (4.19), (4.22), and (4.13) into (4.18), the speed-of-sound differential equation becomes:

$$\frac{dc}{dx} = \frac{\Gamma - 1}{\rho c}\frac{dP}{dx} + \frac{GrM^2 fc}{D_h}\left(3 + \left(\frac{\partial Gr}{\partial P}\right)_s \frac{c^2\rho}{Gr} + Gr - 2\Gamma\right), \tag{4.23}$$

where,

$$\left(\frac{\partial Gr}{\partial P}\right)_s = \frac{\rho}{T}\left(\frac{\partial^2 T}{\partial \rho \partial P}\right)_s + \frac{Gr(1 - Gr)}{\rho c^2}. \tag{4.24}$$

After inspecting (4.23) one can perceive that dc/dx variation along the nozzle depends on the fluid's thermodynamic state measured by Γ, Gr, ρ, c and the flow conditions M, dP/dx and f/D_h. And depending on the interaction of these parameters the speed-of-sound could behave in a non-ideal fashion.

After solving the velocity differential equation (4.14), it is possible to calculate the pressure (4.6), density (4.11), and specific enthalpy based on (4.8) to obtain

$$\frac{dh}{dx} = T\frac{ds}{dx} + \frac{1}{\rho}\frac{dP}{dx}. \tag{4.25}$$

Also, the temperature $T(\rho, s)$ can be calculated by

$$\frac{dT}{dx} = \left(\frac{\partial T}{\partial \rho}\right)_s \frac{d\rho}{dx} + \left(\frac{\partial T}{\partial s}\right)_\rho \frac{ds}{dx}, \tag{4.26}$$

after some manipulation, where k is the isothermal compressibility and C_P the specific heat at constant pressure, yields

$$\frac{dT}{dx} = \frac{T}{\rho}\left(Gr\frac{d\rho}{dx} + \frac{k\rho^2 c^2}{C_P}\frac{ds}{dx}\right). \tag{4.27}$$

Notice that for perfect gases the Grüneisen parameter becomes a function of γ, the isentropic expansion coefficient $Gr = \gamma - 1$. After substituting it in Eq. 4.13 and Eq. 4.14, which reproduces the perfect gas expression found in (Zucrow; Hoffman, 1977).

4.1.2 Sonic point

It is noteworthy to mention that the sonic point is not located at the nozzle geometrical throat $dA/dx = 0$ for viscous flow being shifted to a location downstream the throat in the divergent nozzle portion. This occurs due to the viscous effects on the flow (Hodge; Koenig, 1995). For a more general situation (Beans, 1970; Zucrow; Hoffman, 1977), the sonic point is located where the numerator and denominator of Eq. 4.17 vanish simultaneously. Consequently, it leads to an indetermination of Eq. 4.17. At this point it is convenient to use the L'Hôpital's rule of Calculus to obtain the solution, which, after some algebraic manipulation, one obtains

$$\left(\frac{dM}{dx}\right)_{sonic} = -\frac{1}{2c}\frac{dc}{dx} - \frac{1}{2}\Lambda \pm \frac{1}{2}\sqrt{\left(\Lambda + \frac{1}{c}\frac{dc}{dx}\right)^2 - 2\frac{d\Lambda}{dx} + \frac{2}{A}\frac{d^2A}{dx^2} - \frac{2}{A^2}\left(\frac{dA}{dx}\right)^2}, \tag{4.28}$$

After inspecting Eq. 4.28, the existence of two solutions is evident, which depends on the boundary conditions of the flow, being positive for the supersonic or negative for the subsonic solution.

4.1.3 Sonic point displacement

As examined in the last section, the sonic point location is conditioned by the Mach-area relationship Eq. 4.17, which leads to an indetermination as the fluid reaches the local speed-of-sound $M = 1$. Nevertheless, at some conditions the speed-of-sound may never be attained within the nozzle because the of the combination of the following parameters: a high normalized friction factors, f/D_h, a high Gr, and a small area variation within the nozzle dA/dx. Their combined effects on the flow could be calculated by analytical methods after considering locally constants values of f and G_r for a nozzle geometry explicitly formulated as a function of x i.e, $A = A(x)$. Firstly, the sonic point can be

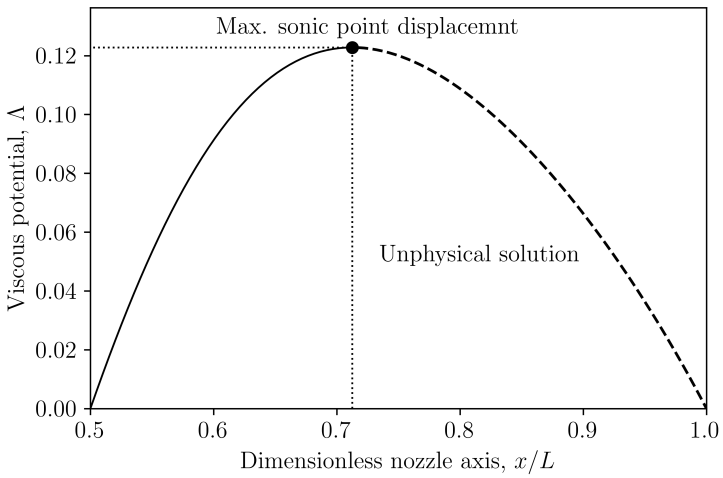

Figure 4.2 – Viscous potential for a respective sonic point displacement dashed line corresponds to the unphysical solution.

calculated by finding the roots of Eq. 4.17 numerator by imposing the sonic condition given by $M = 1$, which yields to

$$\Lambda = \frac{1}{A}\frac{dA}{dx}. \tag{4.29}$$

In order to present a study case, the Arina's nozzle geometry (Arina, 2004) is analysed in non-dimensional coordinates, where L is the nozzle length, and x_{th} is the geometric throat position

$$A(x) = 3.5 - \frac{x}{x_{th}}\left[6 - 4.5\frac{x}{x_{th}} + \left(\frac{x}{x_{th}}\right)^2\right] \quad \text{for } L > x > x_{th}. \tag{4.30}$$

Therefore, by substituting the Arina's area dependence Eq. 4.30 into 4.29, and carrying out the solution, Λ can be obtained for a x sonic point position, given by:

$$\Lambda = \frac{3\,(x - 2x_{th})\,(x - x_{th})}{x^3 - 4.5x^2x_{th} + 6xx_{th}^2 - 3.5x_{th}^3}. \tag{4.31}$$

Figure 4.2 displays the viscous potential from Eq. 4.31 as a function of the Arina's dimensionless axis x/L. By examining the graphics in that figure, one may observe that the sonic condition moves downstream up to $x/L = 0.712$ where the viscous potential is a maximum $\Lambda = 0.123$. Beyond that position, the sonic point cannot be attained any-longer within the nozzle. Mathematical solutions to the right of the maximum displacement sonic point (dashed line) do not have physical meaning.

For a more general nozzle, where $A(x)$ is known, Eq. 4.32 displays a point of maximum for any geometry and viscous potential. That maximum condition is given the imposing that the x-derivative of Eq. 4.29 is null, which yields to

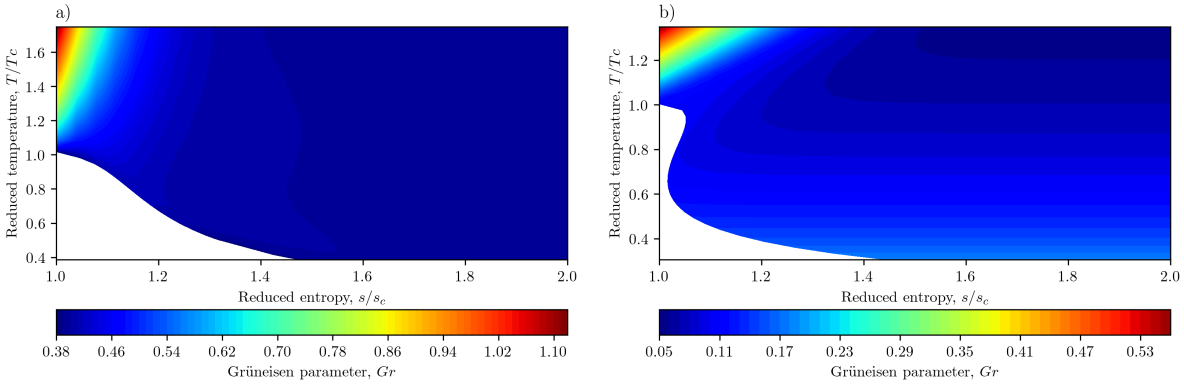

Figure 4.3 – Grüneisen parameter variation for superheated and supercritical vapour of a) Oxygen and b) Isobutane.

$$\frac{d(\Lambda)}{dx} = \frac{d}{dx}\left(\frac{1}{A}\frac{dA}{dx}\right) = 0, \tag{4.32}$$

after carrying out the derivative, one obtains

$$A\frac{d^2A}{dx^2} - \left(\frac{dA}{dx}\right)^2 = 0. \tag{4.33}$$

Hence, Eq. 4.33 solution gives the maximum sonic point displacement position x_{max}, which corresponds to the threshold of establishing a supersonic flow downstream of x_{max}. A higher Λ will inhibit attaining a supersonic flow. Taking for Arina's nozzle geometry as an example, consider a high pressure and low temperature supercritical oxygen state ($Gr = 1.1$) and after employing Eq. 4.16 the maximum admissible f/D_h value is 0.029. In contrast, a low pressure superheated oxygen exhibit a ($Gr = 0.38$), resulting in a maximum admissible f/D_h value of 0.044. Therefore, the maximum normalized friction factor will depend on the fluid thermodynamic state.

Figure 4.3 presents the G_r behaviour in a reduced temperature - specific entropy plane, for an oxygen MPEOS (Schmidt; Wagner, 1985) and for an isobutane EOS (Bücker; Wagner, 2006) in superheated and supercritical phase. The figure shows the G_r low variation for superheated vapours. That trend applies to both fluids. However, Gr steeply varies as the vapour phase becomes supercritical, especially for the region close to the critical point. A considerable difference can be perceived between both fluids due to their different molecular complexity, directly impacting the Gr calculation, and subsequently the viscous effects on the nozzle.

4.1.4 Rankine-Hugoniot relations

If the nozzle exit pressure is higher than the environment discharging pressure, but lower than the critical subsonic solution, a normal shock wave should be formed within the

nozzle. The Rankine-Hugoniot relations (4.34 - 4.36) are widely known for the treatment of discontinuities on compressible flows (e.g, shock-waves, detonations (Thompson, 1971), or even evaporation waves (Simões-Moreira; Shepherd, 1999) and condensation shocks (Bolaños-Acosta et al., 2021). The three conservation equations valid for a discontinuity are presented next, where the index 1 stand for the upstream state and 2 for downstream one:

$$\rho_1 V_1 = \rho_2 V_2, \tag{4.34}$$

$$\rho_1 V_1^2 + P_1 = \rho_2 V_2^2 + P_2, \tag{4.35}$$

$$h_1 + \frac{1}{2} V_1^2 = h_2 + \frac{1}{2} V_2^2. \tag{4.36}$$

4.1.5 Friction factor

The well known Coolebrok-White equation was used for obtaining the Darcy–Weisbach friction factor f_D, ε denotes the channel surface roughness and Re is the Reynolds number

$$\frac{1}{\sqrt{f_D}} = -2 \log \left(\frac{\varepsilon}{3.7 D_\mathrm{h}} + \frac{2.51}{\mathrm{Re}\sqrt{f_D}} \right). \tag{4.37}$$

Note that the Darcy–Weisbach friction factor is four times the Fanning friction factor $f = f_D/4$, and it is calculated for each computation step. The Re number of rectangular cross-section channels were computed using the methodology proposed by Jones (1976) for different aspect ratio geometries.

4.1.6 Numerical solution

The numerical solution scheme of the real viscous gas compressible flow and the shock wave position is depicted in Fig. 4.4; this control volume is discretized using constant steps Δx. Firstly, the sonic point location was found by the numerical root finding of Eq. 4.29 for the divergent nozzle part, where Gr and f values were initially computed for an isentropic sonic point located where $c(h, s) = V$. Next, the solution follows the Hybrd method (More et al., 1980) for the root finding and this routine was implemented through SciPy libraries (Virtanen et al., 2020). After solving the sonic point, the algorithm uses the fourth order Runge-Kutta method (RK-4) backwards until the nozzle inlet is reached. It was necessary to match the reservoir specific entropy s_0, to the one from the solution obtained from the backwards RK-4 integration. After computing the specific entropy at the sonic point, the algorithm proceeded forward using RK-4 until the nozzle exit was found.

Notice that for the sonic solution, $M = 1$, Eq. 4.14 cannot be solved as discussed in section 4.1.2, due to the indetermination of such an equation. Therefore, as the sonic

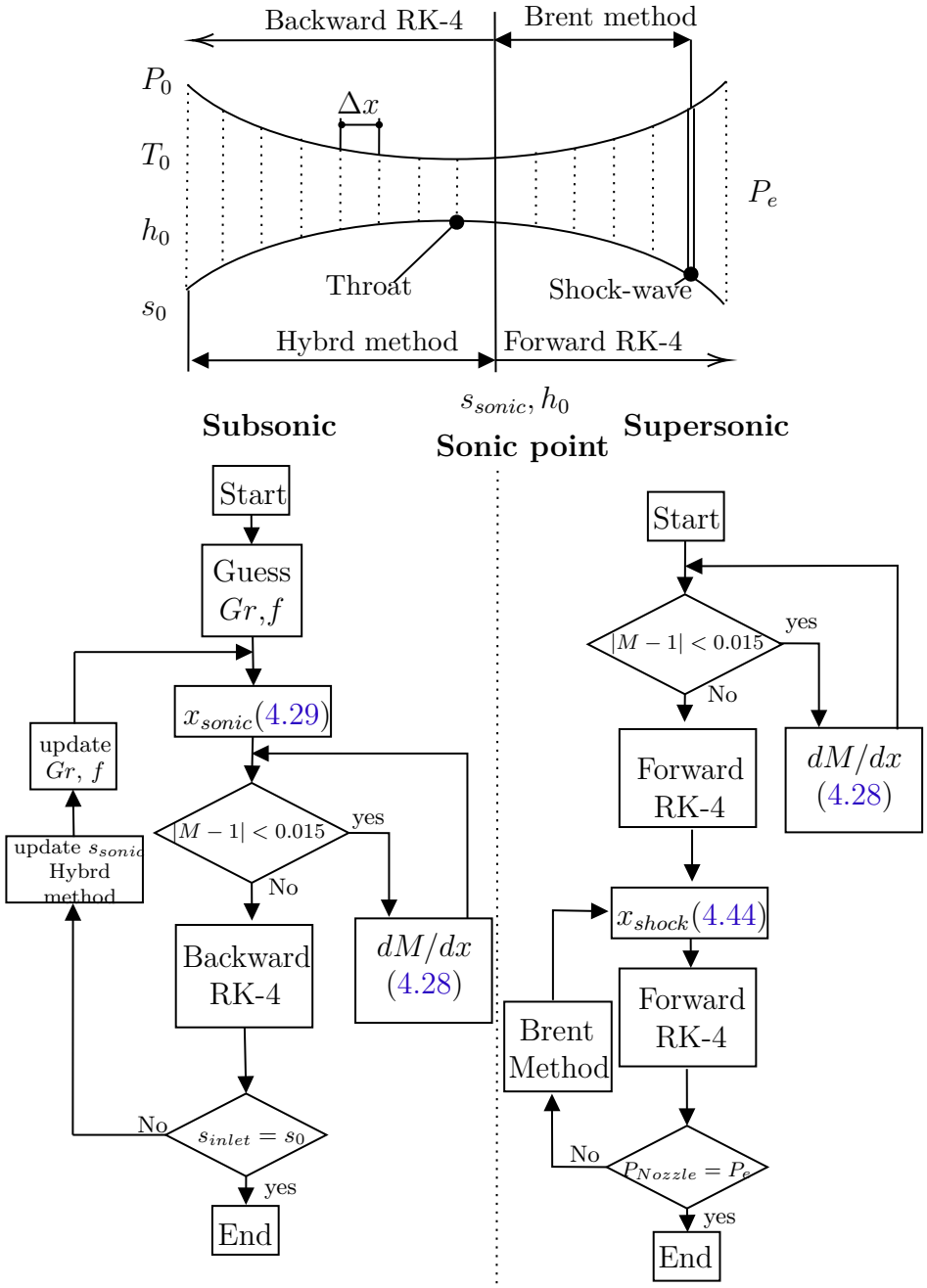

Figure 4.4 – Numerical solution procedure for supersonic viscous flow.

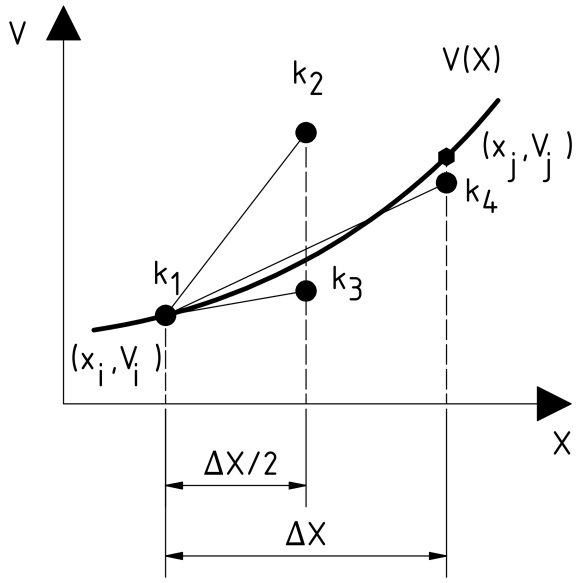

Figure 4.5 – Fourth-order Runge-Kutta.

point has approached the Eq. 4.28 was solved using a predictor–corrector finite difference scheme, for all the required derivatives and these equations were used to solve Eq. 4.28. This looping solution process continued until those derivatives matched the corresponding thermodynamic state.

Flow thermodynamic properties (c, C_P, k, Gr) were computed by using the code developed by Bell et al. (2014). Also, a multidimensional solver was implemented using the Hybrd method for defining the thermodynamic state using specific enthalpy and specific entropy as independent variables (h, s). Specific entropy and enthalpy were computed using Eq. 4.13 and Eq. 4.25 respectively, for each calculation step.

4.1.6.1 Fourth-order Runge-Kutta

As seen in the last section, it is required the discretization and solution of Eq. 4.14, because once calculated the velocity differential equation all other thermodynamic properties can be calculated. In this work was used the classic formulation of the fourth-order Runge-Kutta method (Chapra; Canale, 2010) as the solving integration method. Fig. 4.5 presents a schematic representation of this method.

The Runge-Kutta consists of the evaluation of the function slope in four different points (k_1, k_2, k_3, k_4):

$$k_1 = f\left(x_i, V_i\right), \tag{4.38}$$

$$k_2 = f\left(x_i + \frac{\Delta x}{2}, V_i + \frac{1}{2}\Delta x k_1\right), \tag{4.39}$$

$$k_3 = f\left(x_i + \frac{\Delta x}{2}, V_i + \frac{1}{2}\Delta x k_2\right), \tag{4.40}$$

$$k_4 = f\left(x_i + \Delta x, V_i + \Delta x k_3\right). \tag{4.41}$$

For each function evaluation required by the k_n factors it was calculated the thermodynamic properties required for the flow solution. After this calculation, the velocity differential equation was solved.

$$\frac{dV}{dx} = \frac{1}{6}\left(k_1 + 2k_2 + 2k_3 + k_4\right), \tag{4.42}$$

and the velocity

$$V_j = V_i + \Delta x \frac{dV}{dx} \tag{4.43}$$

Once the velocity was calculated, other properties can be estimated in the same fashion as expressed in Eq. 4.43.

4.1.6.2 Sonic point and shock wave capture

If there were a shock wave inside the nozzle, a new stagnation condition was calculated considering the shock wave downstream conditions obtained after solving the Rankine-Hugoniot relations Eqs. (4.34 - 4.36) by using the Hybrd method. However, the shock wave position depends on the exit pressure, hence, a space marching algorithm is required for the shock capturing.

In this work it was used the Brent scalar minimization (Press et al., 2007) to find the sonic point and shock wave position. This method is widely used in literature to find a scalar minimum function. This approach increases the computational speed compared to a traditional space marching algorithm, because it uses the inverse parabolic interpolation for the first part of the search and once the algorithm is near to the minimum, the algorithm switches for the golden search routine as depicted in Fig. 4.6.

The first step for the solution is the inverse parabolic interpolation, which consists of the use of three points (1,2,3) for the parabola construction, and next it was used their vertex for the estimation of the next solution point (4), so for the next parabola construction is considered the points (1,4,3). This process must be performed several times until the values from the last iterations converge by a defined tolerance. In this stage the algorithm switches for the golden section search, where it was used the golden ratio to find the next calculation point (5), this process is performed several times until the minimum was obtained point (7). The Brent method was implemented using the SciPy code (Virtanen et al., 2020).

$$g(x) = |P_{Nozzle} - P_e| \tag{4.44}$$

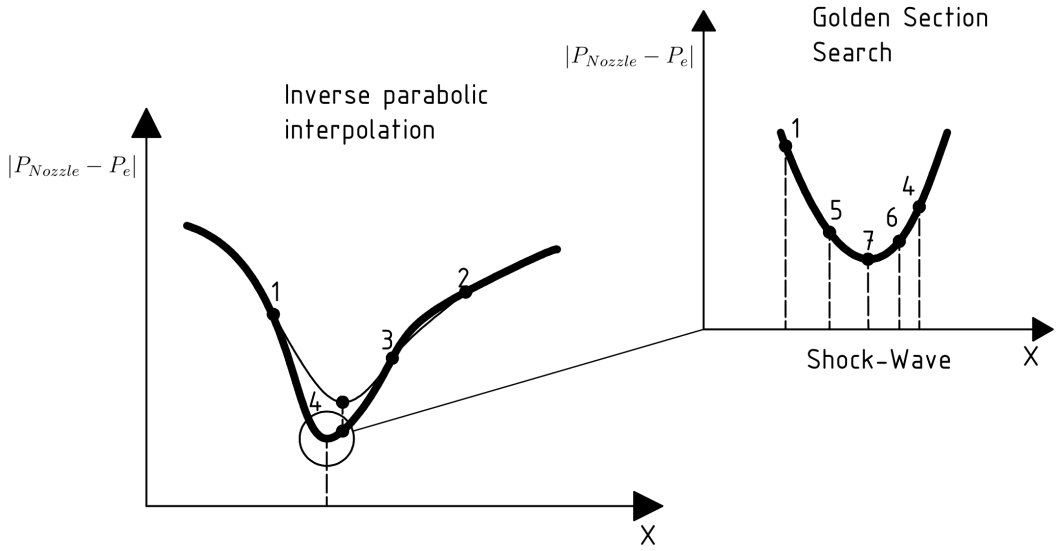

Figure 4.6 – Shock wave capture using Brent scalar minimization.

where P_{nozzle} is the final nozzle pressure with a shock wave position inside the nozzle and P_e is the exit pressure. Therefore, the Brent minimization method starts to march in space in the nozzle divergent part, seeking the condition whereby Eq. 4.44 is minimum.

4.1.7 Perfect viscous gas flow verification

The first step in the proposed approach verification, is to compare the developed methodology to the analytical viscous solution obtained by Ferrari (2021b). Ferrari's expression is developed for a viscid dilute gas in conical axisymmetric nozzles. Figure 4.7 presents the comparison outcomes for a different number of mesh nodes. Figure 4.7a is the subsonic solution obtained for the following conditions: $L = 45$ cm, initial diameter $D_1 = 8$ cm, final diameter $D_2 = 3.5$ cm, $P_0 = 5$ bar, $T_0 = 500$ K, $M_1 = 0.11$ and $f = 0.004$, and Figure 4.7b is the supersonic solution obtained for the following conditions: $L = 60$ cm, initial diameter $D_1 = 5$ cm, final diameter $D_2 = 9$ cm, $P_0 = 2$ bar, $T_0 = 400$ K, $M_1 = 1.1$ and $f = 0.006$. These results are obtained after using the (Lemmon et al., 2000) EOS. Figures 4.7a and 4.7b outcomes show the good performance of the developed method and display the mesh independence of the proposed numerical approach.

4.1.8 Real viscous gas flow validation

Table 4.1 presents the experimental data from open literature used for validating the proposed methodology. That table presents in the first column the tested fluid, followed by stagnation properties (P_0, T_0, and Z_0) used for each case with their respective references for the experimental data shown in the last column.

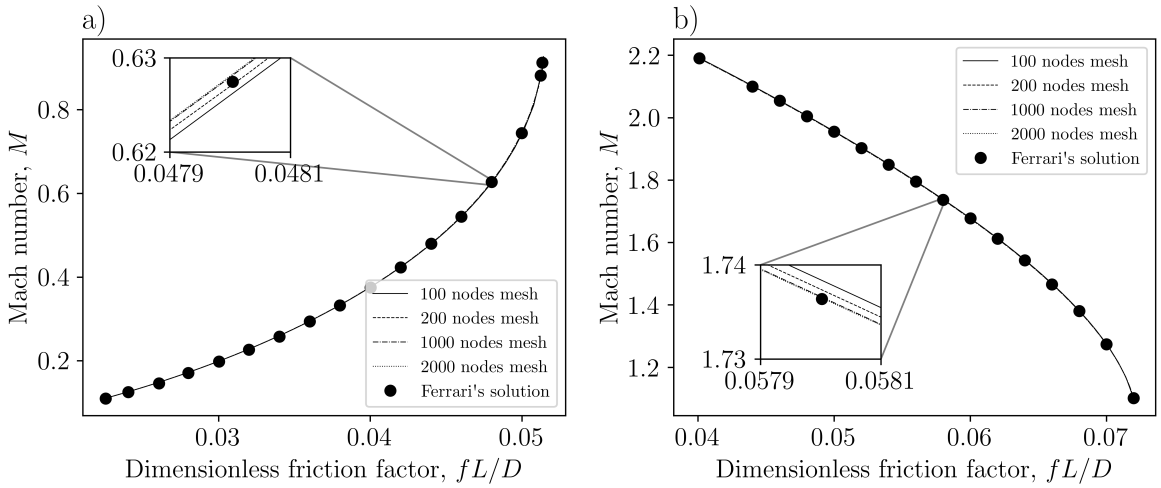

Figure 4.7 – Ferrari (2021b) analytical and numerical results comparison, a) subsonic and b) supersonic solution.

Table 4.1 – Stagnation points, and experimental data used for validation.

Fluid	P_0 (bar)	T_0 (K)	Z_0	Experiment
MDM	9.20	540.7	0.63	(Spinelli et al., 2018)
Steam	100.7	703.15	0.82	(Gyarmathy, 2005)
75 % CO_2-Air mixture	9.98	265.2	0.94	(Bier et al., 1990a)

The experimental data reported by Spinelli et al. (2018) was used for the supersonic flow of octamethyltrisiloxane (MDM) (Thol et al., 2017). That substance has a high molecular weight ($M = 236.53$ g/mol) and, due to this high molecular weight and complexity, this substance exhibits a non-ideal compressible behaviour near to the critical point. Considering the stagnation conditions presented in Table 4.1, a numerical simulation was performed for a 750 uniformly-spaced element mesh. Figure 4.8a presents the numerical simulation for the pressure profile. Figure 4.8b presents the Mach number comparison against the experimental results. Good agreement was found between the simulation and the experimental results. For the last pressure measurement, the deviation reached 7.2 %.

The EOS of Wagner & Pruß (2002) was used for the high-pressure steam simulation. The 4B nozzle of Gyarmathy (2005) was simulated using a 750 element mesh, which was found to be stable and mesh size independent. High deviations in pressure (13.6 %) were found in this simulation for low supersonic Mach numbers; otherwise the simulation gave better results as the viscous effects became more relevant at the nozzle outlet where the pressure deviation fell to (4.6 %).

For the mixture validation, the experimental data of Bier et al. (1990a) was used for a mixture of carbon dioxide and atmospheric dry air. For the sake of simplicity air was treated as being pure nitrogen using the GERG-2008 MPEOS. The formulation of Wilke

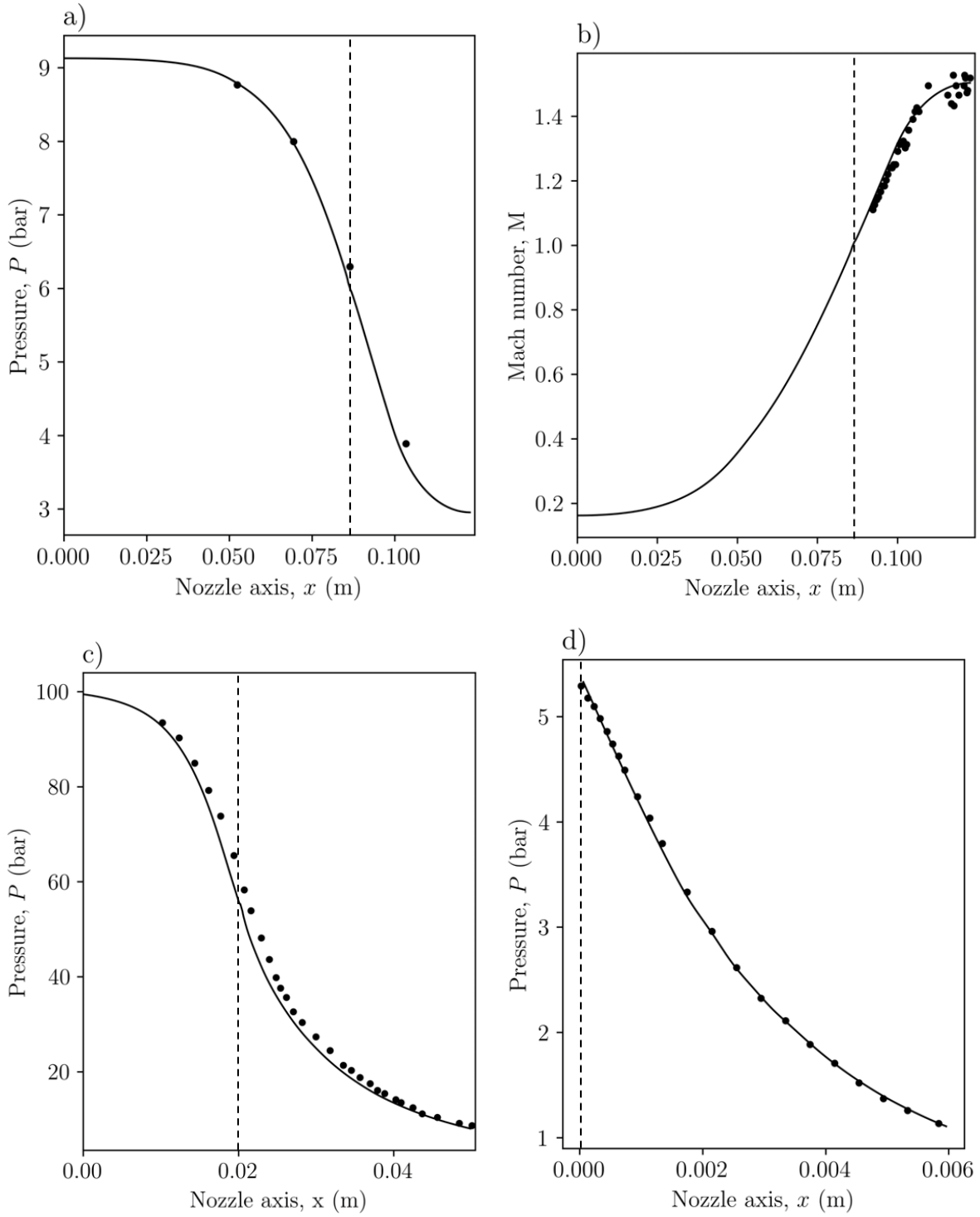

Figure 4.8 – Experimental results used for validation, a) Pressure profile and b) Mach profile MDM, c) Pressure profile for steam d) Pressure profile for 75 % CO_2-Air mixture; the black continuous line represents the numerical solution and the black solid points, the experimental data and dashed line the throat position.

(1950) was used for the mixture dynamic viscosity calculation. Table 4.1 presents the stagnation conditions of the test, and Fig. 4.8d presents the pressure profile comparison between the experimental and simulation for a 500 elements mesh.

4.1.9 Shock wave position verification

For the shock wave model capturing verification, it was used the work by Arina (2004), due to its benchmark widespread use in supersonic nozzles flows. The MPEOS was used for air and nitrogen mixtures (Lemmon et al., 2000). Figure 4.9 presents the nozzle pressure profile; the solution obtained by Arina (2004) was compared reproducing precisely the pressure jump and shock location.

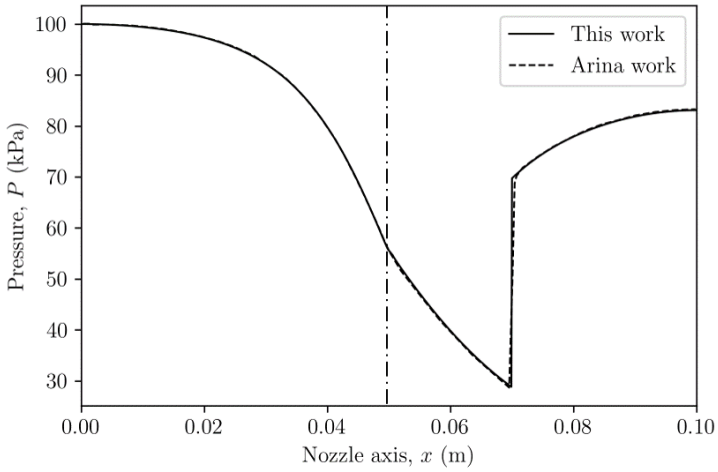

Figure 4.9 – Pressure distribution Arina's nozzle, ($P_0 = 100$ kPa, $T_0 = 288$ K), for dry air, dash-dotted line presents the throat position.

4.2 Prandtl-Meyer expansion waves

As explained by Anderson (1990) when a supersonic flow is turned away from itself, the fluid expands and subsequently their Mach number increases, leading to a decrease in the flow pressure, density and temperature. This is known as expansion waves, as depicted in Fig. 4.10a. Following the same methodology used for an oblique shock wave analysis, one can stablish a series of velocity triangles for the evaluation of expansion waves as shown in Fig. 4.10b.

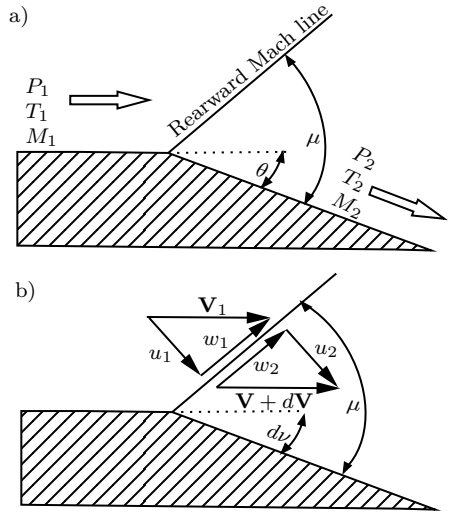

Figure 4.10 – Prandtl-Mayer expansion wave. Adapted from (Hodge; Koenig, 1995).

From this velocity triangle one can stress out that:

$$\mathbf{V}\cos\mu = (\mathbf{V}+d\mathbf{V})\cos(\mu+d\nu), \tag{4.45}$$

where ν is the Prandtl-Meyer angle, and μ the Mach angle:

$$\mu = \sin^{-}1\frac{1}{M}, \tag{4.46}$$

Eq. 4.45 can be rewritten as:

$$\mathbf{V}\cos\mu = (\mathbf{V}+d\mathbf{V})(\cos\mu\cos d\nu - \sin\mu\sin d\nu), \tag{4.47}$$

and after considering the following simplifications:

$$\cos d\nu \approx 1, \tag{4.48}$$

$$\sin d\nu \approx d\nu, \tag{4.49}$$

and after substituting Eqs. 4.53 and 4.49 into 4.52:

$$\mathbf{V}\cos\mu = (\mathbf{V}+d\mathbf{V})(\cos\mu - d\nu\sin\nu), \tag{4.50}$$

After expanding Eq. 4.50 and ingnoring derivative products, it is obtained:

$$\frac{d\mathbf{V}}{\mathbf{V}} = \tan\mu d\nu; \tag{4.51}$$

finally, the Prandtl-Meyer function is obtained after considering the following Mach angle property $\tan\mu = 1/\sqrt{(M^2-1)}$

$$d\nu = \sqrt{M^2-1}\frac{d\mathbf{V}}{\mathbf{V}}, \tag{4.52}$$

The Prandtl-Meyer function can be rearranged and integrated in total velocity and the speed-of-sound terms, after using the Mach number definition Eq. 4.15 , obtaining:

$$\int_0^{\nu} d\nu = \int_{V_{TH}}^{V} \sqrt{\frac{1}{c^2} - \frac{1}{\mathbf{V}^2}}d\mathbf{V} \tag{4.53}$$

Due to thermodynamic properties variation along a real gas process, such equation cannot be solved using analytical methods, and must be used a numerical approach. And the Prandtl-Meyer solution of real gases using MPEOS demands a robust numerical algorithm to achieve the solution at each integration step. In this work, the multiple Simpson's rule was chosen due to their third-order accuracy (Chapra; Canale, 2010), and the solution was obtained after performing 20 integration steps. Next, the work of Cramer & Crickenberger (1992) is used for the algorithm validation under real gas flow conditions. Fig. 4.11 presents the Prandtl-Meyer angle as a function of total velocity and Mach number, Fig. 4.11a shows the solution of Eq. 4.53 as a total velocity function for toluene, which corresponds to stagnation conditions of $T_0 = 1.07T_c$ and $\rho_0 = \rho_c/0.67$, the Mach number Fig.4.11b behaves in the same fashion as presented by Cramer & Crickenberger (1992).

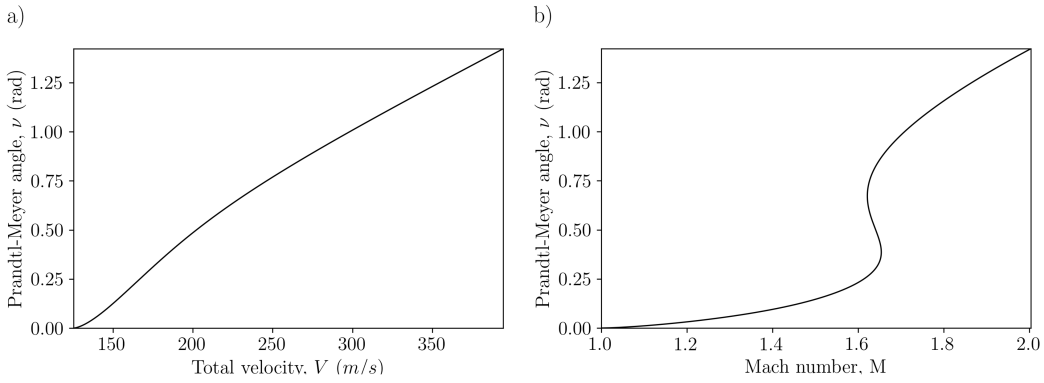

Figure 4.11 – Real gas effects on Prandtl-Meyer angle in function of total velocity (a), and Mach number (b) for Toluene.

4.3 Condensation shock

The condensation shock is a widely known phenomena in the compressible flow analysis, it was first openly discussed in the Volta congress due the formation of unexpected shock waves in nozzles (Tollmien, 1937). Later it was studied on the supersonic flight due to the characteristic mist Mach cone formation or in the hypersonic wind tunnels

operation (Wegener; Mack, 1958). Also, this phenomenon have been of interest for some vapour handling process, because it can affect the equipment behaviour as the case of supersonic ejectors (Yang et al., 2019), compressors (Lettieri et al., 2015) and turbines (Pini et al., 2020). Since, in this case the condensation shock can be undesirable due to the irreversibility that this phenomenon generates due to condensation itself and the possible oblique shock waves production. However, for the supersonic gas separators the condensation shock wave is required to achieve the carbon dioxide separation.

After exposing the condensation shock relevance. One can proceed to explain the methodology used for its solution. Firstly, this work uses a quasi-one-dimensional approach, in order to find the more relevant flow phenomena parameters, such a model is coupled with a MPEOS in order to have a robust thermodynamic framework. So the metastable supersonic flow is computed as shown in section 4.1.1, as the critical nucleation ratio is computed as presented in section 3.5.1, and once its achieves their critical value the condensation shock starts.

The condensation shock is solved by two approaches. The first one uses the discontinuous shock theory presented by Bolaños-Acosta et al. (2021) and the second one presents the new approach developed in this thesis, which consists on the condensation shock structure computation through a continuous approach using a single fluid model hypothesis.

In order to understand the phenomena behind the condensation shock, one must study the droplet growth and the flow regimes present on its developing. And this will be explained in the next section.

4.3.1 Droplet growth phenomena

Once the critical cluster has been formed by homogeneous nucleation, it starts to grow due to the gas-vapour mixture supersaturation. Droplet growth phenomena is a well studied subject in fluid dynamics, due to their widespread application in different fields such as aerosol production, intense cooling, cloud formation and spraying process. Nevertheless, even though this phenomenon is present in our daily life, it is a quite complicated subject to evaluate due to the wide scales present in their development, as presented below:

- $r_d \sim$ 1mm rain drops radius.
- $r_d \sim$ 1µm sprays typical radius.
- $r_d \sim$ 1nm droplet radius produced by homogeneous nucleation.

Therefore, an appropriate theoretical evaluation of the droplet growth, must consider if the continuum approach is valid, because at nano scales this approach is not suitable

for an accurate computation. In order to see the continuum application range, one must compute the Knudsen number K_n:

$$K_n = \frac{\hat{l}}{r_d}, \tag{4.54}$$

where $\hat{l}$, represents the mean free path of the vapour molecules, and it can be expressed as:

$$\hat{l} = \frac{\eta\sqrt{\mathcal{R}T}}{P}, \tag{4.55}$$

where η denotes the dynamic viscosity of the gas mixture, one can substitute Eq. 4.55 into 4.54 to obtain:

$$K_n = \frac{\eta\sqrt{\mathcal{R}T}}{r_d P}. \tag{4.56}$$

So it is clear after inspecting Eq. 4.56 that the pressure and the droplet radius have a direct impact on the Knudsen number computation, and, subsequently in the continuum approach application validity, because the continuum analysis can only be applied for $K_n < 0.01$. Otherwise, other approaches must be used for solving the free molecular flow. Fig. 4.12 presents a graphical representation of a nano droplet immersed in a supersaturated vapour-gas mixture. This figure shows the Knudsen boundary layer and its interface with the continuum region, and the heat $\dot{H}$ and mass $\dot{M}$ exchange rates.

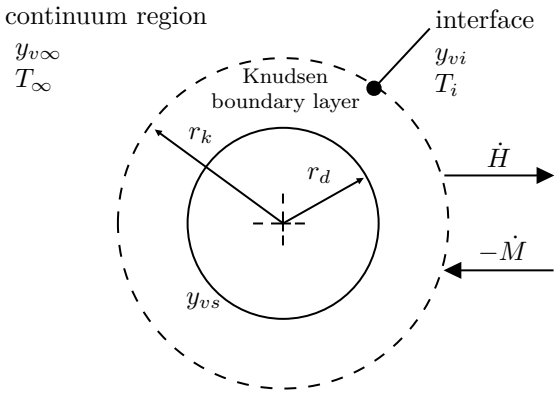

Figure 4.12 – Droplet growth graphical representation. Adapted from (Peeters et al., 2004a).

The importance of the Knudsen boundary layer will depend on the flow regime, because as presented by Luo et al. (2006) if the phenomena is evaluated from a continuum perspective, droplets will grow by the diffusion of the vapour molecules on the droplet interphase in an almost continuous process. Therefore, droplet growth is a diffusion governed process. Otherwise, the droplet growth is controlled by the kinetics process of impingement from the surrounding mixture onto the droplet. It is important to highlight that due to the droplet small diameter their Stokes number tend to be small and consequently, there is not slip between the droplet and the vapour-gas stream (Luo et al., 2006).

For estimating the droplet growth, the energy and mass fluxes estimation in both regimes (continuum and free molecular) is required, therefore, this work uses the formulation proposed by Luo et al. (2006) for computing the mass flow rates $\dot{M}$ in the continuum and free molecular regime

Continuum mass flow rate:

$$\dot{M}^{ct} = 4\pi r \left(\frac{D_m}{\mathcal{R}_v T_m} \right) \left(P_v^{eq} - P_v \right). \tag{4.57}$$

Free molecular mass flow rate:

$$\dot{M}^{fm} = 4\pi r^2 \left(\frac{P_v^{eq}}{\sqrt{2\pi \mathcal{R}_v T_d}} - \frac{P_v}{\sqrt{2\pi \mathcal{R}_v T}} \right). \tag{4.58}$$

and the droplet growth rate can be computed after considering the time-dependent increase of the droplet radius (Peeters et al., 2004b):

$$\dot{M} = \frac{d}{dt} \left(\frac{4}{3} \pi r_d^3 \rho_l \right), \tag{4.59}$$

where D_m is the molecular diffusion coefficient, so after deriving and replacing Eq. 4.59 into 4.57, it is obtained:

$$\left(\frac{dr^2}{dt} \right)^{ct} = \frac{2}{\rho_l} \left(\frac{D_m}{\mathcal{R}_v T} \right) \left(P_v^{eq} - P_v \right) \tag{4.60}$$

and, in analogous fashion for the free molecule regime:

$$\left(\frac{dr}{dt} \right)^{fm} = \frac{1}{\rho_l} \left(\frac{P_v^{eq}}{\sqrt{2\pi \mathcal{R}_v T_d}} - \frac{P_v}{\sqrt{2\pi \mathcal{R}_v T}} \right), \tag{4.61}$$

Hence, one can perceive after inspecting Eqs. 4.60 and 4.61, that the driving force for the droplet growth is the difference between the equilibrium and the free stream pressure.

In conclusion, the droplet growth process is the phenomenon responsible for the condensation shock wave, because as the droplet grows there is a release of latent heat from the droplet towards the gas-vapour free stream (Emmons, 1958; Thompson, 1971) The heat time rate $\dot{H}$ released by the droplet growth can be calculated by:

$$\dot{H} = \dot{M} L, \tag{4.62}$$

where L is the latent heat, please note that $\dot{M}$ will depend on the nature of the droplet growth process. Therefore, the heat transfer will affect the flow similarly than a Rayleigh flow, resulting in a flow deceleration which implies an increase on the flow pressure. Being

this the main characteristic of the experimental evaluation of the condensation shock because the nozzle pressure profile departs from the isentropic solution. Once the main physical phenomena behind the condensation shocks was explained, one will proceed to explain how the condensation shock can be evaluated for supersonic real gas nozzle flows.

4.3.2 Single fluid model

The single fluid model relies on considering the two-phase condensing mixture as a single fluid. This assumption simplifies the condensation shock calculation, because the interphase phenomena can be neglected. Instead, this method estimates the macroscopic average quantities of the flow, such as flow velocity, pressure, density, etc. Also, it establishes that the mixture density ρ_m can be computed as a function of the densities of the phases and the liquid mass fraction ratio y (Dykas; Wróblewski, 2011):

$$\rho_m = \frac{\rho_v}{\mathrm{y}\left(\frac{\rho_v}{\rho_l} - 1\right) + 1}. \tag{4.63}$$

For the single fluid model implementation one must establish the following assumptions (Bolaños-Acosta et al., 2021):

- The stagnation enthalpy and the mass flow rate must be conserved along the flow.
- There is no slip between the droplets and vapour.
- Droplet-droplet or droplet-wall interactions can be neglected.

Guha (1992) identify two different relaxations mechanisms inside a shock, the first one related to the velocity slip between the liquid-vapour phases and the second one related to the sub-cooling degree $\Delta T = T_s - T_g$. The last one is the more relevant for our problem due to small droplet radius. Therefore, the specific entropy production due to the relaxation process for a perfect gas, can be approximated as:

$$\frac{ds}{dx} \approx \frac{(1-\mathrm{y})c_P}{T_s^2 V}\frac{\Delta T^2}{\hat{\tau}}. \tag{4.64}$$

where $\hat{\tau}$ is the relaxation time. Hence, as the flow reaches the thermodynamic equilibrium the entropy production by the relaxation mechanism ends and the flow can be regarded as isentropic (Guha, 1994).

4.3.3 Discontinuity shock

The discontinuous condensation shock was one of the first approaches for solving nozzle condensing flows, Wegener & Mack (1958) and Emmons (1958) were the pioneers

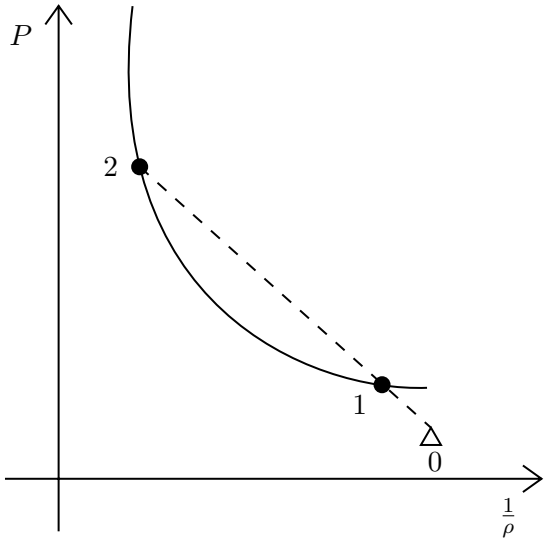

Figure 4.13 – Hugoniot curve (solid) and Rayleigh line (dashed) solution for a discontinuous condensation shock.

of this approach implementation, later Thompson (1971) suggest the use of the Hugoniot curve for solving the condensation shock. Guha (1994) performes an extensive research on the interaction of shock waves and wet supersonic flows, also he extends the analysis for computing the condensation shock with negligible area change. More recently Korpela (2019) uses this approach for turbo-machinery evaluation. Moreover, all the aforementioned approaches rely on the perfect gas assumption. Bolaños-Acosta et al. (2021) show that the discontinuous condensation shock can be applied for real gases, because they compute the condensation shock in high pressure steam and carbon dioxide nozzle flows.

The discontinuous condensation shock analysis consists in using the classical detonation solution method, which relies on the Hugoniot and Rayleigh curves intersection computation for the condensation downstream conditions calculation, as depicted in Fig. 4.13, where the solid and dashed line represents the Hugoniot curve and Rayleigh line respectively. So, in the analysis of condensation shocks point 0 represents the metastable vapour and points 1 and 2 the weak and strong equilibrium solution, respectively. Consequently, the condensation shock could have 2 solutions, Bolaños-Acosta et al. (2021) found that the weak solution is more likely to occur. The Rayleigh-Hugoniot intersection points are found, after solving the Rankine-Hugoniot relations Eqs. 4.34 - 4.36 and imposing that the downstream condition (Points 1 and 2) are in thermodynamic equilibrium. As presented by Acosta (2022) the Hugoniot curve is obtained after solving:

$$h_2 - h_1 = \frac{1}{2}\left(\frac{1}{\rho_2} + \frac{1}{\rho_1}\right)(P_2 - P_1). \tag{4.65}$$

And the Rayleigh line:

$$\mathsf{J}^2 = -\frac{P_2 - P_1}{1/\rho_2 - 1/\rho_1} \tag{4.66}$$

where J is the mass flux through the condensation shock. The discontinuous condensation shock is a simple and reliable method for computing the shock downstream conditions. However, due to the infinitesimal shock thickness assumption, this method overestimate the pressure jump when it was compared against the experimental results. That is because the droplet growth process is not as fast as expected, so the shock thickness is not negligible. Therefore, this method is not able to consider the interaction between the area profile change dA/dx and the shock. Based on the last statements, this work proposes a new method for solving the condensation shock, which is partly based on the discontinuity approach, and in the next section, it will be presented.

4.3.4 Continuous condensation shock

Fig. 4.14 presents a typical pressure profile for a condensation shock wave in nozzle flows. If the viscous effects are negligible the supersonic flow can be regarded as isentropic (See Eq. 4.13), the isentropic expansion ends at point a, where the condensation shock starts.

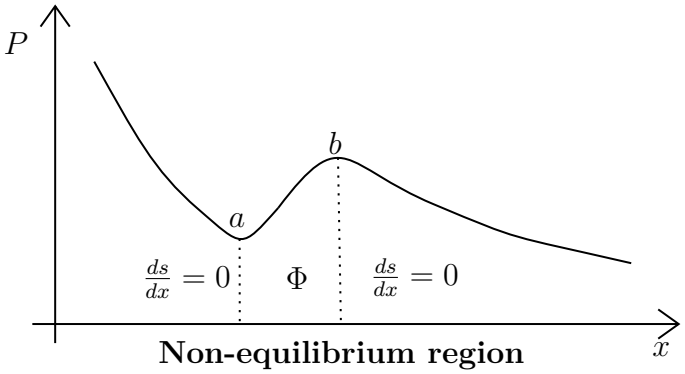

Figure 4.14 – Typical pressure profile for a condensation shock.

Therefore, between points a and b, there is an entropy production in the nozzle due to the irreversibility of the droplet growth and the heat transfer towards the vapour-gas mixture. Such a region is named as non-equilibrium region because the metastable vapour has not reached equilibrium yet. Then, one can establish a control volume which accounts the two-phase flow entropy rise on the non-equilibrium region, where the viscous effects, work and heat transfer are neglected, as presented in Fig. 4.15. For this control volume one can use the set of differential equations developed for viscous compressible flow Eqs. 4.5 and A.1, and the momentum equation 4.6 can be rewritten to ignore the viscous effects, so after considering these assumptions, it was established the non-conservative differential equations for the condensation shock control volume:

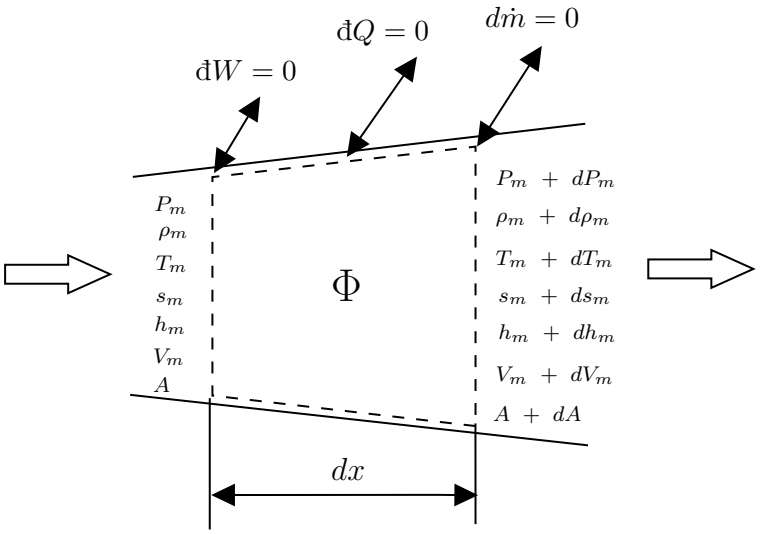

Figure 4.15 – Condensation shock control volume.

$$\frac{1}{\rho_m}\frac{d\rho_m}{dx} + \frac{1}{V_m}\frac{dV_m}{dx} + \frac{1}{A}\frac{dA}{dx} = 0, \tag{4.67}$$

$$\frac{dP_m}{dx} + \rho V_m \frac{dV_m}{dx} = 0, \tag{4.68}$$

$$\frac{dh_m}{dx} + V_m \frac{dV_m}{dx} = 0, \tag{4.69}$$

where the subindex m denotes the two-phase mixture. Nevertheless, due to the entropy generation by the phase-change process, it is required to use a source term Φ to incorporate the entropy production into the control volume analysis:

$$\frac{ds_m}{dx} = \Phi. \tag{4.70}$$

Now, one can proceed similarly as done in the deduction of the velocity differential for the viscous flow Eq. 4.14 to obtain:

$$\frac{dV_m}{dx} = \frac{\left(\frac{G_r T_m}{c_m^2}\Phi - \frac{1}{A}\frac{dA}{dx}\right) V_m}{(1 - M_m^2)}. \tag{4.71}$$

Eq. 4.71 gives some important information about the flow with condensation, firstly due to the second law of thermodynamics $\Phi > 0$, therefore, the entropy production will decelerate the flow for $M_m > 1$. Otherwise, it will be accelerated for subsonic velocities. Also, Eq. 4.71 considers the interaction between the nozzle area change dA/dx.

One can define a criterion for considering if the viscous effect is important in the condensation shock solution, after comparing the Eq. 4.13 magnitude order to Φ result in:

$$\Phi \gg \frac{2V^2 f}{T D_h}, \tag{4.72}$$

if that criterion is satisfied, the viscous effects can be neglected.

One can note that Eq. 4.71 needs the computation of the mixture two-phase speed-of-sound, this equation is developed in Appendix C, resulting in:

$$c_m^{-2} = \frac{\left(\frac{\rho_v}{\rho_l}\right)^2 \frac{\mathrm{y}}{c_l^2} - \rho_v \left(\frac{\rho_\mathrm{v}}{\rho_1} - 1\right) \left(\frac{\partial \mathrm{y}}{\partial P}\right)_{s_m} - \frac{\mathrm{y}-1}{c_v^2}}{\left(\mathrm{y} - 1 - \frac{\rho_\mathrm{v}}{\rho_1}\mathrm{y}\right)^2} \tag{4.73}$$

and for the mixture Grüneisen parameter:

$$Gr^{-1} = \frac{\frac{\mathrm{y}\rho_v^2}{\rho_l Gr_l T_l} - \rho_v \left(\frac{\rho_\mathrm{v}}{\rho_1} - 1\right) \left(\frac{\partial \mathrm{y}}{\partial T}\right)_{s_m} - \frac{(\mathrm{y}-1)\rho_v}{Gr_v T_v}}{\left(\mathrm{y} - 1 - \frac{\rho_\mathrm{v}}{\rho_1}\mathrm{y}\right)^2} \frac{T}{\rho_m} \tag{4.74}$$

where y is the mixture liquid mass fraction. Note that the terms $\partial \mathrm{y}/\partial \mathrm{P}$ and $\partial \mathrm{y}/\partial \mathrm{T}$ can not be calculated from the thermodynamic equilibrium. Therefore, it was used a backward finite difference method for their computation from the condensation shock solution. In addition, one needs to compute y, and this can be calculated as:

$$d\mathrm{y} = \Psi \frac{ds_m}{\frac{h_v - h_l}{T_m} + s_l - s_v} \tag{4.75}$$

This expression was derivate from Young (1995) work for evaluating the flow from a single fluid point of view. Where Ψ denotes and adjust coefficient used to ensure that the condensation shock ends in a thermodynamic equilibrium.

For solving the condensation shock wave, one needs to compute Φ. Nevertheless, this source term intrinsically depends on the two-phase change phenomena. So, in order to avoid their computation directly from the droplet-growth process, due to the complexness of computing the transport and thermodynamic properties for a binary metastable mixture. This approach keeps the essence of using the Rankine-Hugoniot relations for solving the condensation shock. However, the Rankine-Hugoniot is used for computing the maximum specific entropy jump produced by the condensation shock, different from the approach used on the discontinuous condensation shock where it was used for the direct computation of the shock downstream thermodynamic state. The calculation of the maximum entropy jump is done by computing the specific entropy for the strong detonation solution (See point 2 in Fig. 4.13). As aforementioned, one can calculate the maximum entropy production for a condensation shock after solving the Rankine-Hugoniot relations. However, there is another approach for having an approximate solution, which consists in consider the condensation shock as a weak shock as a function of the non-dimensional pressure jump (Thompson, 1971):

$$\Pi = \frac{[P_2 - P_1]}{\rho c_1^2} \tag{4.76}$$

Therefore, in the next section presents a new methodology developed in this work for computing the maximum entropy jump in a real gas weak shock.

4.3.5 Maximum entropy jump for a real gas weak shock

This section shows the formulation of a new analytical expression for the maximum entropy jump computing in a real gas weak shock, this formulation starts with the specific enthalpy expansion in a fourth grade Taylor's series, as a function of pressure and entropy, for a constant composition mixture or pure substance $h(P, s)$, and neglecting the second and higher order of the entropy jump as established by Zel'dovich & Raizer (1966):

$$\begin{aligned} h_2 = h_1 &+ \left(\frac{\partial h}{\partial s}\right)_P (s_2 - s_1) + \left(\frac{\partial h}{\partial P}\right)_s (P_2 - P_1) + \frac{1}{2}\left(\frac{\partial^2 h}{\partial P^2}\right)_s (P_2 - P_1)^2 \\ &+ \frac{1}{6}\left(\frac{\partial^3 h}{\partial P^3}\right)_s (P_2 - P_1)^3 + \frac{1}{24}\left(\frac{\partial^4 h}{\partial P^4}\right)_s (P_2 - P_1)^4 . \end{aligned} \tag{4.77}$$

Using the Maxwell relations, it is obtained:

$$T = \left(\frac{\partial h}{\partial s}\right)_P , \tag{4.78}$$

and

$$v = \left(\frac{\partial h}{\partial P}\right)_s . \tag{4.79}$$

Therefore, Eq. 4.77 can be rewritten:

$$\begin{aligned} h_2 = h_1 &+ T_1 (s_2 - s_1) + v_1 (P_2 - P_1) + \frac{1}{2}\left(\frac{\partial v}{\partial P}\right)_s (P_2 - P_1)^2 \\ &+ \frac{1}{6}\left(\frac{\partial^2 v}{\partial P^2}\right)_s (P_2 - P_1)^3 + \frac{1}{24}\left(\frac{\partial^3 v}{\partial P^3}\right)_s (P_2 - P_1)^4 \end{aligned} \tag{4.80}$$

Also, v can be expanded in a Taylor series, as function of pressure and entropy $v(P, s)$

$$v_2 = v_1 + \left(\frac{\partial v}{\partial P}\right)_s (P_2 - P_1) + \frac{1}{2}\left(\frac{\partial^2 v}{\partial P^2}\right)_s (P_2 - P_1)^2 \tag{4.81}$$

Substituting Eqs. 4.80 and 4.81 into the Hugoniot equation 4.65, it is obtained:

$$s_2 - s_1 = \frac{1}{12T_1}\left(\frac{\partial^2 v}{\partial P^2}\right)_s (P_2 - P_1)^3 - \frac{1}{24T_1}\left(\frac{\partial^3 v}{\partial P^3}\right)_s (P_2 - P_1)^4 \tag{4.82}$$

and, this equation can be written in a non-dimensional form (Thompson, 1971), where Γ is the fundamental derivative of gas dynamics , and Π is the non-dimensional pressure jump Eq. 4.76:

$$\frac{T_1(s_2 - s_1)}{c_1^2} = \frac{\Gamma_1}{6}\Pi^3 - \frac{1}{12}\left[\frac{{c_1}^2\Gamma_1}{v_1 T_1}\left(\frac{\partial T}{\partial P}\right)_s - \frac{{c_1}^6}{2{v_1}^4}\left(\frac{\partial^3 v}{\partial P^3}\right)_s\right]\Pi^4 \tag{4.83}$$

Being,

$$\left(\frac{\partial T}{\partial P}\right)_s = \frac{vTGr}{c^2}. \tag{4.84}$$

Therefore, after replacing Eqs. 4.84 into Eq. 4.83, and simplifying:

$$\frac{T_1(s_2 - s_1)}{c_1^2} = \frac{\Gamma_1}{6}\Pi^3 - \frac{1}{12}\left[\Gamma_1 Gr_1 - \frac{c_1^6}{2v_1^4}\left(\frac{\partial^3 v}{\partial P^3}\right)_s\right]\Pi^4 \tag{4.85}$$

Thus, to achieve the maximum non-dimensional pressure jump $\frac{d(s_2 - s_1)}{d\Pi} = 0$ for a weak shock wave, it is obtained:

$$0 = \frac{\Gamma_1}{2}\Pi^2 - \frac{1}{3}\left[\Gamma_1 Gr_1 - \frac{c_1^6}{2v_1^4}\left(\frac{\partial^3 v}{\partial P^3}\right)_s\right]\Pi^3, \tag{4.86}$$

$$\Pi = \frac{3\Gamma_1}{2\left[\Gamma_1 Gr_1 - \frac{c_1^6}{2v_1^4}\left(\frac{\partial^3 v}{\partial P^3}\right)_s\right]}. \tag{4.87}$$

So, after calculating the maximum pressure jump, a new expression for the specific entropy jump can be formulated, after expanding Eq.4.77 considering second order changes in the specific entropy jump, therefore, Eq. 4.77 becomes:

$$h_2 = h_1 + T_1(s_2 - s_1) + v_1(P_2 - P_1) + \frac{1}{2}\left(\frac{\partial T}{\partial s}\right)_P (s_2 - s_1)^2 + \left(\frac{\partial T}{\partial P}\right)_s (P_2 - P_1)(s_2 - s_1) + \frac{1}{2}\left(\frac{\partial v}{\partial P}\right)_s (P_2 - P_1)^2 + \frac{1}{6}\left(\frac{\partial^2 v}{\partial P^2}\right)_s (P_2 - P_1)^3 \tag{4.88}$$

After rearranging and expressing it in non-dimensional pressure jump and the fundamental gas dynamics derivative terms, the following expression is obtained:

$$0 = \frac{1}{2c_p}(s_2 - s_1)^2 + (1 + Gr\Pi)(s_2 - s_1) - \frac{c_1^2 \Gamma \Pi^3}{6T_1} \tag{4.89}$$

Hence, the maximum entropy jump becomes:

$$(s_2 - s_1) = c_p \left[-(1 + Gr\Pi) + \sqrt{(1 + Gr\Pi)^2 + \frac{c_1^2 \Gamma \Pi^3}{3T_1 c_p}} \right] \tag{4.90}$$

This expression gives a qualitative insight for the entropy jump in a weak shock wave. It is important to highlight that the positive solution from the square root, is the only one with a physical sense.

In addition, the specific volume jump can be calculated, using the expressions derived by Thompson (1971):

$$(v_2 - v_1) = -v_1 \Pi + v_1 \Gamma_1 \Pi^2 + \frac{v_1}{6} \left[\Gamma Gr + \frac{c_1^6}{v_1^4} \left(\frac{\partial^3 v}{\partial P^3} \right)_s \right] \Pi^3 \tag{4.91}$$

Notice that the maximum non-dimensional pressure jump signal Eq. 4.87 will depend on the fluid thermodynamic behaviour, because, for non-ideal flows $\Gamma < 0$, the pressure jump could achieve negative values. Nevertheless, the maximum specific entropy jump, will be always positive Eq. 4.90.

4.3.6 Chapman-Jouguet point

The Chapman-Jouguet (CJ) solution is an important point in the RH solution. In this particular case the Rayleigh line is tangent to the Hugoniot curve, resulting in Mach one (Thompson, 1971). Therefore, the CJ point will be found where $c_2 = V_2$. Hence, after combining continuity and momentum Eqs. 4.34 and 4.35 it is obtained the velocity jump across the shock wave:

$$-(V_2 - V_1) = \sqrt{-(P_2 - P_1)(v_2 - v_1)} \tag{4.92}$$

After simplifying and casting in non-dimensional pressure terms (Thompson, 1971):

$$(V_2 - V_1) = -c_1 \Pi + c_1 \frac{\Gamma_1}{2} \Pi^2 + \frac{c_1}{4} \left[\frac{1}{3} Gr\Gamma + \frac{{\Gamma_1}^2}{2} + \frac{{c_1}^6}{3{v_1}^4} \left(\frac{\partial^3 v}{\partial P^3} \right)_s \right] \Pi^3 \tag{4.93}$$

Additionally, for the CJ condition calculation, the jump in the speed of sound must be calculated, Thompson (1971) presents the following expression:

$$(c_2 - c_1) = c_1 (\Gamma_1 - 1)\,\Pi + \frac{c_1}{2}\left[3\Gamma_1^2 + \frac{c_1^6}{2v_1^4}\left(\frac{\partial^3 v}{\partial P^3}\right)_s\right]\Pi^2 + \frac{c_1}{6}\left[\frac{\Gamma_1 c_1^4}{2v_1^2 T_1}\left(\frac{\partial^2 T}{\partial P^2}\right)_s + Gr\Gamma + 15\Gamma_1^3 - 3\Gamma_1^2 + \frac{c_1^6}{2v_1^4}(9\Gamma_1 - 1)\left(\frac{\partial^3 v}{\partial P^3}\right)_s + \frac{c_1^8}{2v_1^5}\left(\frac{\partial^4 v}{\partial P^4}\right)_s\right]\Pi^3 \tag{4.94}$$

So Eq. 4.93 and 4.94 were combined to achieving the non-dimensional pressure ratio for the CJ condition

$$0 = A_{CJ} + B_{CJ}\Pi_{CJ} + C_{CJ}\Pi_{CJ}^2 + D_{CJ}\Pi_{CJ}^3 \tag{4.95}$$

where:

$$A_{CJ} = \frac{V_1}{c_1} - 1, \tag{4.96}$$

$$B_{CJ} = -\Gamma, \tag{4.97}$$

$$C_{CJ} = \frac{\Gamma}{2} - \frac{1}{2}\left[3\Gamma_1^2 + \frac{c_1^6}{2v_1^4}\left(\frac{\partial^3 v}{\partial P^3}\right)_s\right], \tag{4.98}$$

$$D_{CJ} = \frac{1}{4}\left[\frac{1}{3}Gr\Gamma + \frac{{\Gamma_1}^2}{2} + \frac{{c_1}^6}{3{v_1}^4}\left(\frac{\partial^3 v}{\partial P^3}\right)_s\right] - \frac{1}{6}\left[\frac{\Gamma_1 c_1^4}{2v_1^2 T_1}\left(\frac{\partial^2 T}{\partial P^2}\right)_s + Gr\Gamma + 15\Gamma_1^3 - 3\Gamma_1^2 + \frac{c_1^6}{2v_1^4}(9\Gamma_1 - 1)\left(\frac{\partial^3 v}{\partial P^3}\right)_s + \frac{c_1^8}{2v_1^5}\left(\frac{\partial^4 v}{\partial P^4}\right)_s\right]. \tag{4.99}$$

Therefore, Eq. 4.95 real root is an interesting result because it gives the Π_{CJ} and one can compute their corresponding specific entropy jump after substituting it in Eq. 4.90. Nevertheless, as Kuo (2005) and Thompson (1971) stressed out, this point represents the minimum entropy production for a detonation process. Therefore, any feasible specific entropy jump, must be greater than the obtained for this point, resulting in $\Pi > \Pi_{CJ}$.

As one can just obtain the specific entropy approximation at the end of the condensation shock, it is required to define a function for the specific entropy production in the shock, so this work established a third order polynomial as presented in Fig. 4.16, where it was used as boundary conditions that the ds/dx at the beginning and ending of the condensation shock must be zero for an isentropic expansion before and after the condensation shock. This specific entropy profile behaves as expected for condensing shocks properties variation as presented by Blythe & Shih (1976) and Young & Guha (1991). The polynomial coefficients are then computed in the function of the condensation shock length Δx and the initial and final specific entropy values s_1 and s_2 respectively. So, the adjust polynomial can be expressed as:

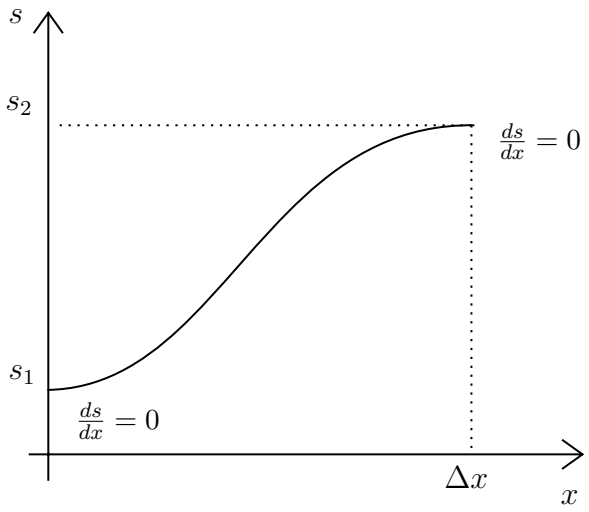

Figure 4.16 – Specific entropy profile in a condensation shock.

$$\Phi = 2a_{ds}(x - x_0) + 3b_{ds}(x - x_0)^2, \tag{4.100}$$

where:

$$a_{ds} = \frac{3(s_2 - s_1)}{\Delta x^2}, \tag{4.101}$$

$$b_{ds} = \frac{-2(s_2 - s_1)}{\Delta x^3}, \tag{4.102}$$

being a_{ds} and b_{ds} the proposed adjust coefficients, and x_0 the condensation shock start position.

However, for achieving a successful approach implementation one needs to calculate the condensation shock thickness in order to compute Φ. Analytic approaches have been used for normal shock wave thickness computation in a perfect gas (Thompson, 1971; Bird et al., 2002). Nevertheless, for real gases an analytical approach is not possible, therefore, this must be solved through a numerical procedure, and this will explained in the next section.

4.3.7 Numerical solution

The numerical solution procedure of the continuous condensation shock is presented in Fig. 4.17. It starts from the nucleation rate computation, once it achieves its critical value, the condensation shock begins. Next, the specific entropy jump must be computed through the R-H relations, or the weak shock approximation. For starting the condensation shock solution, one requires an initial guess for the shock thickness estimation and the Ψ value. Finally, the differential equation system is solved 4.67 - 4.71 through the four order

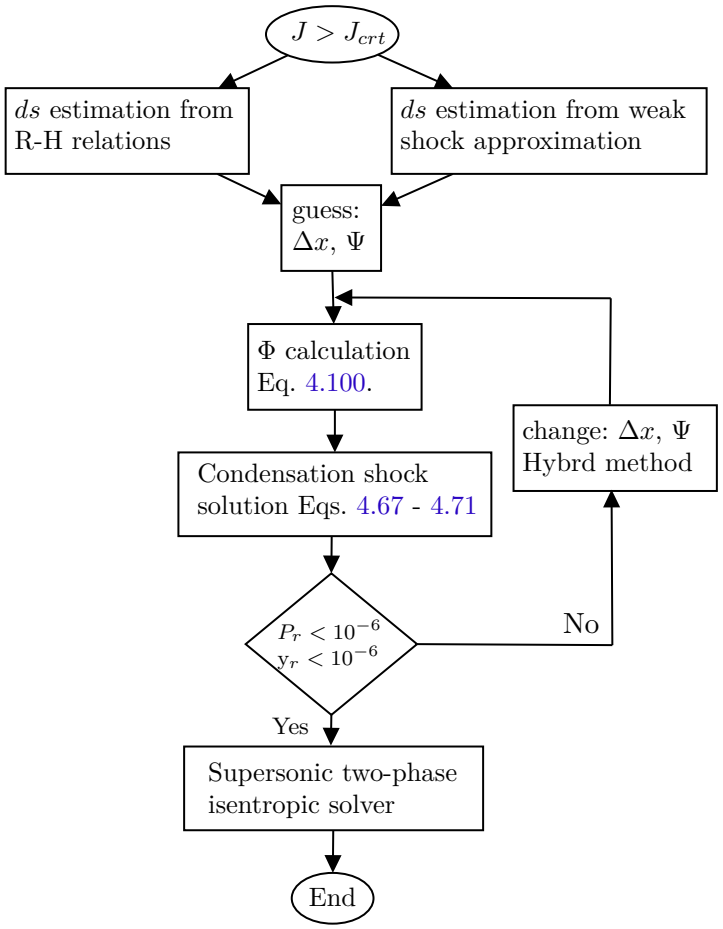

Figure 4.17 – Continuous condensation shock numerical solution.

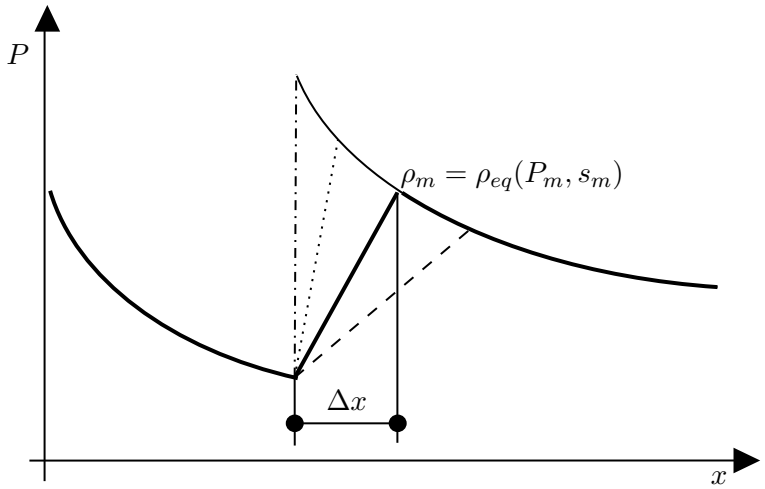

Figure 4.18 – Solution proceedure for the condensation shock thickness, discontinuous solution (dashed-dotted line), initial solutions (dashed lines) and the correct solution (continuous line).

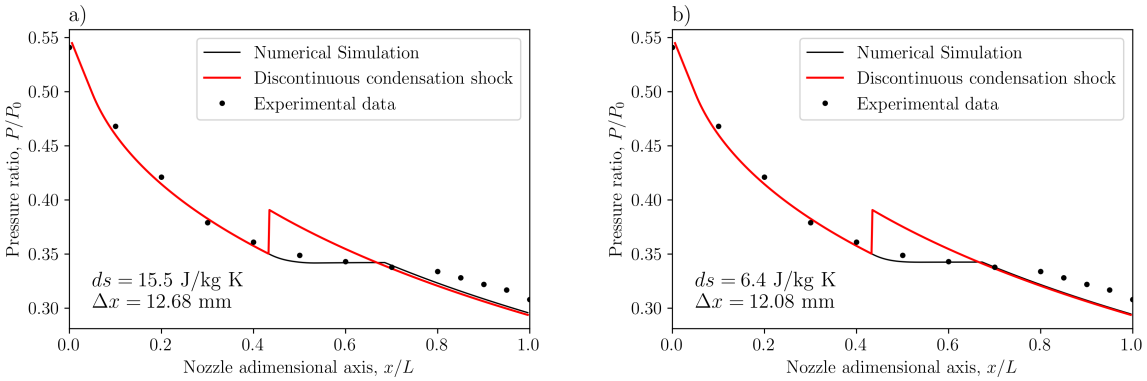

Figure 4.19 – Numerical results for Bakhtar & Zidi (1989) experiment a) Results for Rankine-Hugoniot maximum entropy production, b) Real gas weak shock approximation, (Water, $P_0 = 35.5$ bar, $T_0 = 548.6$ K).

Runge-Kutta method as presented in section 4.1.6, and subsequently the conditions at shock exit are computed. Nevertheless, the thermodynamic equilibrium must be reached at this position, and it is measured through the pressure and liquid fraction residual values $P_r = (P - P_{eq})/P_o$ and $\mathrm{y}_r = (\mathrm{y} - \mathrm{y}_{eq})/\mathrm{y}_{eq}$, respectively. If the tolerance value 10^{-6} is not achieved, the algorithm uses the Hybrd routine to achieve the Δx and Ψ values. Because as presented in Fig. 4.18 Δx is higher or lower than this value the condensation shock will not reach the equilibrium. Next, after achieving the tolerance value the condensation shock ends and the fluid expands in an isentropic two phase flow manner.

4.3.8 Condensation shock results

After employing the numerical solution procedure explained in the last section, one can solve the supersonic condensation shock for real gases. Firstly, it was performed pure substance simulations for steam and carbon dioxide, in order to assess the procedure's reliability. For this part, it was not calculated the droplet nucleation rate, instead, the condensation shock starting point was defined after using experimental data. Later it was used the work of Bier et al. (1990a) for the real gas mixture validation. In both cases, it was compared the discontinuous condensation shock pressure profile result, against the continuous shock solutions after using the weak shock approximation and the numerical solution of the R-H relations, in order to compare their entropy jump and the condensation shock thickness outcomes. All the simulations were performed using a constant mesh step of 750 elements, this mesh size achieves independent mesh results for all the cases studied.

4.3.8.1 Pure substance

Fig. 4.19 presents the condensation shock numerical simulation for the experimental conditions reported by Bakhtar & Zidi (1989). This work evaluates experimentally the steam supersonic condensation in a convergent-divergent nozzle. Fig. 4.19a presents the

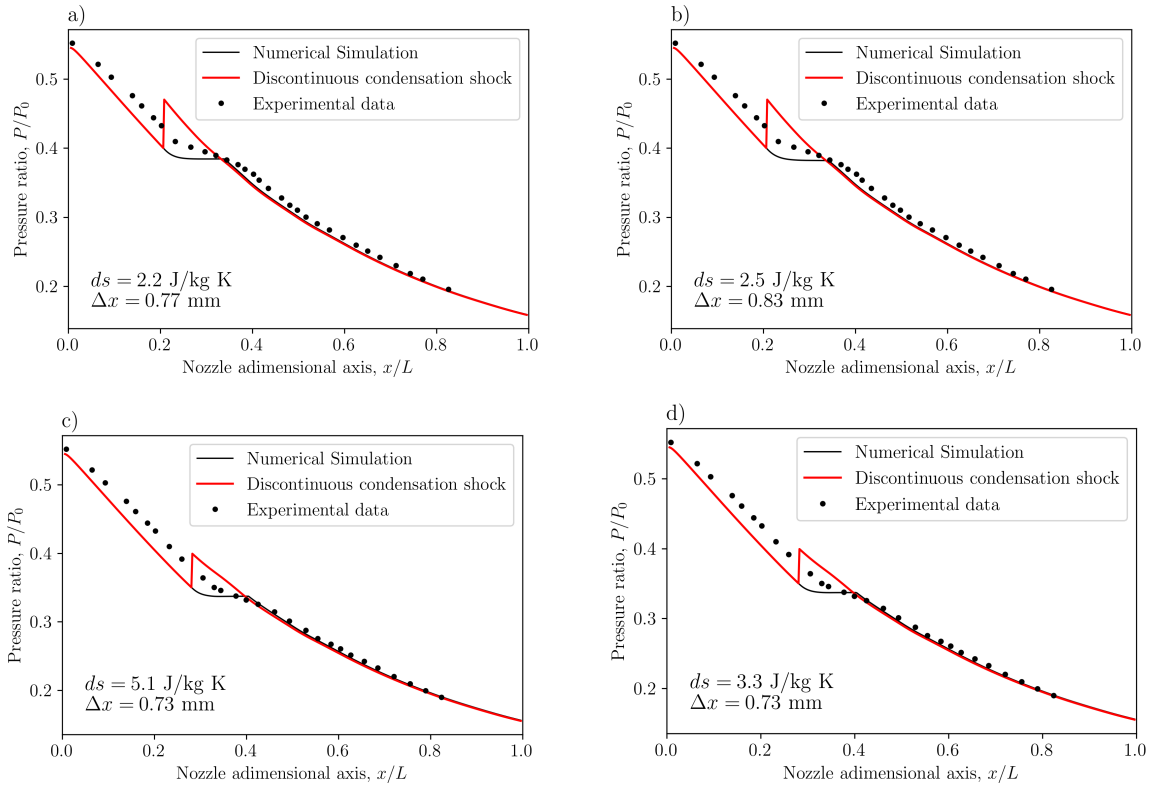

Figure 4.20 – Numerical results for Bier et al. (1990b) carbon dioxide condensation experiment a) and c) Results for Rankine-Hugoniot maximum entropy production, b) and d) Real gas weak shock approximation, for two stagnations temperature conditions $T_0 = 300.1$ K Figs. a and b, $T_0 = 304.1$ K Figs. c and d, respectively.

results for continuous condensation shock after solving the R-H relations, which results in a specific entropy jump of $ds = 15.5$ Jkg^{-1}K^{-1} and in a $\Delta x = 12.68$ mm, it is important to stress out the low deviation of the discontinuous shock downstream isentropic expansion and the continuous solution. It was also achieved a low deviation (4%) after comparing the experimental results to the numerical solution. Fig. 4.19b shows the condensation shock after employing the weak shock specific entropy solution. It is important to highlight that the specific entropy jump obtained by the weak shock has a significant deviation after comparing it against the R-H solution results. Nevertheless, the condensation shock thickness and the pressure profile do not display a significant reduction after comparing it to Fig. 4.19a outcomes. For both cases (steam and carbon dioxide) it was found that the discontinuous and continuous approaches have very close results after the condensation shock, nevertheless, as explained before the discontinuous condensation shock overestimates the initial pressure peak, due to the infinitesimal shock assumption.

Fig. 4.20 presents the pure carbon dioxide simulation results. The experimental data obtained by Bier et al. (1990b) were used to validate the presented approach, where the stagnation temperature variation effects on the condensation shock were evaluated. Figs. 4.20a and 4.20b present the results for a stagnation temperature of $T_0 = 300.1$ K and

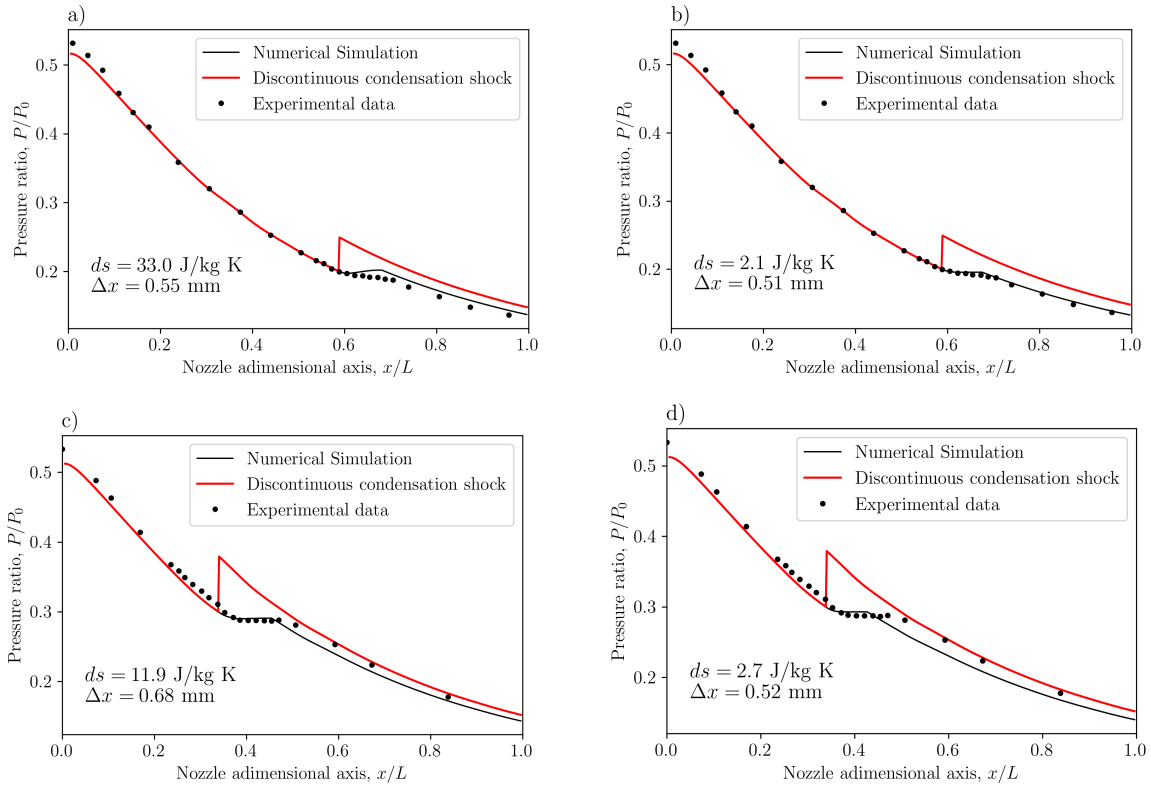

Figure 4.21 – Numerical results for Bier et al. (1990a) carbon dioxide - dry air condensation experiment a) and c) Results for Rankine-Hugoniot maximum entropy production, b) and d) Real gas weak shock approximation, for two stagnations conditions i = (P_0 = 9.98 bar, T_0 = 249.4 K, CO_2 $\bar{x}_0$ = 0.75), and ii (P_0 = 16.73 bar, T_0 = 243.3 K, CO_2 $\bar{x}_0$ = 0.5).

Figs. 4.20c and 4.20d $T_0 = 304.1$ K, the four simulations used the same stagnation pressure $P_0 = 45$ bar. As performed for the steam study case, it was analysed the differences between the R-H solution (Figs. 4.20a and c) and the weak shock approximation (Figs. 4.20b and d). The condensation shock results behave in the same fashion as presented in the water simulation, showing that there is a difference between the entropy jump computed through the R-H relation solution and the weak shock approximation, nevertheless, the effect of this difference on the condensation shock solution is almost negligible. The higher experimental deviation value is 7.2% and it is presented in the metastable vapour region before the condensation shock.

4.3.8.2 Mixture

Finally, Fig. 4.21 presents the numerical results' validation obtained for a CO_2 - dry air mixture based on the experimental data reported by Bier et al. (1990a), for these simulations was considered a critical nucleation rate of $J_{crt} = 1 \times 10^{22}$. For this case two different stagnation conditions were evaluated:

- $P_0 = 9.98$ bar, $T_0 = 249.4$ K, CO_2 $\bar{x}_0 = 0.75$: This stagnation condition is presented

in Figs. 4.21a and 4.21b, for the R-H relation numerical solution and the weak shock approximation, respectively. It is clear that there is a difference on the specific entropy jump calculation, between both approaches. However, in both cases the condensation shock thickness estimation is close to the experiment. Nevertheless, due to the lower entropy production obtained by the weak shock approximation, the flow pressure increase is lower allowing a better fitting compared to the experimental results. In this case, the discontinuous condensation shock solution has higher deviations after comparing it to the continuous shock solution.

- $P_0 = 16.73$ bar, $T_0 = 243.3$ K, CO_2 $\bar{x}_0 = 0.5$: This stagnation condition is presented in Figs. 4.21c and 4.21d, for the R-H relation numerical solution and the weak shock approximation, respectively. The weak shock approximation achieves a maximum deviation of 8.7%. However, the R-H solution and the discontinuous condensation shock achieve a good agreement after comparing it to experimental data.

Therefore, the continuous condensation shock approach is validated after considering the last presented outcomes, and this method is a simple and reliable tool for the condensation shock evaluation in real gas mixtures and could be used as preliminary tool for the condensation shock assessment, without the requirement to compute transport properties such as the diffusion molecular coefficient and the thermal conductivity or the surface tension. These parameters could be complicated to be computed for mixtures at high pressures, for metastable mixtures, or non-equilibrium processes. The weak shock approach gives a fair agreement with the experimental data, this method can be used for preliminary assessment or as guess estimation for the numerical solution of the R-H relations.

After developing the compressible real gas dynamic theory required for evaluating and developing supersonic gas separators. This work proceeds to show the application of these developed concepts. Mainly in the method of characteristics application, this is a powerful tool for developing supersonic nozzle geometries, which can be used for ensuring a shock wave-free supersonic gas separator design.

4.4 Method of characteristics

For some applications such as rocket nozzles design or gas dynamic lasers (Anderson, 1990) it is required to minimize the supersonic nozzle length. Typically, the gases expansion occurs at a sharp corner, which is followed by, some undesired flow phenomena, such as oblique shock-waves formation or boundary layer detachment (Zucrow; Hoffman, 1977). A common technique used to overcome this problem is the use of the method of characteristics (MOC), which solves the full potential velocity equation. The goal is to build an algorithm

to cancel out the Prandtl-Meyer expansion fan created at sharp corners that allows the flow to reach the exit Mach number at the design condition (Liepmann; Roshko, 1957). The MOC classic approach relies mostly on the assumption of ideal gas behavior, which is not accurate enough for real gas supersonic flow calculations. In view of recent demands for real gas operation, a few studies have been carried out using the MOC for real gases, such as the work of Aldo & Argrow (1995) using the Van der Waals EOS (VdWEOS), whose response is just qualitative and not suitable for precise calculations; Guardone (2010) used the VdWEOS for the designing of supersonic nozzles at carbon dioxide supercritical operation for a planar flow model; Guardone et al. (2013) show the effects of fluid's molecular complexity on the planar supersonic nozzle construction for several fluids and MPEOS; more recent works (Bufi; Cinnella, 2018; White et al., 2017; Zocca, 2018) have used a modern EOS for Organic Rankine Cycle (ORC) applications. Their analyses were developed for planar flow as well; Zebbiche (2019) performed a minimum length nozzle sizing for a qualitative EOS (Berthelot) for both planar and axisymmetric flow geometries. Compared to previous works, this work presents a novel methodology for designing both planar and axisymmetric supersonic nozzles operating with pure substances and real gas mixtures using a reliable EOS (MPEOS), even valid at low compressibility factors Z or supercritical states. This methodology allows one to constructs the nozzle wall contour geometry to achieve an uniform Mach number or a thermodynamic property (pressure, temperature, density, etc.) at the nozzle outlet, avoiding oblique shock wave formation within the nozzle.

The methodology was applied for two pure substances and a carbon dioxide - methane mixture, as well. The pure substances evaluated were carbon dioxide CO_2 and the refrigerant R1234yf. CO_2 presents an ideal speed-of-sound behavior, which means that the speed of sound varies monotonically along the expansion. On the other hand, R1324yf presents a non-ideal behavior that influences the nozzle wall shape construction. CO_2 was studied due to their common use in refrigeration and power cycles (ORC and supercritical Brayton cycle) (Bianchi et al., 2021), and these cycles normally require supersonic expansion for their operation (Zhu et al., 2017; Uusitalo et al., 2019; Quan et al., 2020). Refrigerant R1234yf was analyzed because it has become an important commercial refrigerant in the air conditioning industry. In addition, supersonic convergent-divergent nozzles are usually used as supersonic motive nozzles for ejector refrigeration cycles (Elbarghthi et al., 2020). Besides, this work explores the design of supersonic real gas mixtures in short nozzles due to performance benefits that real gas mixtures induce on the operation of such cycles (Invernizzi, 2017; Invernizzi et al., 2019; Aidoun et al., 2019).

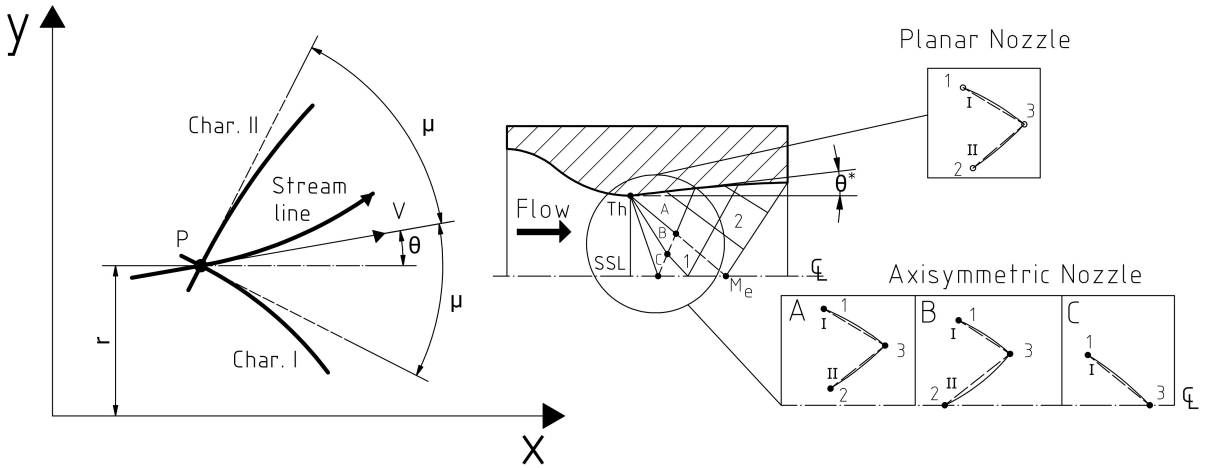

Figure 4.22 – Streamline, characteristic lines and interior operator.

4.4.1 Method of characteristics theory

The governing partial differential equation of steady inviscid irrotational axisymmetric compressible flow is known as the full potential velocity equation (Shapiro, 1953)

$$\left(1-\frac{\phi_x^2}{c^2}\right)\phi_{xx}+\left(1-\frac{\phi_r^2}{c^2}\right)\phi_{rr}-\frac{2\phi_x\phi_r}{c^2}\phi_{xr}+\frac{\phi_r}{r}=0 \tag{4.103}$$

This equation can be classified as either elliptic, parabolic or hyperbolic depending on the Mach number. Φ represents the velocity potential, x the axial coordinate and r the radius. If the flow is supersonic, Equation (4.103) becomes hyperbolic and it is possible to use the MOC to solve it. The method of characteristics consists in flow calculations along the characteristic lines, in case of supersonic flow these lines are also Mach lines (Zucrow; Hoffman, 1977). Fig. 4.22 shows the characteristic lines for a point (P) in a fluid streamline, along with both characteristic lines I, II and the angle of their tangent lines μ with respect to the flow streamline angle θ.

The advantage of solving the flow along the characteristic lines is the problem complexity reduction, because of in this particular case Eq. 4.103 is simplified from a non-linear partial differential equation to a set of two ordinary differentials equations, which are called characteristic equations

$$\left(\frac{dr}{dx}\right)_{I,II}=\tan(\theta\mp\mu). \tag{4.104}$$

Along with compatibility equations:

$$(d\theta)_{I,II}\pm(d\nu)_{I,II}=\pm\frac{\sin\mu\sin\theta}{\sin(\theta\mp\mu)}\frac{(dr)_{I,II}}{r} \tag{4.105}$$

Further information about the developing of Eqs. 4.104 and 4.105, is reported in Appendix B. These equations are also valid for an axisymmetric real gas supersonic flow. Planar nozzles can also be considered as an axisymmetric nozzle having an infinity curvature radius $r \to \infty$ (Thompson, 1971). Therefore, the characteristic and compatibility equations for a planar flow become

$$\left(\frac{dy}{dx}\right)_{I,II} = \tan(\theta \mp \mu) \tag{4.106}$$

$$(d\theta)_{I,II} \pm (d\nu)_{I,II} = 0 \tag{4.107}$$

4.4.2 Numerical implementation

With the purpose of applying the method of characteristics, an initial line value is required for the design of minimum nozzle length. A straight sonic line (SSL) is typically assumed (SSL) at the nozzle throat location (th) as illustrated in Fig. 4.22, such an assumption will lead to shorter nozzles (Argrow; Emanuel, 1988) compared to other MOC approaches. In addition, Argrow & Emanuel (1991) shows that SSL approach gives good results for viscous flows. Nevertheless, the transonic effects become relevant for nozzles with sudden changes in the convergent part, and the MOC is not recommended.

In the SSL approach, from the nozzle throat a set of expansion waves emanates (expansion fan) until the desired exit Mach number M_e is attained as presented by Argrow & Emanuel (1988). That expansion fan ends up in a determined streamline angle θ^* and this angle can be calculated for planar nozzles according to

$$\theta^* = \frac{\nu(M_e)}{2}. \tag{4.108}$$

Further, in case of axisymmetric nozzles, this angle does not have an algebraic relationship due to the variation of the characteristic lines through the flow field. Therefore, an iterative solver scheme has been used to find θ^* required in order to achieve the desired exit Mach number.

4.4.2.1 Axisymmetric flow Solution

The MOC technique applied to an axisymmetric flow consists in the discretization and solution of Eqs. 4.104 and 4.105. That was achieved using unit operators in a characteristic network as depicted in Fig. 4.22. Each intersection of those characteristic lines (Point 3) was solved considering that the information propagated along each characteristic line (I Point 1) and (II Point 2).

The equations were discretized according to the finite difference method, and the second-order Euler predictor-corrector algorithm for the solutions (Shapiro, 1953; Zebbiche, 2019) of the operator points displayed in Fig. 4.22 (A,B,C).

Firstly, the predictor Eq. 4.109 was calculated for characteristic line I and II based on points 1 and 2 . Subsequently, the total velocity was calculated from the Prandtl-Meyer angle predictor (ν_{13}, ν_{23}) , and once the total velocity was computed, the Mach number and angle (μ_{13}, μ_{23}) were obtained.

$$\begin{aligned} \theta_{13} = \theta_1, \quad \nu_{13} = \nu_1, \quad y_{13} = y_1, \\ \theta_{23} = \theta_2, \quad \nu_{23} = \nu_2, \quad y_{23} = y_2. \end{aligned} \tag{4.109}$$

Eqs. 4.104 and 4.105 were discretized using finite differences for each characteristic line, resulting in Eqs. 4.110 and 4.111 applicable to the I characteristic, and Eqs. 4.112 and 4.113 for the II characteristic. Finally a linear system of equations with four unknowns $(x_3, y_3, \nu_3, \theta_3)$ was obtained:

$$\frac{y_3 - y_1}{x_3 - x_1} = \tan\left(\theta_{13} - \mu_{13}\right), \tag{4.110}$$

$$\theta_3 - \theta_1 + \nu_3 - \nu_1 = \frac{\sin\mu_{13}\sin\theta_{13}}{\sin\left(\theta_{13} - \mu_{13}\right)}\frac{y_3 - y_1}{y_{13}}, \tag{4.111}$$

$$\frac{y_3 - y_2}{x_3 - x_2} = \tan\left(\theta_{23} + \mu_{23}\right), \tag{4.112}$$

$$\theta_3 - \theta_2 - \nu_3 + \nu_2 = -\frac{\sin\mu_{23}\sin\theta_{23}}{\sin\left(\theta_{23} + \mu_{23}\right)}\frac{y_3 - y_2}{y_{23}}. \tag{4.113}$$

After solving the characteristic and compatibility equations for the prediction step, the algorithm starts calculating the corrector step:

$$\begin{aligned} \theta_{13} = \tfrac{1}{2}(\theta_1 + \theta_3^{i-1}), \quad \nu_{13} = \tfrac{1}{2}(\nu_1 + \nu_3^{i-1}), \quad y_{13} = \tfrac{1}{2}(y_1 + y_3^{i-1}) \\ \theta_{23} = \tfrac{1}{2}(\theta_2 + \theta_3^{i-1}), \quad \nu_{23} = \tfrac{1}{2}(\nu_2 + \nu_3^{i-1}), \quad y_{23} = \tfrac{1}{2}(y_2 + y_3^{i-1}). \end{aligned} \tag{4.114}$$

This process is performed several times by employing Eqs. 4.110 to 4.113, until the maximum residual from the last iteration is lower than 10^{-8} (Zebbiche, 2019).

$$\max[\mid x_3^i - x_3^{i-1} \mid, \mid y_3^i - y_3^{i-1} \mid, \mid \nu_3^i - \nu_3^{i-1} \mid, \mid \theta_3^i - \theta_3^{i-1} \mid] < 10^{-8} \tag{4.115}$$

Nevertheless, since r effects on the differential equation solution, the analysis has to be classified into three different cases, as described in Fig. 4.22 with points A, B, and C.

- Point A. In this case, the flow can be solved as described previously.

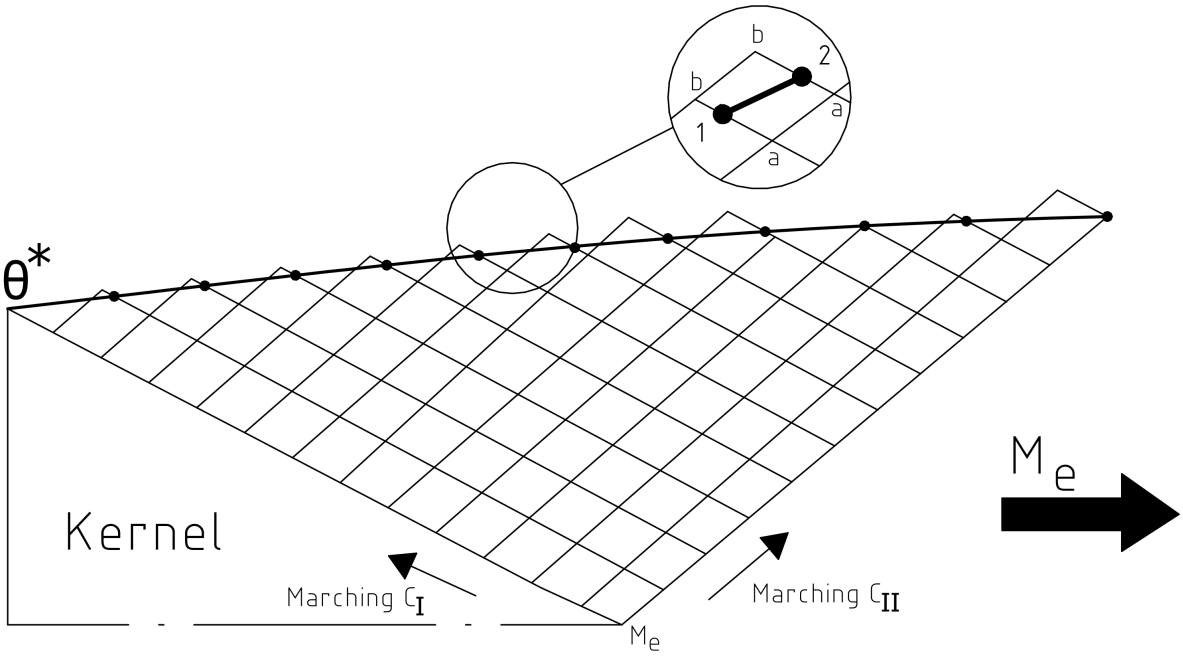

Figure 4.23 – Wall construction for axisymmetric nozzles.

- Point B. In this case, Eq. (4.105) is indeterminate at point 2 ($r_2 = 0$) and as described by Shapiro (Shapiro, 1953), the right side of the equation can be expressed as

$$\lim_{\substack{r_2 \to 0 \\ \theta_2 \to 0}} \frac{\sin\theta_2 \sin\mu_2}{r_2 \sin(\theta_2 + \mu_2)} \cong \frac{\theta_3}{r_3}. \tag{4.116}$$

  After performing this substitution, this point can be solved as presented for point A.

- Point C. In this case, it is just required for solving of one characteristic line I, because point 3 is partially defined by $r_3 = 0$ and $\theta_3 = 0$. Therefore, point 3 was achieved after solving Eqs. 4.110 and 4.111.

Once point 3 is solved, the algorithm marches downstream in space until it reaches the desired exit Mach number for the nozzle kernel region (1 in Fig. 4.22) (Argrow; Emanuel, 1988). Afterwards, the algorithm proceeds to construct the wall profile, firstly the routine starts to march along the I characteristic line, and then, the solver detects an intersection from the wall projection from the last I characteristic line, as depicted in Fig. 4.23 by point 2. The first wall angle θ^* was obtained by the kernel construction procedure, and for the following iterations, quadratic interpolation was used, considering the θ and r values along each I characteristic line. After finishing the calculation for each I characteristic, the algorithm marches along the II characteristic direction until the nozzle exit diameter is reached.

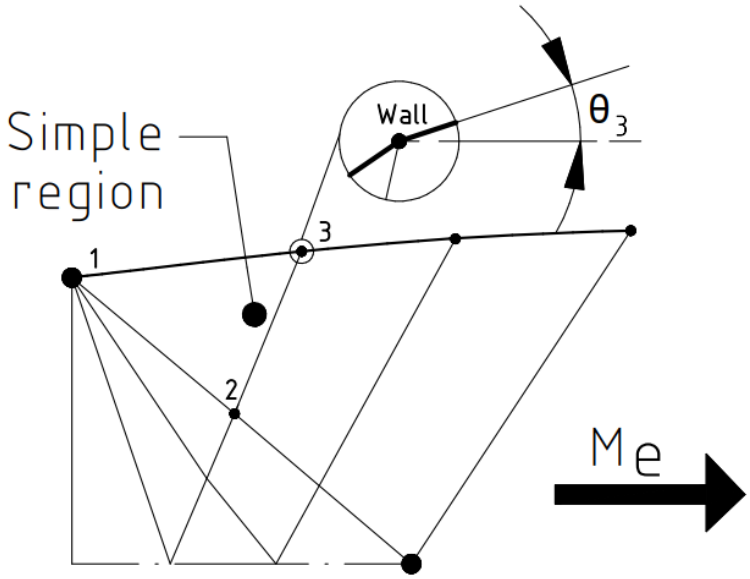

Figure 4.24 – Planar wall shape construction.

4.4.2.2 Planar flow solution

The MOC solution applied to supersonic planar flow results from a direct integration of Eq. 4.107 for each one of the characteristic lines, i.e.,

$$\theta + \nu = K_I, \tag{4.117}$$

$$\theta - \nu = K_{II}, \tag{4.118}$$

where K is an integration constant which holds valid along each characteristic line. Therefore, applying these Eqs. 4.117 and 4.118 to point 1 and 2, it is obtained $\theta_3 = 1/2(K_I + K_{II})$ and $\nu_3 = 1/2(K_I - K_{II})$ for an interior point as depicted in Fig. 4.22. Once the streamline and Prandtl-Meyer angles were calculated, the characteristic equation 4.106 can be solved considering the average values for the streamline $\theta_{i3} = 1/2(\theta_i + \theta_3)$ and Mach angles $\mu_{i3} = 1/2(\mu_i + \mu_3)$. Consequently, the position of point 3, i.e, the coordinate position (x_3,y_3) is obtained. After calculating the nozzle kernel, the wall shape is constructed, by using the expansion wave cancellation as depicted in Fig. 4.24, where due to the nature of the planar flow, the flow outside the kernel region is a simple region, which allows the characteristic lines to be modelled as straight lines, which will intersect the last iteration (points 1 and 2 in Fig. 4.24) so in the intersection of those lines it is obtained the wall point. Finally, considering the θ angle of the points 1 and 2 it was calculated the point 3, $\theta_3 = (\theta_1 + \theta_2)/2$ is calculated, and it will be considered in the next point of the wall shape construction (Anderson, 1990).

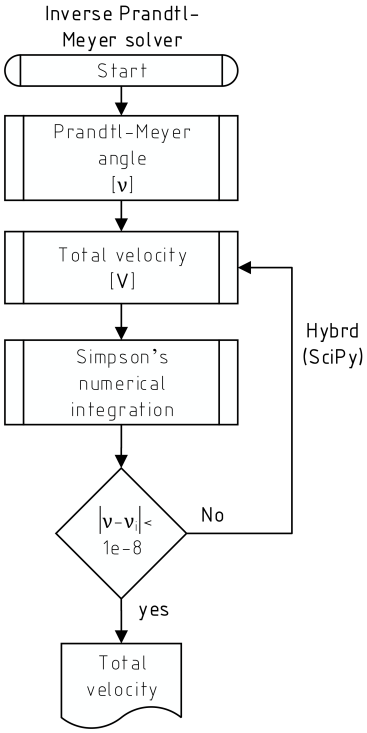

Figure 4.25 – Inverse Prandtl-Meyer angle algorithm solver.

4.4.3 Real gas isentropic solver

In this analysis the flow is considered irrotational, hence stagnation specific enthalpy h_o and specific entropy s are constant along the flow. As a consequence of those properties being constants and considering that the stagnation specific enthalpy definition is given by $h_o = h + \mathbf{V}^2/2$, it is possible to conclude that any thermodynamic property $\mathcal{M}$ become a function of the total velocity $\mathbf{V}$ only

$$\mathcal{M}[h, s] = \mathcal{M}[\mathbf{V}] \tag{4.119}$$

This work implements an algorithm for calculation of thermodynamic properties of pure and gas mixture as a function of the total velocity. The system of non-linear equations that governs the isentropic flow was solved through the Hybrd method (More et al., 1980) implemented through the SciPy libraries (Virtanen et al., 2020). To improve the convergence, that methodology uses the perfect gas solution as initial guesses for the first Jacobian matrix estimation. Temperature and density were used as input pairs for the EOS evaluation because those variables are explicit in the MPEOS formulation. The last step on the MOC solution is the Prandtl-Meyer angle estimation, and this is performed as indicated in section 4.2. Also, one needs an inverse solver for the velocity computation of the total velocity during the Eqs. 4.110 - 4.113 and 4.117-4.118. The inverse solver changes the total velocity until the Prandtl–Meyer angle matches the MOC solution, as shown in Fig. 4.25. After calculating the total velocity all the thermodynamic properties can be

computed due to the isentropic condition.

Finally, Fig. 4.26 shows the short nozzles MOC implementation flow diagram for axisymmetric and planar nozzles.

4.4.4 Results

The described methodology was implemented for pure and real gas mixtures with 150 characteristic lines for planar nozzles and 200 for axisymmetric nozzles.

Fig. 4.27 presents the results for carbon dioxide at a stagnation pressure and temperature of 15 MPa and 450 K that results in an exit pressure and temperature of 1.97 MPa and 279.6 K, after using the MPEOS data reported by Span & Wagner (1996). The results showed an uniform Mach number at the given exit conditions for both planar and axisymmetric nozzles, it also presents the built wall profile for both nozzles. Besides that, Fig. 4.27 shows the difference on the flow field between planar and axisymmetric nozzles. The variation between them relies mostly on the effect of the radius on the characteristic lines across the flow field, which leads to a shorter nozzle in comparison to the planar geometry.

Fig. 4.28 shows the results of a R1234yf supersonic expansion with a Mach number of 2 using the MPEOS proposed by Richter et al. (2011). Considering a stagnation pressure and temperature of 4.56 MPa and 394.6 K, respectively, which results in an outlet pressure and temperature of 0.5 MPa and 300 K. It is relevant to compare these outcomes to the results previously obtained for CO_2 given in Fig. 4.27, because both cases were simulated for the same Mach number but the nozzle wall profile differs greatly. The main reason for that is the high difference between the speed-of-sound in both fluids (e.g 284.4 $ms^{-}1$ and 108 $ms^{-}1$ for CO_2 and R1234yf, respectively at the nozzle throat). A key factor for nozzle designing is the initial wall nozzle angle θ^* (See Fig. 4.22) as presented in Eq. 4.108. That angle can be calculated for planar nozzles and as a function of ν. After a detailed inspection of the Prandtl-Meyer differential equation 4.53, one may conclude that low c values will lead to high ν angles and therefore larger nozzles will be obtained, even that θ^* cannot be calculated directly in the axisymmetric case. That family of nozzles follows the same trend.

Fig. 4.29 presents the solution for a real gas mixture of carbon dioxide and methane having a 50 % CO_2 mass fraction and a stagnation pressure and temperature of 42 MPa and 350 K with the corresponding binary interactions parameters of $\beta_v = 0.9995, \beta_T = 1.0226, \gamma_v = 1.0028, \gamma_T = 0.97567$ (Kunz; Wagner, 2012b). The exit pressure and temperature obtained was 6.45 MPa and 234.1 K, respectively. As one would expect, the nozzle flow behaves in the same fashion as the carbon dioxide pure substance case.

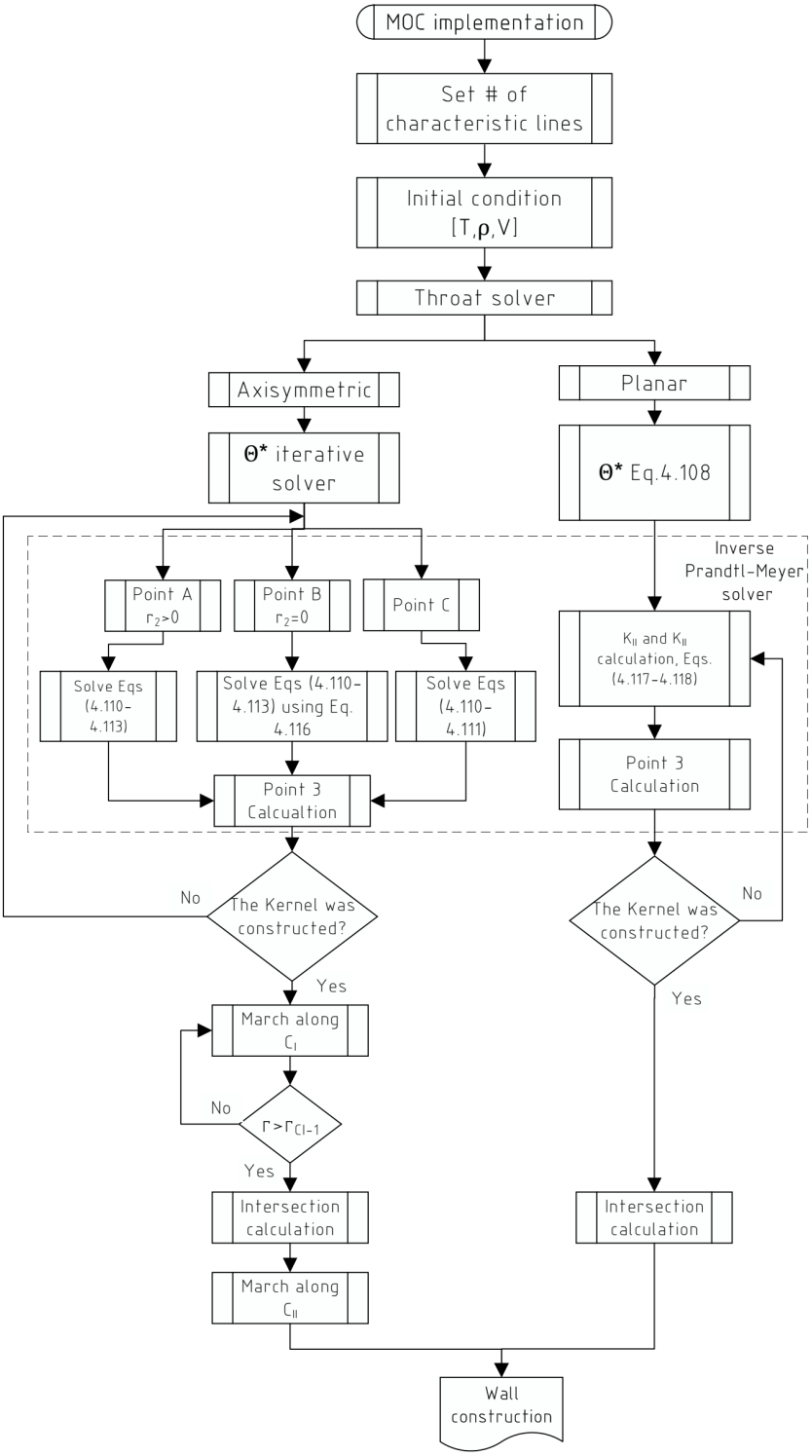

Figure 4.26 – Flow diagram of MOC implementation for short axisymmetric and planar nozzles.

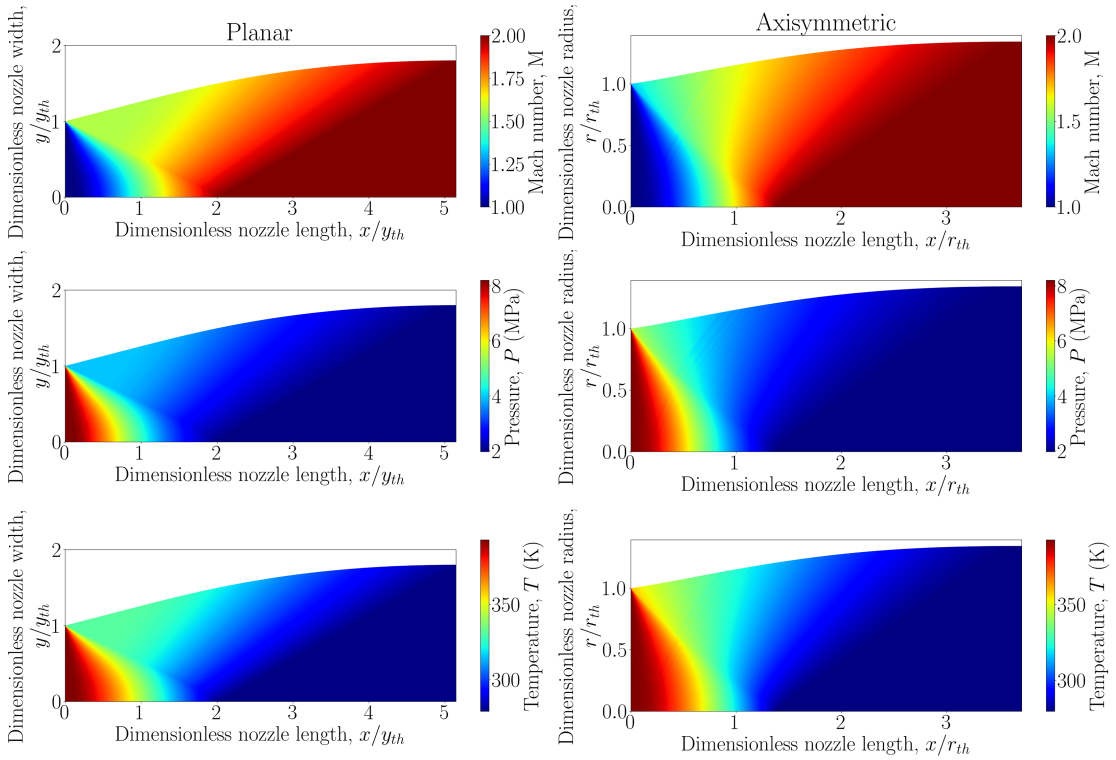

Figure 4.27 – Mach, pressure and temperature surfaces for planar (left) and axisymmetric (right) nozzles, for Carbon dioxide.

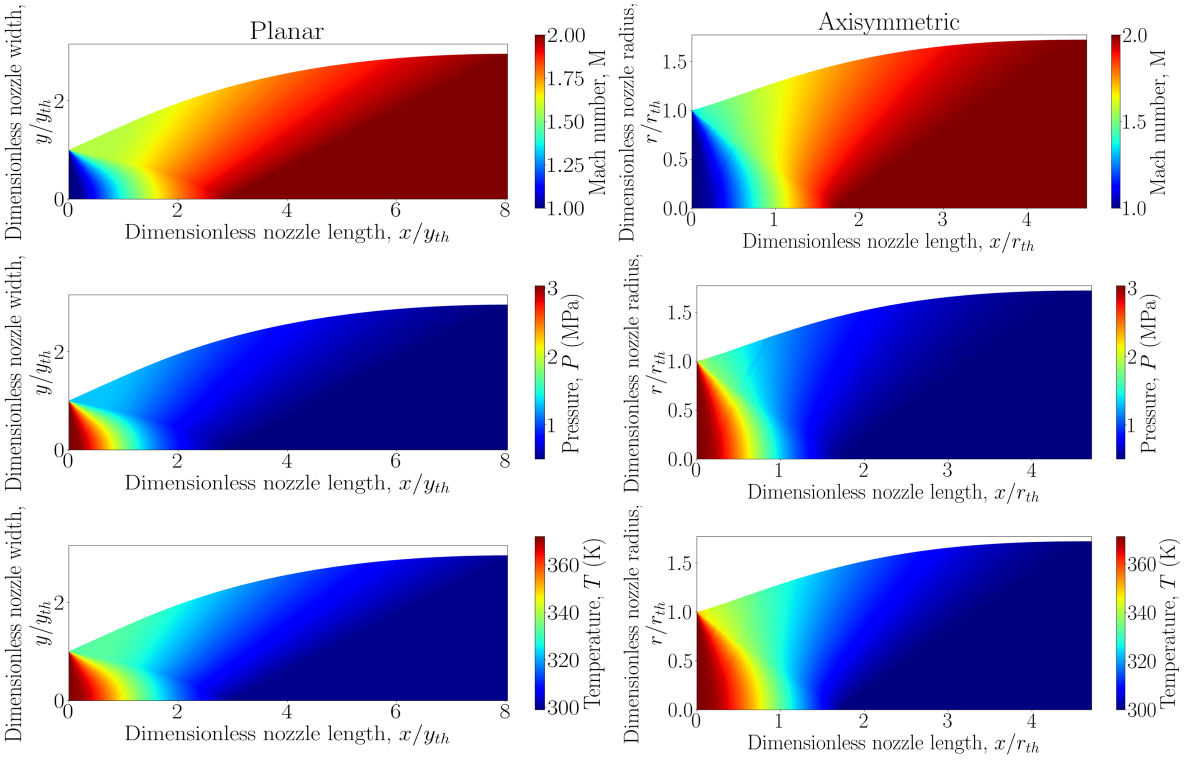

Figure 4.28 – Mach, pressure and temperature surfaces for planar (left) and axisymmetric (right) nozzles, for R1234yf under supercritical stagnation conditions.

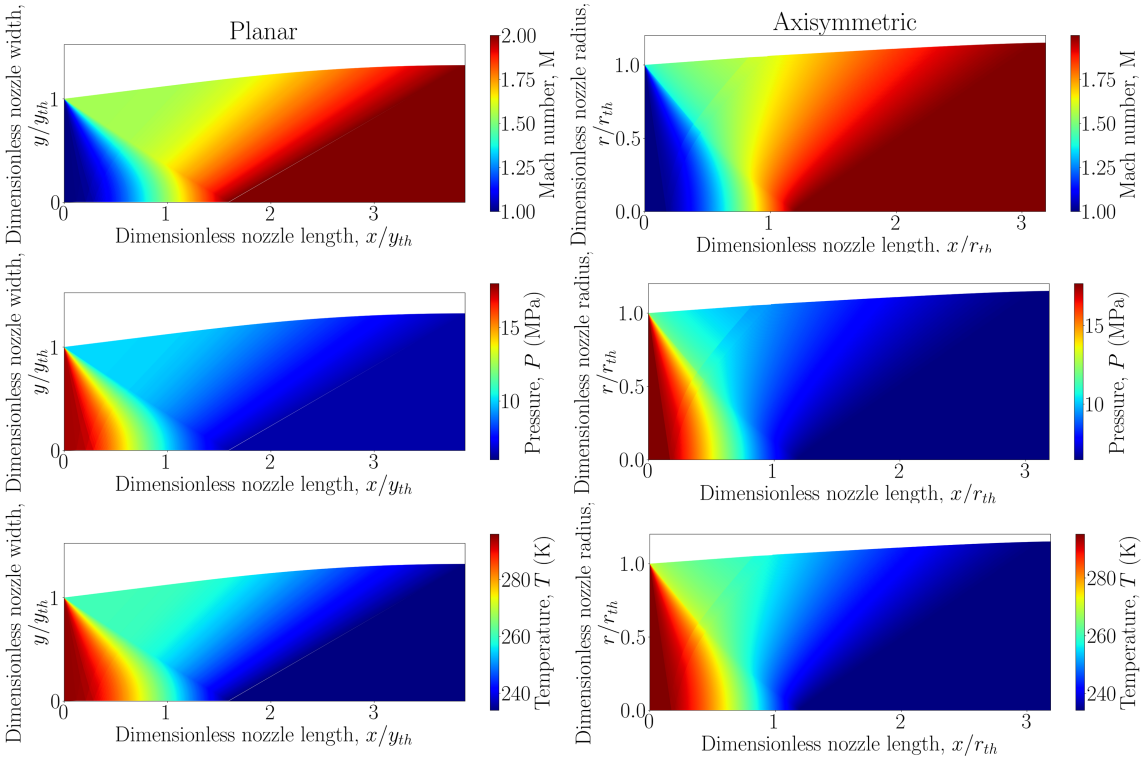

Figure 4.29 – Mach, pressure and temperature surfaces for planar (left) and axisymmetric (right) nozzles, for a carbon dioxide (50% mass fraction) methane mixture under high pressure stagnation conditions

4.4.5 Wall shape verification

As the MOC analysis is derived from the full potential velocity equation 4.103, such an analysis cannot take into account viscous effects for the nozzle wall designing. Therefore, the wall constructed by the MOC was simulated in a commercial CFD code (ANSYS Fluent 2021) in a steady-state regime to verify the nozzle's wall boundary layer behavior in the real gas supersonic expansion. The fluent density-based solver was used in an implicit formulation. Also, the Roe flux difference splitting along the third-order MUSCL schemes for spatial discretization were used. In addition, the $k-\omega$ SST turbulence model with compressible effects correction was employed due to their good performance for viscous supersonic flows (Kolář; Dvořák, 2011; Mazzelli et al., 2015; Besagni; Inzoli, 2017). Finally, a mesh sensitivity analysis was carried out to achieve an independent mesh simulation, resulting in a $\sim$ 30k mesh nodes for each case and a non-dimensional wall distance $y^+ \sim 1$. Fig. 4.30 presents the outcomes obtained for the nozzles shapes presented in figures 4.27 and 4.28 for carbon dioxide and r1234yf respectively, after selecting the same MPEOS used for the MOC formulation, the solution was obtained after the residuals values of the conservation equations achieve values lowers than 1×10^{-6}. The Fig. presents the uniform outlet behavior of the nozzle constructed by the MOC, as expected by the MOC formulation. Fig. 4.31, presents the Mach profile at the nozzle's outlet for the four investigated cases, a nearly uniform profile was obtained, the carbon dioxide

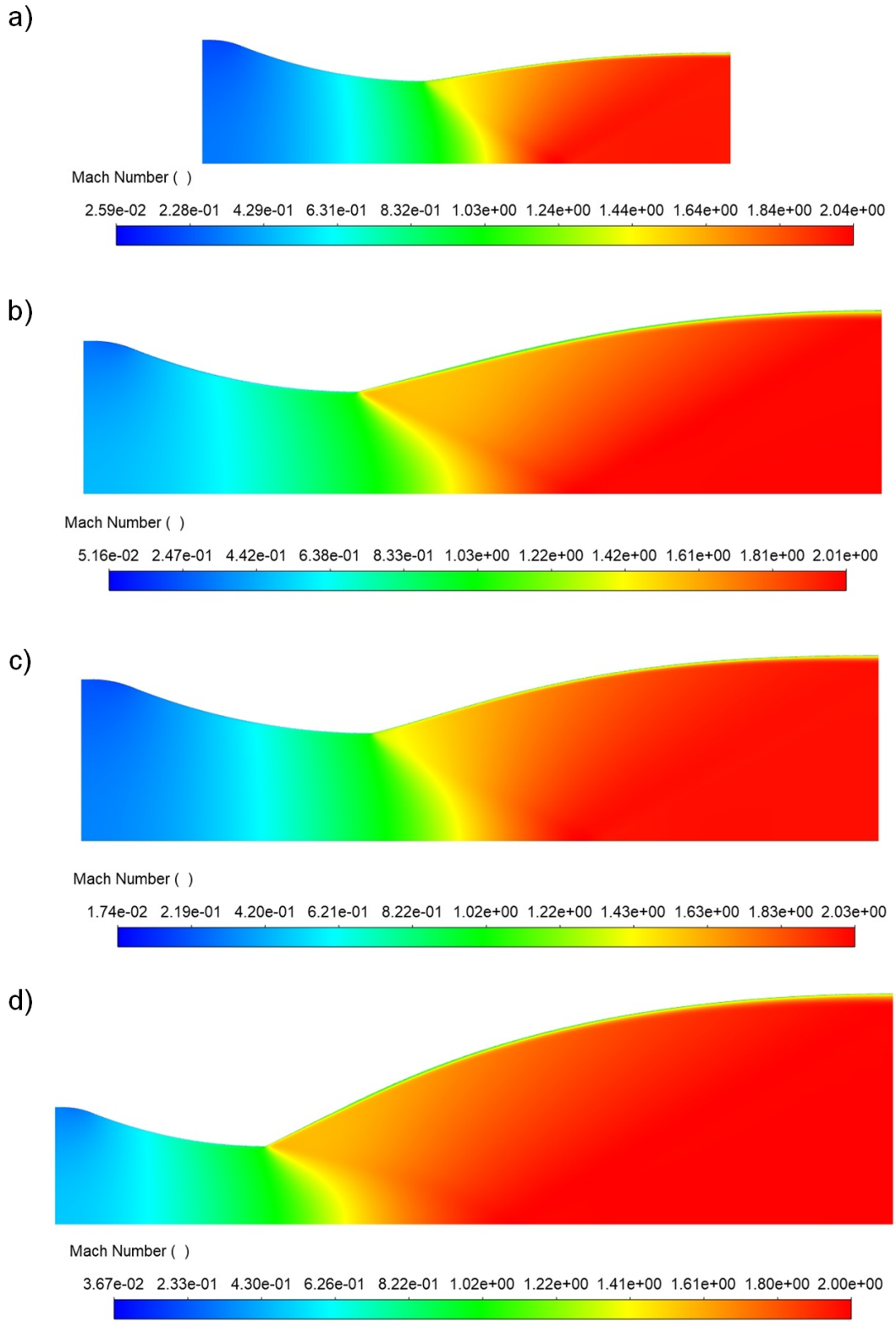

Figure 4.30 – Viscous simulation for carbon dioxide a) axisymmetric, b) planar and R1234yf c) axisymmetric d) planar nozzles.

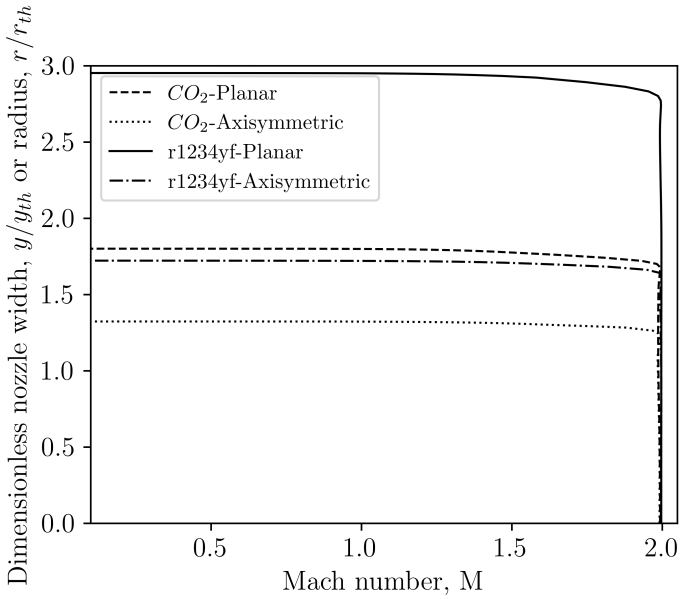

Figure 4.31 – Mach profile at nozzle outlet for different fluids and configurations.

axisymmetric nozzle presents the maximum deviation (0.76%). Therefore, the inviscid analysis is accurate enough for nozzle designing. These solutions were achieved for a wall radius in the convergent part of 3 times the nozzle's throat diameter.

4.4.6 Supersonic gas separator design

After verifying the implementation of the method of characteristic for real gases, one can proceed to use it for designing supersonic gas separators, as presented in Fig. 4.32. In this figure, it is presented the design of a supersonic nozzle with central body at a stagnation pressure and temperature of 10 MPa and 300 K and CH_4-CO_2 50% mass mixture, being a typical design between the commercial makers of supersonic gas separators. The central body is normally used for carbon dioxide separation purposes. The central body can be easily constructed by the method of characteristics, after imposing the required radius central body radius in the point C computation (See Fig. 4.22). Also, the central body can be constructed by a spline, and in this case, the spline slope must be computed at the characteristic intersection position and used it in the point C computation.

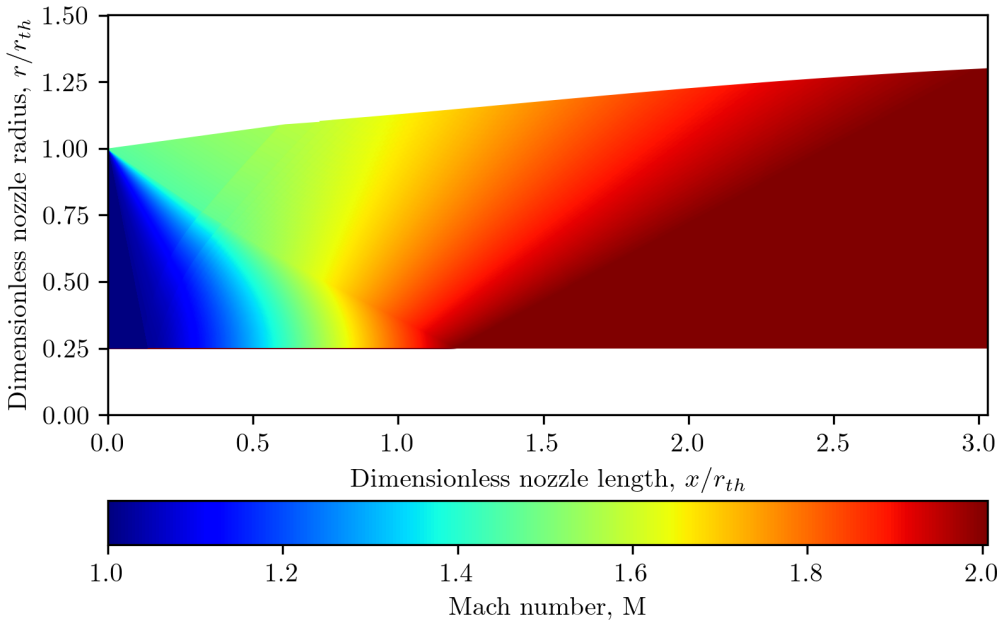

Figure 4.32 – Supersonic nozzle with central body, for CH_4-CO_2 50% mass mixture.

5 Experimental test-rig

As presented in Section 2 there is a research gap in the experimental evaluation of supersonic gas separators, mainly related to optical access and mixture preparation. So, this section explains the test-rig design process, devoted to achieving a robust experimental analysis of the phenomena involved in the device operation. The main phenomena that are analysed are indicated in Fig. 5.1.

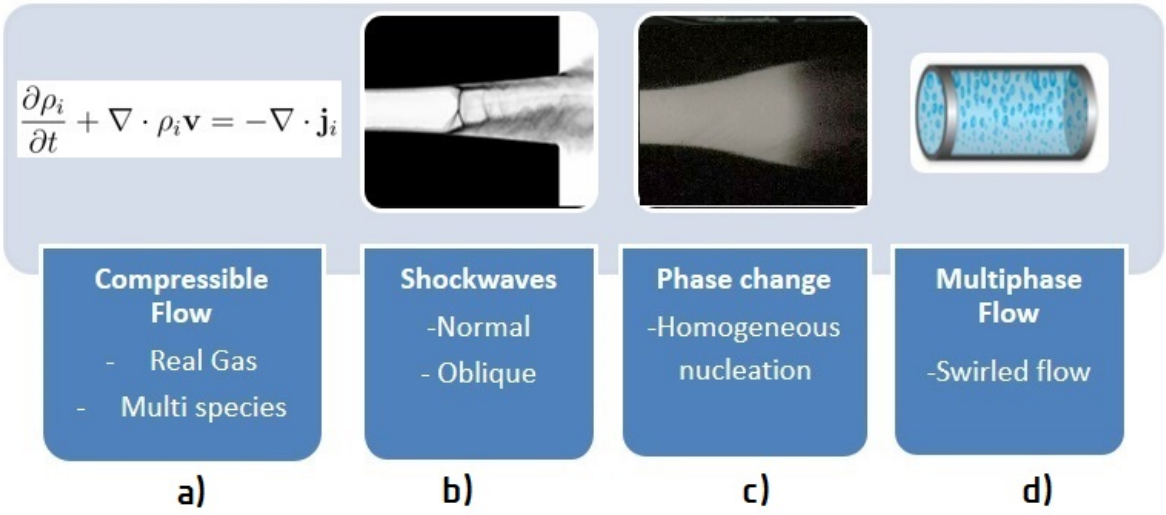

Figure 5.1 – Phenomena involved in the supersonic separation operation. a) Real gas compressible flow of multiphase species, b) Shock waves formation and photographic documentation, c) Phase change formation, d) multiphase supersonic flow.

The first step on the test-rig designing is selecting the more appropriate methodology in order to achieve the supersonic flow in the device. According to (Hodge; Koenig, 1995; Anderson, 1990) there are several test-rig design options for achieving supersonic flow, as presented bellow :

- Open supersonic wind tunnel: This is the simple possible arrangement for supersonic

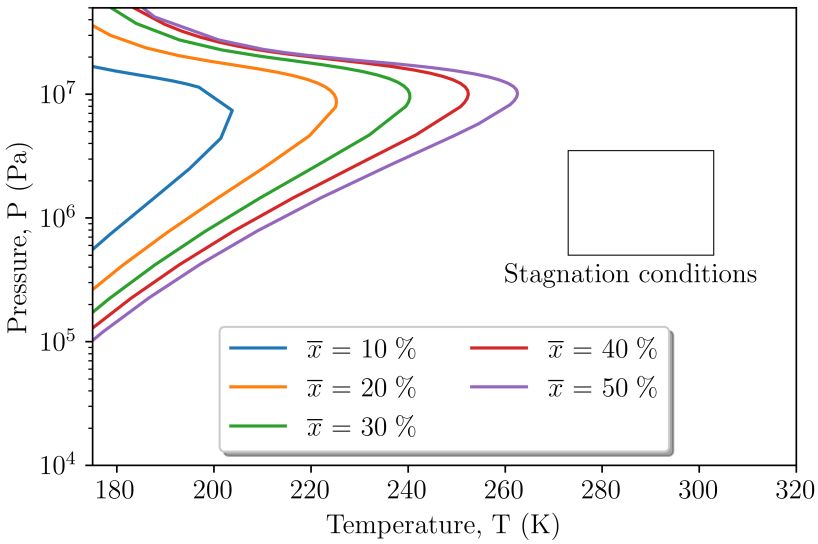

Figure 5.2 – Operation region test rig for a carbon dioxide - nitrogen mixture, coloured lines represent the binodal line for several CO_2 molar fractions, $\bar{x}$.

wind tunnel designing, it consists of an inline compressor - test zone connection, their main restriction is the compressor size, because a high capacity compressor will imply high operational and capital costs.

- Closed-loop supersonic wind tunnel: This arrangement uses a compressor coupled to a series of vanes and ducts in a closed loop, in order to keep recirculating the test fluid, due to its continuous nature this design achieves long testing times, nevertheless, their capital cost are high.

- Blow-down supersonic wind tunnel: This test concept uses high pressure and/or vacuum reservoirs in order to achieve a supersonic flow regime. So the operation time will dependd on the reservoirs' pressure and volume.

- Shock-tubes: This device allows testing at high pressure, or also to evaluating reactions or condensation during a very short operation time, the supersonic regime is achieved after a membrane rupture or a plug displacement.

In order to develop an experimental test-rig capable of characterizing gas mixtures with different concentrations, pressures, and temperatures. The test-rig design must allow the use of different supersonic separators arrangements and designs with a reasonable throat area $\sim$ 500 mm^2. Nevertheless, high operation pressure implies a high blocked mass flow, which leads to several issues for the construction of the new laboratory as the purchase of expensive compressors and electrical power consumption. To avoid these issues it was decided to use a blow-down supersonic wind tunnel design, due to the cheaper

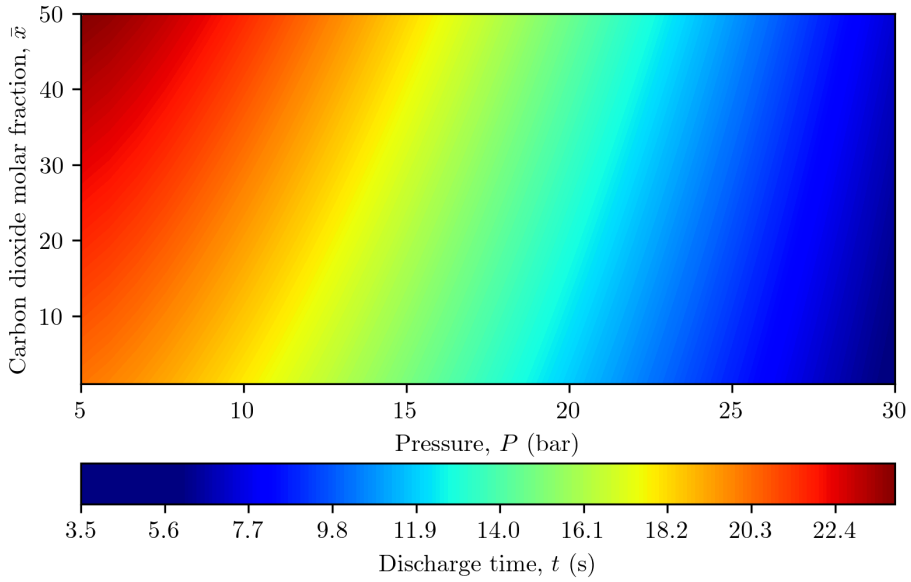

Figure 5.3 – Tank discharge time.

construction and, also, the high pressure reservoir can be used for the mixture preparation. Bearing this in mind, it was developed a test rig with the following characteristics:

- Stagnation pressure 45 bar.
- Stagnation temperature -5 °C to 30 °C.
- CO_2 molar concentration up to 50%.
- Storage tank volume of 4 m^3.

This new test rig must ensure that the supersonic flow exceeds the binodal line for air and carbon dioxide mixtures, as presented in Fig. 5.2. Also, one must guarantee that the tank storage conditions will allow the supersonic flow development for the frame time required by the device assessment. In Appendix D it is presented the development of an equation devoted to calculating the tank discharge time, resulting in:

$$t = \frac{2\forall \left[\left(\frac{P}{P_i}\right)^{\frac{1-\gamma_{Pv}}{2\gamma_{Pv}}} - 1\right]}{\left(\gamma_{Pv} - 1\right) A_{th} \sqrt{\frac{P_i \gamma_{Pv}}{\rho_i} \left(\frac{2}{\gamma_{Pv}+1}\right)^{\frac{\gamma_{Pv}+1}{\gamma_{Pv}-1}}}} \tag{5.1}$$

where γ_{Pv} is the isentropic real gas coefficient (Nederstigt, 2017),

$$\gamma_{Pv} = c^2 \frac{\rho}{P}. \tag{5.2}$$

For this equation development, the viscous and heat transfer effects were neglected, therefore, it is used as an approximation for the testing time computation. Fig. 5.3

presents the Eq. 5.1 results, for the following parameters: $A_{throat} = 600$ mm^2, $P_i = 40$ bar, $T_i = 295$ K, $\mathsf{V} = 4$ m^3. Therefore, according to the outcomes presented in Fig. 5.3 lower CO_2 molar concentrations and high test pressures will lead to short operating times. After finding the main test parameters and in their impact on the test time, one proceeds to show the designed test-rig. This test-rig is divided into two different sections, the first one is related to the gas preparation and the second one drives out the supersonic condensation takes place, as presented in Fig. 5.4. The test-rig was designed and constructed at the Renewable and Alternative Energy Systems Laboratory - SISEA, located at escola politécnica in the Universidade de São Paulo.

5.1 Gas preparation section

On the left side of Fig. 5.4 it is presented the gas preparation section, which consists of: a compressor, an adsorption dryer unit (Dew point temperature of -70 °C), control valves and storage tank (See Appendix G for further details). Firstly the tank is filled with compressed dry air pressure; next, the carbon dioxide line is opened and the dry air is closed. Special care must be taken to avoid the carbon dioxide concentration on the bottom of the tank, therefore, it was established that the carbon dioxide must be loaded on the superior tank inlet line, to ensure their homogenization. After achieving the required tank concentration and pressure, the filling process ends. The carbon dioxide molar fraction is measured by the FELIX F-920 on-line gas analyser (3% relative accuracy). Figure 5.5 shows the gas preparation design, corresponding to the following parts: 1) 4m^3 mixture tank, 2) Discharge pneumatic controlled valve, 3) Discharge pipe, 4) Compressed air and CO_2 inlet line, 5) Cooling line, 6) Air dryer and compressor, 7) CO_2 bottles, 8) Discharge hose, 9) Discharge pipe support. This service was contracted with an external supplier according to our design as presented in Fig. 5.5. Figure 5.6 presents the comparison between the initial laboratory state and the final laboratory construction. Finally, a pneumatic actuated ball valve (V-1 in Fig. 5.4) is mounted at the 4 inches discharge pipe, and this valve opens the flow for the test rig section.

5.2 Test section

This section describes in a succinct form the test-rig development process which ends with the infrastructure presented in Fig. 5.7. The scope of this work embrace the mechanical design of the test-rig. The method of characteristics was used for the supersonic nozzle design and the finite element method was used to predict the critical parts' mechanical resistance, such as the supersonic planar nozzle assembly and the 3D adapter.

The test-rig frame was constructed by 50 x 50 or 50 x 100 mm reinforced aluminium profiles in order to ensure the experimental set-up robustness. Also, welding-neck and

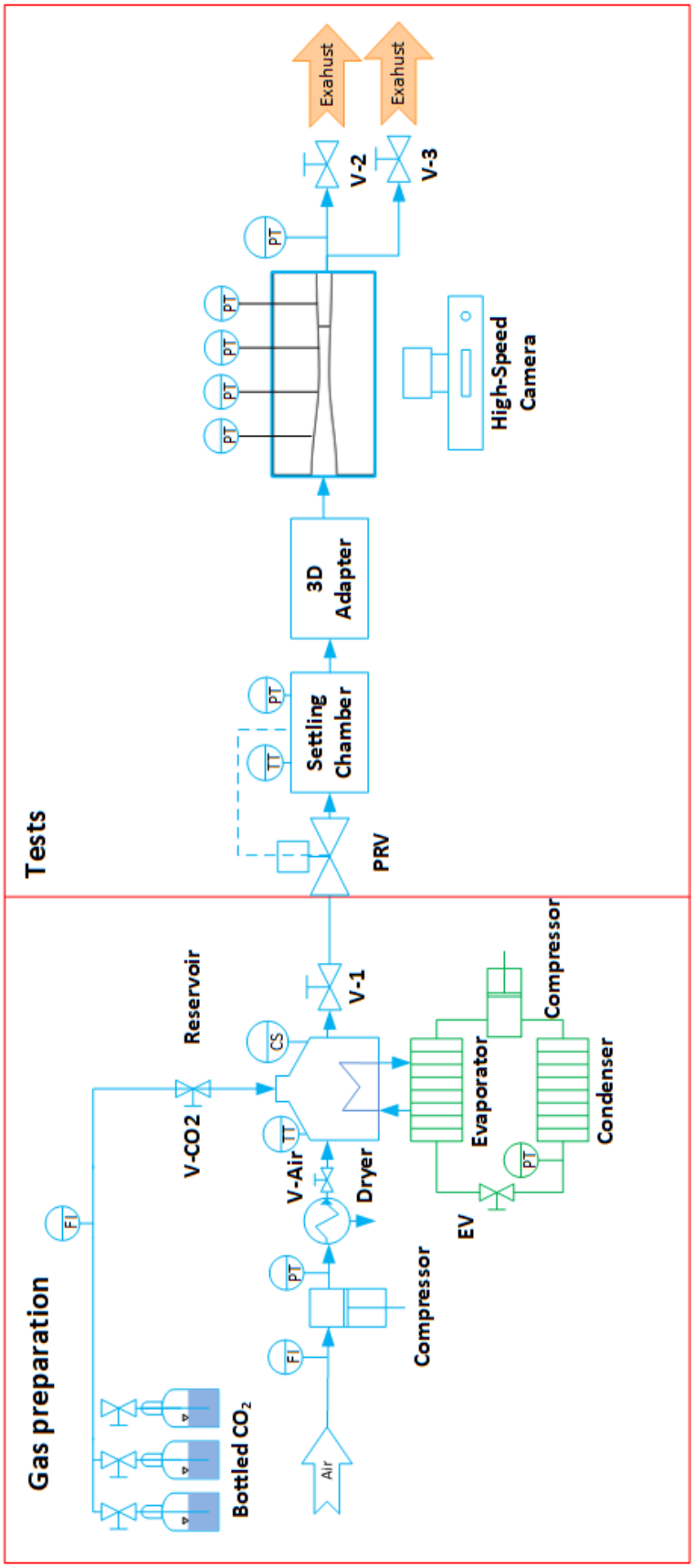

Figure 5.4 – Test-rig P&ID.

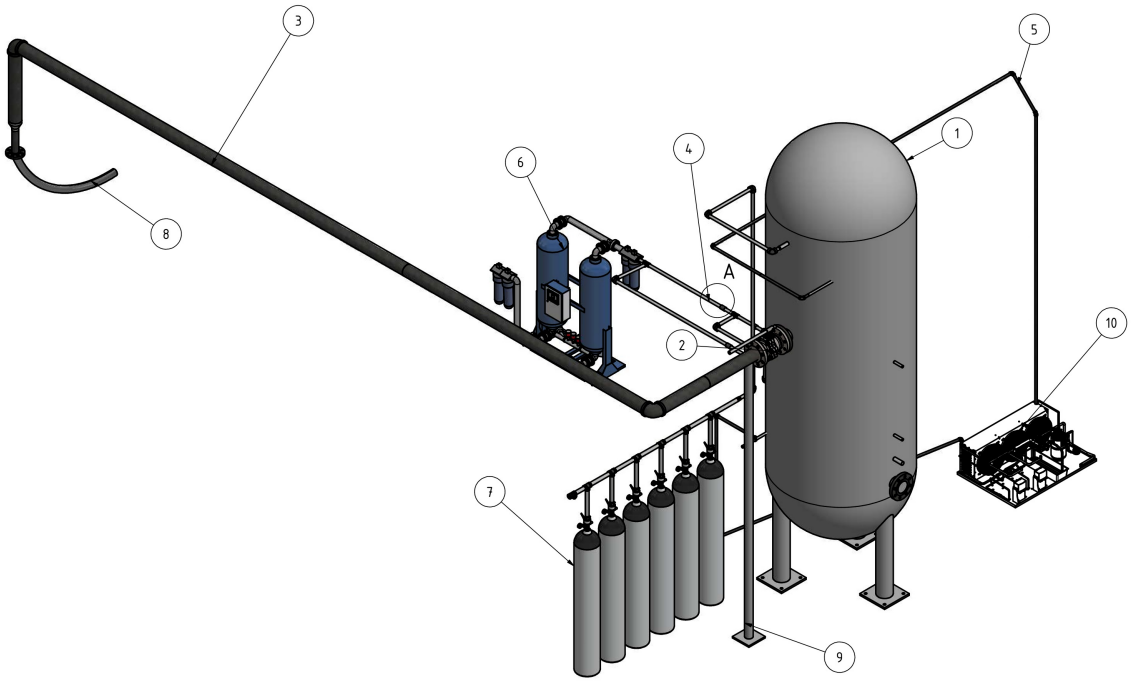

Figure 5.5 – Gas preparation section design.

Figure 5.6 – Laboratory refinishing a) Year 2018 b) Year 2022.

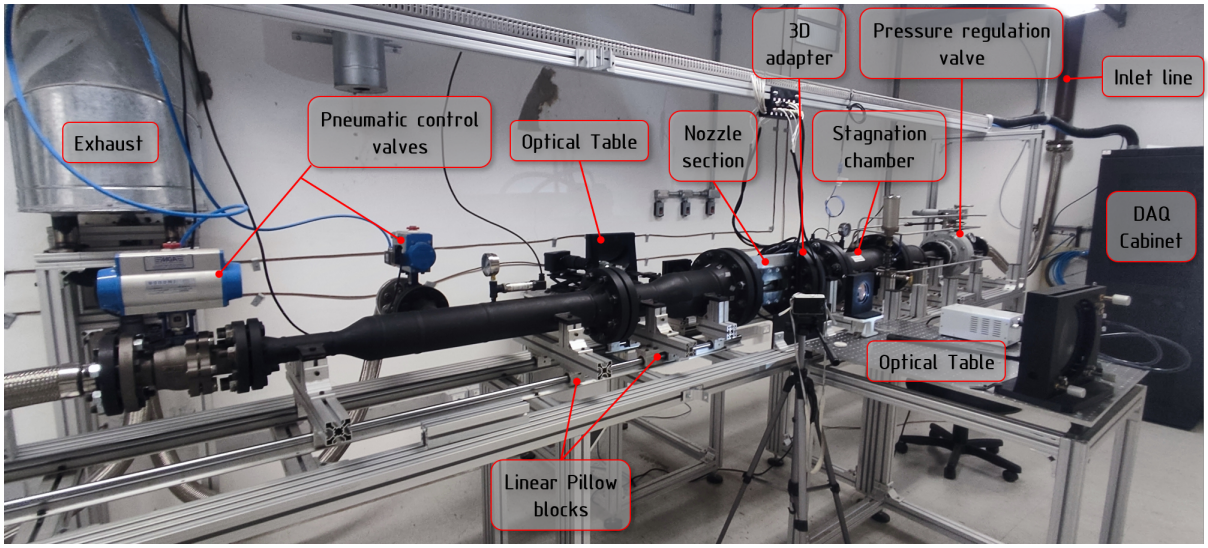

Figure 5.7 – Supersonic nozzle test-rig.

slip-on 300 class flanges and schedule 40 carbon steel piping were used on the piping design, these flanges were selected to withstand the maximum testing pressure at the respective working temperature. Moreover, high pressure stainless steel reinforced hoses were used to connect the test-rig external connections and, a series of heavy-duty linear pillow blocks were used in order to allow the axial movement of the downstream nozzle components, without losing the nozzle alignment. The more important elements of the test-rig are:

- Pressure regulation valve;
- Flow rectifier;
- Stagnation chamber and 3D adapter;
- Supersonic nozzle;
- Discharge side;
- Optical tables.

Each one of the above presented elements will be shown in the next subsections.

5.2.1 Pressure regulation valve

The first element on the test section line is the pressure regulator valve Fig. 5.8, this valve uses a sensing line located at their downstream side to "measure" the pressure at the outlet and if there is an offset between the discharge and the set pressure, the valve central body moves in order to control the process. The main benefit of using this kind of valve relies on its mechanical working principle, which doesn't require any electronic

control. Because in some cases it could become problematic for processes with variable composition, especially on their control variables setup.

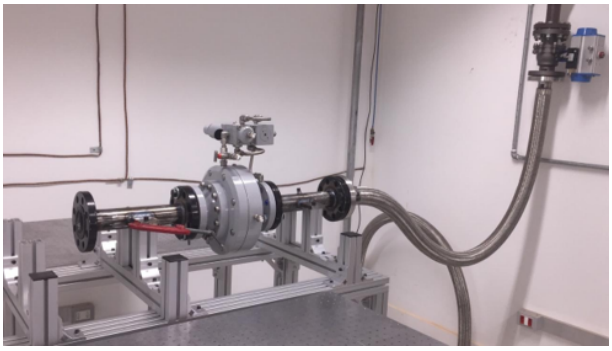

Figure 5.8 – Pressure regulation valve.

Nevertheless, this valve needs to be set with different load springs in order to achieve the required discharge pressure. Table 5.1 presents the required spring for each pressure operation range:

Table 5.1 – Springs used in the pressure regulation valve, data from manufacturer.

Spring	Code	Pressure range (bar)
Green	01.49.65	1-4.5
Red small	01.49.64-50	4.5-12
Brown	01.49.33	11-17
Red big	01.51.94A	16-30
Yellow	01.51.94	27-40

Therefore, in order to achieve the required setup pressure the spring located at the valve pilot must be changed, later the control screw must be rotated until the setup pressure is achieved.

5.2.2 Flow rectifier

The second section consists in the control of tank discharge conditions and the flow rectification before the supersonic nozzle, where the tests will be carried out. For the flow conditioning, we used the K-Lab NOVA design after employing the dimensions and design methodology established by the Brazilian standard ABNT NBR ISO 5167-1 to withstand the maximum stagnation pressure (45 bar). Figure 5.9 shows the flow conditioner after machining and their posterior installation on the test rig.

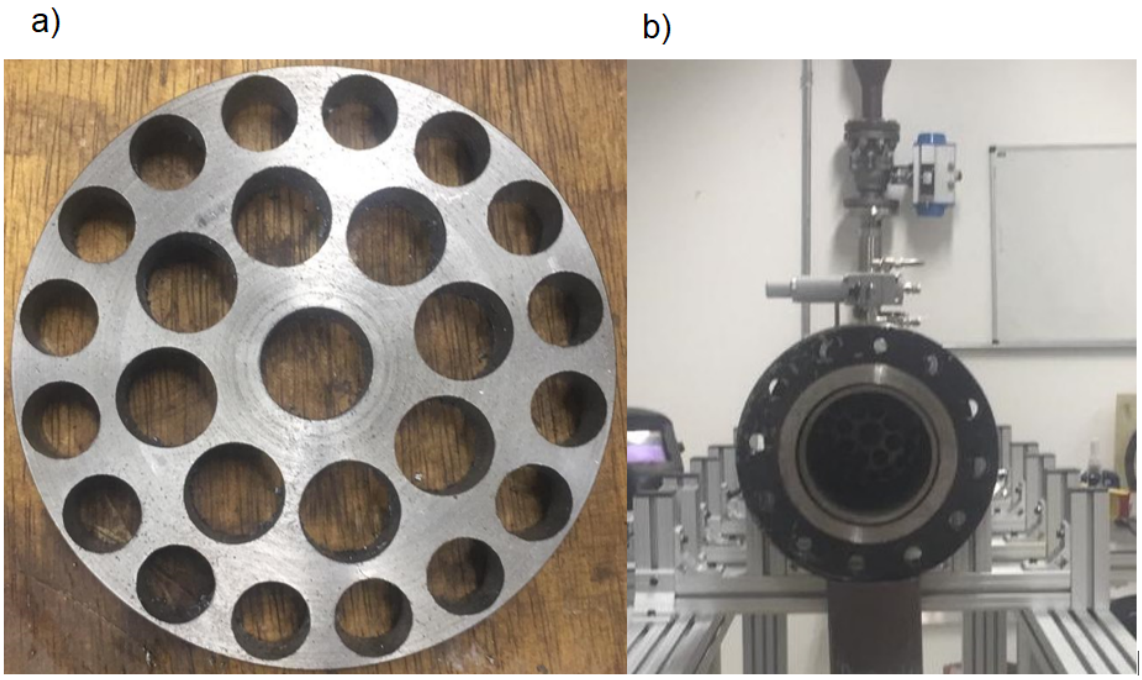

Figure 5.9 – K-Lab NOVA flow conditioner a) Part after machining b) installed in piping.

Source: Author

5.2.3 Stagnation chamber and 3D adapter

The stagnation chamber was installed after the flow conditioner to ensure flow rectification. Additionally, pressure, temperature, and concentration measurements will be taken in this section. To ensure reliable measurement in the stagnation section, the flow velocity was controlled to achieve values lower than 5 m/s. Fig. 5.10 presents the used arrangement for the thermocouple installation, it was used a stainless steel tube and a slot was machined at the tube centre in order to protect and locate the exposed thermocouple part, It was used a tip diameter of 0.8 mm in order to have a fast thermocouple response, also it was selected a T type thermocouple for accurate measurement at low temperatures. Pressure and concentration measurements were taken at the stagnation chamber connections.

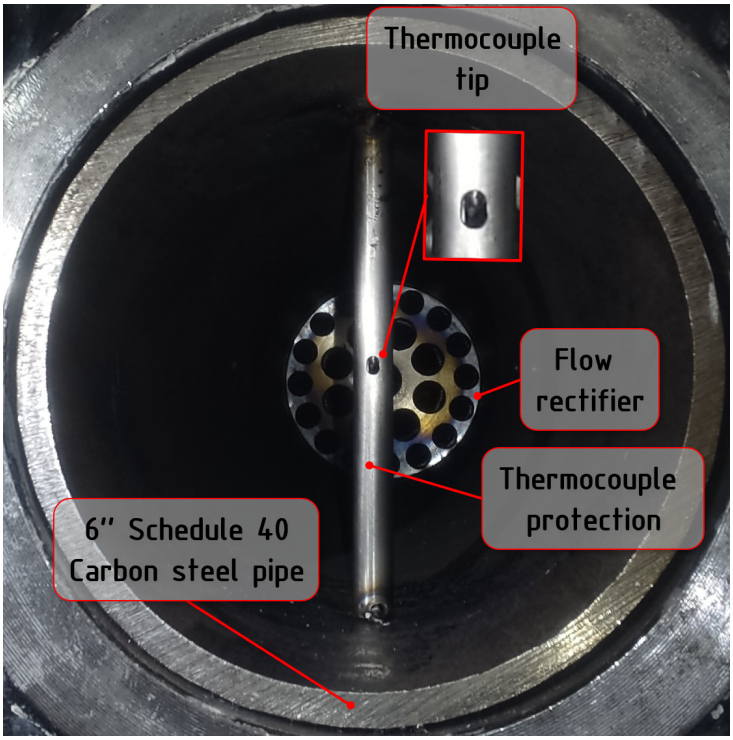

Figure 5.10 – Termocouple installation in the stagnation chamber.

Later, at the stagnation chamber downstream, a three-dimensional adapter is placed to smoothly convert the flow from a circular to a rectangular cross section. For their construction, an analytical technique was used based on the work of White & Sayma (2018), where the profile cross section was constructed after using a super-ellipse equation,

$$\left|\frac{x}{a_{adp}}\right|^{n_{adp}} + \left|\frac{y}{b_{adp}}\right|^{n_{adp}} = 1, \tag{5.3}$$

where $a_{adp}(x)$ and $b_{adp}(x)$ are fourth-order degree functions to define the adapter profile, and $n_{adp}(x)$ is the super-ellipse exponent, given by

$$n_{adp}(x) = 2 + 3.845 \times 10^{-3} \cdot \exp\left(10.148x\right). \tag{5.4}$$

Figure 5.11a presents the profiles generated by the super-ellipse equation and the $a_{ds}(x)$ and $b_{ds}(x)$ profiles in the three-dimensional adaptor, due to their inherent geometric complexity. This part was constructed using additive manufacturing with ABS. However, this material does not resist the maximum stagnation pressure (45 bar), therefore, it was constructed in ABS, after using a welded steel reinforcement as shown in Fig. 5.11b.

5.2.4 Supersonic planar nozzle

5.2.4.1 Mechanical design

The supersonic nozzle was placed at the three-dimensional adaptor outlet. To improve the supersonic nozzle optical measurements, the nozzle has a lap joint flange

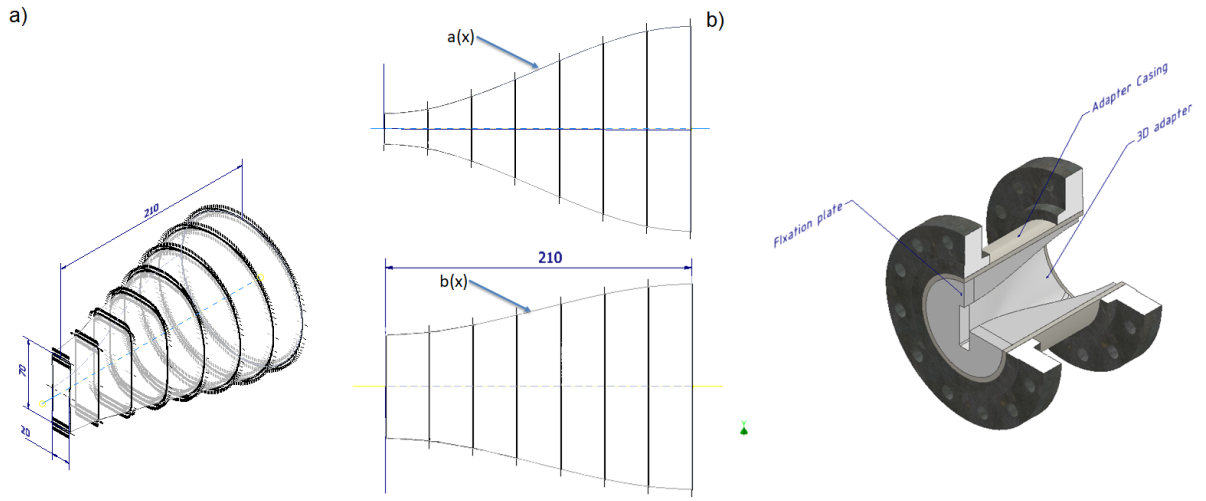

Figure 5.11 – 3D adaptor construction a) super-ellipses and profiles b) mechanical construction.

design, which facilitates the nozzle rotation and ensures the perpendicularity between the nozzle and the optical test rig. The supersonic nozzle was designed to achieve the following goals: 1) High pressure resistance, 2) Low deformation, and 3) Nozzle profile interchangeability. To achieve these goals, we performed several design iterations, until accomplished these design guidelines. All design iterations were simulated using the Inventor Nastran FEA software. This software was used to predict the stress and displacement distribution in the supersonic nozzle assembly, and in this analysis the tempered borosilicate optical window, the nozzle frame and the window cover were considered. In addition, the bolt preload and the contact between the assembly pieces were taken into account.

Fig.5.12 shows the simulation outcomes. Fig. 5.12a presents the Von Mises stresses results and Fig. 5.12b the assembly displacement at a nozzle stagnation pressure of (45bar). Note that even at the higher stagnation pressure the maximum assembly displacement is (70µm). This value is small enough to not interfere with the nozzle profile, and therefore ensure the test reliability. The nozzle's body and profile were constructed in martensitic stainless steel (17-4 PH) to guarantee an appropriate mechanical behaviour and wear resistance to carbon dioxide droplets or particles at high speeds, and the window cover was constructed in AISI 4340.

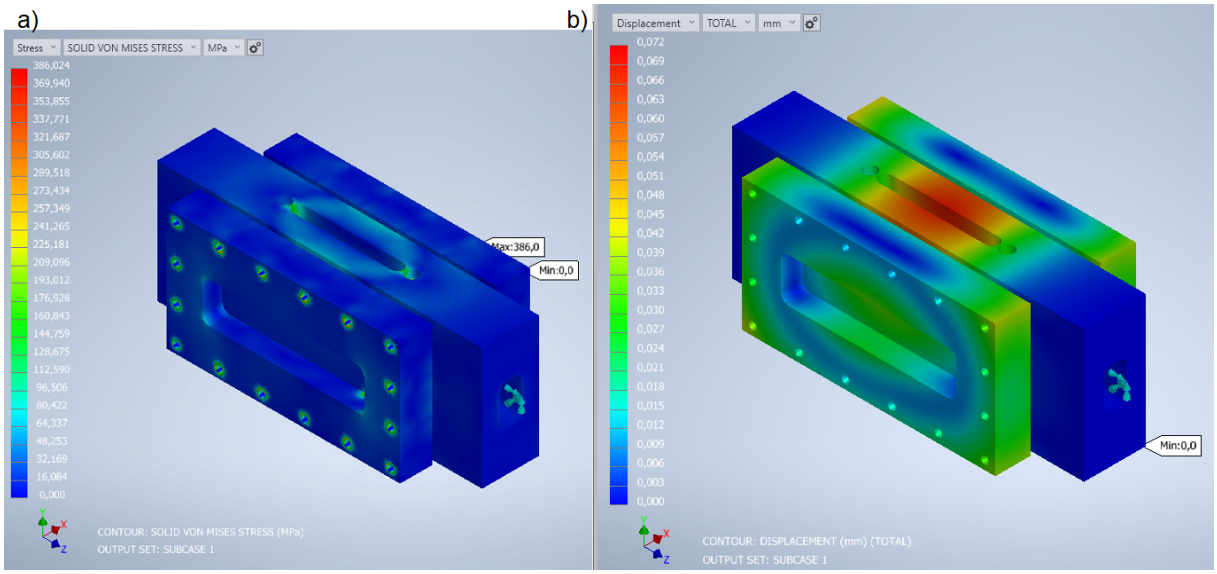

Figure 5.12 – Finite element analysis of the supersonic nozzle, a) Von Misses stress results, b) Displacement.

5.2.4.2 Supersonic channel design

After ensuring the mechanical reliability of the supersonic nozzle design, the nozzle profile was designed. To ensure a shock-free flow, the method of characteristics was used to design the supersonic nozzle part. However, in order to analyse several flow regimes in the nozzle and see their effects on the supersonic condensation, the supersonic channel design procedure uses a different approach than the methodology explained in Appendix B. Fig. 5.13 presents the new methodology, in this nozzle construction procedure one can perceive the presence of two different regions: the expansion and the cancellation section. So in the expansion section the flow behaves as a normal nozzle, and the wall contour in this section is given by:

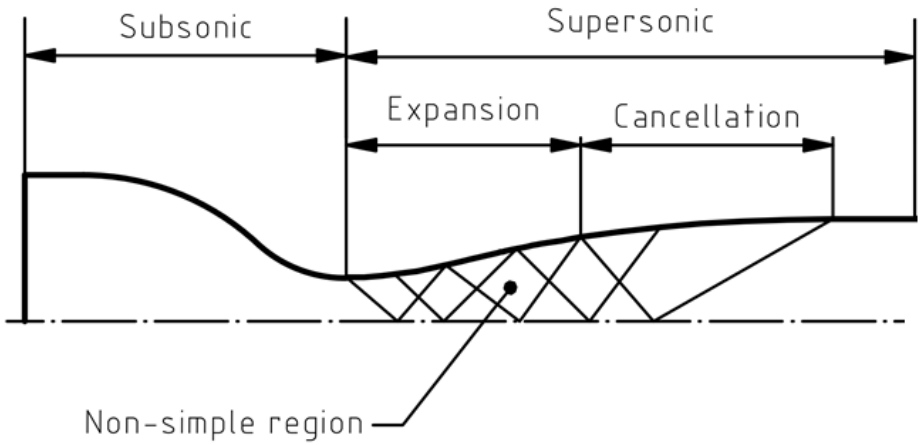

Figure 5.13 – Characteristic lines network for the nozzle supersonic part construction.

$$y = 1 + 0.01x + 0.025x^2. \tag{5.5}$$

In this part of the supersonic nozzle, the characteristic lines are continuously reflected at the nozzle wall, therefore, a wall point unit operator must be used, so the Prandtl-Meyer angle can be computed as:

$$\nu_2 = \theta_2 - K_{II} \tag{5.6}$$

where K is an integration constant introduced in section 4.4.2.2. And θ_2 can be computed from the profile line Eq. 5.5 derivative:

$$\theta_2 = \arctan\left(\frac{dy}{dx}\right) \tag{5.7}$$

All the thermodynamic properties at the wall can be computed after using the inverse Prandtl-Meyer algorithm solver presented in Fig. 4.25. Once $K_I = \nu(M_e = 2.5)$, the cancellation region started to be constructed, in this region the wall nozzle was constructed to cancel all characteristic line reflections, ensuring a completely parallel flow at the nozzle outlet. The convergent part was constructed after using two tangent circles, being the inner circle tangent of the nozzle throat. Finally, as described in subsection 4.1.1 the viscous effects could be relevant in the supersonic flow development in nozzles, so, in order to avoid the viscous effects, the nozzle deep is 40 mm, therefore, their hydraulic diameter will be high even at the nozzle throat, avoiding the formation of high viscous potential values (see Eq. 4.16) and therefore, decreasing the viscous effects on the nozzle.

Figure 5.14 presents the method of characteristic results for several carbon dioxide compositions. The nozzle profile becomes wider as the carbon dioxide fraction increases because the mixture density increases. However, as the nozzle is used to test several carbon dioxide molar fractions, the nozzle was fabricated after considering an average profile for the compositions considered in Fig. 5.14.

After we used the method of characteristics for the general nozzle design, we detailed the nozzle assembly as presented in Appendix F for the nozzle body and the nozzle profile. In the nozzle body design process, special care was taken to ensure the nozzle hermetic sealing, this was attained using O-ring seals. Furthermore, we have established tight dimension tolerances to eliminate the flow recirculation inside the nozzle, and tight geometric tolerances to ensure the parallelism of the nozzle inserts. Fig. 5.15 presents the o'ring groove and tap hole detail. We employed a special design for the pressure tap fabrication, because it is required that the pressure tap holes be perpendicular to the flow in the supersonic region to avoid shock wave production. In addition, these holes have to be as small as possible to decrease eddy formations in the pressure taps which

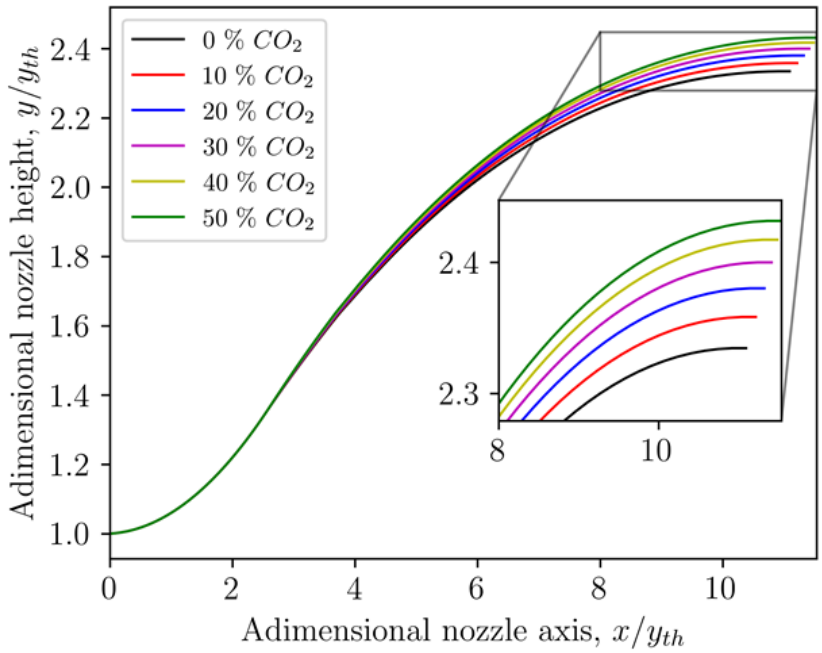

Figure 5.14 – Wall profile construction for different carbon dioxide molar compositions.

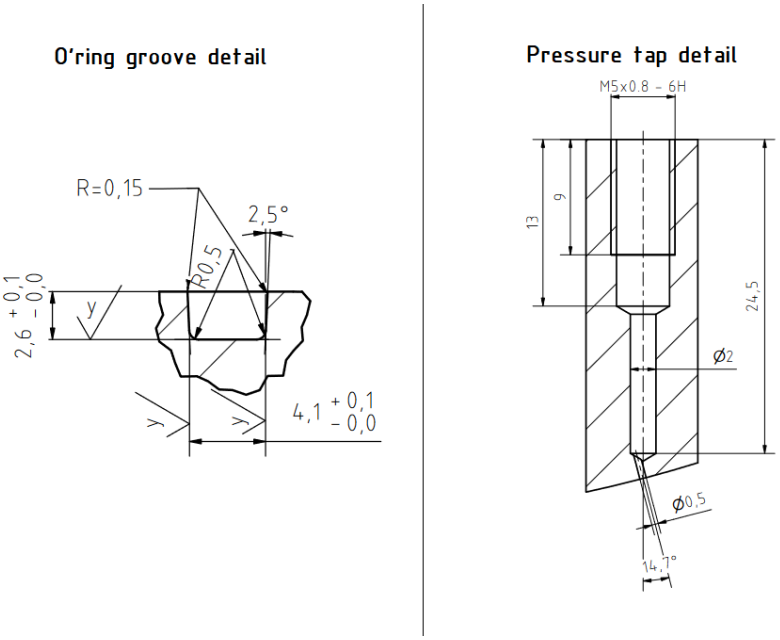

Figure 5.15 – O'ring groove and tap hole detail, units in mm.

could interfere in the pressure measurement. For the absolute static pressure measurement was used the Kulite XTE-190SM model transducers, these transducers were selected due to their high natural frequency $550 - 700$ kHz and accuracy. Fig. 5.16a shows the parts after their machining, and Fig. 5.16b presents the two nozzles developed for testing, these nozzles have throat width of 15 mm and 5 mm, for the nozzle 1 and 2 respectively. Finally, the supersonic channel profile coordinates and the tap positions are presented in Appendix E.

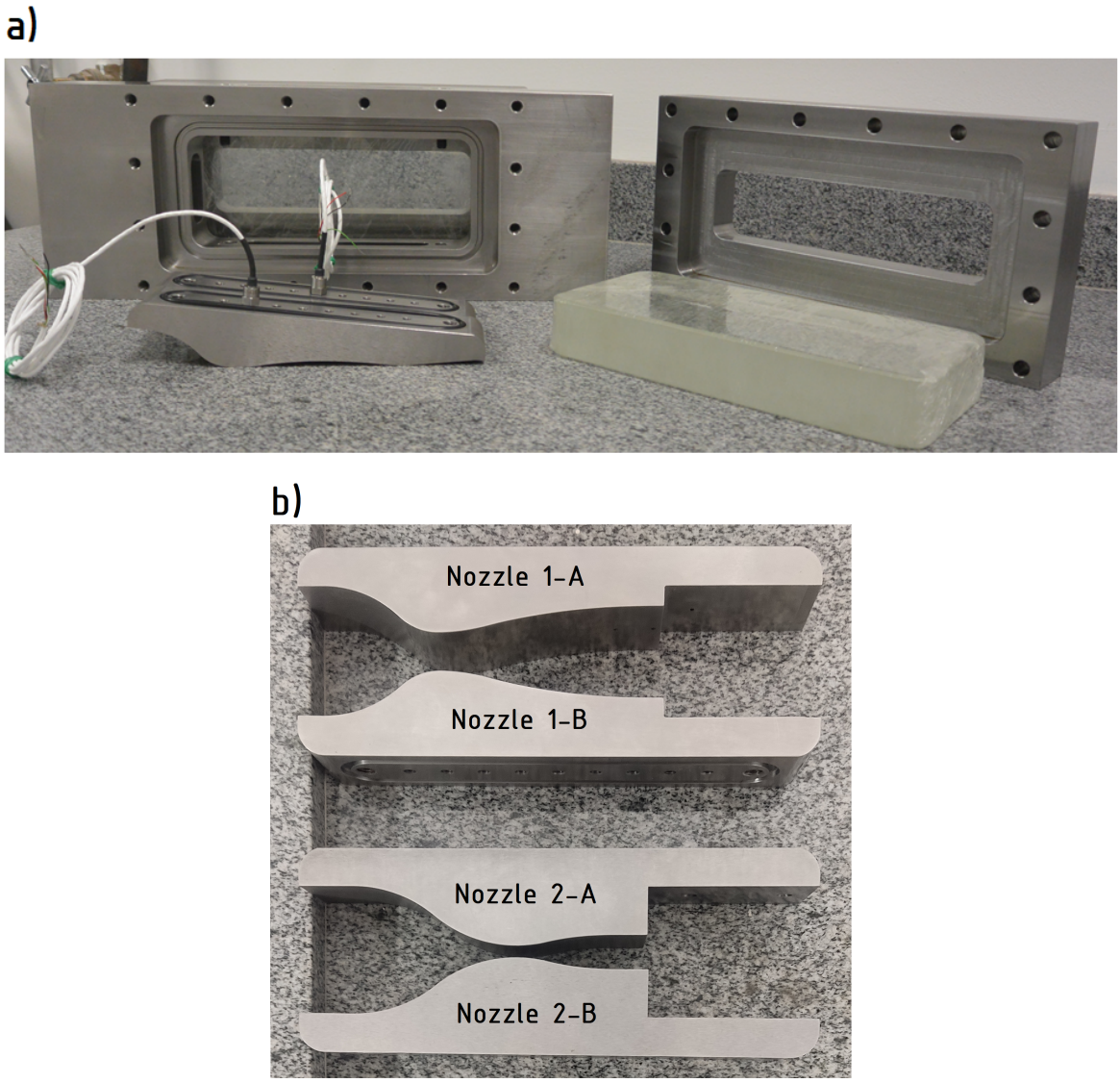

Figure 5.16 – Nozzle parts after machining a) Nozzle support, profiles, windows and cover, b) Nozzle profiles.

5.3 Downstream section

Figure 5.17 presents the assembly of the supersonic nozzle and the downstream equipment, such as: pneumatic control valves, hoses, silencers and exhaustion ducts. Fast opening pneumatic valves were used to open the discharge section and achieve the supersonic flow in the nozzle. All these parts were mounted on high-precision rails to facilitate the test-rig operation.

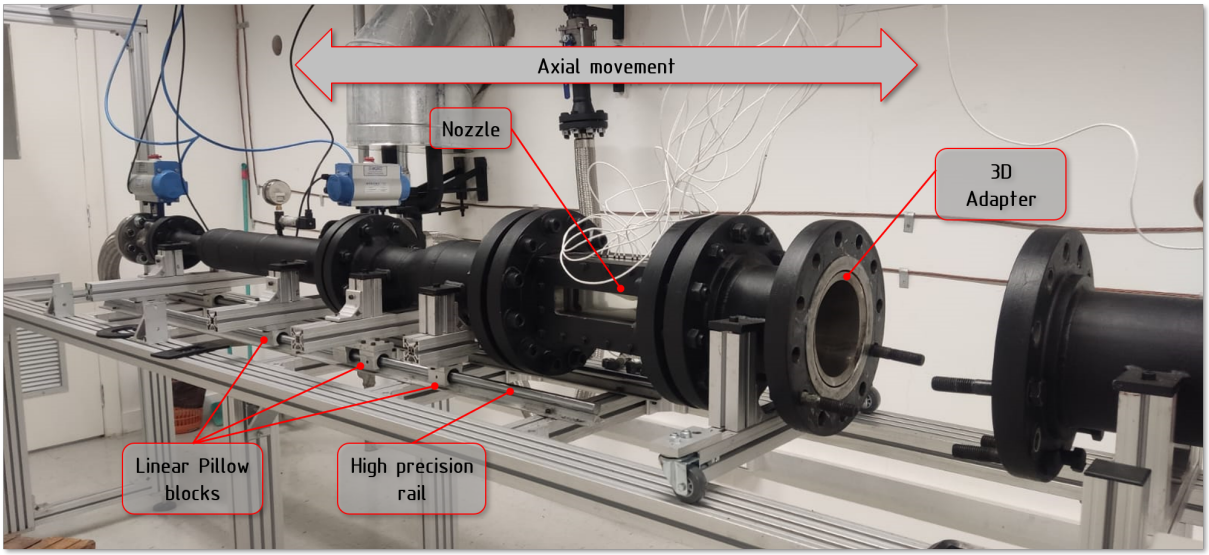

Figure 5.17 – Supersonic nozzle and downstream section.

5.4 Optical methods

As a result of the supersonic flow particularities, direct measurement of the flow field properties is complex, due to the fact that any flow perturbation could lead to a shock wave formation. Therefore, in this context the use of optical methods are required because it allows studying the flow characteristics without any perturbation. This work implements two different optical approaches, explained bellow:

- Direct visualization: This method uses a light tunnel and a diffuse window in order to create a uniformly lighted background, with the purpose of the condensation shock starting point characterization.
- Schlieren: This is a classical technique used for the compressible flow qualitative characterization, it captures the density spatial gradients inside the flow and allow to have an insight on the shock wave formation and propagation.

Each one of these techniques will be explained in the following subsections. Nevertheless, both approaches require an accurate optical table alignment and levelling. This was performed after using a laser level in order to align the table optical centreline and height as depicted in Fig. 5.18. In addition, both approaches used the same high-speed camera (Chronos 1.4) and the same 2300 lm led lamp (Photonita P1100L).

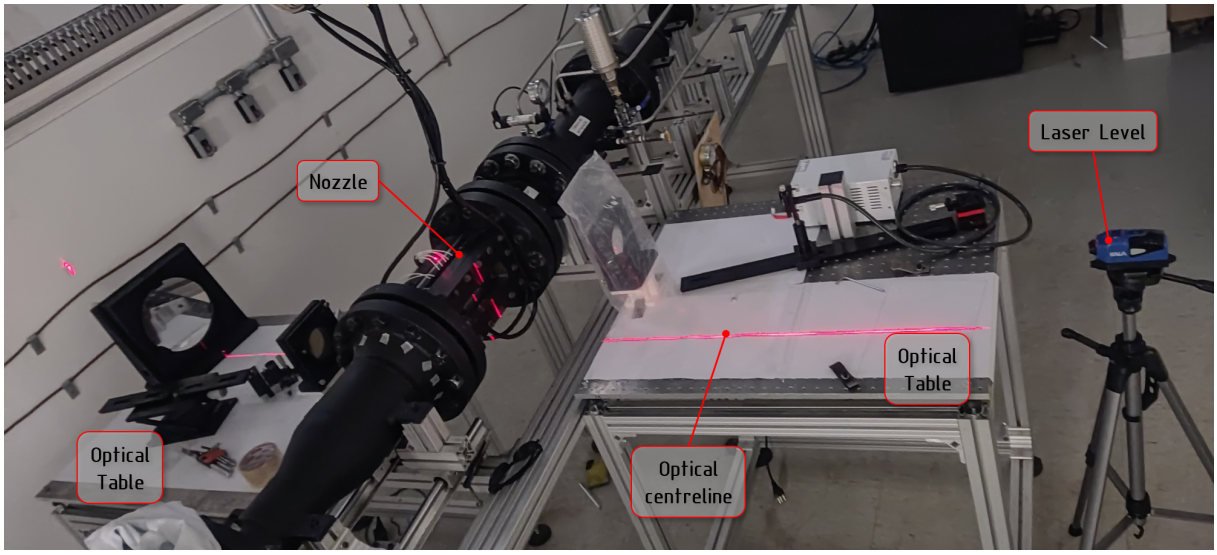

Figure 5.18 – Optical tables alignment.

5.4.1 Direct optical arrangement

As stated in the last section uniform background lightning is a technique used to evaluate the condensation shock formation shape and location. In this arrangement the high-speed camera was configured for a frame rate of 1069 frames per second (FPS) and a camera sensor exposure of 120 µs, also the led lamp was regulated for the lower operational lightning intensity in order that the light does not vanish the condensation shock. This was necessary because the Schlieren technique requires a higher light intensity which results in an information loss at the condensation shock beginning. Fig. 5.19 presents the direct optical arrangement.

5.4.2 Schlieren optical method

This work uses a Z-type schlieren set-up (Settles, 2001) as presented in Fig. 5.20, this set-up is used due to the laboratory space constrains, and it consists in a optical path created by several mirrors, lens and a knife-edge, as explained bellow:

- Light source ①: High-intensity led lamp;
- Optical fibre ②: Transfer the light from the lamp towards the condensing lens optical axis, this option was used to improve the set-up robustness and flexibility;
- Condensing lens ③: Lens used to concentrate the light from the optical fiber into the parabolic mirror focus;
- Planar mirrors ④ e ⑧ : Due to the optical table constrains it is no possible to put the parabolic mirror in the condensing lens axis, therefore the flat mirror connect both optical axis;

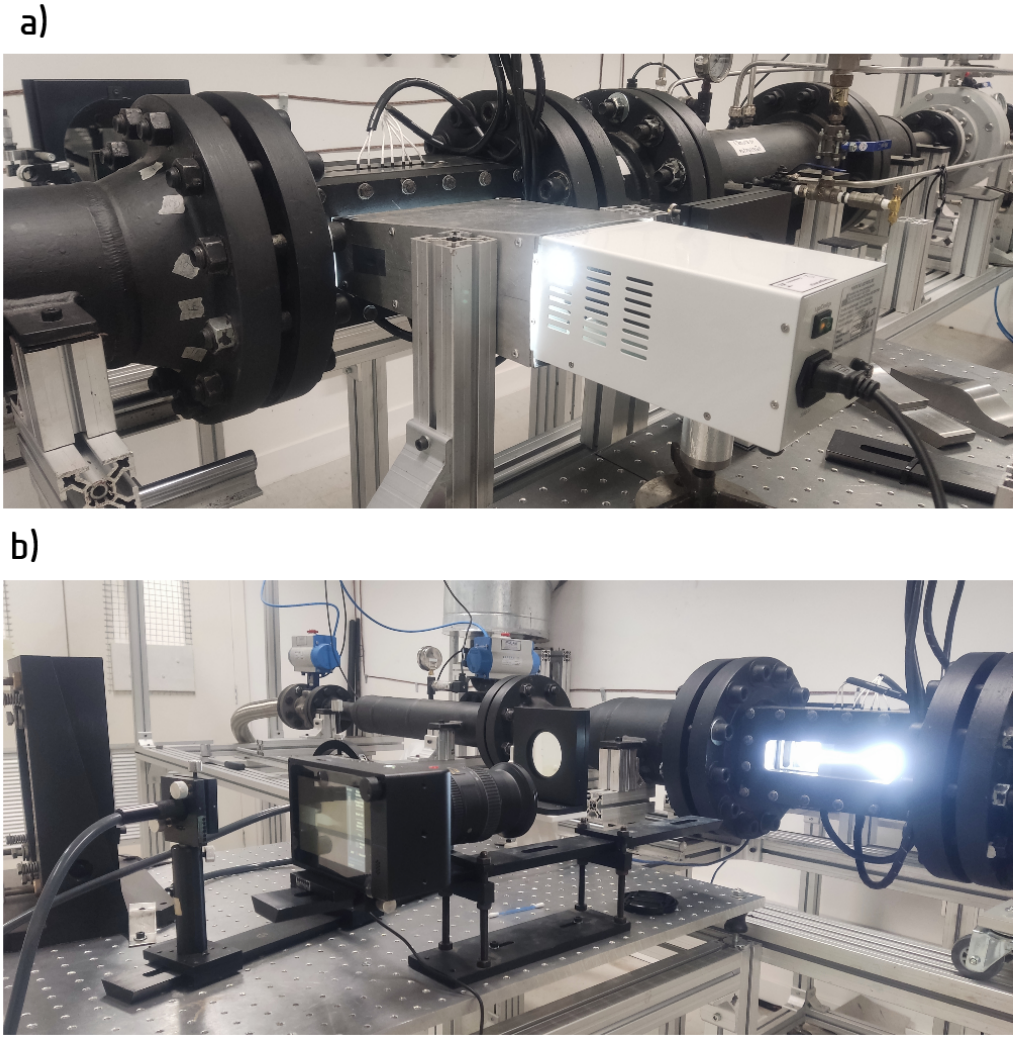

Figure 5.19 – Direct optical arrangement, a) Lamp and light tunnel configuration, b) High-speed camera location.

- Parabolic mirrors ⑤ e ⑦: These mirrors create the testing section in this region the light beam must have a constant diameter;
- Direct camera ⑥: Camera used to take still pictures of the phenomena from outside the optical path;
- Knife-edge ⑨: Steel blade used to cut-off the image perturbations created by the density gradient in the nozzle;
- High-speed camera ⑩: Camera used for recording the experiment, it was used a frame rate of 2038 FPS and a 1 µs sensor exposure.

Several tests were carried out in order to achieve a correct optical path alignment. Nevertheless, it was found that the light beam at the second parabolic mirror focus was not small enough to obtain a schlieren with high spatial resolution. However, the proposed

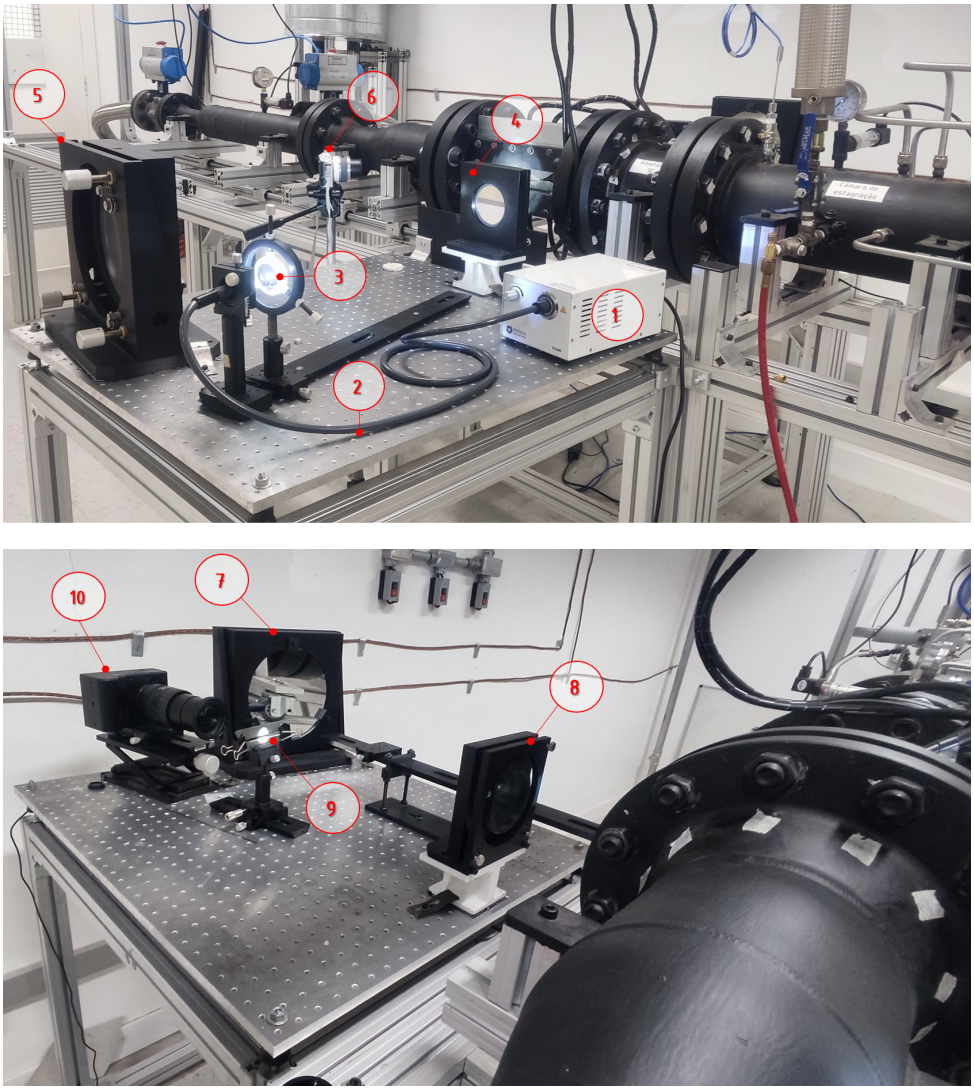

Figure 5.20 – Schlieren arrengment, ① Light source, ② optical fibre, ③ condensing lens, ④ flat mirror, ⑤ parabolic mirror, ⑥ direct still picture camera, ⑦ parabolic mirror, ⑧ flat mirror, ⑨ knife edge, ⑩ high-speed camera.

arrangement was good enough to capture the Mach lines and shock waves emission and propagation.

Finally, the stagnation chamber and nozzle instrumentation calibration procedure is presented in the Appendix H, and it will be used in the next chapter.

5.5 First tests results

After assembling all test-rig components and performing the hydrostatic test (40 bar by 1 h), it was performed the initial test. Nevertheless, after analysing the pressure profile results it was found that the nozzle did not achieve the supersonic flow regime. After opening the test-rig, it was found that the supersonic nozzle gasket at the nozzle outlet flange expanded due to the bolt tightening and created a secondary throat. So, all

the nozzle gaskets were changed to avoid this problem. In addition, it was performed a test to check the pressure regulation valve response and the stagnation temperature behaviour during a test as presented in Fig. 5.21. This figure shows the good valve response, which holds the testing pressure (10 bar) along the test. Also, one can notice the stagnation temperature behaviour, which initially is at an equilibrium temperature of 19 °C an as the flow starts its value increases due to the higher fluid temperature inside the tank, nevertheless as the flow expansion occurs it decreases.

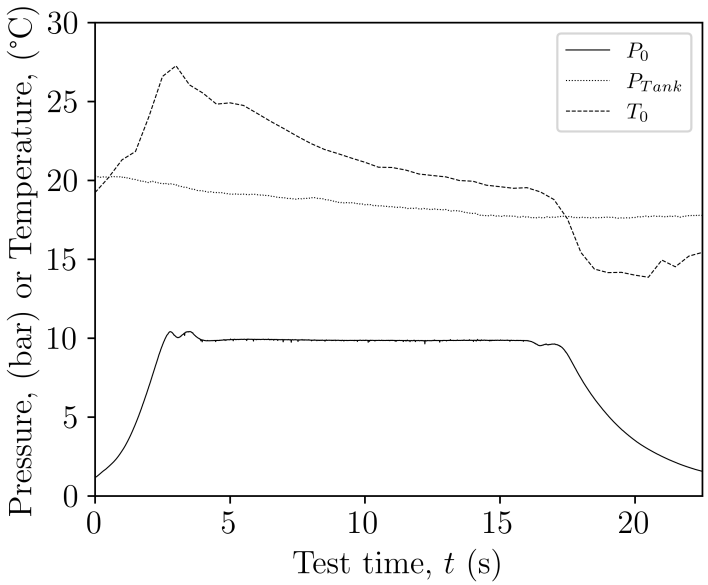

Figure 5.21 – Typical test, tank pressure and stagnation temperature and pressure behaviour during a test.

Afterwards, several tests were carried out. However, it was found that nozzle 1 was unable to achieve a complete supersonic flow, and a shock train was occurring inside the nozzle as presented in Fig. 5.22 for nozzle 1 for a $P_0 = 6$ bar, $T_0 = 293.5$ K and dry air. The discharge hoses were disconnected at the nozzle outlet, and it was found that the high mass flow-rate produced by nozzle 1 throat created high pressure losses in piping, hoses and silencers located at the nozzle downstream. Such pressure losses acted as a partially closed valve, and this generated a shock wave train inside the divergent nozzle section. So, in order to circumvent this problem, a new profile was designed (Profile 2) with a nozzle throat width of 5 mm which resulted in a reduction of the mass flow-rate compared to nozzle 1 and a subsequent reduction of the downstream pressure losses. Fig. 5.23 presents the results obtained for the new profile and after installing again the discharge hoses and piping. It was found an excellent match against the perfect gas theory after evaluating the theoretical pressure ratio at the nozzle throat 0.529 vs 0.528, for the experimental and the perfect gas theory respectively. Nevertheless, it was not achieved a complete supersonic shock free flow, however, the maximum achieved supersonic theoretical Mach number (2.2) is high enough for supersonic condensation evaluation purposes. In addition, these first

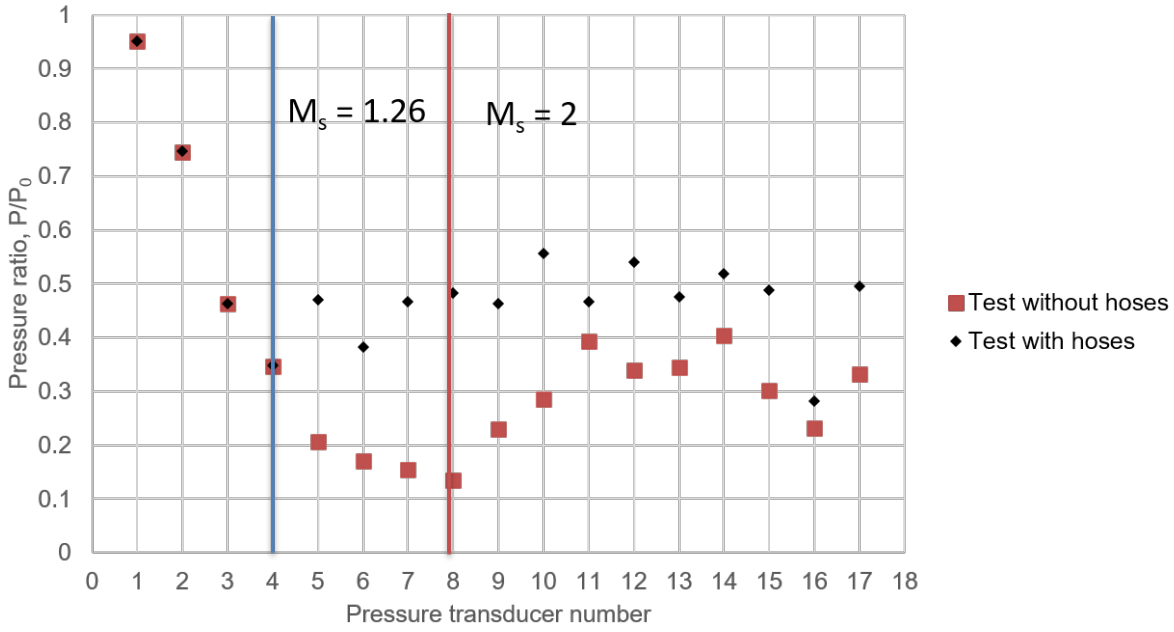

Figure 5.22 – First tests pressure profile nozzle 1, dry air $P_0 = 6$ bar, $T_0 = 293.5$.

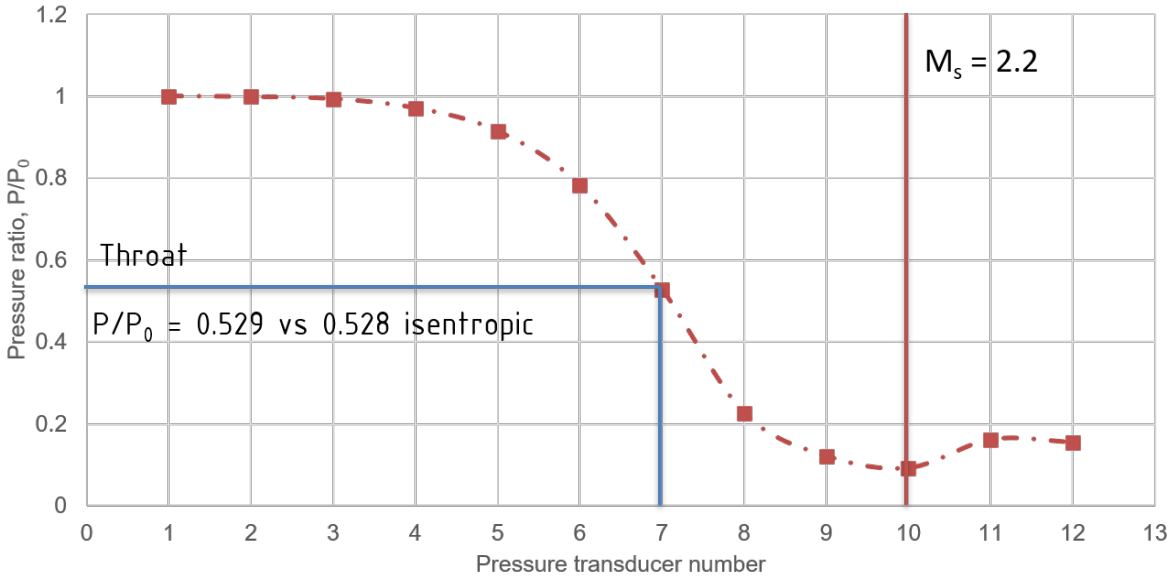

Figure 5.23 – First tests pressure profile nozzle 2, dry air $P_0 = 6$ bar, $T_0 = 295.3$.

tests were also used to assess the dry air quality, because the corresponding temperature ratio for the maximum Mach number is $T/T_0 = 0.5081$, therefore, if there is any trace of water vapour, it should condense at such low temperature ratio.

5.6 Test rig Operation checklist

After describe the test-rig design and construction, the checklist required for its operation is presented:

1. Turn on secondary compressed air line (purge water from the tank under lab stairs, if necessary) ☐
2. Connect data acquisition system to the electrical power ☐
3. Review all flange and nozzle window cover bolts (The bolts must be tight) ☐
4. Close stagnation chamber venting valves. ☐
5. Check if the spring installed in the pressure regulating valve corresponds to the test pressure ☐
6. **Put security glasses and hearing protectors on** ☐
7. Pressurize the test-rig by opening the V1 valve ☐
8. Close valve V1 ☐
9. Regulate the pressure valve to the test pressure ☐
10. Calibrate the CO_2 gas analyser (see device manual to perform the procedure) ☐
11. Measure and record the molar carbon dioxide fraction ☐
12. Measure and record barometric pressure ☐
13. Measure and record room temperature ☐
14. Turn on the lab ventilation system ☐
15. Open the labview routine for the test control and recording ☐
16. Turn on the high-speed camera ☐
17. Start writing the test data from the labview interface ☐
18. Open valve V1 ☐
19. Open valve V2 ☐
20. Open valve V3 ☐

21. Stop recording data ☐
22. Close valve V3 ☐
23. Close valve V1 ☐
24. Close valve V2 when a pressure of two bar is achieved. ☐
25. Measure and record the molar carbon dioxide fraction ☐
26. Open valve V2 for test-rig depressurizing ☐
27. Close valve V2 ☐

6 Experimental results and analysis

After designing, mounting and commissioning the experimental test rig, a series of tests were performed in order to assess the carbon dioxide supersonic condensation, and to reveal the nozzle supersonic channel geometry effects on the condensation characteristics.

The data were obtained after setting different CO_2 concentration fractions in the mixture tank. Once the tank concentration was homogenous the regulation valve was setted to the maximum operation pressure through the regulation pressure valve. Short duration test time (3 - 10 s) was established for each test in order to keep enough stagnation pressure for the following tests, and also to reduce the CO_2 concentration change along the experiment. The data were collected with a 10000 sample per second rate.

Table 6.1 summarizes selected test results achieved with the developed test-rig. This table shows the stagnation conditions (pressure, temperature and concentration), being the concentration calculated as the average value of the outcomes obtained before and after of each test. In addition, Table 6.1 presents the environmental atmospheric pressure and temperature.

Due to the method of characteristic use for the nozzle designing, this nozzle exhibits different flow regimes as a function of the nozzle wall shape variation, which resulted in different condensation shock topologies, which can be classified as follows:

- Classical: The iso-Mach line that drives the condensation shock follows the conventional topology, as reported by several authors on the literature, being the more relevant the work presented by Lettieri et al. (2018) and Schnerr (1988).
- Transition: Due to effects of the nozzle wall construction by the method of characteristics, the wall profile start to cancel out the expansion waves emanated from the nozzle kernel, hence, in this transition region the condensation shock achieves a different topology due to the cancellation wave process.

- Mach wave: In this classification, the condensation shock behaves as a Mach wave, once the condensation shock starts and propagates to the downstream flow section.

Fig. 6.1 presents all aforementioned flow regimes, for a typical convergent-divergent supersonic nozzle. In order to facilitate the interpretation of the results this chapter evaluates the outcome of the more relevant tests (bold rows in Table 6.1), which will be presented in the following sections. The complete set of results are included in the Appendix I.

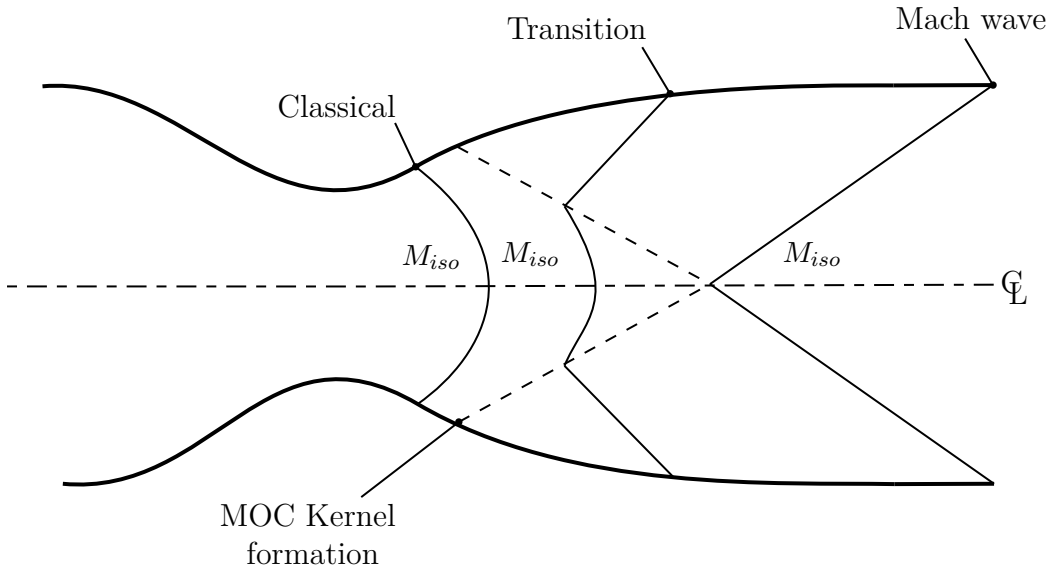

Figure 6.1 – Supersonic flow regimes evaluated.

6.1 Classical condensation shock

As presented in Fig. 6.1 the classical flow regime, consists in achieving a traditional iso-Mach line on the nozzle that starts at the nozzle wall and achieves a maximum x offset at the nozzle centreline. Experimental results reported in Fig. 6.2 for the Test 38 A illustrates clearly this regime. Fig. 6.2a presents a still Schlieren picture of the nozzle divergent part (flow from left to right), due to the CO_2 phase-change process the light rays cannot pass through the fog and appears as a black region in the picture. In order to assess the condensation shock starting point, the Fig. 6.2a was computationally processed in order to retrieve the gray pixel intensity along the nozzle centreline. Fig. 6.2b presents a plot with this information. The criteria used to define the condensation shock start point was to find the point where the trend of the pixel intensity starts to decrease, and if this value achieves a lower value than the points located at the upstream nozzle side, one can consider that the condensation shock starts there. Fig. 6.2c presents the pressure profile at the nozzle walls and compares it against the condensation shock starting point obtained by optical means. Also it was compared against an isentropic quasi-one dimensional expansion.

Table 6.1 – Supersonic condensation tests

Test	Optical System	Video file	P_0 (bar)	T_0 (°C)	T_{env} (°C)	P_{atm} (kPa)	$\bar{x}_{CO_2}$ 1	$\bar{x}_{CO_2}$ 2	$\bar{x}_{CO_2}$ average	Shock Topology
21 A	**Schlieren**	**test21.mp4**	**22.2**	**23.0**	**21.5**	**93.84**	**0.134**	**0.138**	**0.136**	**Transition**
22 A	Direct	test22.mp4	23.87	27.9	21.5	93.84	0.134	0.135	0.135	Mach wave
22 B	Direct	test22.mp4	24.57	24.1	21.5	93.84	0.134	0.135	0.135	Transition
23 A	Direct	test23.mp4	26.74	24.9	21.5	93.84	0.128	0.128	0.128	Transition
23 B	Direct	test23.mp4	26.82	22.5	21.5	93.84	0.128	0.128	0.128	Transition
24 A	Schlieren	test24.mp4	26.21	26.5	21.5	93.84	0.126	0.126	0.126	Mach wave
24 B	Schlieren	test24.mp4	26.23	23.3	21.5	93.84	0.126	0.126	0.126	Transition
25 A	Direct	test25.mp4	26.96	26.0	20.5	93.84	0.100	0.097	0.098	Mach wave
25 B	Direct	test25.mp4	27.08	23.5	20.5	93.84	0.100	0.097	0.098	Transition
26 A	**Schlieren**	**test26.mp4**	**24.47**	**25.3**	**20.5**	**93.84**	**0.097**	**0.083**	**0.090**	**Mach wave**
27 A	Schlieren	test27.mp4	18.53	24.9	20.5	93.84	0.101	0.102	0.101	Mach wave
28 A	Direct	test28.mp4	18.44	23.9	20.5	93.84	0.101	0.097	0.099	Mach wave
30 A	**Schlieren**	**test30.mp4**	**10.28**	**23.3**	**20.5**	**93.84**	**0.097**	**0.096**	**0.097**	**NA**
31 A	**Schlieren**	**test31.mp4**	**26.8**	**28.8**	**20.5**	**93.84**	**0.268**	**0.265**	**0.267**	**Transition**
31 B	**Schlieren**	**test31.mp4**	**27.41**	**24.6**	**20.5**	**93.84**	**0.268**	**0.265**	**0.267**	**Conventional**
32 A	Direct	test32.mp4	26.95	26.6	20.5	93.84	0.268	0.252	0.260	Transition
33 A	Direct	test33.mp4	18.88	26.3	20.5	93.84	0.252	0.238	0.245	Transition
34 A	Schlieren	test34.mp4	19.42	24.6	20.5	93.84	0.238	0.225	0.232	Transition
36 A	Direct	test36.mp4	9.68	22.0	20.5	93.84	0.223	0.209	0.216	Mach wave
38 A	**Schlieren**	**test38.mp4**	**25.65**	**21.4**	**20.5**	**93.84**	**0.328**	**0.324**	**0.326**	**Conventional**

In both figures Fig. 6.2b, and c the nozzle throat position was established as the zero coordinate. Finally, Fig. 6.2d presents the stagnation P_0, throat P_{th}, exit absolute pressure P_e and stagnation temperature T_0 time profile during the test operation. It is important to highlight from this figure the good pressure adjustment performed by the pressure regulation valve, as seen in the P_0 and P_{th} pressure profiles. However, the P_e presents an unsteady behaviour due the oblique shock formation and dissipation at the nozzle outlet. One of the more important remarks of this test is the good match of the condensation shock starting position, between the optical approach and the pressure profile deviation against the isentropic expansion.

6.2 Transition condensation shock

As stressed out in the previous section, the transition condensation shock is formed by the expansion wave cancellation procedure performed by the method of characteristics as shown in Fig. 6.1. Figs. 6.4 Test 21 and 6.5 Test 31 present the more representative experimental test results that exhibit such a feature. For the three cases it was performed the same analysis previously shown in section 6.1. However, due to the stagnation temperature variation in the Test 31, it was decided to perform two different analysis for the same test run. The left side of the Fig. 6.5 (Test 31 A) presents the test at the start of the high speed video camera and acquisition data system recording $t = 0$ s, and the right side (Test 31 B) the acquired data at $t = 4.5$ s. In all the three cases one can perceive that the condensation shock starts as previously shown in Fig. 6.1. Therefore, the topology of the condensation shock depends on the expansion wave propagation and cancellation due to the nozzle wall reflection. Moreover, after analysing Figs. 6.4a and 6.5a, d one can observe a clearer region at the nozzle core, and this occurs due to the expansion waves cancellation procedure, because as presented in Fig. 6.3, the droplet produced by the condensation shock follows the streamline angle θ produced by the method of characteristics, generating a darker area on the nozzle wall neighbour region and a subsequent droplet density separation, because the darker area represents a rich droplet region.

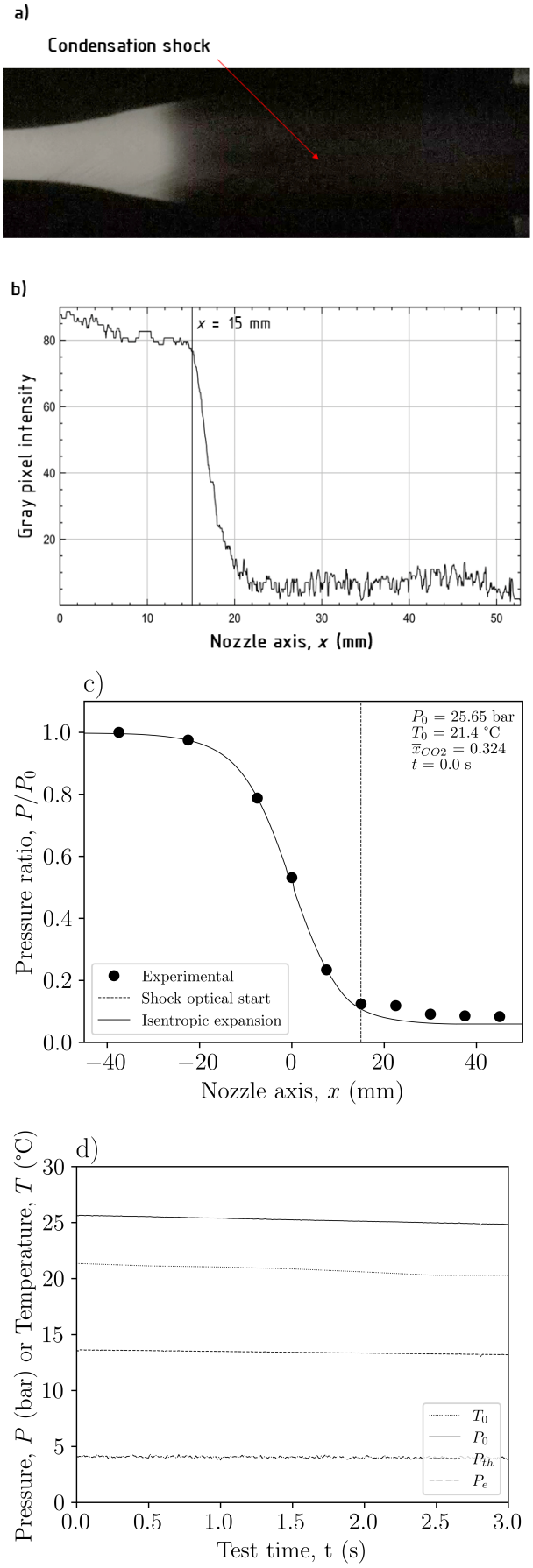

Figure 6.2 – Test 38 results a) Supersonic channel schlieren still picture, b) Nozzle pressure profile for a $t = 0$ s, c) Stagnation P_0, throat P_{th}, exit pressure P_e and stagnation temperature T_0 test evolution.

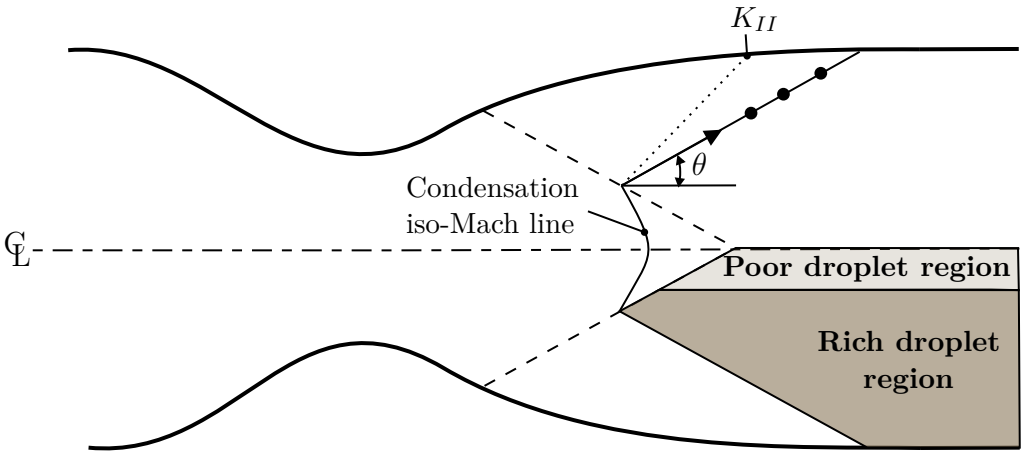

Figure 6.3 – Droplet separation on the transition regime.

Additionally, other pieces of information can be drawn from Fig. 6.4a, because of the interaction of the oblique condensation shock waves with the two-phase fluid. Due to the over-expanded nozzle operation, there are several oblique shock waves at the nozzle outlet, which produces a pressure and temperature increase, resulting in a local phase change. Nevertheless, due to the shock diamond structure, an expansion wave is created and this originates a secondary condensation shock. All of that can be tracked by the nozzle centreline pixel intensity presented in Fig. 6.4b.

6.3 Mach wave condensation shock

Figure 6.6 presents a Mach wave condensation shock topology, if the condensation shock is located downstream of the nozzle kernel region, the condensation shock will behave as a Mach wave due to the wall cancellation process as the perturbation created by the nozzle wall cannot be "sensed" by the flow and it will expand as a Mach wave starting from the maximum Mach point (Located at the centreline). One important feature of this kind of condensation shock is the x offset distance between the pressure profile and the optical shock position, which achieves a value of 13 mm for this case.

In the last sections, it was presented the condensation shock experimental topologies achieved in this work development. However, it is also important to highlight the nozzle behaviour in the absence of condensation shocks, this case is presented in Fig. 6.7 (Test 30 A). This nozzle result cannot achieve the condensation shock, and therefore the pressure rise produced by the shock is not presented. This implies in a substantial change in the nozzle operation behaviour, because due to the absence of the pressure rise, the nozzle cannot achieve the required pressure to keep a normal shock wave at the nozzle exit. Consequently, the pressure shock wave is formed inside the nozzle, as presented in Fig. 6.7a, and this results in an important change in the pressure profile 6.7b compared to previous cases.

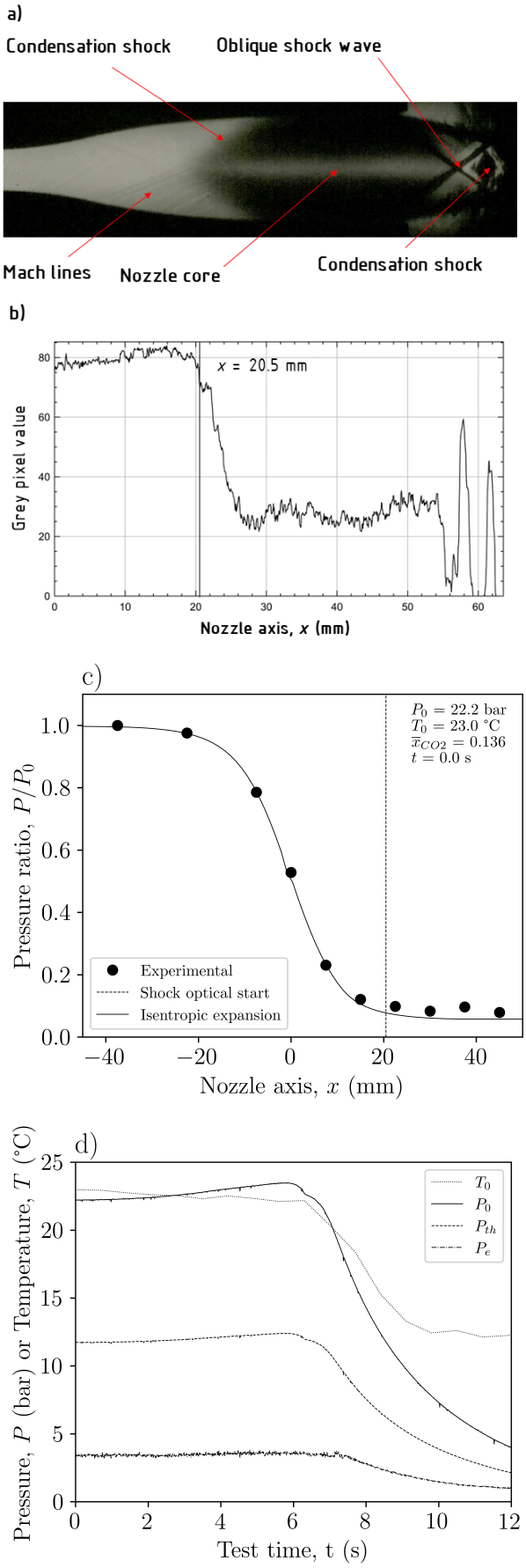

Figure 6.4 – Test 21 results, a) Supersonic channel schlieren still picture b) Nozzle centre-line grey pixel intensity, c) Nozzle pressure profile for a $t = 0$ s, d) Stagnation P_0, throat P_{th}, exit pressure P_e and stagnation temperature T_0 test evolution.

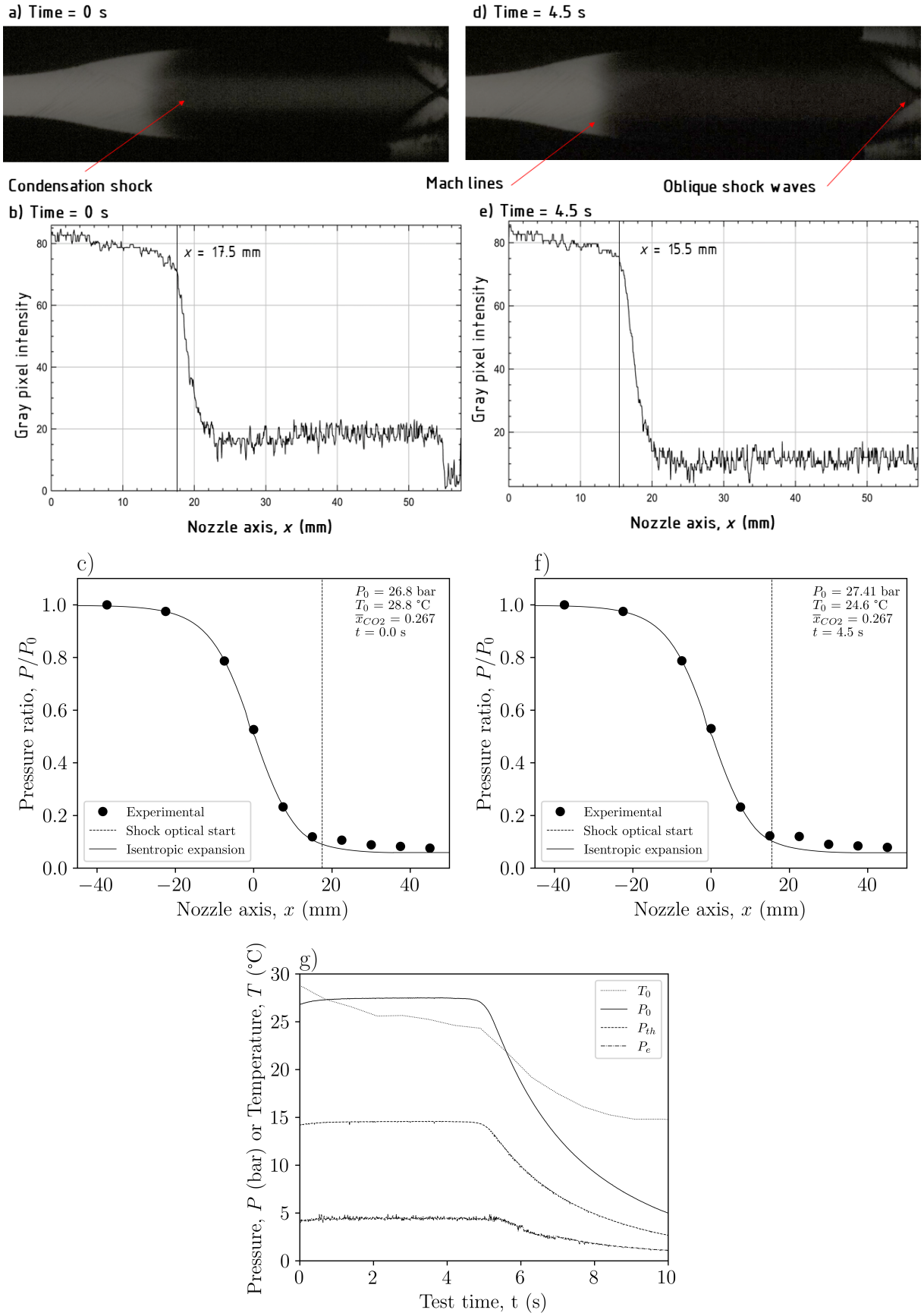

Figure 6.5 – Test 31 results, left $t = 0$ s and right $t = 4.5$ s. a and b) Supersonic channel schlieren still picture, c and d) Nozzle centreline grey pixel intensity, e and f) Nozzle pressure profile and g) Stagnation P_0, throat P_{th}, exit pressure P_e and stagnation temperature T_0 test evolution.

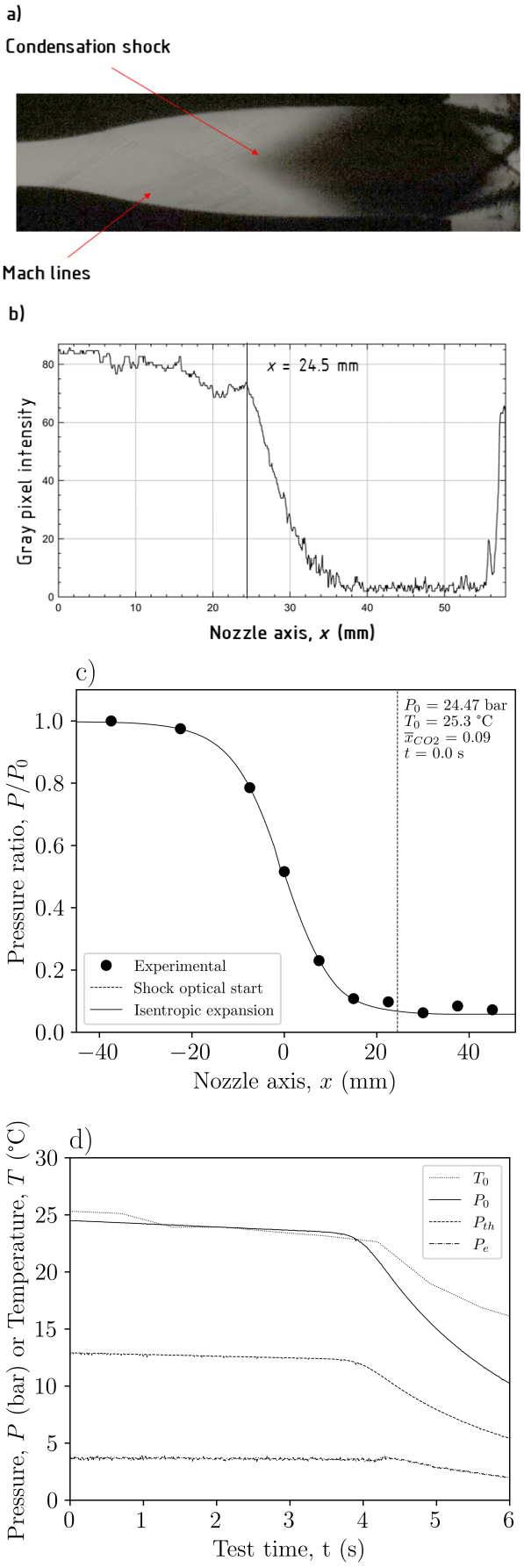

Figure 6.6 – Test 26 results, a) Supersonic channel schlieren still picture b) Nozzle centre-line grey pixel intensity, c) Nozzle pressure profile for a $t = 0$ s, d) Stagnation P_0, throat P_{th}, exit pressure P_e and stagnation temperature T_0 test evolution.

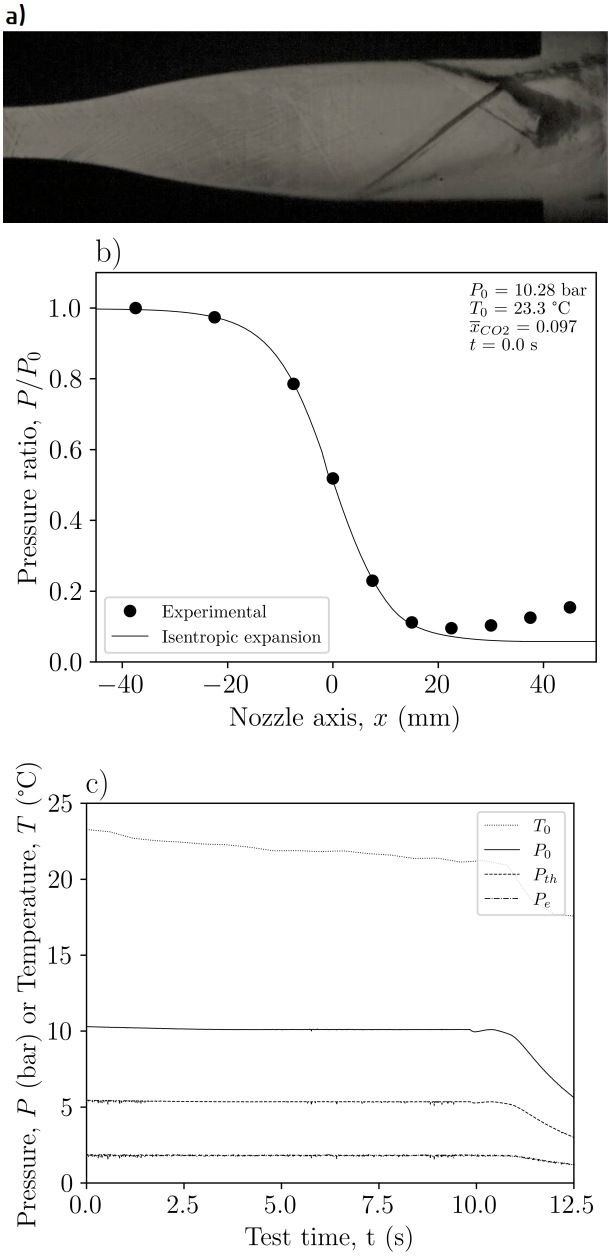

Figure 6.7 – Test 30 results, a) Supersonic channel schlieren still picture, b) Nozzle pressure profile for a $t = 0$ s, c) Stagnation P_0, throat P_{th}, exit pressure P_e and stagnation temperature T_0 test evolution.

6.4 Condensation shock theory validation

6.4.1 Critical nucleation rate criteria

After analysing the more important results of the experimental evaluation, the collected data were used for the validation of this thesis proposed theoretical models. The first model analysed was the condensation shock starting point computation. This model was established under the hypothesis that the carbon dioxide condensation will start once the supersonic expansion achieves a critical nucleation rateJ_{crt} value. Fig. 6.8

presents a comparison between experimental data and the proposed model. One can perceive a fair adjustment to the proposed model ($\pm 5\%$) for a $J_{crt} = 1 \times 10^{10}$ m^{-3}s^{-1}. However, the critical nucleation approach fails to be a universal criterion, because the characteristic critical nucleation rate found for the Bier et al. (1990a) nozzle as presented in subsection 4.3.8 ($J_{crt} = 1 \times 10^{22}$ m^{-3}s^{-1}) is not valid for our current tests, because, as exposed by Luijten (1998b), the nucleation rate can exhibit several order of deviation after comparing the theoretical approach against experimental results. Nevertheless, note that results exposed in Table 6.1 cover a wide stagnation concentration and pressure range, and different condensation shock topologies, therefore the critical nucleation rate criteria can be used for constrained operational regions. In addition, Table 6.2 lists the Mach numbers and temperatures achieved at the condensation shock start from for a $J_{crt} = 1 \times 10^{10}$ m^{-3}s^{-1}. It is clear the condensation was achieved for $M > 2$values, which results in low phase-change temperatures.

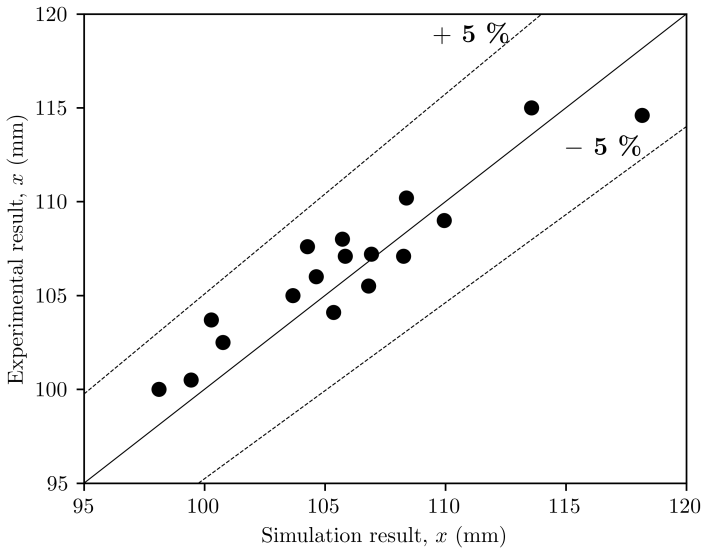

Figure 6.8 – Condensation shock starting position for $J_{crt} = 1 \times 10^{10}$ m^{-3}s^{-1}.

Table 6.2 – Mach numbers and temperatures at the condensation shock start.

Test	M	T (K)
21 A	2.35	141.3
22 A	2.39	141.5
22 B	2.33	143.0
23 A	2.33	143.5
23 B	2.30	144.2
24 A	2.36	142.3
24 B	2.32	143.2
25 A	2.42	138.0
25 B	2.39	138.6
26 A	2.47	134.7
27 A	2.52	131.7
28 A	2.52	131.5
31 A	2.14	159.7
31 B	2.08	161.7
32 A	2.12	159.9
33 A	2.27	149.4
34 A	2.26	149.4
36 A	2.49	133.9
38 A	2.00	166.5

6.4.2 Continuous condensation shock theory

Figures 6.9 a,b and c present the results of the continuous condensation shock simulation results for tests 31 A, 31 B and 38 A. All the evaluated tests were found a good agreement against the theory presented in subsection 4.3.4. However, it was found that this approach can not be used for condensation shocks with a Mach wave topology at high speeds as exposed in the test 26 A, because this method was unable to find the solution after considering the detonation solution from the Rankine-Hugoniot relations. That happens because for high Mach numbers $M > 2.3$ the detonation solution presents a high entropy jump ds value, in addition the Mach wave is presented where the nozzle dA/dx is small, and after inspecting Eq. 4.71 numerator one can perceive that the velocity derivative will grow negatively, causing a steep pressure rise.

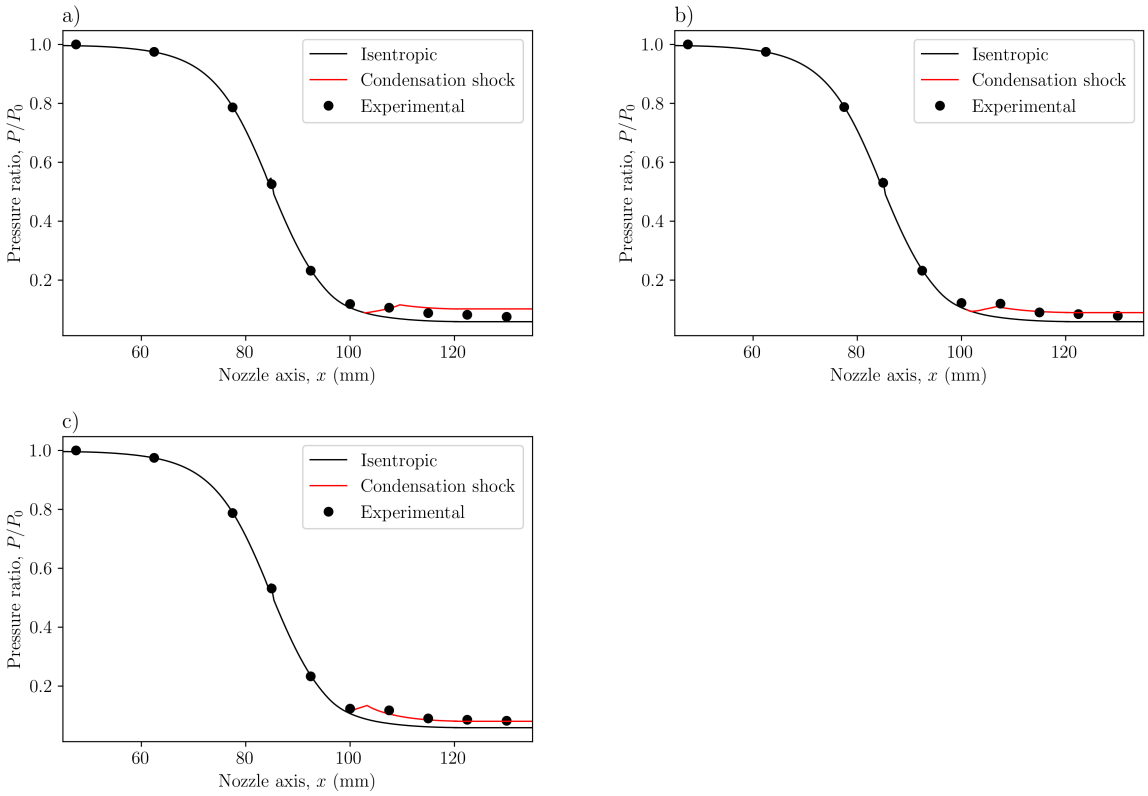

Figure 6.9 – Continuous condensation shock theory comparison, a) Test 31 A, b) Test 31 B and c) Test 38 A.

7 Conclusions and future works

This thesis addresses the supersonic carbon dioxide condensation phenomena from an experimental and theoretical point of view, which results in new theoretical and experimental approaches. For all of them, it was developed a robust thermodynamic framework using a state-of-the-art equation of state. In order to facilitate the conclusion presentation, the conclusions are presented in two different categories (theoretical and experimental), as listed below:

Theoretical:

- It was found the vital role of the Grüneisen parameter on the viscous effects, and also it was evidenced that there is a physical threshold for the supersonic flow formation in viscous nozzle flows. This is relevant for supersonic gas separators preliminary design.
- The role of the viscous potential on the supersonic nozzle flows was revealed.
- The continuous condensation shock approach gives good results as long as the specific entropy shock is not too high compared to the area change ratio. Otherwise, if $GrT_m c_m^{-2}\Phi >> A^{-1}dA/dx$ the maximum entropy approach is not suitable.
- It was found that real gas maximum specific entropy jump for a weak shock gives good results for the pure substance condensation shock analysis.
- After implementing the method of characteristics it was found the relevance of the speed-of-sound variation (measured through the fundamental gas-dynamic derivative Γ) and the EOS selection effect on the nozzle wall construction.

Experimental:

- It was found that a nozzle wall constructed by the method of characteristics means is not quite sensible to the stagnation conditions variation, namely: pressure and CO_2 molar concentration.
- After using the developed optical methods it was found three condensation shock topologies, namely: Classical, transition and Mach wave condensation shock.
- It was shown that the condensation shock does not necessarily start at the nozzle wall, as previously reported in the open literature, e.g (Schnerr, 1996).
- It was found that the critical nucleation ratio could be used for similar operating conditions. Nevertheless, it fails as a universal criterion for the calculation of the condensation shock starting conditions as observed after comparing the experimental findings to the experimental work of Bier et al. (1990a).
- It was found by optical means that the method of characteristic itself could be used for separation purposes.
- After evaluating test case 30, it was found that the condensation shock avoids the aerodynamic shock formation inside the nozzle. Therefore, small condensible vapour fractions injection can be used as an operational strategy for nozzle operation, in conditions where the stagnation parameters (P_0 and T_0) and the outlet pressure P_e must remain constant.

Finally, the recommendation for future works will be presented for the theoretical and experimental section:

Theoretical recommendations:

- To evaluate the interaction of swirling flows on a nozzle constructed through the method of characteristics.
- To formulate a dimensional analysis in order to find a universal critical nucleation ratio, as a function of the nozzle wall geometry variation rate and the stagnation conditions.
- To use the method of characteristic for designing curved collectors in order to increase the efficiency of the supersonic separation process.

Experimental recommendations:

- To evaluate by experimental means the mechanical separation efficiency of supersonic separators.

- To install two additional 2” high-pressure hoses with their corresponding silencers, to decrease the pressure losses at the nozzle downstream section.
- To design a supersonic diffuser at the nozzle outlet in order to decrease the stagnation pressure losses and achieve a completely supersonic flow at the nozzle divergent section.
- To propose a correlation between the pressure regulate springs compression length and the setting pressure, for facilitating the test-rig operation.
- To use optical quantitative techniques as the background oriented schlieren, or interferometry for the purpose of extracting more information from the fluid field.
- To perform an inverse analysis from the oblique shock waves formed at the nozzle outlet, in order to assess the nozzle outlet quality, velocity and specific entropy.
- From the Mach wave condensation shock compute the Mach number at the beginning of the condensation shock.
- To explore the use of collectors for the effective separation of the particles separated by the method of characteristics.
- To evaluate the carbon dioxide phase change at transonic speeds.

Bibliography

Abbott, M. M.; Van Ness, H. C. H. C. *Schaum's outline of theory and problems of thermodynamics*. 2. ed. : McGraw-Hill, 1989. 362 p. ISBN 0070000425.

Abraham, F. F. *Homogeneous Nucleation Theory*. : Elsevier, Academic Press, 1974. ISBN 978-0-12-038361-0.

Acosta, A. F. B. *Two approximations for solving non-equilibrium condensation shocks in supersonic nozzle flows*. Dissertação (Mestrado) — Escola Politécnica, 2022.

Aidoun, Z.; Ameur, K.; Falsafioon, M.; Badache, M. Current Advances in Ejector Modeling, Experimentation and Applications for Refrigeration and Heat Pumps. Part 1: Single-Phase Ejectors. *Inventions*, Multidisciplinary Digital Publishing Institute, v. 4, n. 1, p. 15, Mar 2019. ISSN 2411-5134.

Aldo, A. C.; Argrow, B. M. Dense Gas Flow in Minimum Length Nozzles. *J. Fluids Eng.*, American Society of Mechanical Engineers Digital Collection, v. 117, n. 2, p. 270–276, Jun 1995. ISSN 0098-2202.

Anderson, J. D. *Modern compressible flow : with historical perspective*. : McGraw-Hill, 1990. 650 p. ISBN 0070016739.

Argrow, B. M.; Emanuel, G. Comparison of Minimum Length Nozzles. *J. Fluids Eng.*, American Society of Mechanical Engineers Digital Collection, v. 110, n. 3, p. 283–288, Sep 1988. ISSN 0098-2202.

Argrow, B. M.; Emanuel, G. Computational Analysis of the Transonic Flow Field of Two-Dimensional Minimum Length Nozzles. *J. Fluids Eng.*, American Society of Mechanical Engineers Digital Collection, v. 113, n. 3, p. 479–488, Sep 1991. ISSN 0098-2202.

Arina, R. Numerical simulation of near-critical fluids. *Appl. Numer. Math.*, North-Holland, v. 51, n. 4, p. 409–426, Dec 2004. ISSN 0168-9274.

Aursand, P.; Gjennestad, M. A.; Aursand, E.; Hammer, M.; Wilhelmsen, Ø. The spinodal of single- and multi-component fluids and its role in the development of modern equations of state. *Fluid Phase Equilibria*, Elsevier, v. 436, p. 98–112, mar 2017. ISSN 0378-3812. Available on: <https://www.sciencedirect.com/science/article/pii/S0378381216306227>.

Bakhtar, F.; Zidi, K. Nucleation Phenomena in Flowing High-Pressure Steam: Experimental Results. *Proceedings of the Institution of Mechanical Engineers, Part A: Journal of Power Engineering*, SAGE Publications, v. 203, n. 3, p. 195–200, ago. 1989. ISSN 0954-4046.

Baladao, L. *Avaliação da Equação de Estado GERG- 2008 para o Gás Natural*. 148 p. Tese (Doutorado) — Federal university of Rio Grande do Sul, 2015.

Beans, E. W. Computer solution to generalized one- dimensional flow. *Journal of Spacecraft and Rockets*, v. 7, n. 12, p. 1460–1464, 1970.

Beegle, B. L.; Modell, M.; Reid, R. C. Thermodynamic stability criterion for pure substances and mixtures. *AIChE Journal*, John Wiley & Sons, Ltd, v. 20, n. 6, p. 1200–1206, nov 1974. ISSN 0001-1541. Available on: <http://doi.wiley.com/10.1002/aic.690200621>.

Bell, I. H.; Jäger, A. Calculation of critical points from Helmholtz-energy-explicit mixture models. *Fluid Phase Equilibria*, Elsevier, v. 433, p. 159–173, feb 2017. ISSN 0378-3812. Available on: <https://www.sciencedirect.com/science/article/pii/S0378381216305349>.

Bell, I. H.; Wronski, J.; Quoilin, S.; Lemort, V. Pure and pseudo-pure fluid thermophysical property evaluation and the open-source thermophysical property library coolprop. *Industrial and Engineering Chemistry Research*, v. 53, n. 6, p. 2498–2508, 2014. ISSN 08885885. Available on: <https://pubs.acs.org/doi/10.1021/ie4033999.>

Beltrao, R. L. C.; Leite, S. C.; V.M., L. A. C.; Fagundes, N. J. R.; Dias, H. C. C. SS: Pre-salt Santos basin - Challenges and New Technologies for the Development of the Pre-salt Cluster, Santos Basin, Brazil. In: *Offshore Technology Conference*. Offshore Technology Conference, 2009. Available on: <http://www.onepetro.org/doi/10.4043/19880-MS>.

Besagni, G.; Inzoli, F. Computational fluid-dynamics modeling of supersonic ejectors: Screening of turbulence modeling approaches. *Appl. Therm. Eng.*, Pergamon, v. 117, p. 122–144, May 2017. ISSN 1359-4311.

Bianchi, G.; Besagni, G.; Tassou, S. A.; Markides, C. N. Overview and outlook of research and innovation in energy systems with carbon dioxide as the working fluid. *Appl. Therm. Eng.*, Pergamon, v. 195, p. 117180, Aug 2021. ISSN 1359-4311.

Bier, K.; Ehrler, F.; Niekrawietz, M. Experimental Investigation and Computer Analysis of Spontaneous Condensation in Stationary Nozzle Flow of CO2-Air Mixtures. In: *Adiabatic Waves in Liquid-Vapor Systems*. Berlin, Germany: Springer, 1990. p. 113–127. ISBN 978-3-642-83589-6.

Bier, K.; Ehrler, F.; Theis, G. Spontaneous Condensation in Stationary Nozzle Flow of Carbon Dioxide in a Wide Range of Density. In: *Adiabatic Waves in Liquid-Vapor Systems*. Berlin, Germany: Springer, 1990. p. 129–141.

Bird, R.; Stewart, W.; Lightfoot, E. *Transport Phenomena*. : J. Wiley, 2002. ISBN 9780471364740.

Blythe, P. A.; Shih, C. J. Condensation shocks in nozzle flows. *Journal of Fluid Mechanics*, v. 76, n. 3, p. 593–621, 1976. ISSN 14697645.

Bolaños-Acosta, A. F.; Restrepo, J. C.; Simões-Moreira, J. R. Two semi-analytical approaches for solving condensation shocks in supersonic nozzle flows. *Int. J. Heat Mass Transfer*, Pergamon, v. 173, p. 121212, Jul 2021. ISSN 0017-9310.

Boltachev, G. S.; Baidakov, V. G. The thermodynamic properties of nitrogen, argon, oxygen, and their mixtures in the region of the liquid-gas phase transition. *Russian Journal of Physical Chemistry*, v. 80, n. 4, p. 501–504, apr 2006. ISSN 0036-0244. Available on: <http://link.springer.com/10.1134/S0036024406040030>.

Bufi, E.; Cinnella, P. Preliminary design method for dense-gas supersonic axial turbine stages. *Journal of Engineering for Gas Turbines and Power*, v. 140, 03 2018.

Buresti, G.; Casarosa, C. One-dimensional adiabatic flow of equilibrium gas–particle mixtures in long vertical ducts with friction. *J. Fluid Mech.*, Cambridge University Press, v. 203, p. 251–272, Jun 1989. ISSN 1469-7645.

Butt, H.; Graf, K.; Kappl, M. *Physics and Chemistry of Interfaces*. Wiley, 2003. ISBN 9783527404131. Available on: <https://onlinelibrary.wiley.com/doi/book/10.1002/3527602313>.

Bücker, D.; Wagner, W. Reference Equations of State for the Thermodynamic Properties of Fluid Phase n-Butane and Isobutane. *J. Phys. Chem. Ref. Data*, American Institute of Physics, v. 35, n. 2, p. 929–1019, Jun 2006. ISSN 0047-2689.

Campagna, M. M.; Hrubý, J.; Dongen, M. E. H. van; Smeulders, D. M. J. Homogeneous water nucleation: Experimental study on pressure and carrier gas effects. *J. Chem. Phys.*, American Institute of Physics, v. 153, n. 16, p. 164303, out. 2020. ISSN 0021-9606.

Cao, X.; Bian, J. Supersonic separation technology for natural gas processing: A review. *Chem. Eng. Process. Process Intensif.*, Elsevier, v. 136, p. 138–151, Feb 2019. ISSN 0255-2701.

Cao, X.; Yang, W. The dehydration performance evaluation of a new supersonic swirling separator. *Journal of Natural Gas Science and Engineering*, Elsevier B.V, v. 27, p. 1667–1676, 2015. ISSN 18755100. Available on: <http://dx.doi.org/10.1016/j.jngse.2015.10.029>.

Carey, V. P. *Liquid Vapor Phase Change Phenomena*. 2. ed. : Taylor and Francis, 1992. 399–452 p. ISBN 1591690358.

Chang, P.; Bai, B. An improved method of gas well deliquification using supersonic nozzle. *International Journal of Heat and Mass Transfer*, Elsevier Ltd, v. 108, p. 2262–2272, 2017. ISSN 00179310. Available on: <http://dx.doi.org/10.1016/j.ijheatmasstransfer.2017.01.054>.

Chapra, S. C.; Canale, R. P. *Numerical Methods for Engineers*. : McGraw-Hill Higher Education, 2010. ISBN 978-007126759-5.

Colonna, P.; Nannan, N. R.; Guardone, A.; Stelt, T. P. van der. On the computation of the fundamental derivative of gas dynamics using equations of state. *Fluid Phase Equilib.*, Elsevier, v. 286, n. 1, p. 43–54, Nov 2009. ISSN 0378-3812.

Cramer, M.; Crickenberger, A. Prandtl-meyer function for dense gases. *AIAA journal*, v. 30, n. 2, p. 561–564, 1992.

Debenedetti, P. G. *Metastable liquids : concepts and principles*. Princenton: Princeton University Press, 1996. 411 p. ISBN 9780691085951. Available on: <https://press.princeton.edu/titles/5912.html>.

Ding, H.; Wang, C.; Chen, C. Non-equilibrium condensation process of water vapor in moist air expansion through a sonic nozzle. *Flow Measurement and Instrumentation*, Elsevier, v. 40, p. 238–246, 2014. ISSN 09555986. Available on: <http://dx.doi.org/10.1016/j.flowmeasinst.2014.08.002>.

Dykas, S.; Wróblewski, W. Single- and two-fluid models for steam condensing flow modeling. *Int. J. Multiphase Flow*, Pergamon, v. 37, n. 9, p. 1245–1253, nov. 2011. ISSN 0301-9322.

d'Almeida, K. S.; C.Vilela, P.; Cardoso, R. A.; Fernandes, R. F.; Souza, M. F. *Ocorrência de CO2 em campos petrolíferos na margem leste brasileira*. 2018.

Elbarghthi, A. F. A.; Mohamed, S.; Nguyen, V. V.; Dvorak, V. CFD Based Design for Ejector Cooling System Using HFOS (1234ze(E) and 1234yf). *Energies*, Multidisciplinary Digital Publishing Institute, v. 13, n. 6, p. 1408, Mar 2020. ISSN 1996-1073.

Emanuel, G. *Advanced Classical Thermodynamics*. American Institute of Aeronautics & Astronautics, 1988. (AIAA Education Series). ISBN 9781600860010. Available on: <https://books.google.com.br/books?id=yK7h9xs_wJgC>.

Emmons, H. W. *Fundamentals of gas dynamics.* : Princeton University Press, 1958. 749 p. ISBN 9780691626499.

Feder, J.; Russell, K. C.; Lothe, J.; Pound, G. M. Homogeneous nucleation and growth of droplets in vapours. *Adv. Phys.*, Taylor & Francis, v. 15, n. 57, p. 111–178, jan. 1966. ISSN 0001-8732.

Ferrari, A. Analytical solutions for one-dimensional diabatic flows with wall friction. *J. Fluid Mech.*, Cambridge University Press, v. 918, Jul 2021. ISSN 0022-1120.

Ferrari, A. Exact solutions for quasi-one-dimensional compressible viscous flows in conical nozzles. *J. Fluid Mech.*, Cambridge University Press, v. 915, May 2021. ISSN 0022-1120.

Garret, L.; Oehlschlager, W, K.; Tomich, J, F. Vapor-Liquid Separation at Supersonic Velocities. *Journal of engineering for industry*, v. 90, n. 4, p. 609–612, 1968.

Gernert, G. J. *A New Helmholtz Energy Model for Humid Gases and CCS Mixtures*. 221 p. Tese (Doutorado) — Ruhr-Universität Bochum, 2013.

Gernert, J.; Span, R. EOS–CG: A Helmholtz energy mixture model for humid gases and CCS mixtures. *J. Chem. Thermodyn.*, Academic Press, v. 93, p. 274–293, Feb 2016. ISSN 0021-9614.

Goodwin, A. R.; Sengers, J.; Peters, C. J. (Ed.). *Applied Thermodynamics of Fluids*. Cambridge: Royal Society of Chemistry, 2010. ISBN 978-1-84755-806-0. Available on: <http://ebook.rsc.org/?DOI=10.1039/9781849730983>.

Goulart, M. B. R. et al. Technology readiness assessment of ultra-deep salt caverns for carbon capture and storage in Brazil. *Int. J. Greenhouse Gas Control*, Elsevier, v. 99, p. 103083, ago. 2020. ISSN 1750-5836.

Guardone, A. Real-gas effects in supercritical carbon dioxide gasdynamic nozzles. *HEFAT 2010*, International Conference on Heat Transfer, Fluid Mechanics and Thermodynamics, 2010.

Guardone, A.; Spinelli, A.; Dossena, V. Influence of Molecular Complexity on Nozzle Design for an Organic Vapor Wind Tunnel. *J. Eng. Gas Turbines Power*, American Society of Mechanical Engineers Digital Collection, v. 135, n. 4, Apr 2013. ISSN 0742-4795.

Guardone, A.; Vimercati, D. Exact solutions to non-classical steady nozzle flows of Bethe–Zel'dovich–Thompson fluids. *J. Fluid Mech.*, Cambridge University Press, v. 800, p. 278–306, Aug 2016. ISSN 0022-1120.

Guha, A. Jump conditions across normal shock waves in pure vapour–droplet flows. *J. Fluid Mech.*, Cambridge University Press, v. 241, p. 349–369, ago. 1992. ISSN 1469-7645.

Guha, A. A unified theory of aerodynamic and condensation shock waves in vapor-droplet flows with or without a carrier gas. *Phys. Fluids*, American Institute of Physics, v. 6, n. 5, p. 1893–1913, maio 1994. ISSN 1070-6631.

Gyarmathy, G. Nucleation of steam in high-pressure nozzle experiments. *Proceedings of the Institution of Mechanical Engineers, Part A: Journal of Power and Energy*, IMECHE, v. 219, n. 6, p. 511–521, Jan 2005. ISSN 0957-6509.

Haghighi, M. *Supersonic separators: a Gas Dehydration Device*. Tese (Doutorado) — Memorial Universtiy of Newfoundland, 2010.

Hodge, B. K.; Koenig, K. *Compressible Fluid Dynamics with Personal Computer Applications*. Upper Saddle River, NJ, USA: Prentice Hall, 1995. ISBN 978-0-13308552-5.

Hoffman, J. D. Approximate analysis of nonisentropic flow in conical nozzles. *Journal of Spacecraft and Rockets*, v. 6, n. 11, p. 1329–1334, 1969. Available on: <https://doi.org/10.2514/3.29824>.

Imaev, S. Z.; Bagirov, L. A.; Borisov, V. E.; Voytenkov, E. V.; Engineering, E. New low temperature process of CO2 recovery from natural gases. In: *SPE Asia Pacific Oil & Gas Conference and Exhibition*. 2014. p. SPE–171427–MS.

Invernizzi, C. M. Prospects of Mixtures as Working Fluids in Real-Gas Brayton Cycles. *Energies*, Multidisciplinary Digital Publishing Institute, v. 10, n. 10, p. 1649, Oct 2017. ISSN 1996-1073.

Invernizzi, C. M.; Ayub, A.; Marcoberardino, G. D.; Iora, P. Pure and Hydrocarbon Binary Mixtures as Possible Alternatives Working Fluids to the Usual Organic Rankine Cycles Biomass Conversion Systems. *Energies*, Multidisciplinary Digital Publishing Institute, v. 12, n. 21, p. 4140, Oct 2019. ISSN 1996-1073.

Jones, O. C. An Improvement in the Calculation of Turbulent Friction in Rectangular Ducts. *J. Fluids Eng.*, American Society of Mechanical Engineers Digital Collection, v. 98, n. 2, p. 173–180, Jun 1976. ISSN 0098-2202.

Kolář, J.; Dvořák, V. Verification of K-ω SST Turbulence Model for Supersonic Internal Flows. *International Journal of Mechanical and Mechatronics Engineering*, v. 5, n. 9, p. 1715–1719, Sep 2011. Available on: <https://publications.waset.org/13952/verification-of-k-o-sst-turbulence-model-for-supersonic-internal-flows>.

Korpela, S. A. *Principles of Turbomachinery, 2nd Edition*. Hoboken, NJ, USA: Wiley, 2019. ISBN 978-1-119-51809-9. Available on: <https://www.wiley.com/en-us/Principles+of+Turbomachinery%2C+2nd+Edition-p-9781119518099>.

Kunz, O.; Wagner, W. The GERG-2008 Wide-Range Equation of State for Natural Gases and Other Mixtures: An Expansion of GERG-2004. *Journal of Chemical & Engineering Data*, American Chemical Society, v. 57, n. 11, p. 3032–3091, nov 2012. ISSN 0021-9568. Available on: <http://pubs.acs.org/doi/10.1021/je300655b>.

Kunz, O.; Wagner, W. The GERG-2008 Wide-Range Equation of State for Natural Gases and Other Mixtures: An Expansion of GERG-2004. *J. Chem. Eng. Data*, American Chemical Society, v. 57, n. 11, p. 3032–3091, Nov 2012. ISSN 0021-9568.

Kunz O, K. R. W. W.; Jaeschke, M. *The GERG-2004 wide-range equation of state for natural gases and other mixtures*. 2007. Available on: <https://www.osti.gov/etdeweb/biblio/20924249>.

Kuo, K. K.-y. *Principles of Combustion, 2nd Edition*. Hoboken, NJ, USA: Wiley, 2005. ISBN 978-0-471-04689-9. Available on: <https://www.wiley.com/en-us/Principles+of+Combustion%2C+2nd+Edition-p-9780471046899>.

Lemmon, E. W.; Jacobsen, R. T.; Penoncello, S. G.; Friend, D. G. Thermodynamic Properties of Air and Mixtures of Nitrogen, Argon, and Oxygen From 60 to 2000 K at Pressures to 2000 MPa. *J. Phys. Chem. Ref. Data*, American Institute of Physics, v. 29, n. 3, p. 331–385, May 2000. ISSN 0047-2689.

Lettieri, C.; Paxson, D.; Spakovszky, Z.; Bryanston-Cross, P. Characterization of Nonequilibrium Condensation of Supercritical Carbon Dioxide in a de Laval Nozzle. *Journal of Engineering for Gas Turbines and Power*, v. 140, n. 4, p. 041701, 2017. ISSN 15288919.

Lettieri, C.; Paxson, D.; Spakovszky, Z.; Bryanston-Cross, P. Characterization of Nonequilibrium Condensation of Supercritical Carbon Dioxide in a de Laval Nozzle. *J. Eng. Gas Turbines Power*, American Society of Mechanical Engineers Digital Collection, v. 140, n. 4, Apr 2018. ISSN 0742-4795.

Lettieri, C.; Yang, D.; Spakovszky, Z. An Investigation of Condensation Effects in Supercritical Carbon Dioxide Compressors. *J. Eng. Gas Turbines Power*, American Society of Mechanical Engineers Digital Collection, v. 137, n. 8, ago. 2015. ISSN 0742-4795.

Liepmann, H.; Roshko, A. *Elements of Gas Dynamics*. : John Wiley & Sons, 1957. ISBN 9780486316857.

Liu, H.; Liu, Z.; Feng, Y.; Gu, K.; Yan, T. Characteristics of a supersonic swirling dehydratation system of natural gas. *Chinese Journal of Chemical Engineering*, v. 13, n. 1, p. 9–12, 2005.

Louisos, W. F.; Hitt, D. L. Viscous Effects on Performance of Two-Dimensional Supersonic Linear Micronozzles. *Journal of Spacecraft and Rockets*, May 2012.

Luijten, C. *Nucleation and droplet growth at high pressure*. Tese (Doutorado) — Applied Physics, 1998.

Luijten, C. C. M. *Nucleation and Droplet Growth at High Pressure*. 209 p. Tese (PhD Thesis) — Eindhoven university of technology, 1998.

Luo, X.; Prast, B.; Dongen, M. E. H. van; Hoeijmakers, H. W. M.; Yang, J. On phase transition in compressible flows: modelling and validation. *J. Fluid Mech.*, Cambridge University Press, v. 548, p. 403–430, fev. 2006. ISSN 1469-7645.

Machado, P. B.; Monteiro, J. G. M.; Medeiros, J. L.; Epsom, H. D.; Araujo, O. Q. F. Supersonic separation in onshore natural gas dew point plant. *Journal of Natural Gas Science and Engineering*, v. 6, p. 43–49, 2012. Available on: <https://ac.els-cdn.com/S1875510012000273/1-s2.0-S1875510012000273-main.pdf?{_}tid=b81381d1-82ed-4335-8644-2eda3a898787{&}acdnat=1546742941{_}31f3f82cf3add5bb159a5ea>.

Majidi, D.; Farhadi, F. Supersonic separator's dehumidification performance with specific structure: Experimental and numerical investigation. *Applied Thermal Engineering*, v. 179, p. 115551, 2020. ISSN 1359-4311. Available on: <https://www.sciencedirect.com/science/article/pii/S1359431120330337>.

Matthis Thorade. *Entropiebasierte Bewertungskriterien für den Wärmeübergang in Kraftwerksprozessen und ihre Relevanz für praktische Anwendungen*. 184 p. Tese (Doutorado) — Technischen Universität Hamburg-Harburg, 2014. Available on: <https://tubdok.tub.tuhh.de/bitstream/11420/1209/1/Thorade{_}2014{_}EntropieBewertu>.

Mazzelli, F.; Little, A. B.; Garimella, S.; Bartosiewicz, Y. Computational and experimental analysis of supersonic air ejector: Turbulence modeling and assessment of 3D effects. *Int. J. Heat Fluid Flow*, Elsevier, v. 56, p. 305–316, Dec 2015. ISSN 0142-727X.

Meneghini, J. R. et al. *Dispositivo de separação de componentes gasosos através de um bocal convergente-divergente supersônico com área variável*. Brazil patent, BR 20 2020 017289 7 U2, August 2020.

More, J. J.; Garbow, B. S.; Hillstrom, K. E. User guide for minpack-1. [in fortran]. 8 1980. Available on: <https://www.osti.gov/biblio/6997568>.

Muitjens, M. J. E. H.; Kalikmanov, V. I.; Dongen, M. E. H. V.; Hirschberg, A.; Derks, P. A. H. On Mist Formation in Natural Gas. *Rev. Inst. Fr. Pét.*, EDP Sciences, v. 49, n. 1, p. 63–72, jan. 1994. ISSN 0020-2274.

Mulero, A.; Cachadiña, I.; Parra, M. I. Recommended Correlations for the Surface Tension of Common Fluids. *Journal of Physical and Chemical Reference Data*, American Institute of Physics for the National Institute of Standards and Technology, v. 41, n. 4, p. 043105, dec 2012. ISSN 0047-2689. Available on: <http://aip.scitation.org/doi/10.1063/1.4768782>.

Nederstigt, P. *Real Gas Thermodynamics: and the isentropic behavior of substances*. 112 p. Tese (MSc Thesis) — Delft University of technology, 2017. Available on: <https://repository.tudelft.nl/islandora/object/uuid:ee16f7e5-4251-4629-9192-8f4a2e3d599b/datastream/OBJ/download>.

Niknam, P. H.; Mortaheb, H. R.; Mokhtarani, B. Dehydration of low-pressure gas using supersonic separation: Experimental investigation and CFD analysis. *Journal of Natural*

Gas Science and Engineering, Elsevier, v. 52, n. November 2017, p. 202–214, 2018. ISSN 18755100. Available on: <https://doi.org/10.1016/j.jngse.2017.12.007>.

Nunes, S.; Peinemann, K. *Membrane technology: in the chemical industry*. Second. 2006. 358 p. ISBN 9783527313167. Available on: <http://books.google.com/books?hl=en{&}lr={&}id=jRX8BTrdDUsC{&}oi=fnd{&}pg=PR5{&}dq=Membrane+Technology+-+in+the+chemical+industry{&}ots=ykDC3I14Ps{&}sig=JttfWf>.

Oddone, D. *O&G Industry in Brazil Improvements, goals and opportunities*. Rio de Janeiro, 2018. 49 p. Available on: <http://www.anp.gov.br/images/Palestras/Decio{_}Oddone{_}Citi{_}Abri>.

Peeters, P.; Pieterse, G.; Dongen, M. E. H. van. Multi-component droplet growth. II. A theoretical model. *Phys. Fluids*, American Institute of Physics, v. 16, n. 7, p. 2575–2586, jul. 2004. ISSN 1070-6631.

Peeters, P.; Pieterse, G.; Hrubý, J.; Dongen, M. E. H. van. Multi-component droplet growth. I. Experiments with supersaturated n-nonane vapor and water vapor in methane. *Phys. Fluids*, American Institute of Physics, v. 16, n. 7, p. 2567–2574, jul. 2004. ISSN 1070-6631.

Pini, M.; Azzini, L.; Vitale, S.; Colonna, P. A Discrete Adjoint Method for Two-Phase Condensing Flows Applied to the Shape Optimization of Turbine Cascades. *J. Turbomach.*, American Society of Mechanical Engineers Digital Collection, v. 142, n. 11, nov. 2020. ISSN 0889-504X.

Prast, B.; Lammers, B.; Betting, M. CFD for Supersonic Gas Processing. In: *5th International Conference on CFD in the Process Industries*. 2006. p. 1–6.

Pratt, R. Using the Peng-Robinson Equation of State. *CHEMICAL ENGINEERING EDUCATION*, n. 35, p. 112–139, 2001.

Press, W. H.; Teukolsky, S. A.; Vetterling, W. T.; Flannery, B. P. *Numerical Recipes 3rd Edition: The Art of Scientific Computing*. 3. ed. USA: Cambridge University Press, 2007. ISBN 0521880688.

Quan, Y. et al. Aerodynamic design of an axial impulse turbine for the high-temperature organic Rankine cycle. *Appl. Therm. Eng.*, Pergamon, v. 167, p. 114708, Feb 2020. ISSN 1359-4311.

Raman, S. K.; Kim, H. D. Solutions of supercritical CO2 flow through a convergent-divergent nozzle with real gas effects. *Int. J. Heat Mass Transfer*, Pergamon, v. 116, p. 127–135, Jan 2018. ISSN 0017-9310.

Restrepo, J. C.; Bolaños-Acosta, A. F.; Simões-Moreira, J. R. Short nozzles design for real gas supersonic flow using the method of characteristics. *Appl. Therm. Eng.*, Pergamon, v. 207, p. 118063, May 2022. ISSN 1359-4311.

Richter, M.; McLinden, M. O.; Lemmon, E. W. Thermodynamic Properties of 2,3,3,3-Tetrafluoroprop-1-ene (R1234yf): Vapor Pressure and p–ρ–T Measurements and an Equation of State. *J. Chem. Eng. Data*, American Chemical Society, v. 56, n. 7, p. 3254–3264, Jul 2011. ISSN 0021-9568.

Samawe, R.; Rostani, K.; Jalil, A.; Esa, M.; Othman, N. Concept proofing of supersonic nozzle separator for CO2 separation from natural gas using a flow loop. *Offshore Technology Conference Asia*, p. 2373–2376, 2014. ISSN 01603663.

Schmidt, R.; Wagner, W. A new form of the equation of state for pure substances and its application to oxygen. *Fluid Phase Equilib.*, Elsevier, v. 19, n. 3, p. 175–200, Dec 1985. ISSN 0378-3812.

Schnerr, G. 2-D transonic flow with energy supply by homogeneous condensation: Onset condition and 2-D structure of steady Laval nozzle flow. *Exp. Fluids*, Springer-Verlag, v. 7, n. 3, p. 145–156, dez. 1988. ISSN 1432-1114.

Schnerr, G. H. Instabilities of Compressible Flows with Internal Heat Addition. In: *Control of Flow Instabilities and Unsteady Flows*. Wien, Austria: Springer, Vienna, 1996. p. 293–325.

Settles, G. S. *Schlieren and Shadowgraph Techniques*. Berlin, Germany: Springer, 2001. ISBN 978-3-642-56640-0. Available on: <https://link.springer.com/book/10.1007/978-3-642-56640-0>.

Shapiro, A. H. *The Dynamics and Thermodynamics of Compressible Fluid Flow, Volume 2.* : Ronald Press Company, 1953.

Simões-Moreira, J. R.; Shepherd, J. E. Evaporation waves in superheated dodecane. *J. Fluid Mech.*, Cambridge University Press, v. 382, p. 63–86, Mar 1999. ISSN 1469-7645.

Sirignano, W. A. Compressible flow at high pressure with linear equation of state. *J. Fluid Mech.*, Cambridge University Press, v. 843, p. 244–292, May 2018. ISSN 0022-1120.

Span, R. *Multiparameter equations of state : an accurate source of thermodynamic property data.* : Springer, 2000. 367 p. ISBN 9783540673118.

Span, R.; Wagner, W. A New Equation of State for Carbon Dioxide Covering the Fluid Region from the Triple-Point Temperature to 1100 K at Pressures up to 800 MPa. *J. Phys. Chem. Ref. Data*, American Institute of Physics, v. 25, n. 6, p. 1509–1596, Nov 1996. ISSN 0047-2689.

Spinelli, A. et al. Experimental evidence of non-ideal compressible effects in expanding flow of a high molecular complexity vapor. *Exp. Fluids*, Springer Berlin Heidelberg, v. 59, n. 8, p. 126–16, Jul 2018. ISSN 1432-1114.

Tester, J. W.; Modell, M. *Thermodynamics and its applications*. 1. ed. : Prentice Hall PTR, 1997. 6 p. ISBN 013915356X.

Thol, M.; Dubberke, F. H.; Baumhögger, E.; Vrabec, J.; Span, R. Speed of Sound Measurements and Fundamental Equations of State for Octamethyltrisiloxane and Decamethyltetrasiloxane. *J. Chem. Eng. Data*, American Chemical Society, v. 62, n. 9, p. 2633–2648, Sep 2017. ISSN 0021-9568.

Thompson, P. A. *Compressible-fluid dynamics*. : McGraw-Hill, 1971. 665 p. ISBN 9780070644052.

Tollmien, W. Convegno di Scieze Fisiche, Matematiche e Naturali, 30 Settembre - 6. Ottobre 1935 - XIII. Tema: Le Alte Velocita in Aviazione (Reale Accademia d'Italia, Fondanzione Alessandro Volta, Istituta della Società Edison de Milano, Atti dei Convegni, Bd. 5). 694 S. Rom 1936. XIV, Reale Accademia d'Italia. Preis 50 Lire. *Z. angew. Math. Mech.*, John Wiley & Sons, Ltd, v. 17, n. 6, p. 371–372, jan. 1937. ISSN 0044-2267.

Tosto, F.; Lettieri, C.; Pini, M.; Colonna, P. Dense-vapor effects in compressible internal flows. *Phys. Fluids*, American Institute of Physics, v. 33, n. 8, p. 086110, ago. 2021. ISSN 1070-6631.

Uusitalo, A.; Ameli, A.; Turunen-Saaresti, T. Thermodynamic and turbomachinery design analysis of supercritical Brayton cycles for exhaust gas heat recovery. *Energy*, Pergamon, v. 167, p. 60–79, Jan 2019. ISSN 0360-5442.

Vehkamaki Hanna. *Classical nucleation theory in multicomponent systems.* : Springer, 2006. 176 p. ISBN 9783540292135.

Vieira, M. M. *Estudo experimental da evaporação de jatos de iso-octano superaquecido.* Tese (Doutorado) — Escola Politécnica, 2005.

Vimercati, D.; Guardone, A. On the numerical simulation of non-classical quasi-1D steady nozzle flows: Capturing sonic shocks. *Appl. Math. Comput.*, Elsevier, v. 319, p. 617–632, Feb 2018. ISSN 0096-3003.

Virtanen, P. et al. SciPy 1.0: Fundamental Algorithms for Scientific Computing in Python. *Nature Methods*, v. 17, p. 261–272, 2020.

Virtanen, P. et al. SciPy 1.0: Fundamental Algorithms for Scientific Computing in Python. *Nature Methods*, 2020.

Vlasenko, V.; Slesarenko, V.; Bashirov, K. Experimental study of a combined supersonic separator. In: *2018 International Multi-Conference on Industrial Engineering and Modern Technologies (FarEastCon).* 2018. p. 1–4.

Wagner, W.; Pruß, A. The IAPWS Formulation 1995 for the Thermodynamic Properties of Ordinary Water Substance for General and Scientific Use. *J. Phys. Chem. Ref. Data*, American Institute of Physics, v. 31, n. 2, p. 387–535, Jun 2002. ISSN 0047-2689.

Wegener, P.; Mack, L. Condensation in supersonic and hypersonic wind tunnels. In: Dryden, H.; von Kármán, T. (Ed.). Elsevier, 1958, (Advances in Applied Mechanics, v. 5). p. 307–447. Available on: <https://www.sciencedirect.com/science/article/pii/S006521560870022X>.

Wen, C.; Cao, X.; Yang, Y.; Zhang, J. Swirling effects on the performance of supersonic separators for natural gas separation. *Chemical Engineering and Technology*, v. 34, n. 9, p. 1575–1580, 2011. ISSN 09307516.

White, M.; Sayma, A. I.; Markides, C. N. Supersonic flow of non-ideal fluids in nozzles: An application of similitude theory and lessons for ORC turbine design and flexible use considering system performance. *Journal of Physics: Conference Series*, IOP Publishing, v. 821, p. 012002, mar 2017. Available on: <https://doi.org/10.1088%2F1742-6596%2F821%2F1%2F012002>.

White, M. T.; Sayma, A. I. Design of a closed-loop optical-access supersonic test facility for organic vapours. *American Society of Mechanical Engineers Digital Collection*, American Society of Mechanical Engineers Digital Collection, Aug 2018.

Wilke, C. R. A Viscosity Equation for Gas Mixtures. *J. Chem. Phys.*, American Institute of Physics, v. 18, n. 4, p. 517–519, Apr 1950. ISSN 0021-9606.

Wyslouzil, B. E.; Heath, C. H.; Cheung, J. L.; Wilemski, G. Binary condensation in a supersonic nozzle. *Journal of Chemical Physics*, v. 113, n. 17, p. 7317–7329, 2000. ISSN 00219606.

Yang, Y.; Zhu, X.; Yan, Y.; Ding, H.; Wen, C. Performance of supersonic steam ejectors considering the nonequilibrium condensation phenomenon for efficient energy utilisation. *Appl. Energy*, Elsevier, v. 242, p. 157–167, maio 2019. ISSN 0306-2619.

Yeddula, S. R.; Guzmán-Iñigo, J.; Morgans, A. S. A solution for the quasi-one-dimensional linearised Euler equations with heat transfer. *J. Fluid Mech.*, Cambridge University Press, v. 936, Apr 2022. ISSN 0022-1120.

Yeom, G.-S.; Choi, J.-I. Efficient exact solution procedure for quasi-one-dimensional nozzle flows with stiffened-gas equation of state. *Int. J. Heat Mass Transfer*, Pergamon, v. 137, p. 523–533, Jul 2019. ISSN 0017-9310.

Young, J. B. The fundamental equations of gas-droplet multiphase flow. *Int. J. Multiphase Flow*, Pergamon, v. 21, n. 2, p. 175–191, abr. 1995. ISSN 0301-9322.

Young, J. B.; Guha, A. Normal shock-wave structure in two-phase vapour-droplet flows. *J. Fluid Mech.*, Cambridge University Press, v. 228, p. 243–274, jul. 1991. ISSN 1469-7645.

Younglove, B. A.; Frederick, N. V.; McCarty, R. D. *Speed of sound data and related models for mixtures of natural gas constituents*. : NIST, 1993. Monograph.

Zebbiche, T. Stagnation pressure effect on the supersonic minimum length nozzle design. *Aeronautical Journal*, v. 123, n. 1265, p. 1013–1031, 2019. ISSN 00019240.

Zel'dovich, Y.; Raizer, Y. *Physics of Shock Waves and High-temperature Hydrodynamic Phenomena*. : Academic Press, 1966. (Physics of Shock Waves and High Temperature Hydrodynamic Phenomena). ISBN 9780127787015.

Zhu, Y.; Wang, Z.; Yang, Y.; Jiang, P.-X. Flow visualization of supersonic two-phase transcritical flow of CO2 in an ejector of a refrigeration system. *Int. J. Refrig.*, Elsevier, v. 74, p. 354–361, Feb 2017. ISSN 0140-7007.

Zocca, M. M. *Experimental observation of supersonic non-ideal compressible-fluid flows*. 135 p. Tese (Phd Thesis) — Politecnico de Milano, 2018.

Zucrow, M.; Hoffman, J. *Gas Dynamics*. Krieger Publishing Company, 1977. (Gas Dynamics, v. 2). ISBN 9780898748406. Available on: <https://books.google.com.br/books?id=Pa3vAAAAMAAJ>.

Appendix

A Droplet thermodynamics

For this analysis was considered a droplet flowing inside of a supersonic separator as presented in Fig. A.1, an energy balance was performed considering all their possible fluxes between the particle and surroundings, as expressed in:

$$dU = đQ - đW + \sum_i \mu_i dN_i, \tag{A.1}$$

for a molar, work and heat exchange.After considering this as a reversible process, it is possible to express the heat differential in function of temperature and entropy

$$đQ = TdS, \tag{A.2}$$

and also estimate the work performed between the droplet and surroundings, as a

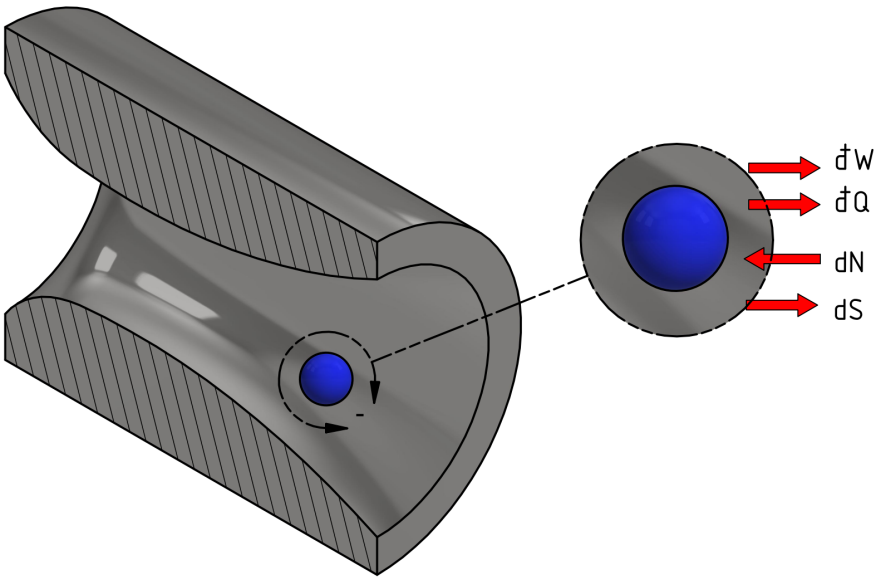

Figure A.1 – Droplet in a supersonic separator.

Table A.1 – Conjugates of the fundamental equation

C_1	T	X_1	S
C_2	$-P$	X_2	V
C_3	σ	X_3	A
C_4	μ	X_4	N

sum of boundary work and surface tension work

$$đW = Pd\mathsf{V} - \sigma dA. \tag{A.3}$$

Finally, after replacing Eq.A.2 and A.3 in A.1 the fundamental equation of thermodynamics was obtained (Vehkamaki Hanna., 2006) for a multicomponent system with surface tension work :

$$dU = TdS - Pd\mathsf{V} + \sigma dA + \sum_i \mu_i dN_i \tag{A.4}$$

expressed in therms of their extensive properties (S, V, N, A) and intensive properties (T,P,μ, σ). Such expression can be expressed in an algebraic fashion after considering U as homogeneous function of degree one (Emanuel, 1988), Therefore, it becomes:

$$U = TS - P\mathsf{V} + \sigma A + \sum_i \mu_i N_i \tag{A.5}$$

The Eq. A.4 allow express the change in a thermodynamic system in function of their extensive properties, nevertheless, this fundamental equation is expressed considering the entropy as an independent variable. Due to the complexness of entropy measuring, is desired to switch this variable for a more useful measurable property as the pressure, temperature and volume.

As expressed in the last section, it is desired to express the fundamental equation A.4 in terms of measurable variables, for this propose will be used the Legendre transform to change the independent variables of the system conserving all their thermodynamic information. Consequently, we will be decomposed the fundamental equation in function of their conjugates

$$dY = C_1 dX_1 + C_2 dX_2 + C_3 dX_3 + C_4 dX_4, \tag{A.6}$$

where C_i is the conjugate and X_i the natural independent variable. Table A.1 shows the C_i and X_i for the fundamental equation of thermodynamics, as explained by Abbott & Van Ness (1989).

Table A.2 – Legendre transforms

Legendre transform	Conjugate combination	Properties	Potential	Equation
$\mathscr{F}_1$	(C_1, X_2, X_3, X_4)	(T, V, A, N)	F	$= U - TS$
$\mathscr{F}_2$	(X_1, C_2, X_3, X_4)	$(S, -P, A, N)$	H	$= U + P\mathsf{V}$
$\mathscr{F}_3$	(X_1, X_2, C_3, X_4)	$(S, \mathsf{V}, \sigma, N)$	$U_{\sigma A}$	$= U - \sigma A$
$\mathscr{F}_4$	(X_1, X_2, X_3, C_4)	(S, V, A, μ)	$U_{\mu N}$	$= U - \mu N$
$\mathscr{F}_{1,2}$	(C_1, C_2, X_3, X_4)	$(T, -P, A, N)$	G	$= U - TS + P\mathsf{V}$
$\mathscr{F}_{1,3}$	(C_1, X_2, C_3, X_4)	$(T, \mathsf{V}, \sigma, N)$	$F_{\sigma A}$	$= U - TS - \sigma A$
$\mathscr{F}_{1,4}$	(C_1, X_2, X_3, C_4)	(T, V, A, μ)	$F_{\mu N}$	$= U - TS - \mu N$
$\mathscr{F}_{2,3}$	(X_1, C_2, C_3, X_4)	$(S, -P, \sigma, N)$	$H_{\sigma A}$	$= U + P\mathsf{V} - \sigma A$
$\mathscr{F}_{2,4}$	(X_1, C_2, X_3, C_4)	$(S, -P, A, \mu)$	$H_{\mu N}$	$= U + P\mathsf{V} - \mu N$
$\mathscr{F}_{3,4}$	(X_1, X_2, C_3, C_4)	$(S, \mathsf{V}, \sigma, \mu)$	$U_{\sigma A, \mu N}$	$= U - \sigma A - \mu N$
$\mathscr{F}_{1,2,3}$	(C_1, C_2, C_3, X_4)	$(T, -P, \sigma, N)$	$G_{\sigma A}$	$= U - TS - P\mathsf{V} - \sigma A$
$\mathscr{F}_{1,2,4}$	(C_1, C_2, X_3, C_4)	$(T, -P, A, \mu)$	$G_{\mu N}$	$= U - TS - P\mathsf{V} - \mu N$
$\mathscr{F}_{1,3,4}$	(C_1, X_2, C_3, C_4)	$(T, \mathsf{V}, \sigma, \mu)$	$F_{\sigma A, \mu N}$	$= U - TS - \sigma A - \mu N$
$\mathscr{F}_{2,3,4}$	(X_1, C_2, C_3, C_4)	$(S, -P, \sigma, \mu)$	$H_{\sigma A, \mu N}$	$= U + P\mathsf{V} - \sigma A - \mu N$
$\mathscr{F}_{1,2,3,4}$	(C_1, C_2, C_3, C_4)	$(T, -P, \sigma, \mu)$	$G_{\sigma A, \mu N}$	$= U - TS + P\mathsf{V} - \sigma A - \mu N$

After considering all the conjugates of the equation, it will be calculated the number of auxiliary functions that will be generated $2^4 - 1 = 15$, all of these new functions will be known as thermodynamic potentials, as presented in Table A.2.

Table A.2 shows all the possible potentials which will hold the required information about the process thermodynamic state, all of them are derived from the classical thermodynamic potentials as internal Energy U, enthalpy H, Helmholtz Free Energy F and Gibbs free energy G. However, it is hard to estimate how each potential is coupled with others, for this reason as presented in Fig. A.3, it was drawn a four dimension Hypercube for showing all the thermodynamic potentials and their connections.

Where each node represents a new Legendre transform and each edge express the change in their conjugate combination. The original function is the internal energy located in the coordinate (0,0,0,0) and all other potential starts from this point. All thermodynamic potentials are transformed in four ways as represented in Fig. A.3, according to the axes and sign conventions expressed in Fig. A.2.

Nevertheless, not all this thermodynamics potentials have engineering interest in our process, then, it was chosen all the potentials in function of measurables properties, as listed in table A.3 where was obtained the respective exact differential expression and their partial derivatives for the conjugate variables. The exact derivative Eq. A.7 was obtained from the Eq. A.4 using their transformation conjugates.

$$d\mathscr{F} = dU + \sum_i (C_i dX_i + X_i dC_i) \tag{A.7}$$

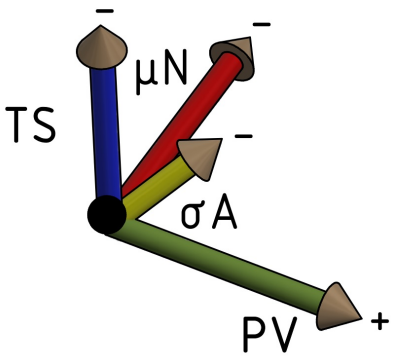

Figure A.2 – Axes and signs convention.

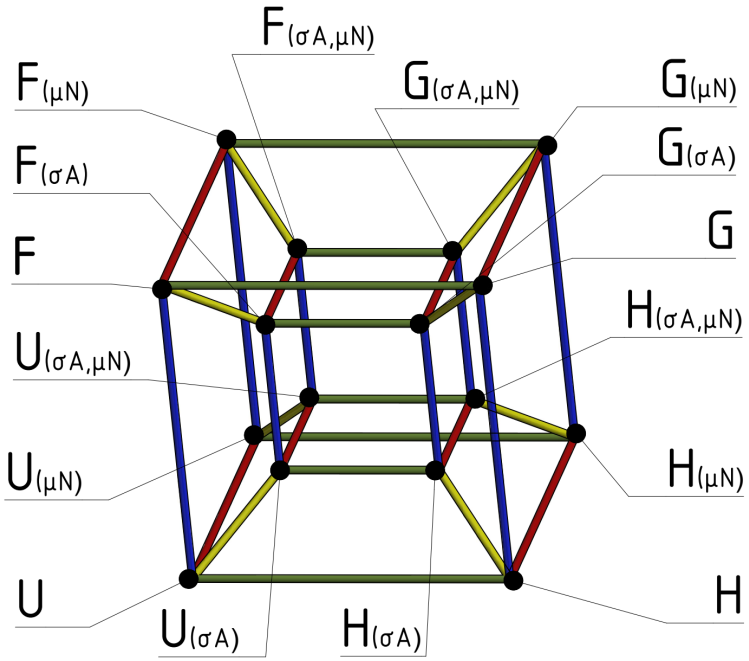

Figure A.3 – Thermodynamic potential 4D hypercube.

There are some important definitions about the properties in table A.3 , especially in the definition of surface tension and chemical potential:

- $\sigma = \left(\frac{\partial \mathscr{F}}{\partial A}\right)_{C1,(C2,X2)(C4,X4)}$ This is the thermodynamic definition of surface tension, it represents the variation of the corresponding thermodynamic potential in function of the surface area without other perturbation on the system.
- $\mu = \left(\frac{\partial \mathscr{F}}{\partial N}\right)_{C1,(C2,X2)(C3,X3)}$ This is the thermodynamic definition of chemical potential, it represents the variation of the corresponding thermodynamic potential in function of the moles without other perturbation on the system.

Table A.4 presents all the Maxwell relations for each thermodynamic potential, obtained through the definition of exact differential equation Eq. A.8, where was used the Schwarz theorem to obtain all the possible derivatives relations of the system:

$$d\mathscr{F} = C_1 dX_1 + C_2 dX_2 + C_3 dX_3 + C_4 dX_4, \tag{A.8}$$

$$\left(\frac{\partial C_1}{\partial X_2}\right)_{X1X3X4} = \left(\frac{\partial C_2}{\partial X_1}\right)_{X2X3X4} \tag{A.9}$$

$$\left(\frac{\partial C_1}{\partial X_3}\right)_{X1X2X4} = \left(\frac{\partial C_3}{\partial X_1}\right)_{X2X3X4} \tag{A.10}$$

$$\left(\frac{\partial C_1}{\partial X_4}\right)_{X1X2X3} = \left(\frac{\partial C_4}{\partial X_1}\right)_{X2X3X4} \tag{A.11}$$

$$\left(\frac{\partial C_2}{\partial X_3}\right)_{X1X2X4} = \left(\frac{\partial C_3}{\partial X_2}\right)_{X1X3X4} \tag{A.12}$$

$$\left(\frac{\partial C_2}{\partial X_4}\right)_{X1X2X3} = \left(\frac{\partial C_4}{\partial X_2}\right)_{X1X3X4} \tag{A.13}$$

$$\left(\frac{\partial C_3}{\partial X_4}\right)_{X1X2X3} = \left(\frac{\partial C_4}{\partial X_3}\right)_{X1X2X4} \tag{A.14}$$

There are some important relations obtained from table A.4

$$\left(\frac{\partial P}{\partial \sigma}\right)_{TV\mu} = \left(\frac{\partial A}{\partial \mathsf{V}}\right)_{T\sigma\mu} \tag{A.15}$$

Being obtained the relation of the pressure and surface tension in function of the droplet geometry, nevertheless, for a spherical droplet the ratio between the change in volume and area remains constant as expressed in Eq. A.16, resulting in:

$$\frac{dA}{d\mathsf{V}} = \frac{2}{r}, \tag{A.16}$$

$$\left(\frac{\partial P}{\partial \sigma}\right)_{TV\mu} = \frac{2}{r}. \tag{A.17}$$

As the chemical potential, temperature and volume are constants for all the species, it is possible to consider this system in equilibrium,

$$\int_{P_{vap}}^{P_{liq}} dP = \int_{\sigma_{vap}}^{\sigma_{liq}} \frac{2d\sigma}{r}, \tag{A.18}$$

therefore, one could solve this differential equation by variable separation, leading to the Eq.A.18 integrating for the interface between the liquid and vapour phase.

$$P_{liq} - P_{vap} = \frac{2(\sigma_{liq} - \cancel{\sigma_{vap}})}{r} \tag{A.19}$$

After reorder the terms, we obtain the pressure inside the liquid spheric droplet in function of the surface tension and the vapour pressure

Table A.3 – Thermodynamic potentials

Potential differential Form	S	P	V	σ	A	μ	N
$dF = -SdT - PdV + \sigma dA + \sum \mu dN$	$-\left(\frac{\partial F}{\partial T}\right)_{VAN}$	$-\left(\frac{\partial F}{\partial V}\right)_{TAN}$		$\left(\frac{\partial F}{\partial A}\right)_{TVN}$		$\left(\frac{\partial F}{\partial N}\right)_{TVA}$	
$dF_{\sigma A} = -SdT - PdV - Ad\sigma + \sum \mu dN$	$-\left(\frac{\partial F}{\partial T}\right)_{V\sigma N}$	$-\left(\frac{\partial F}{\partial V}\right)_{T\sigma N}$			$-\left(\frac{\partial F}{\partial \sigma}\right)_{TVN}$	$\left(\frac{\partial F}{\partial N}\right)_{TV\sigma}$	
$dF_{\mu N} = -SdT - PdV + \sigma dA - \sum Nd\mu$	$-\left(\frac{\partial F}{\partial T}\right)_{VA\mu}$	$-\left(\frac{\partial F}{\partial V}\right)_{TA\mu}$		$\left(\frac{\partial F}{\partial A}\right)_{TV\mu}$			$-\left(\frac{\partial F}{\partial \mu}\right)_{TVA}$
$dF_{\sigma A,\mu N} = -SdT - PdV - Ad\sigma - \sum Nd\mu$	$-\left(\frac{\partial F}{\partial T}\right)_{V\sigma\mu}$	$-\left(\frac{\partial F}{\partial V}\right)_{T\sigma\mu}$			$-\left(\frac{\partial F}{\partial \sigma}\right)_{TV\mu}$		$-\left(\frac{\partial F}{\partial \mu}\right)_{TV\sigma}$
$dG = -SdT + VdP + \sigma dA + \sum \mu dN$	$-\left(\frac{\partial G}{\partial T}\right)_{PAN}$		$\left(\frac{\partial G}{\partial P}\right)_{TAN}$	$\left(\frac{\partial G}{\partial A}\right)_{TPN}$		$\left(\frac{\partial G}{\partial N}\right)_{TPA}$	
$dG_{\sigma A} = -SdT + VdP - Ad\sigma + \sum \mu dN$	$-\left(\frac{\partial G}{\partial T}\right)_{P\sigma N}$		$\left(\frac{\partial G}{\partial P}\right)_{T\sigma N}$		$-\left(\frac{\partial G}{\partial \sigma}\right)_{TPN}$	$\left(\frac{\partial G}{\partial N}\right)_{TP\sigma}$	
$dG_{\mu N} = -SdT + VdP + \sigma dA - \sum Nd\mu$	$-\left(\frac{\partial G}{\partial T}\right)_{PA\mu}$		$\left(\frac{\partial G}{\partial P}\right)_{TA\mu}$	$\left(\frac{\partial G}{\partial A}\right)_{TP\mu}$			$-\left(\frac{\partial G}{\partial \mu}\right)_{TPA}$
$dG_{\sigma A,\mu N} = -SdT + VdP - Ad\sigma - \sum Nd\mu$	$-\left(\frac{\partial G}{\partial T}\right)_{P\sigma\mu}$		$\left(\frac{\partial G}{\partial P}\right)_{T\sigma\mu}$		$-\left(\frac{\partial G}{\partial \sigma}\right)_{TP\mu}$		$-\left(\frac{\partial G}{\partial \mu}\right)_{TP\sigma}$

Table A.4 – Maxwell Relations

$\left(\frac{\partial S}{\partial V}\right)_{TAN} = \left(\frac{\partial P}{\partial T}\right)_{VAN}$	$-\left(\frac{\partial S}{\partial A}\right)_{TVN} = \left(\frac{\partial \sigma}{\partial T}\right)_{VAN}$	$-\left(\frac{\partial S}{\partial N}\right)_{TVA} = \left(\frac{\partial \mu}{\partial T}\right)_{VAN}$	$-\left(\frac{\partial P}{\partial A}\right)_{TVN} = \left(\frac{\partial \sigma}{\partial V}\right)_{TAN}$	$-\left(\frac{\partial P}{\partial N}\right)_{TVA} = \left(\frac{\partial \mu}{\partial V}\right)_{TAN}$	$\left(\frac{\partial \sigma}{\partial N}\right)_{TVA} = \left(\frac{\partial \mu}{\partial A}\right)_{TVN}$
$\left(\frac{\partial S}{\partial V}\right)_{T\sigma N} = \left(\frac{\partial P}{\partial T}\right)_{V\sigma N}$	$\left(\frac{\partial S}{\partial \sigma}\right)_{TVN} = \left(\frac{\partial A}{\partial T}\right)_{V\sigma N}$	$-\left(\frac{\partial S}{\partial N}\right)_{TV\sigma} = \left(\frac{\partial \mu}{\partial T}\right)_{V\sigma N}$	$\left(\frac{\partial P}{\partial \sigma}\right)_{TVN} = \left(\frac{\partial A}{\partial V}\right)_{T\sigma N}$	$-\left(\frac{\partial P}{\partial N}\right)_{TV\sigma} = \left(\frac{\partial \mu}{\partial V}\right)_{T\sigma N}$	$-\left(\frac{\partial A}{\partial N}\right)_{TV\sigma} = \left(\frac{\partial \mu}{\partial \sigma}\right)_{TVN}$
$\left(\frac{\partial S}{\partial V}\right)_{TA\mu} = \left(\frac{\partial P}{\partial T}\right)_{VA\mu}$	$-\left(\frac{\partial S}{\partial A}\right)_{TV\mu} = \left(\frac{\partial \sigma}{\partial T}\right)_{VA\mu}$	$\left(\frac{\partial S}{\partial \mu}\right)_{TVA} = \left(\frac{\partial N}{\partial T}\right)_{VA\mu}$	$-\left(\frac{\partial P}{\partial A}\right)_{TV\mu} = \left(\frac{\partial \sigma}{\partial V}\right)_{TA\mu}$	$\left(\frac{\partial P}{\partial \mu}\right)_{TVA} = \left(\frac{\partial N}{\partial V}\right)_{TA\mu}$	$-\left(\frac{\partial \sigma}{\partial \mu}\right)_{TVA} = \left(\frac{\partial N}{\partial A}\right)_{TV\mu}$
$\left(\frac{\partial S}{\partial V}\right)_{T\sigma\mu} = \left(\frac{\partial P}{\partial T}\right)_{V\sigma\mu}$	$\left(\frac{\partial S}{\partial \sigma}\right)_{TV\mu} = \left(\frac{\partial A}{\partial T}\right)_{V\sigma\mu}$	$\left(\frac{\partial S}{\partial \mu}\right)_{TV\sigma} = \left(\frac{\partial N}{\partial T}\right)_{V\sigma\mu}$	$\left(\frac{\partial P}{\partial \sigma}\right)_{TV\mu} = \left(\frac{\partial A}{\partial V}\right)_{T\sigma\mu}$	$\left(\frac{\partial P}{\partial \mu}\right)_{TV\sigma} = \left(\frac{\partial N}{\partial V}\right)_{T\sigma\mu}$	$\left(\frac{\partial A}{\partial \mu}\right)_{TV\sigma} = \left(\frac{\partial N}{\partial \sigma}\right)_{TV\mu}$
$-\left(\frac{\partial S}{\partial P}\right)_{TAN} = \left(\frac{\partial V}{\partial T}\right)_{PAN}$	$-\left(\frac{\partial S}{\partial A}\right)_{TPN} = \left(\frac{\partial \sigma}{\partial T}\right)_{PAN}$	$-\left(\frac{\partial S}{\partial N}\right)_{TPA} = \left(\frac{\partial \mu}{\partial T}\right)_{PAN}$	$\left(\frac{\partial V}{\partial A}\right)_{TPN} = \left(\frac{\partial \sigma}{\partial P}\right)_{TAN}$	$\left(\frac{\partial V}{\partial N}\right)_{TPA} = \left(\frac{\partial \mu}{\partial P}\right)_{TAN}$	$\left(\frac{\partial \sigma}{\partial N}\right)_{TPA} = \left(\frac{\partial \mu}{\partial A}\right)_{TPN}$
$-\left(\frac{\partial S}{\partial P}\right)_{T\sigma N} = \left(\frac{\partial V}{\partial T}\right)_{P\sigma N}$	$\left(\frac{\partial S}{\partial \sigma}\right)_{TPN} = \left(\frac{\partial A}{\partial T}\right)_{P\sigma N}$	$-\left(\frac{\partial S}{\partial N}\right)_{TP\sigma} = \left(\frac{\partial \mu}{\partial T}\right)_{P\sigma N}$	$-\left(\frac{\partial V}{\partial \sigma}\right)_{TPN} = \left(\frac{\partial A}{\partial P}\right)_{T\sigma N}$	$\left(\frac{\partial V}{\partial N}\right)_{TP\sigma} = \left(\frac{\partial \mu}{\partial P}\right)_{T\sigma N}$	$-\left(\frac{\partial A}{\partial N}\right)_{TP\sigma} = \left(\frac{\partial \mu}{\partial \sigma}\right)_{TPN}$
$-\left(\frac{\partial S}{\partial P}\right)_{TA\mu} = \left(\frac{\partial V}{\partial T}\right)_{PA\mu}$	$\left(\frac{\partial S}{\partial A}\right)_{TP\mu} = \left(\frac{\partial \sigma}{\partial T}\right)_{PA\mu}$	$\left(\frac{\partial S}{\partial \mu}\right)_{TPA} = \left(\frac{\partial N}{\partial T}\right)_{PA\mu}$	$\left(\frac{\partial V}{\partial A}\right)_{TP\mu} = \left(\frac{\partial \sigma}{\partial P}\right)_{TA\mu}$	$-\left(\frac{\partial V}{\partial \mu}\right)_{TPA} = \left(\frac{\partial N}{\partial P}\right)_{TA\mu}$	$-\left(\frac{\partial \sigma}{\partial \mu}\right)_{TPA} = \left(\frac{\partial N}{\partial A}\right)_{TP\mu}$
$-\left(\frac{\partial S}{\partial P}\right)_{T\sigma\mu} = \left(\frac{\partial V}{\partial T}\right)_{P\sigma\mu}$	$\left(\frac{\partial S}{\partial \sigma}\right)_{TP\mu} = \left(\frac{\partial A}{\partial T}\right)_{P\sigma\mu}$	$\left(\frac{\partial S}{\partial \mu}\right)_{TP\sigma} = \left(\frac{\partial N}{\partial T}\right)_{P\sigma\mu}$	$-\left(\frac{\partial V}{\partial \sigma}\right)_{TP\mu} = \left(\frac{\partial A}{\partial P}\right)_{T\sigma\mu}$	$-\left(\frac{\partial V}{\partial \mu}\right)_{TP\sigma} = \left(\frac{\partial N}{\partial P}\right)_{T\sigma\mu}$	$\left(\frac{\partial A}{\partial \mu}\right)_{TP\sigma} = \left(\frac{\partial N}{\partial \sigma}\right)_{TP\mu}$

$$P_{liq} = \frac{2\sigma}{r} + P_{vap}, \tag{A.20}$$

this equation is known as the Laplace Young equation Eq. A.20 (Carey, 1992).

In addition to the last equation, we could find other important relationship exposed in the Eq. A.21, where the left side of the equation is defined as molecular volume Eq. A.22.

$$\left(\frac{\partial \mathsf{V}}{\partial N}\right)_{TPA} = \left(\frac{\partial \mu}{\partial P}\right)_{TAN} \tag{A.21}$$

$$\upsilon_i = \left(\frac{\partial \mu}{\partial P}\right)_{TAN} \tag{A.22}$$

For a system with constant temperature and mole numbers, the Eq. A.22 could be simplified to Eq. A.23 which shows the relation between pressure, molecular volume and chemical potential.

$$d\mu_i = \upsilon_i dP \tag{A.23}$$

Other important relation is described in Eq. A.24, where it is shown the relation between area and entropy and surface tension and temperature for a system with constant volume and mole number. It is possible to conclude that an increase in entropy and area will lead a temperature increase and a surface tension reduction, as reported in literature (Mulero et al., 2012).

$$\left(\frac{\partial S}{\partial A}\right)_{TVN} = -\left(\frac{\partial \sigma}{\partial T}\right)_{VAN} \tag{A.24}$$

Finally, it is possible to analyse the effect of chemical potential on the surface tension, starting with the relation expressed in the Eq. A.25, obtained from the Maxwell relations established in table A.4.

$$\left(\frac{\partial \sigma}{\partial N}\right)_{TVA} = \left(\frac{\partial \mu}{\partial A}\right)_{TVN} \tag{A.25}$$

For an isotherm and isochoric process the Eq. A.25 could be simplified to Eq. A.26.

$$\frac{d\sigma}{dN} = \frac{d\mu}{dA} \tag{A.26}$$

Finally, we could consider the mass flux across the interface as $N'' = \frac{dN}{dA}$, allowing to understand the variation of surface tension in function of the chemical potential and

molar flux expressed in the Eq. A.27, this phenomenon is known as Marangoni effect (Butt et al., 2003).

$$d\sigma = d\mu N'' \tag{A.27}$$

B

Development of compability and characteristic equations

In this appendix is presented the formulation for the characteristic lines based on the book of Shapiro (1953) and Anderson (1990). The governing partial differential equation of inviscid steady irrotational compressible flow is known as the full potential velocity equation .

$$\left(1-\frac{\phi_x^2}{c^2}\right)\phi_{xx}+\left(1-\frac{\phi_r^2}{c^2}\right)\phi_{rr}-\frac{2\phi_x\phi_r}{c^2}\phi_{xr}+\frac{\phi_r}{r}=0 \tag{B.1}$$

Being:

$$u=\frac{\partial\phi}{\partial x}=\phi_x \tag{B.2}$$

$$v=\frac{\partial\phi}{\partial r}=\phi_r \tag{B.3}$$

Replacing Eqs. (B.2) and (B.3) in Eq. (B.1) and multiply by c^2, it was obtained,

$$\left(c^2-u^2\right)\phi_{xx}+\left(c^2-v^2\right)\phi_{rr}-2uv\phi_{xr}=-c^2\frac{v}{r} \tag{B.4}$$

Also as du and dv are exacts derivatives, it were obtained

$$(dx)\phi_{xx}+(dr)\phi_{xr}=du \tag{B.5}$$

$$(dx)\phi_{xr}+(dr)\phi_{rr}=dv \tag{B.6}$$

The Eqs. (B.4) to (B.6), are a system of partial differential equations, with three unknowns $(\phi_{xx},\phi_{xr},\phi_{rr})$, for example the system of equations can be solved for (ϕ_{xr}) using the Cramer's rule becomes:

$$\phi_{xr} = \frac{\begin{vmatrix} c^2-u^2 & -c^2\frac{v}{r} & c^2-v^2 \\ dx & du & 0 \\ 0 & dv & dr \end{vmatrix}}{\begin{vmatrix} c^2-u^2 & -2uv & c^2-v^2 \\ dx & dr & 0 \\ 0 & dx & dr \end{vmatrix}} = \frac{N}{D} \tag{B.7}$$

By the physics of the flow (ϕ_{xr}) must be determinate, nevertheless, if the determinant and numerator becomes zero, this will not happen. Although this sounds incongruous, the conditions where its happen shows the direction where the equation complexity is reduced, so was calculated the conditions where the numerator and denominator of Eq. (B.7) becomes zero. And in this direction will propagate the characteristics lines.

B.1 Characteristic Equation

The characteristic equation is result to evaluate the determinant of denominator in Eq. (B.7), resulting in

$$\left(c^2-u^2\right)\left(\frac{dr}{dx}\right)^2 + 2uv\frac{dr}{dx} + \left(c^2-v^2\right) = 0 \tag{B.8}$$

Solving Eq. (B.8) for dr/dx:

$$\frac{dr}{dx} = \frac{-uv \pm \sqrt{u^2v^2 - \left(c^2-u^2\right)\left(c^2-v^2\right)}}{c^2-u^2} \tag{B.9}$$

Simplifying :

$$\frac{dr}{dx} = \frac{\frac{-uv}{c^2} \pm \sqrt{\frac{(u^2+v^2)}{c^2} - 1}}{\left(1-\frac{v^2}{c^2}\right)} \tag{B.10}$$

If:

$$M^2 = \frac{\mathbf{V}^2}{c^2} \tag{B.11}$$

It was obtained:

$$\frac{dr}{dx} = \frac{-\frac{uv}{c^2} \pm \sqrt{M^2-1}}{\left(1-\frac{v^2}{c^2}\right)} \tag{B.12}$$

Considering the definition of Mach angle:

$$\cot^2\mu = M^2 - 1 \tag{B.13}$$

And the decomposition of the total velocity

$$u = \mathbf{V}\cos\theta \tag{B.14}$$

$$v = \mathbf{V}\sin\theta \tag{B.15}$$

Replacing Eqs. (B.13) to (B.15) in Eq. (B.12):

$$\frac{dr}{dx} = \frac{-\frac{\cos\theta\sin\theta}{\sin^2\mu} \pm \cot\mu}{1 - \frac{\cos^2\theta}{\sin^2\mu}} \tag{B.16}$$

Simplifying Eq. (B.16):

$$\left(\frac{dr}{dx}\right)_{I\,II} = \tan(\theta \pm \mu) \tag{B.17}$$

B.2 Compatibility Equation

For the Compatibility equation was performed the same procedure done for the characteristic equation, instead of the denominator was selected the numerator of Eq. (B.7), therefore it was obtained:

$$\left(c^2 - u^2\right) dr du + c^2 \frac{v}{r} + \left(c^2 - v^2\right) dx dv = 0 \tag{B.18}$$

Rearranging:

$$\frac{dv}{du} = \left(-\left(\frac{dr}{dx}\right)_{I\,II} - \frac{c^2 v}{r\left(c^2 - u^2\right) du dx}\right)\frac{c^2 - u^2}{c^2 - v^2} \tag{B.19}$$

Replacing equation (B.14) to (B.16) in equation (B.19) and rearranging.

$$\frac{1}{\mathbf{V}}\frac{d\mathbf{V}}{d\theta} = \mp\tan\mu + \frac{\sin\mu\tan\mu\sin\theta}{\sin(\theta \mp \mu)}\frac{1}{r}\frac{dr}{d\theta} \tag{B.20}$$

After multiplying Eq. (B.20) by $d\theta/\tan\mu$:

$$(d\theta)_{I\,II} \pm \frac{\cot\mu}{\mathbf{V}}(dV)_{I\,II} \mp \frac{\sin\theta\sin\mu}{\sin(\theta \mp \mu)}\frac{(dr)_{I\,II}}{r} = 0 \tag{B.21}$$

Considering the Prandtl-Meyer function

$$d\nu = \frac{\cot\mu}{\mathbf{V}}d\mathbf{V} = \frac{\sqrt{M^2 - 1}}{\mathbf{V}}d\mathbf{V} \tag{B.22}$$

And replacing it in Eq. (B.21)

$$(d\theta)_{I\,II} \pm (d\nu)_{I\,II} = \pm\frac{\sin\mu\sin\theta}{\sin(\theta \mp \mu)}\frac{(dr)_{I\,II}}{r} \tag{B.23}$$

C

Two-Phase thermodynamic properties

The calculation of a condensation shock wave require the computation of the two-phase thermodynamic properties. First we can start after defining the two-phase density mixture definition

$$\rho_m = \frac{\rho_v}{\mathrm{y}\left(\frac{\rho_v}{\rho_l} - 1\right) + 1} \tag{C.1}$$

where ρ is each phase density and y the two-phase liquid mass fraction. Firstly, one can obtain the mixture speed of sound, after considering its definition:

$$c_m^2 = \left(\frac{\partial \rho_m}{\partial P}\right)_{s_m}^{-1} \tag{C.2}$$

so after deriving Eq. C.1 as stated by Eq. C.2, one can obtain:

$$c_m^{-2} = -\frac{-\rho_l^2 \rho_v \left(\frac{\partial \mathrm{y}}{\partial P}\right)_{s_m} + \rho_l^2 \mathrm{y} \left(\frac{\partial \rho_v}{\partial P}\right)_{s_m} - \rho_l^2 \left(\frac{\partial \rho_v}{\partial P}\right)_{s_m} + \rho_l {\rho_v}^2 \left(\frac{\partial \mathrm{y}}{\partial P}\right)_{s_m} - \rho_v^2 \mathrm{y} \left(\frac{\partial \rho_l}{\partial P}\right)_{s_m}}{\left(\rho_l \mathrm{y} - \rho_l - \rho_v \mathrm{y}\right)^2} \tag{C.3}$$

after rearranging, it becomes:

$$c_m^{-2} = \frac{\left(\frac{\rho_v}{\rho_l}\right)^2 \mathrm{y} \left(\frac{\partial \rho_l}{\partial P}\right)_{s_m} - \rho_v \left(\frac{\rho_\mathrm{v}}{\rho_1} - 1\right) \left(\frac{\partial \mathrm{y}}{\partial P}\right)_{s_m} - (\mathrm{y} - 1) \left(\frac{\partial \rho_v}{\partial P}\right)_{s_m}}{\left(\mathrm{y} - 1 - \frac{\rho_\mathrm{v}}{\rho_1} \mathrm{y}\right)^2} \tag{C.4}$$

if the liquid and vapour derivatives are calculated for a single phase isentropic state, Eq. C.4 is simplified to:

$$c_m^{-2} = \frac{\left(\frac{\rho_v}{\rho_l}\right)^2 \frac{\mathrm{y}}{c_l^2} - \rho_v \left(\frac{\rho_\mathrm{v}}{\rho_1} - 1\right) \left(\frac{\partial \mathrm{y}}{\partial P}\right)_{s_m} - \frac{\mathrm{y} - 1}{c_v^2}}{\left(\mathrm{y} - 1 - \frac{\rho_\mathrm{v}}{\rho_1} \mathrm{y}\right)^2} \tag{C.5}$$

In an analogous fashion one can compute the Grüneisen parameter:

$$Gr^{-1} = \left(\frac{\partial \rho_m}{\partial T}\right)_{s_m} \frac{T}{\rho_m} \tag{C.6}$$

$$Gr^{-1} = \frac{\left(\frac{\rho_v}{\rho_l}\right)^2 \mathrm{y} \left(\frac{\partial \rho_l}{\partial T}\right)_{s_m} - \rho_v \left(\frac{\rho_\mathrm{v}}{\rho_1} - 1\right) \left(\frac{\partial \mathrm{y}}{\partial T}\right)_{s_m} - (\mathrm{y}-1) \left(\frac{\partial \rho_v}{\partial T}\right)_{s_m}}{\left(\mathrm{y} - 1 - \frac{\rho_\mathrm{v}}{\rho_1}\mathrm{y}\right)^2} \frac{T}{\rho_m} \tag{C.7}$$

$$Gr^{-1} = \frac{\frac{\mathrm{y}\rho_v^2}{\rho_l Gr_l T_l} - \rho_v \left(\frac{\rho_\mathrm{v}}{\rho_1} - 1\right) \left(\frac{\partial \mathrm{y}}{\partial T}\right)_{s_m} - \frac{(\mathrm{y}-1)\rho_v}{Gr_v T_v}}{\left(\mathrm{y} - 1 - \frac{\rho_\mathrm{v}}{\rho_1}\mathrm{y}\right)^2} \frac{T}{\rho_m} \tag{C.8}$$

D

Discharge time analytical expression

For the discharge time computation it was used the mass conservation integral equation for a discharging tank, resulting in:

$$0 = \frac{\partial}{\partial t}\int_{\text{cv}} \rho d\forall_{tank} + \int_{cs} \rho V \cdot dA \tag{D.1}$$

Applying the Eq. D.1 for a rigid tank control volume, with a sonic throat at the outlet:

$$0 = \frac{d}{dt}\left(\rho \forall\right) + \dot{m}_e, \tag{D.2}$$

the last term of Eq. D.2 represents the blocked mass flow rate, and after employing Nederstigt (2017) formulation for the analytical computation of the blocked mass flow rate, which is:

$$\dot{m}_e = A\sqrt{\gamma_{Pv}\rho P}\left(\frac{2}{\gamma_{Pv}+1}\right)^{\frac{\gamma_{Pv}+1}{2(\gamma_{Pv}-1)}}, \tag{D.3}$$

where γ_{Pv} denotes the isentropic real gas coefficient, which can be expressed as:

$$\gamma_{Pv} = c^2\frac{\rho}{P}. \tag{D.4}$$

After substituting Eq. D.3 into D.2, one obtains

$$0 = \frac{d}{dt}\left(\rho \forall\right) + A\sqrt{\gamma_{Pv}\rho P}\left(\frac{2}{\gamma_{Pv}+1}\right)^{\frac{\gamma_{Pv}+1}{2(\gamma_{Pv}-1)}}. \tag{D.5}$$

One can assume that the discharge process is isentropic in time and space, therefore, it is possible to use the following isentropic relation for real gases (Nederstigt, 2017):

$$\rho = \rho_i \left(\frac{P}{P_i}\right)^{\frac{1}{\gamma_{pv}}} \tag{D.6}$$

The Eq. D.2 first term can be derived as follows:

$$\frac{d}{dt}(\rho \mathsf{V}) = \mathsf{V}\frac{d}{dt}\left(\rho_i \left(\frac{P}{P_i}\right)^{\frac{1}{\gamma_{pv}}}\right) = \mathsf{V}\gamma_{Pv}^{-1}\rho_i P_i^{\frac{1}{\gamma_{Pv}}} P^{\frac{1-\gamma_{pv}}{\gamma_{Pv}}} \frac{dP}{dt} \tag{D.7}$$

after replacing it in Eq. D.5 and rearranging, one obtains:

$$\frac{\mathsf{V}\gamma_{Pv}^{-1}\rho_i P_i^{\frac{1}{\gamma_{Pv}}} P^{\frac{1-\gamma_{pv}}{\gamma_{Pv}}} dP}{A\sqrt{\gamma_{Pv}\rho P}\left(\frac{2}{\gamma_{Pv}+1}\right)^{\frac{\gamma_{Pv}+1}{2(\gamma_{Pv}-1)}}} = -dt \tag{D.8}$$

this differential equation can be solved through variable separation and integration, which yields:

$$\int_{P_i}^{P} \frac{\mathsf{V}\gamma_{Pv}^{-1}\rho_i P_i^{\frac{1}{\gamma_{Pv}}} P^{\frac{1-\gamma_{pv}}{\gamma_{Pv}}} dP}{A\sqrt{\gamma_{Pv}\rho P}\left(\frac{2}{\gamma_{Pv}+1}\right)^{\frac{\gamma_{Pv}+1}{2(\gamma_{Pv}-1)}}} = \int_0^t -dt \tag{D.9}$$

after integrating and rearranging, one can obtain a mathematical expression for the discharge time:

$$t = \frac{2V\left[\left(\frac{P}{P_i}\right)^{\frac{1-\gamma_{Pv}}{2\gamma_{Pv}}} - 1\right]}{(\gamma_{Pv}-1)\,A\sqrt{\frac{P_i\gamma_{Pv}}{\rho_i}\left(\frac{2}{\gamma_{Pv}+1}\right)^{\frac{\gamma_{Pv}+1}{\gamma_{Pv}-1}}}} \tag{D.10}$$

For this equation development, the heat transfer and the viscous effects were neglected.

E

Nozzles profiles and pressure taps locations

Table E.1 – Preasure tap position nozzle 1.

Profile A			Profile B		
Number	Kulite	x mm	Number	Kulite	x mm
1	KTE01	39.9	1	KTE11	47.4
2	KTE02	54.9	2	KTE12	62.4
3	KTE03	71.93	3	KTE13	78.78
4	KTE04	85.69	4	KTE14	92.85
5	KTE05	100.52	5	KTE15	107.79
6	KTE06	115.23	6	KTE16	122.58
7	KTE07	129.9	7	KTE17	137.4

Table E.2 – Preasure tap position nozzle 2.

Profile A			Profile B		
Number	Kulite	x mm	Number	Kulite	x mm
1	KTE01	40	1	KTE11	47.5
2	KTE02	55	2	KTE12	62.5
3	KTE03	70	3	KTE13	77.5
4	KTE04	85	4	KTE14	92.5
5	KTE05	100	5	KTE15	107.5
6	KTE06	115	6	KTE17	122.5
7	KTE07	130			

Table E.3 – Nozzle channel profile 1, nozzle width 40 mm.

Convergent part				Divergent part			
x mm	y mm	A mm^2	Area ratio	x mm	y mm	A mm^2	Area ratio
0.00	50.00	2000.00	3.33	54.90	15.00	600.00	1.00
3.00	50.00	2000.00	3.33	57.90	15.18	607.19	1.01
6.00	50.00	2000.00	3.33	60.89	15.60	623.94	1.04
9.00	50.00	2000.00	3.33	63.87	16.25	650.11	1.08
12.00	49.91	1996.34	3.33	66.84	17.14	685.58	1.14
14.99	49.43	1977.18	3.30	69.79	18.25	730.11	1.22
17.96	48.54	1941.70	3.24	72.71	19.59	783.46	1.31
20.88	47.25	1890.04	3.15	75.62	21.07	842.93	1.40
23.76	45.56	1822.46	3.04	78.53	22.50	900.09	1.50
26.58	43.48	1739.29	2.90	81.46	23.84	953.46	1.59
29.31	41.02	1640.90	2.73	84.40	25.01	1000.28	1.67
31.96	38.19	1527.74	2.55	87.35	26.14	1045.79	1.74
34.50	35.01	1400.38	2.33	90.30	27.22	1088.96	1.81
36.93	31.48	1259.39	2.10	93.25	28.23	1129.20	1.88
39.23	27.64	1105.44	1.84	96.22	29.16	1166.30	1.94
41.51	23.75	950.09	1.58	99.19	30.01	1200.31	2.00
44.03	20.50	819.95	1.37	102.16	30.78	1231.30	2.05
46.74	17.96	718.42	1.20	105.14	31.48	1259.34	2.10
49.61	16.18	647.34	1.08	108.12	32.11	1284.50	2.14
52.57	15.20	608.07	1.01	111.11	32.67	1306.87	2.18
54.90	15.00	600.00	1.00	114.10	33.16	1326.52	2.21
				117.09	33.59	1343.53	2.24
				120.09	33.95	1357.97	2.26
				123.09	34.25	1369.91	2.28
				126.08	34.49	1379.43	2.30
				129.08	34.67	1386.60	2.31
				132.08	34.79	1391.48	2.32
				135.08	34.85	1394.14	2.32

Table E.4 – Nozzle channel profile 2, nozzle width 40 mm.

Convergent part				Divergent part			
x mm	y mm	A mm^2	Area ratio	x mm	y mm	A mm^2	Area ratio
0.0	50.0	2000.0	10.00	85.0	5.0	200.0	1.00
3.0	50.0	2000.0	10.00	87.0	5.1	204.8	1.02
6.0	50.0	2000.0	10.00	89.0	5.4	216.0	1.08
9.0	50.0	2000.0	10.00	91.0	5.8	233.4	1.17
12.0	50.0	2000.0	10.00	93.0	6.4	257.1	1.29
15.0	50.0	2000.0	10.00	94.9	7.2	286.7	1.43
18.0	50.0	2000.0	10.00	96.9	8.1	322.0	1.61
21.0	50.0	2000.0	10.00	98.8	8.9	356.4	1.78
24.0	49.9	1994.2	9.97	100.8	9.7	387.4	1.94
27.0	49.4	1974.0	9.87	102.8	10.4	415.3	2.08
30.0	48.5	1939.6	9.70	104.7	11.0	440.0	2.20
32.9	47.3	1891.0	9.45	106.7	11.5	460.5	2.30
35.8	45.7	1828.4	9.14	108.7	12.0	478.3	2.39
38.6	43.8	1752.0	8.76	110.7	12.3	493.6	2.47
41.4	41.6	1662.0	8.31	112.7	12.7	506.1	2.53
44.1	39.0	1559.0	7.79	114.7	12.9	516.1	2.58
46.7	36.1	1443.1	7.22	116.7	13.1	523.5	2.62
49.3	32.9	1314.8	6.57	118.7	13.2	528.6	2.64
51.7	29.4	1174.6	5.87	120.7	13.3	531.4	2.66
54.1	25.6	1025.7	5.13				
56.5	22.1	885.5	4.43				
59.0	18.9	757.1	3.79				
61.7	16.0	641.2	3.21				
64.4	13.5	538.1	2.69				
67.2	11.2	448.1	2.24				
70.0	9.3	371.7	1.86				
72.9	7.7	309.0	1.55				
75.8	6.5	260.4	1.30				
78.8	5.6	225.9	1.13				
81.8	5.1	205.7	1.03				
85.0	5.0	200.0	1.00				

F

Technical drawings Test rig

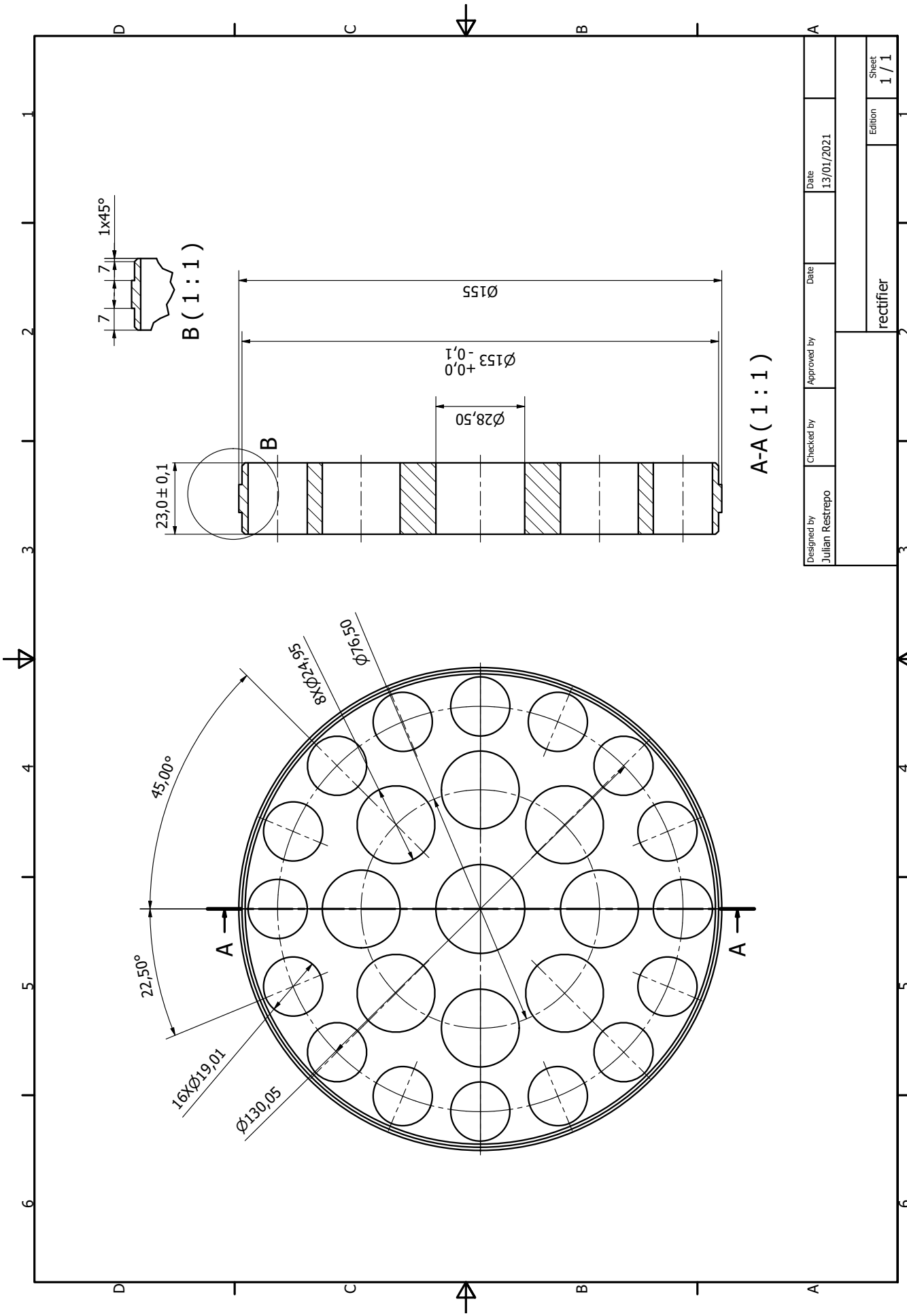

Figure F.1 – Flow rectifier technical drawing according to K-lab nova design established in ABNT NBR ISO 5167-1

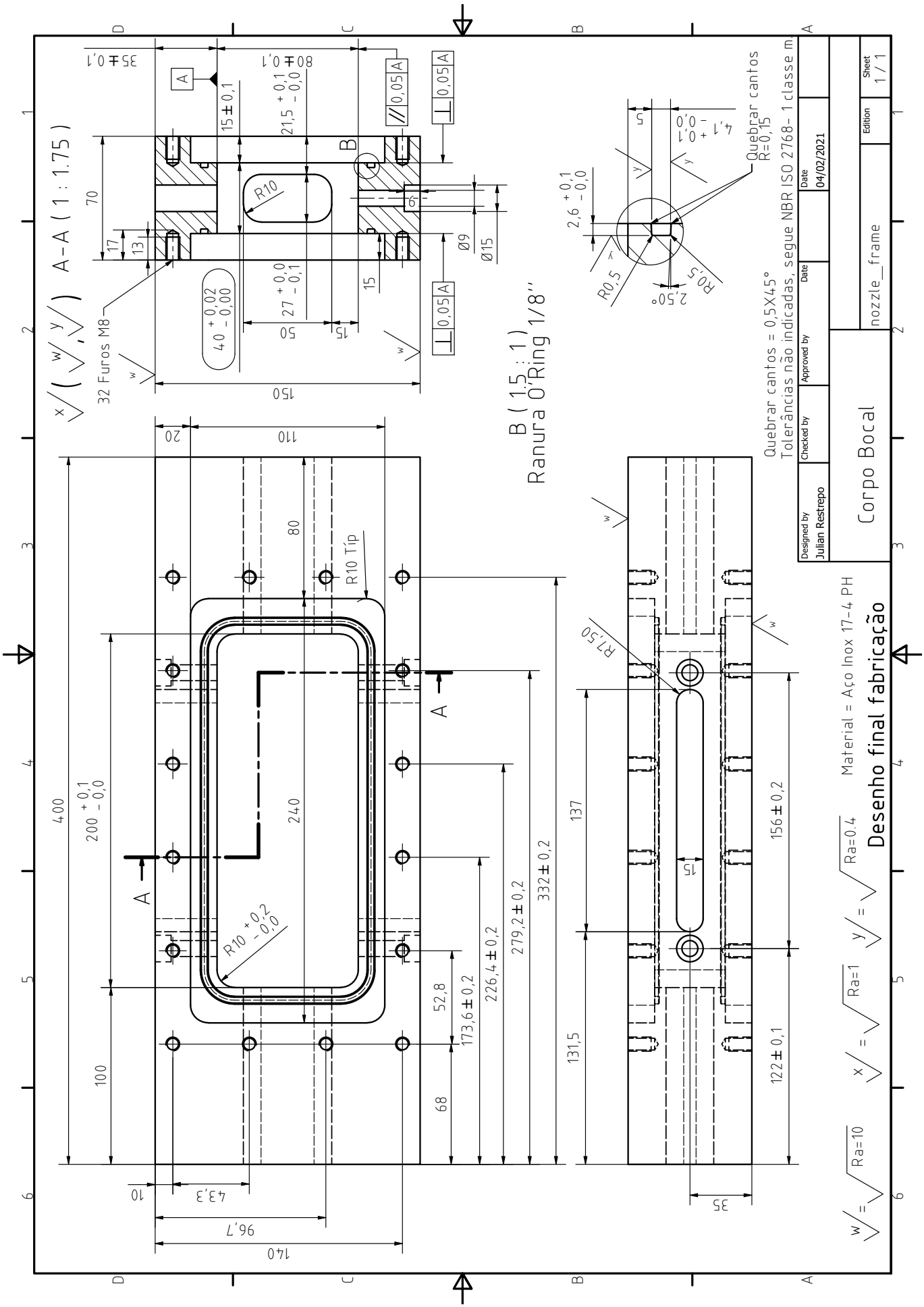

Figure F.2 – Planar nozzle body technical drawing

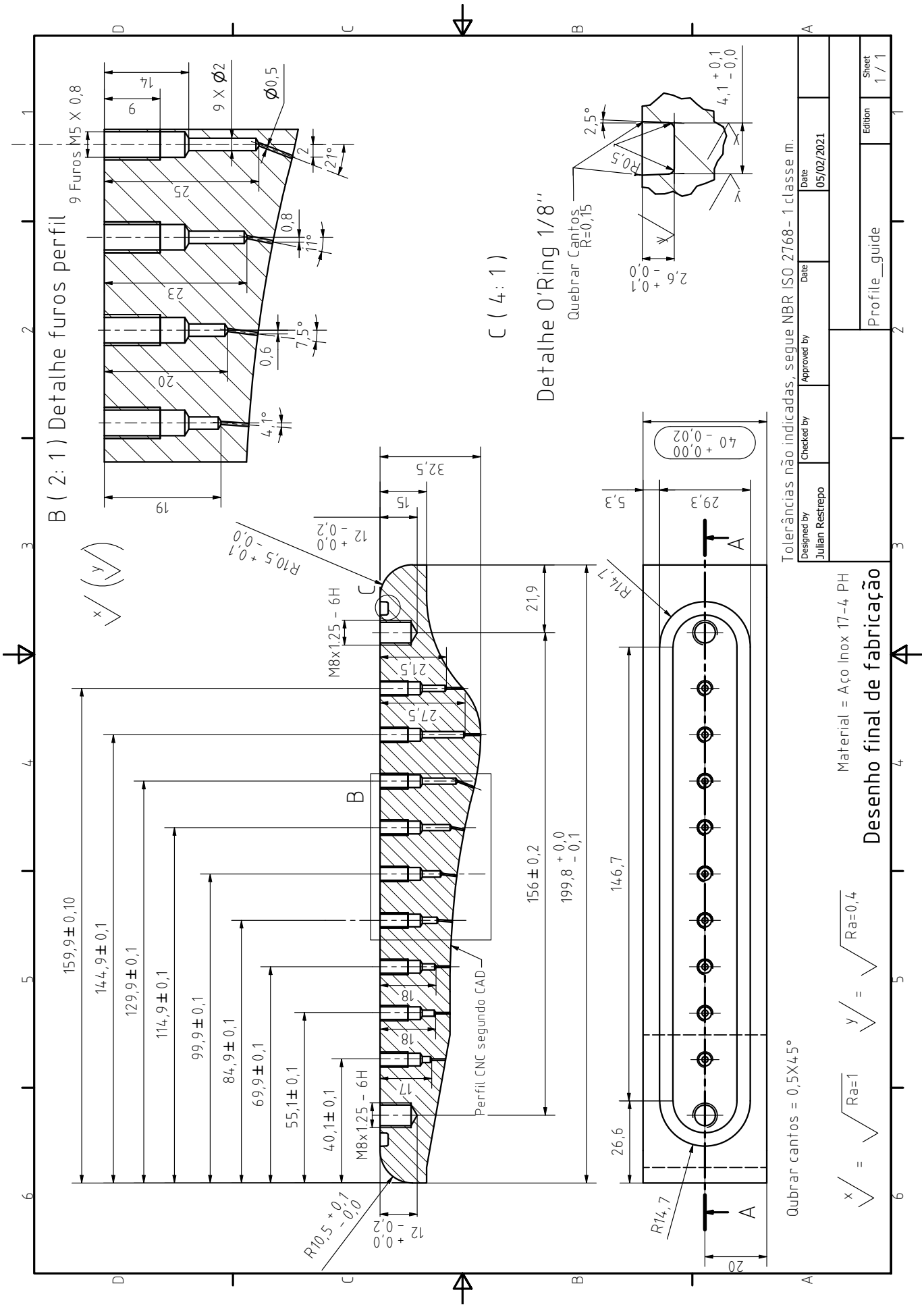

Figure F.3 – Nozzle profile 1A technical drawing.

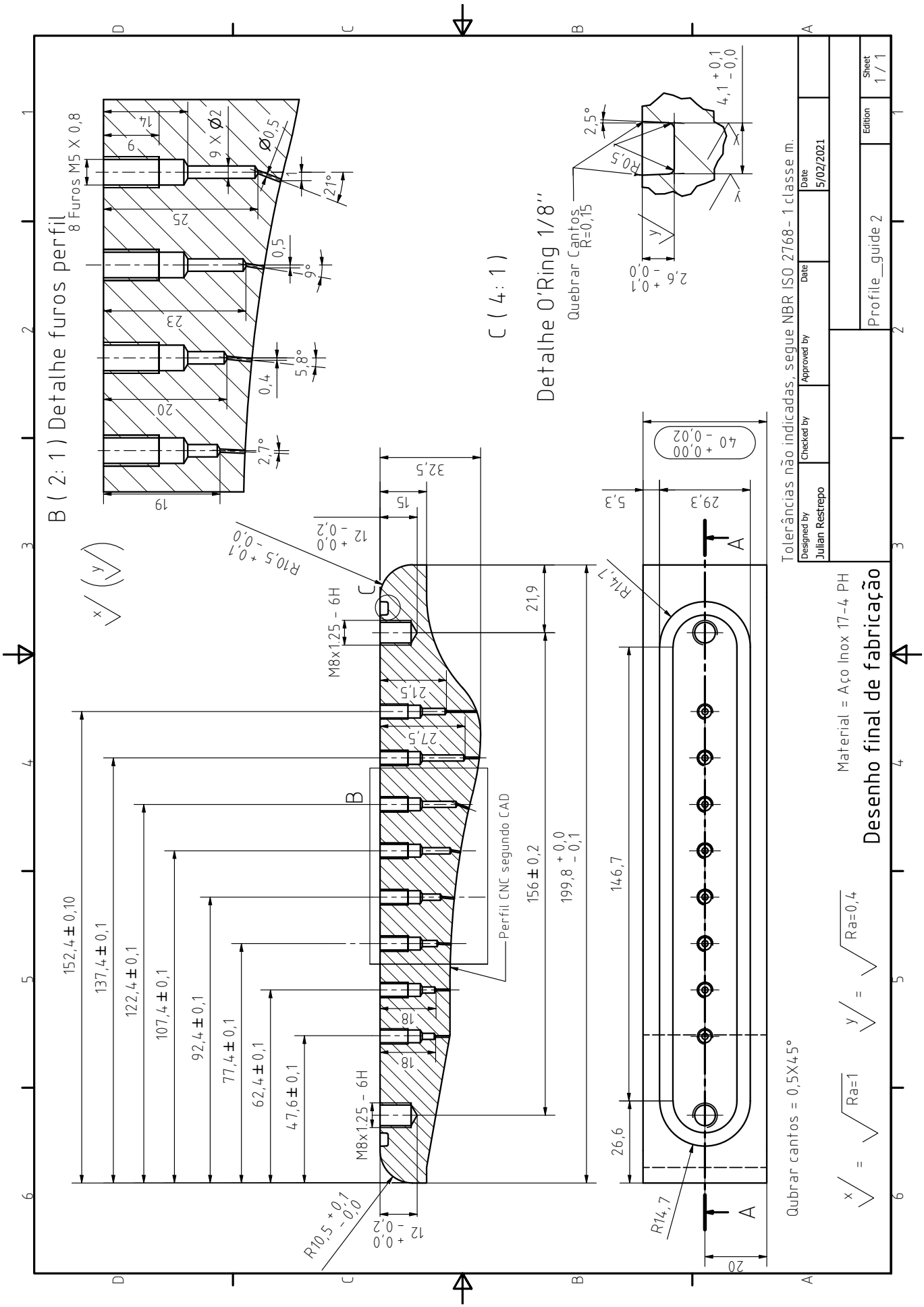

Figure F.4 – Nozzle profile 1B technical drawing.

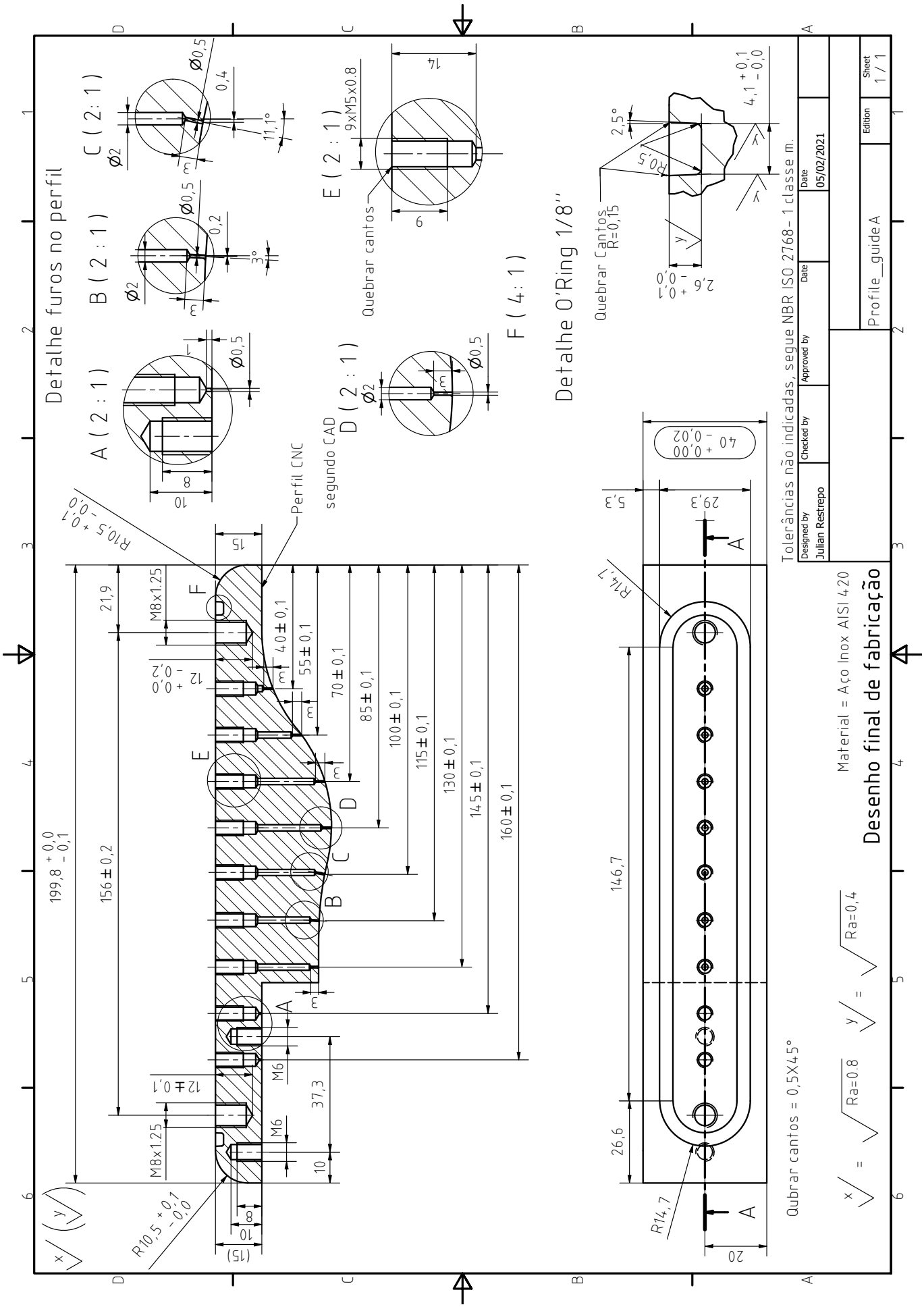

Figure F.5 – Nozzle profile 2A technical drawing.

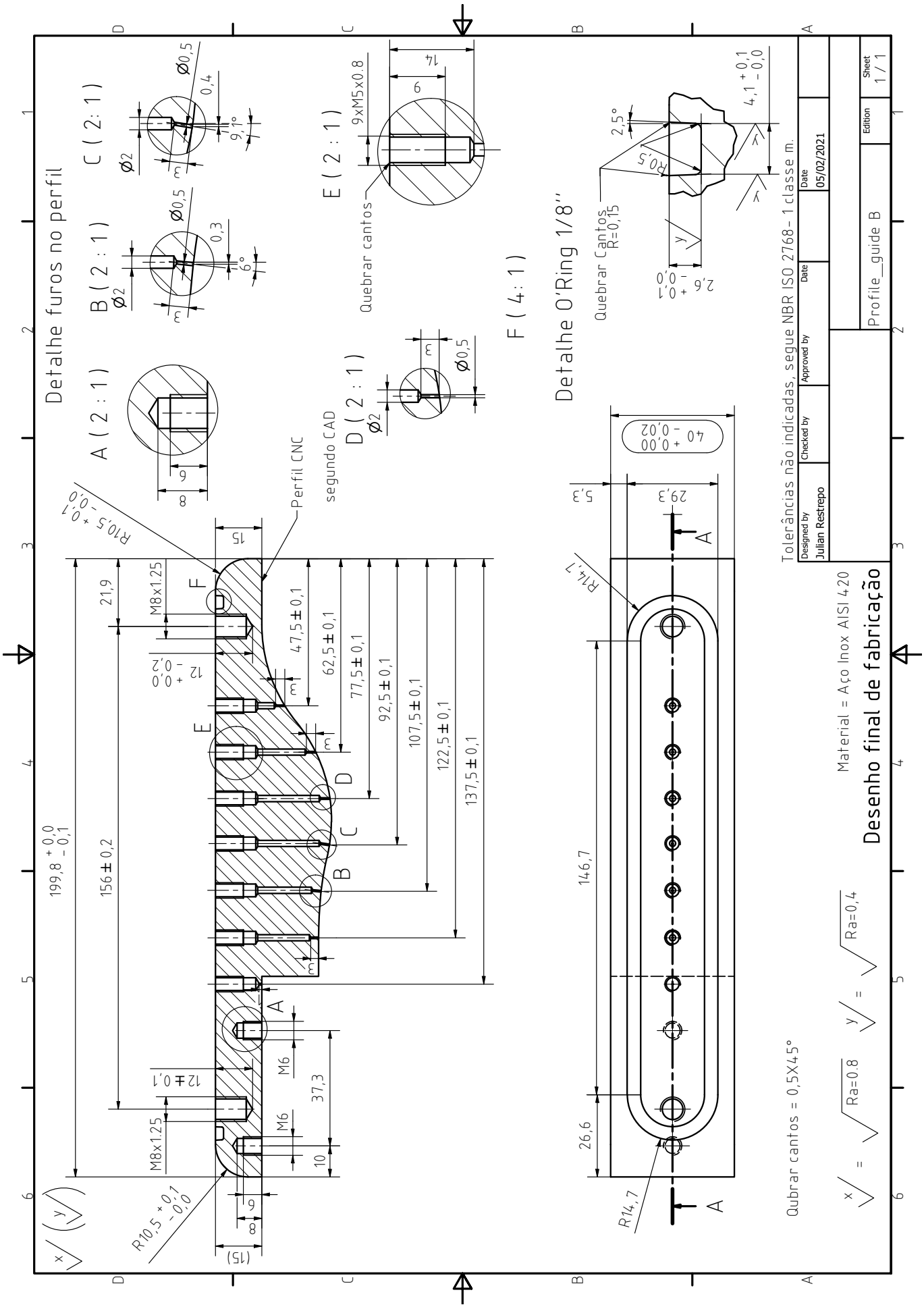

Figure F.6 – Nozzle profile 2B technical drawing.

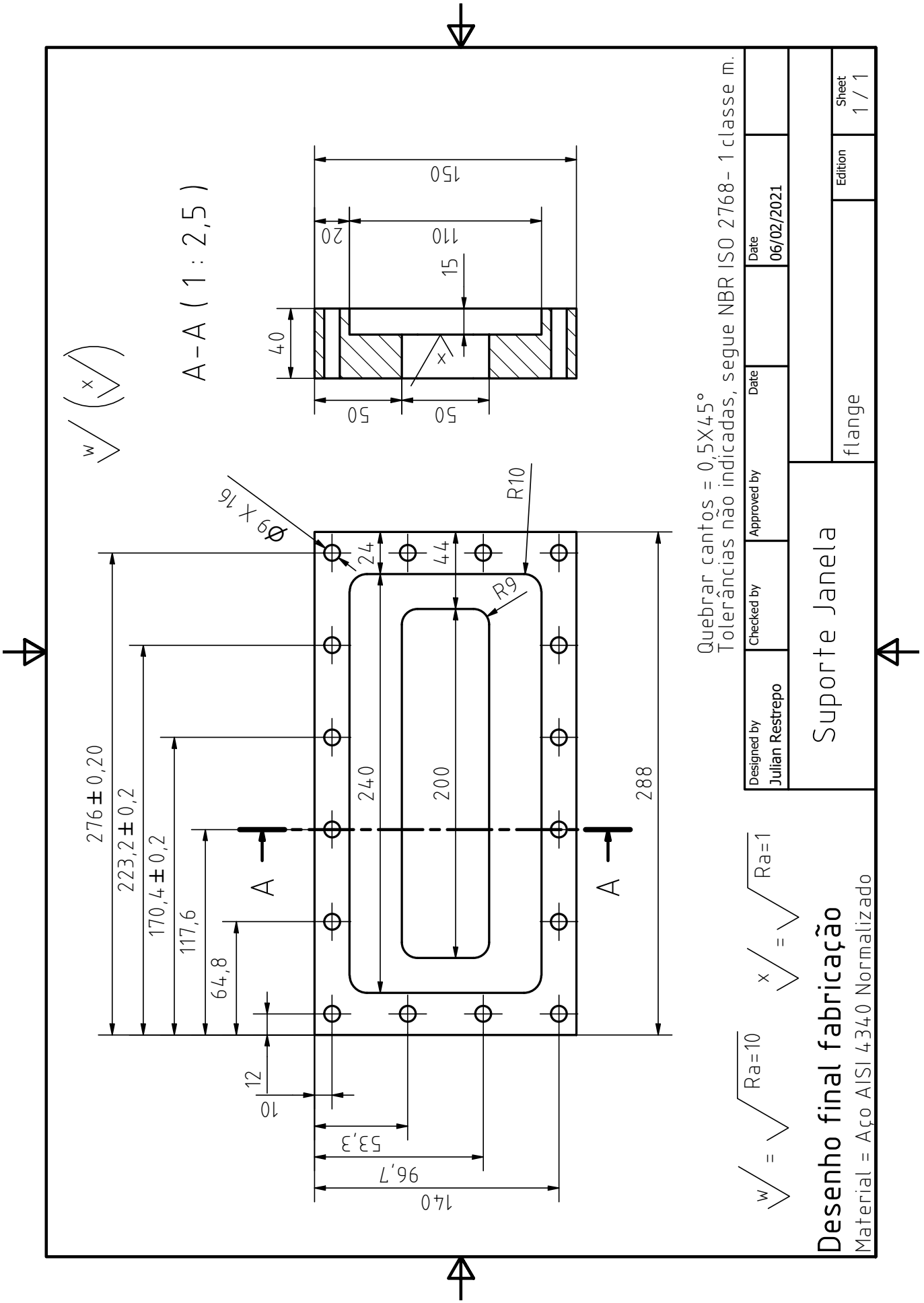

Figure F.7 – Window cover technical drawing.

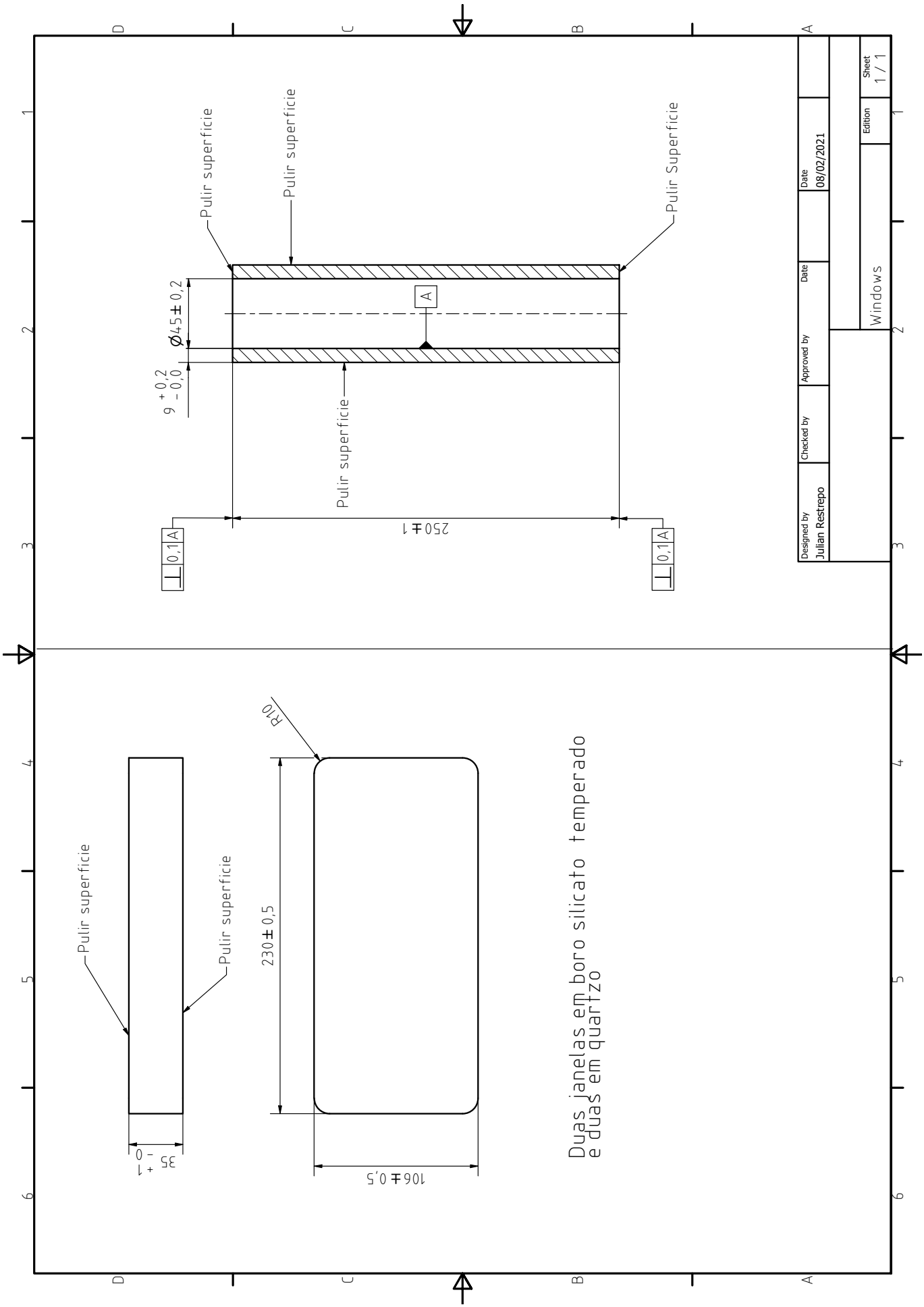

Figure F.8 – Optical windows technical drawing.

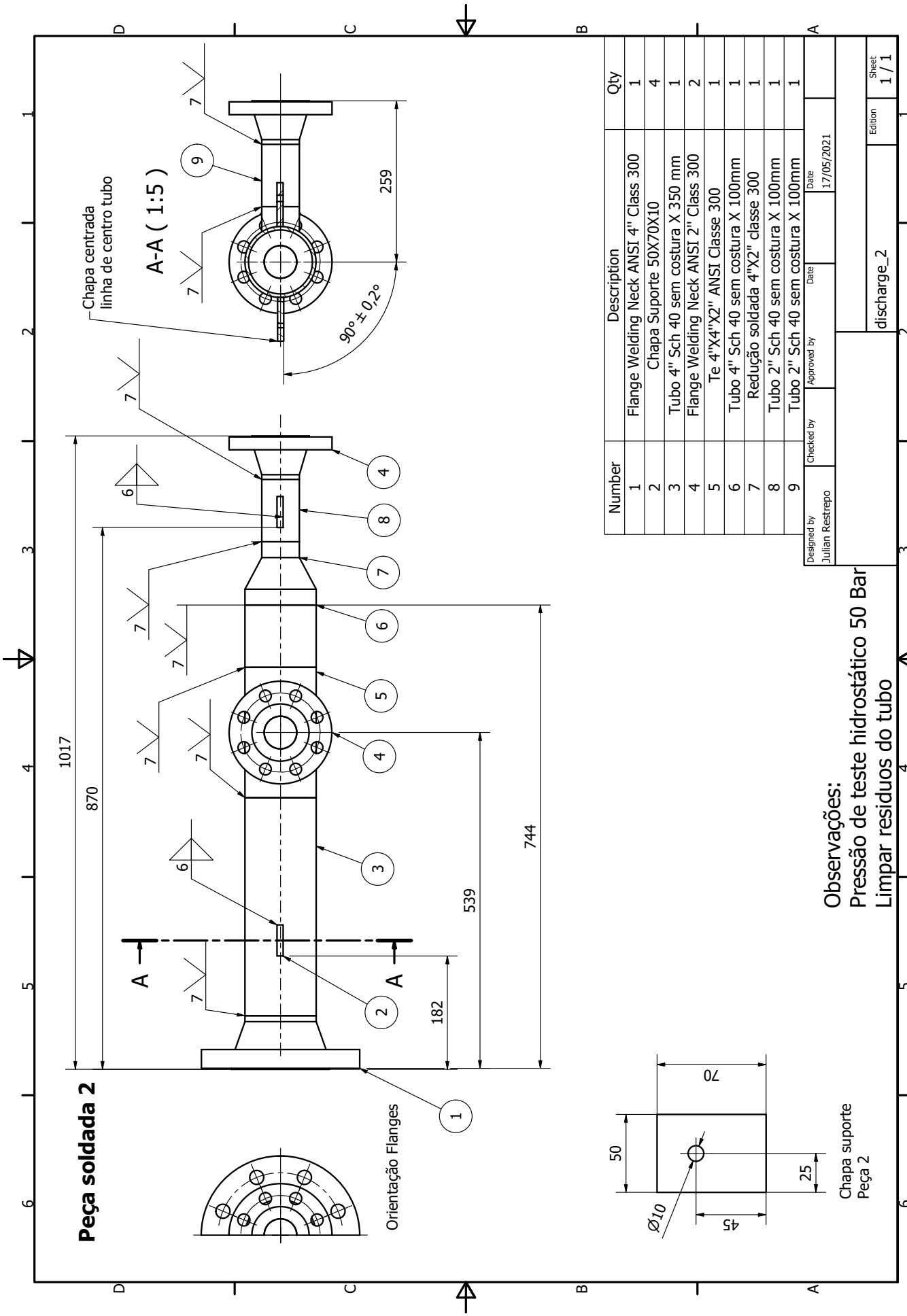

Figure F.9 – Discharge welded assembly 1.

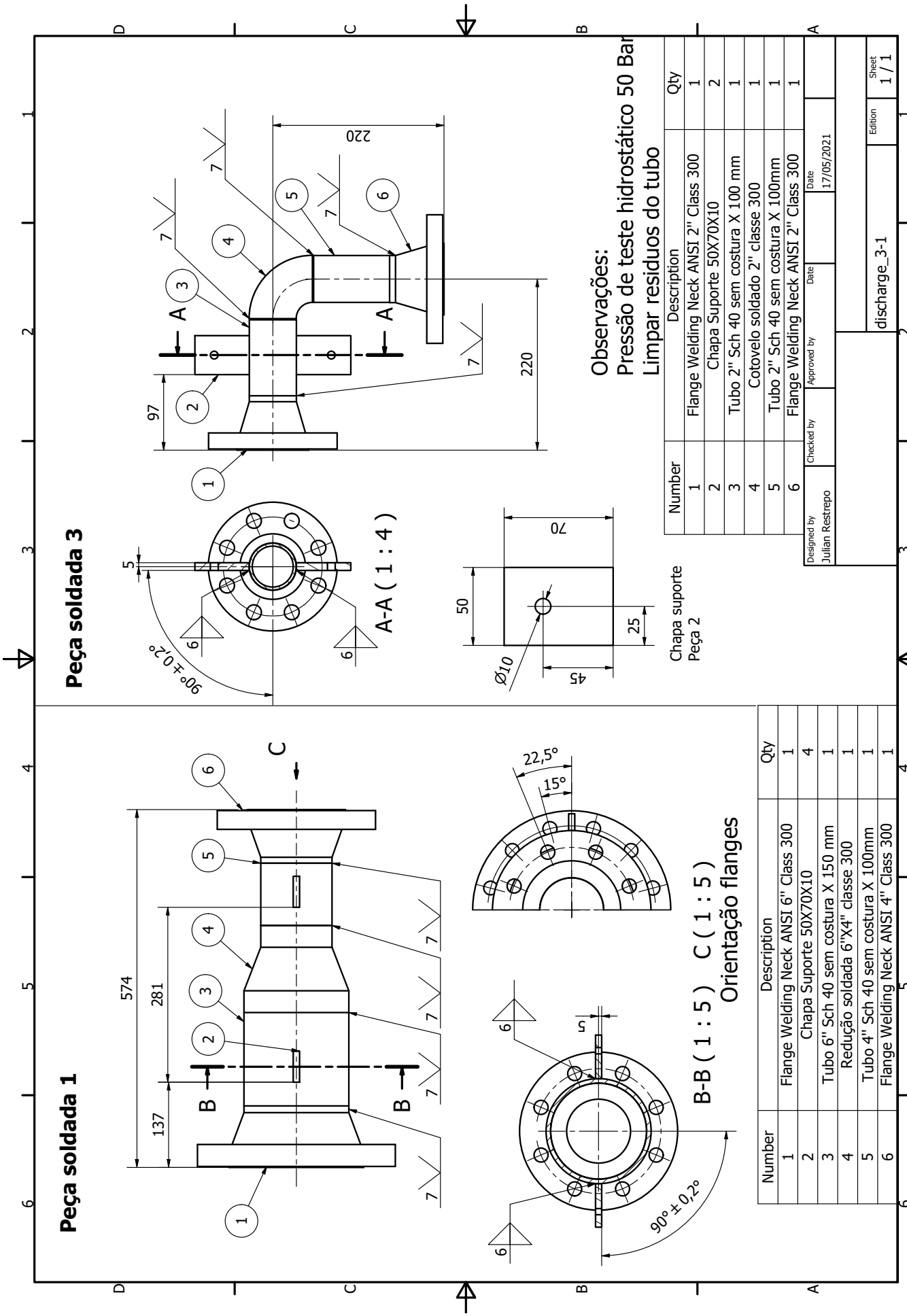

Figure F.10 – Discharge welded assembly 2.

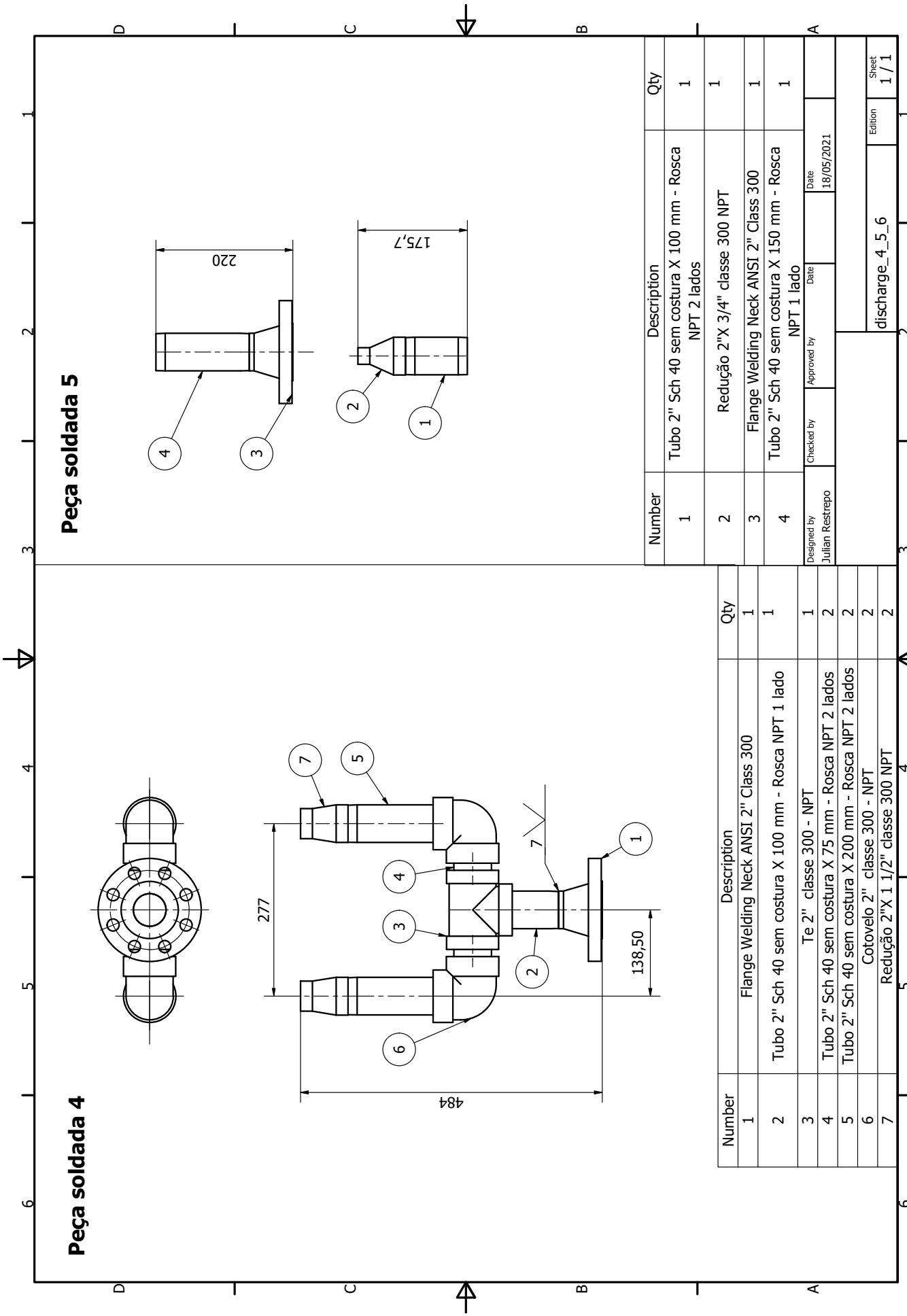

Figure F.11 – Discharge threaded assembly 3.

G Tank and compressor

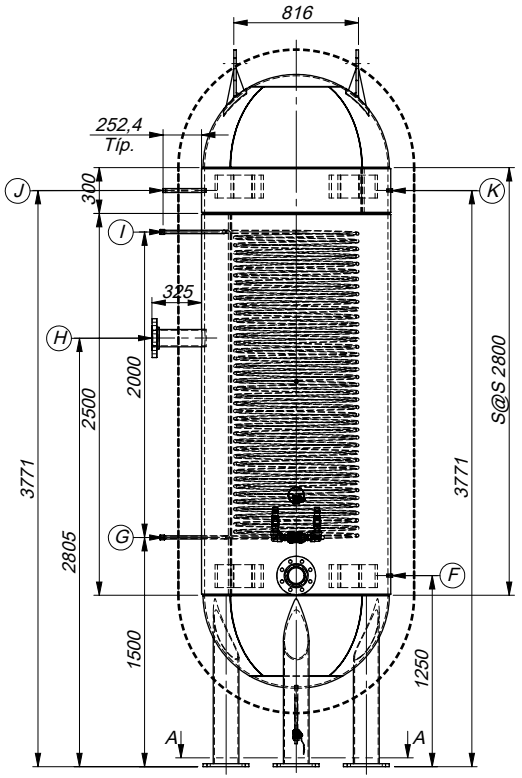

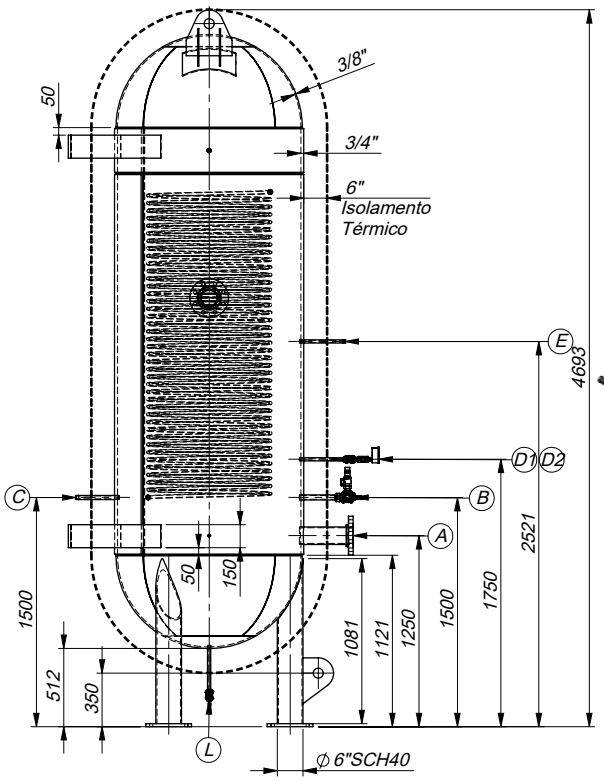

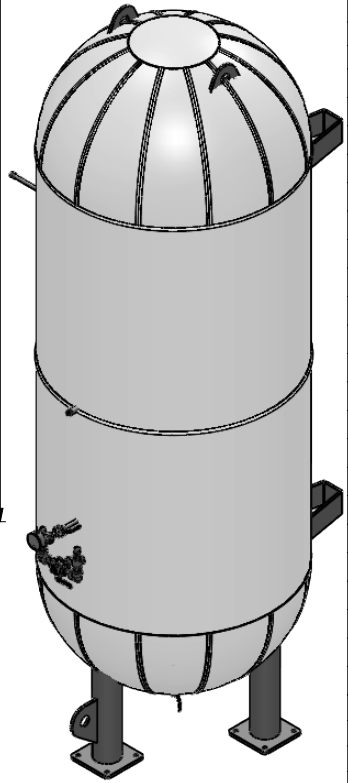

BOCAIS			
BOCAL	D.N.	TIPO	SERVIÇO
A	4"	FLANGE SORF 300#	ENTRADA
B	1"	NIPLE 1"SCH80	SEGURANÇA
C	3/4"	NIPLE 3/4"SCH80	ENTRADA AR COMPRIMIDO
D1	1/2"	TÊ NPT 3000#	MEDIÇÃO DE PRESSÃO
D2			TRANSDUTOR DE PRESSÃO
E	1/2"	TUBO 1/2"SCH80	MEDIÇÃO CONCENTRAÇÃO
F	1/4"	LUVA NPT 3000#	MEDIÇÃO TEMPERATURA
G	1/2"	TUBO 1/2"SCH40	ENTRADA SERPENTINA
H	4"	FLANGE SORF 300#	SAÍDA MISTURA
I	1/2"	TUBO 1/2"SCH40	SAÍDA SERPENTINA
J	3/4"	NIPLE 3/4"SCH80	ENTRADA CO_2
K	1/4"	LUVA NPT 3000#	MEDIÇÃO TEMPERATURA
L	1/2"	NIPLE 1/2"SCH80	DRENO

CARACTERISTICAS TÉCNICAS	
NORMA CONSTRUTIVA	ASME SEC. VIII div.1 2007/08
PRESSÃO MÁX. DE SERVIÇO	45 barg
PRESSÃO DE TESTE PNEUMÁTICO	58,5 barg
TEMPERATURA DE CÁLCULO	-5°C @ 100°C
TEMPERATURA MÁX. DE OPERAÇÃO	60°C
TEMPERATURA DE TESTE	AMBIENTE
ESP. DE CORROSÃO	0
PRODUTO	Ar + CO_2 (50% / 50%)
TRATAMENTO TÉRMICO	NÃO
ULTRASSOM	CONFORME CÓDIGO
COEFICIENTE DE RES. RELATIVA	COSTADO: 1,0 / TAMPOS: 1,0
PÊSO VAZIO	3.200 Kg.
PÊSO CHEIO DE ÁGUA	7.272 Kg.
CAPACIDADE GEOMÉTRICA	4.072 litros
CAPACIDADE ÚTIL	4.072 litros
ISOLAMENTO	6" (poliuretano)
DENSIDADE DO PRODUTO	N/A
MATERIAL	SA516 Gr.70
TAMPOS	SEMIESFÉRICO
CAMISA	ALUMÍNIO

NR:13 GRUPO:3 CLASSE:C CATEGORIA: III

MATERIAIS	
COSTADO	ASTM A516 Gr.70
TAMPOS	ASTM A516 Gr.70
FLANGES	ASTM A105
PÉS DE APOIO	ASTM A106 Gr.B
BASE DE FIXAÇÃO	ASTM A36
OLHAIS DE IÇAMENTO	ASTM A36
LUVAS	ASTM A105
TUBOS	ASTM A106 Gr.B

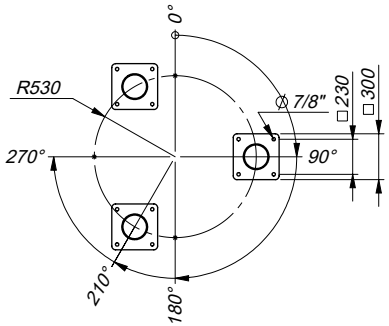

SEÇÃO **A-A**

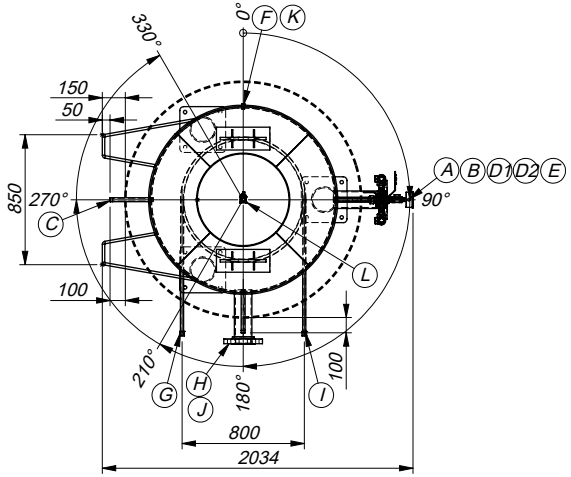

TOLERÂNCIAS LINEARES ADMISSÍVEIS PARA CALDEIRARIA (DIN EN ISO13920:1996)								
DIMENSÕES (mm)	>2,0<30,0	>30,1<400,0	>400,1<1000,0	>1000,1<2000,0	>2000,1<4000,0	>4000,1<8000,0	>8000,1<12000,0	>12000,1<16000,0
TOLERÂNCIAS (mm)	± 1,0	± 2,0	± 3,0	± 4,0	± 6,0	± 8,0	± 10,0	± 12,0

CLIENTE:

NITROTEC

DATA:	DESENHADO POR:	EQUIPAMENTO:
21/11/2019	WAGNER VITORINO	VPV04-45 - Tanque de Ar Comprimido e CO_2
VERIFICADO POR: ARLINDO FORNAS	APROVADO POR: CARLOS FORNAS	TÍTULO: Conjunto Geral
ESCALA: S/E		DESENHO Nº: VPV04-45-00 REV.: 02

(A3 - 297 x 420mm)

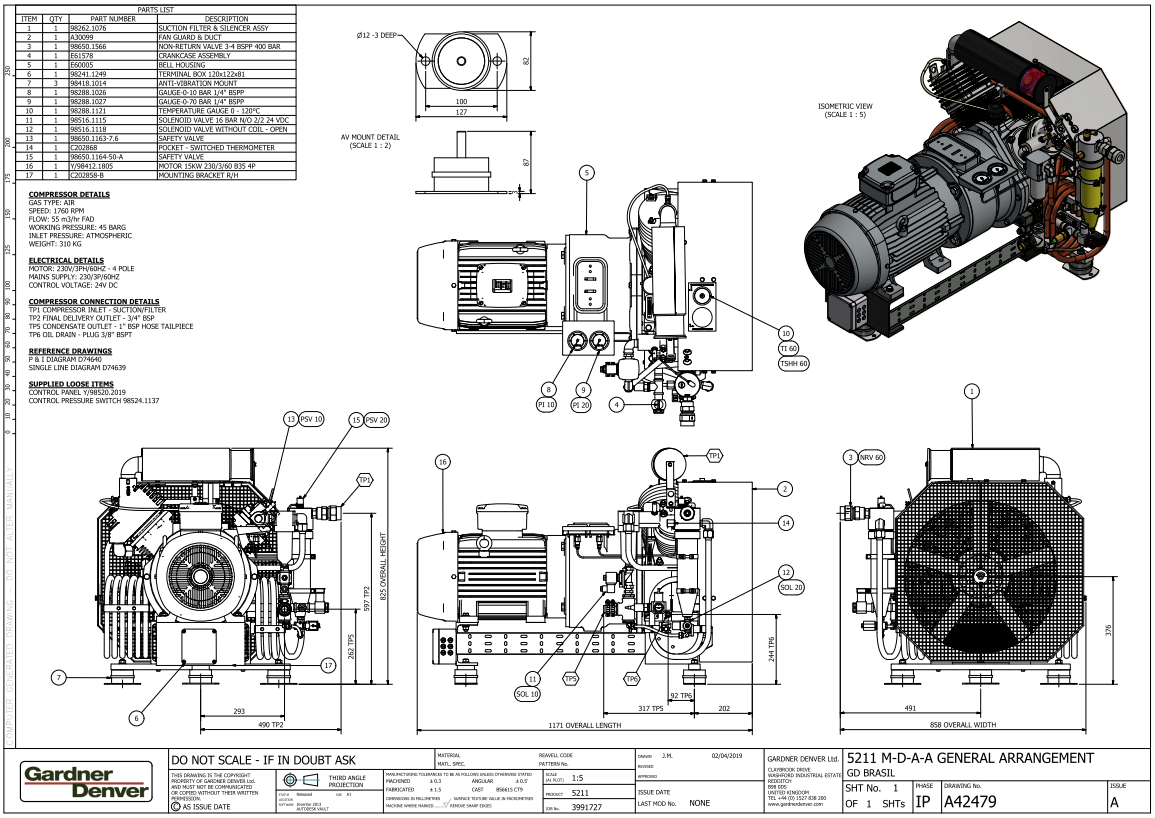

Figure G.1 – Compressor Reavell 5211 layout

H Calibration and uncertainty analysis

H.1 Stagnation temperature calibration

Due to the importance of the temperature stagnation measurements on the experimental outcomes, it is mandatory asses their uncertainties. Bearing this in mind it was bought and used a dry block calibrator (Presys T-25N) in order to calibrate the T type thermocouple and the data acquisition system used (National instruments Chassis CDAQ-9189 and temperature module NI 9213) because the calibration data was processed after being acquired. The calibration range was -20 to 35 °C and due to the ambient humid air condensation and freezing, the calibration proceedure was performed in a decreasing fashion, in order to avoid the ice formation between the thermocouple and the block calibrator. Fig. H.1 presents the thermocouple calibration at -10 °C, it was used a calibrated thermometer in order to validate the used approach.

The routine proposed by Vieira (2005) is used for the calibration uncertainty estimation. Firstly, the linear regression adjust parameters were computed in Microsoft Excel, being the fit constants $y = ax + b$, where a and b are reported in Table H.1. Later, the $error = y - y_{measurement}$ was estimated for all the calibrated points. After assesing the $error$ estimation, the standard error of estimate SEE was computed, this parameter inform us the deviation between the calibrated instrument and the measurement "true" value. It can be computed as:

$$SEE = \sqrt{\frac{\sum(error)^2}{N_{samples} - 2}} \tag{H.1}$$

For level of confidence of 95.45%, the uncertainty related to the thermocouple can be described as:

$$U_T = 2SEE \tag{H.2}$$

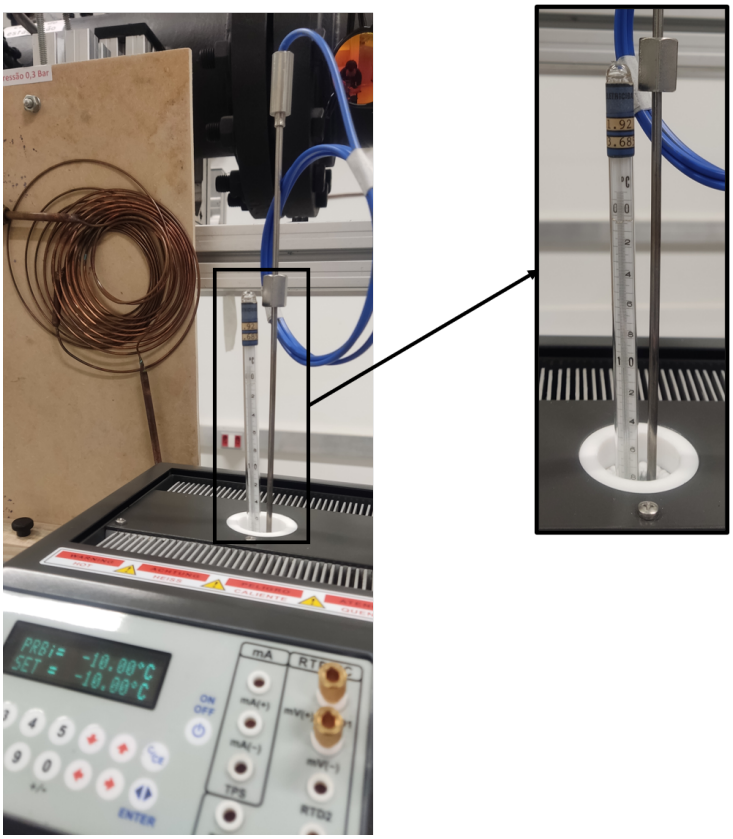

Figure H.1 – Temperature dry block calibrator and reference.

Source: Author

Also one have to consider the ubncertainity related to the dry block calibrator measurement, and according to the device manufacturer is $U_{ref} = 0.1$ °C for a level of confidence of 95.45%. Finally the instrument combined uncertainity can be computed as:

$$U_{combined} = (U_T^2 + U_{ref}^2)^{1/2} \tag{H.3}$$

H.2 Nozzle pressure transducer calibration

As explained in the last section, the nozzle pressure transducers must be assessed in order to guarantee the quality of the experimental results. This also applied for the kulite pressure transducers, due to the relevance on the experimental nozzle characterization. Fig. H.2 presents the connection between the pressure calibrator and the test-rig, because all the transducers were connected at the same time, and the pressure regulation valve was used to change the pressure level as required by the calibration, in addtion, the calibration data considers the signal amplifier (MCS1000 Lynx) and the data a the National instruments Chassis CDAQ-9189 and the corresponding high-speed data acquisition module NI 9220. Therefore, all the data deviations originated by these devices were considered and adjusted in the calibration process.

Table H.1 – Stagnation thermocouple calibration and uncertainty assessment

Linear regression results		
a	b (°C)	R^2
1.0098	-5.3385	0.9999
Uncertainity analysis		
Temp (°C)	Measurement (°C)	*Error* (°C)
35	35.21	-0.21
30	30.09	-0.09
25	25.01	-0.01
20	19.94	0.06
15	14.90	0.10
10	9.79	0.21
5	4.83	0.17
0	-0.07	0.07
-5	-5.03	0.03
-10	-9.96	-0.04
-15	-14.87	-0.13
-20	-19.86	-0.14
	SEE (°C)	0.14
	U_c Thermocouple (°C)	0.27
	U_c Reference (°C)	0.10
	U_{comb} (°C)	0.29

The kulite calibration was performed as presented for the stagnation chamber thermocouple, however, the kulite calibration was divided into two groups, the first one is the calibration of the 17 bar kulites group, presented in Table H.2 and the 35 bar kulites group, presented in Table H.3, on these tables are presented the kulite series number, reference, calibration constants and uncertainties, according to the procedure presented in the last section.

Table H.2 – 17 bar kulites calibration and uncertainty assessment

Series number	195	196	197	199	201	203	205	206	207
Reference	KTE01	KTE02	KTE03	KTE04	KTE05	KTE06	KTE07	KTE08	KTE09
a (bar/V)	1.6988	1.7024	1.7217	1.7043	1.7113	1.6976	1.7025	1.7128	1.6983
b (bar)	0.4766	-0.4492	-0.0224	0.4072	0.2337	0.1956	-0.0161	-0.3612	0.0874
R^2	0.999999	0.999999	0.999999	0.999999	0.999999	0.999999	0.999999	0.999999	0.999999
U_c reference (bar)	0.0014	0.0014	0.0014	0.0014	0.0014	0.0014	0.0014	0.0014	0.0014
U_c kulite (bar)	0.0013	0.0014	0.0016	0.0036	0.0013	0.0014	0.0014	0.0013	0.0142
U_{comb} (bar)	0.0019	0.0019	0.0021	0.0039	0.0019	0.0020	0.0019	0.0019	0.0143

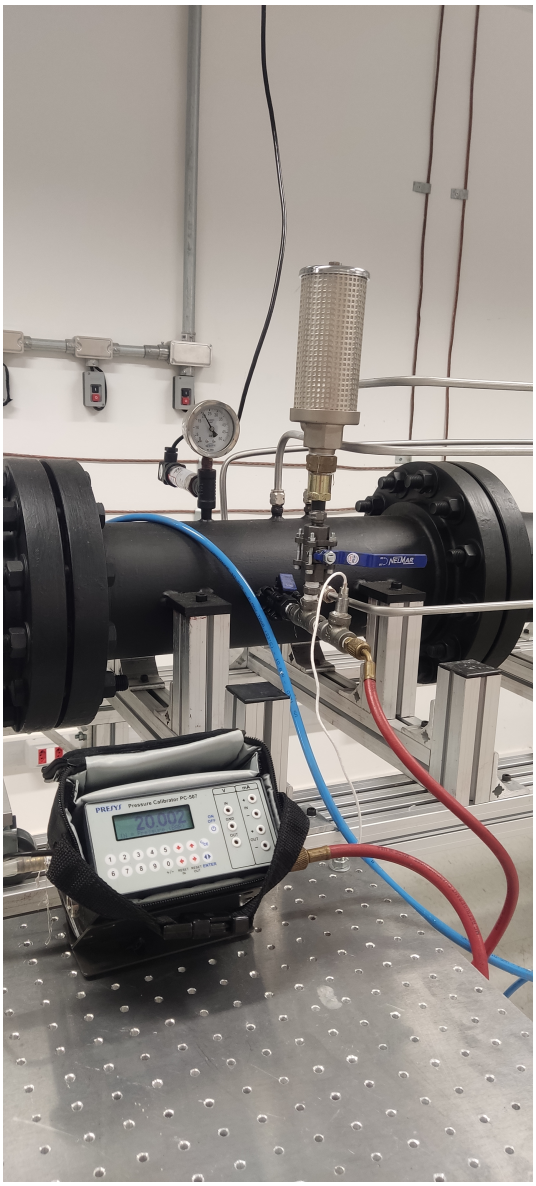

Figure H.2 – Pressure calibrator connection to test-rig.

Source: Author

Table H.3 – 35 bar kulites calibration and uncertainty assessment

Series number	432	433	434	435	436	437	438	439	449
Reference	KTE11	KTE12	KTE13	KTE14	KTE15	KTE16	KTE17	KTE18	KTE19
a (bar/V)	3.4920	3.5079	3.5037	3.4938	3.5089	3.4985	3.4424	3.4868	3.4965
b (bar)	-0.0079	-0.0521	-0.0263	0.1383	0.8349	-0.0860	1.0687	-0.6165	0.6314
R^2	0.999999	0.999999	0.999999	0.999999	0.999999	0.999999	0.999999	0.999999	0.999999
U_c reference (bar)	0.0041	0.0041	0.0041	0.0041	0.0041	0.0041	0.0041	0.0041	0.0041
U_c kulite (bar)	0.0121	0.0152	0.0113	0.0115	0.0129	0.0164	0.0116	0.0134	0.0135
U_{comb} (bar)	0.0128	0.0157	0.0120	0.0122	0.0135	0.0169	0.0123	0.0141	0.0141

I

Experimental results

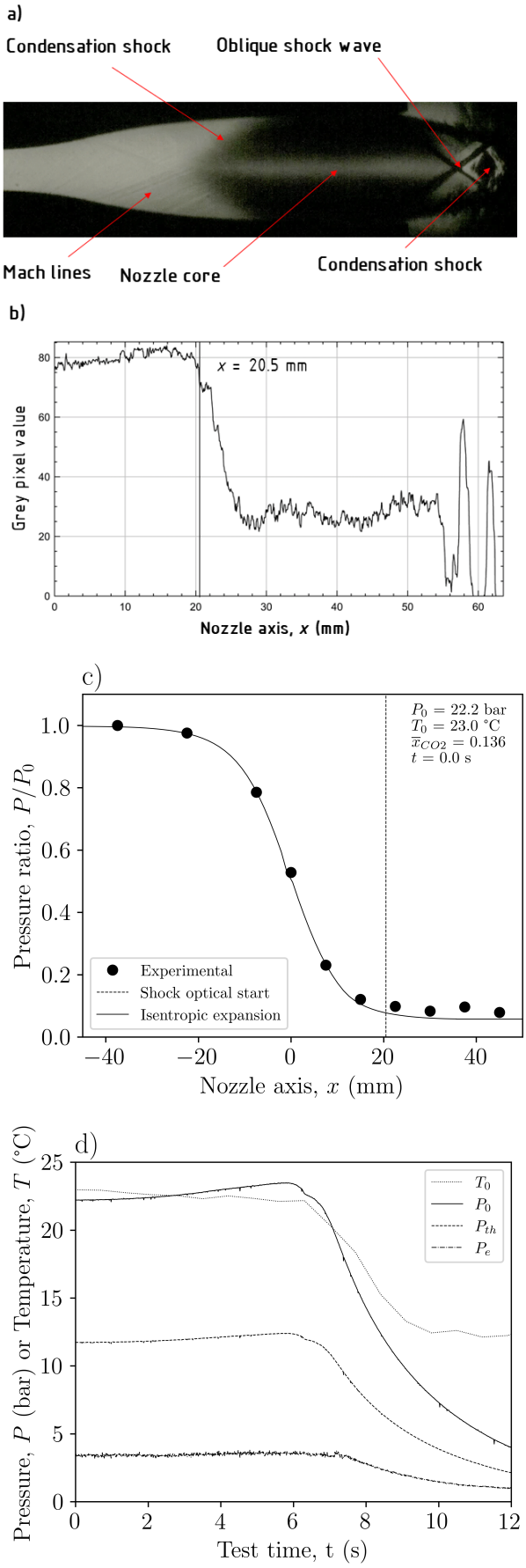

Figure I.1 – Test 21 results, a) Supersonic channel schlieren still picture b) Nozzle centreline grey pixel intensity, c) Nozzle pressure profile for a $t = 0$ s, d) Stagnation P_0, throat P_{th}, exit pressure P_e and stagnation temperature T_0 test evolution.

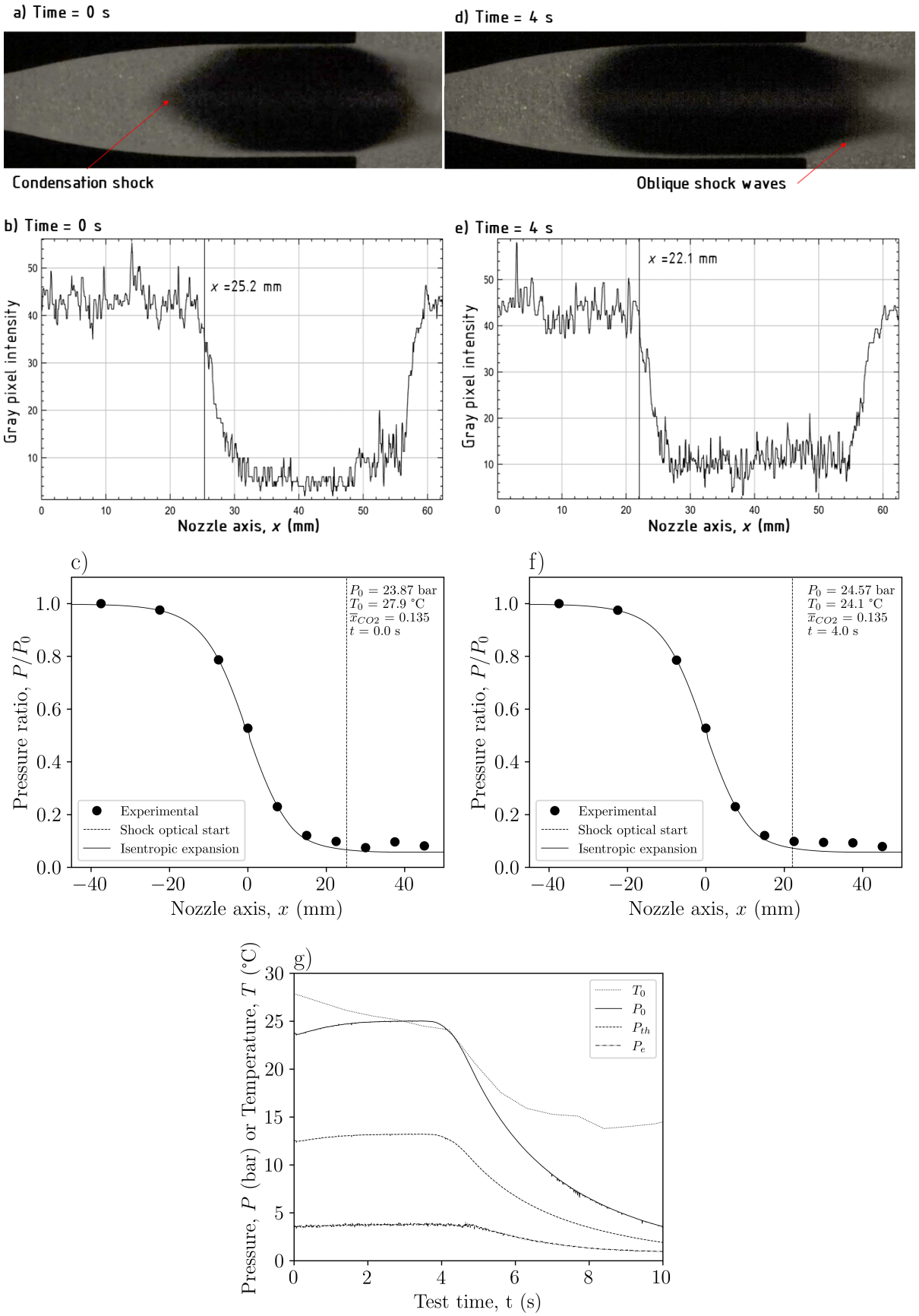

Figure I.2 – Test 22 results, left $t = 0$ s and right $t = 4$ s. a and b) Supersonic channel direct still picture, c and d) Nozzle centreline grey pixel intensity, e and f) Nozzle pressure profile and g) Stagnation P_0, throat P_{th}, exit pressure P_e and stagnation temperature T_0 test evolution.

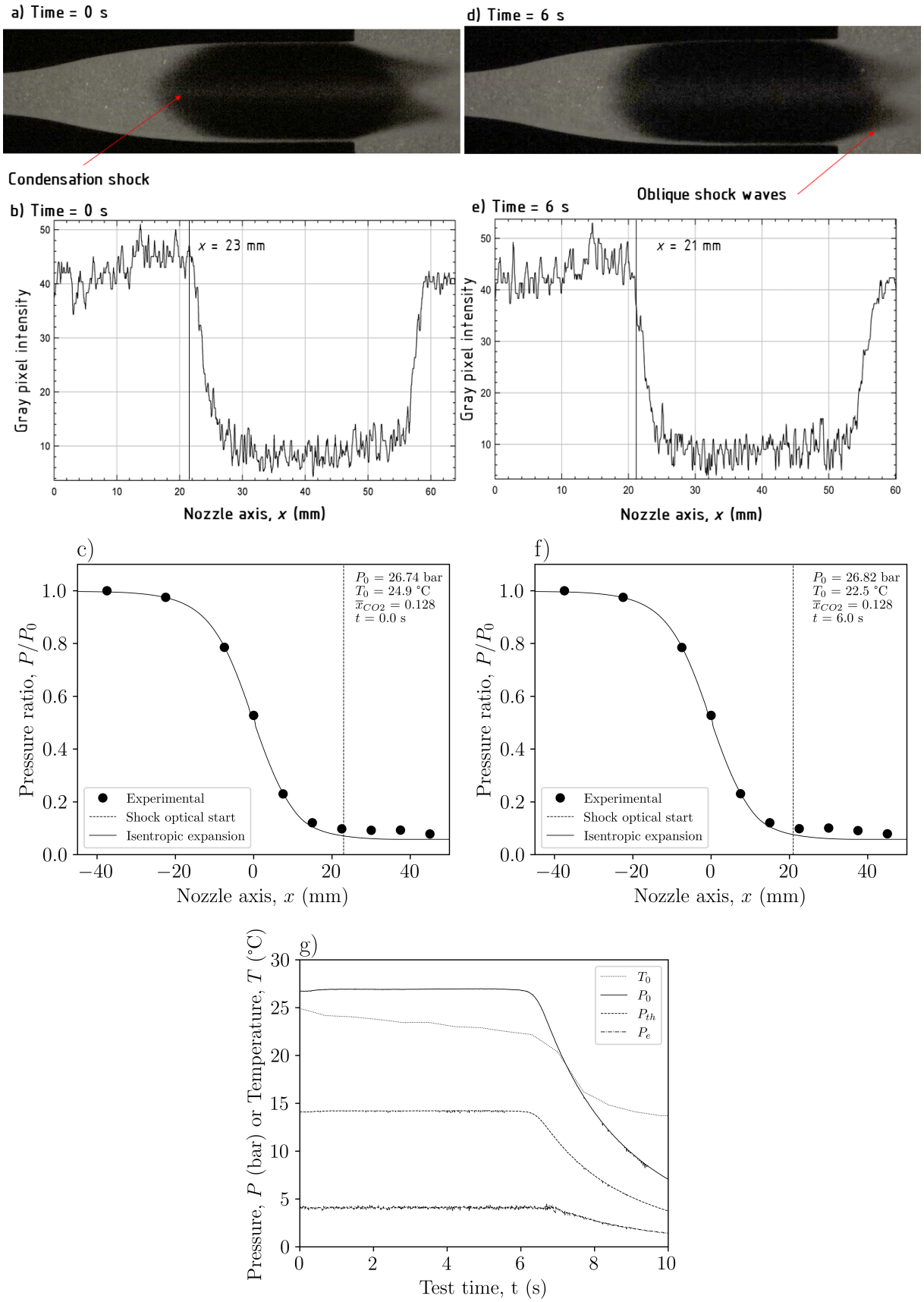

Figure I.3 – Test 23 results, left $t = 0$ s and right $t = 6$ s. a and b) Supersonic channel direct still picture, c and d) Nozzle centreline grey pixel intensity, e and f) Nozzle pressure profile and g) Stagnation P_0, throat P_{th}, exit pressure P_e and stagnation temperature T_0 test evolution.

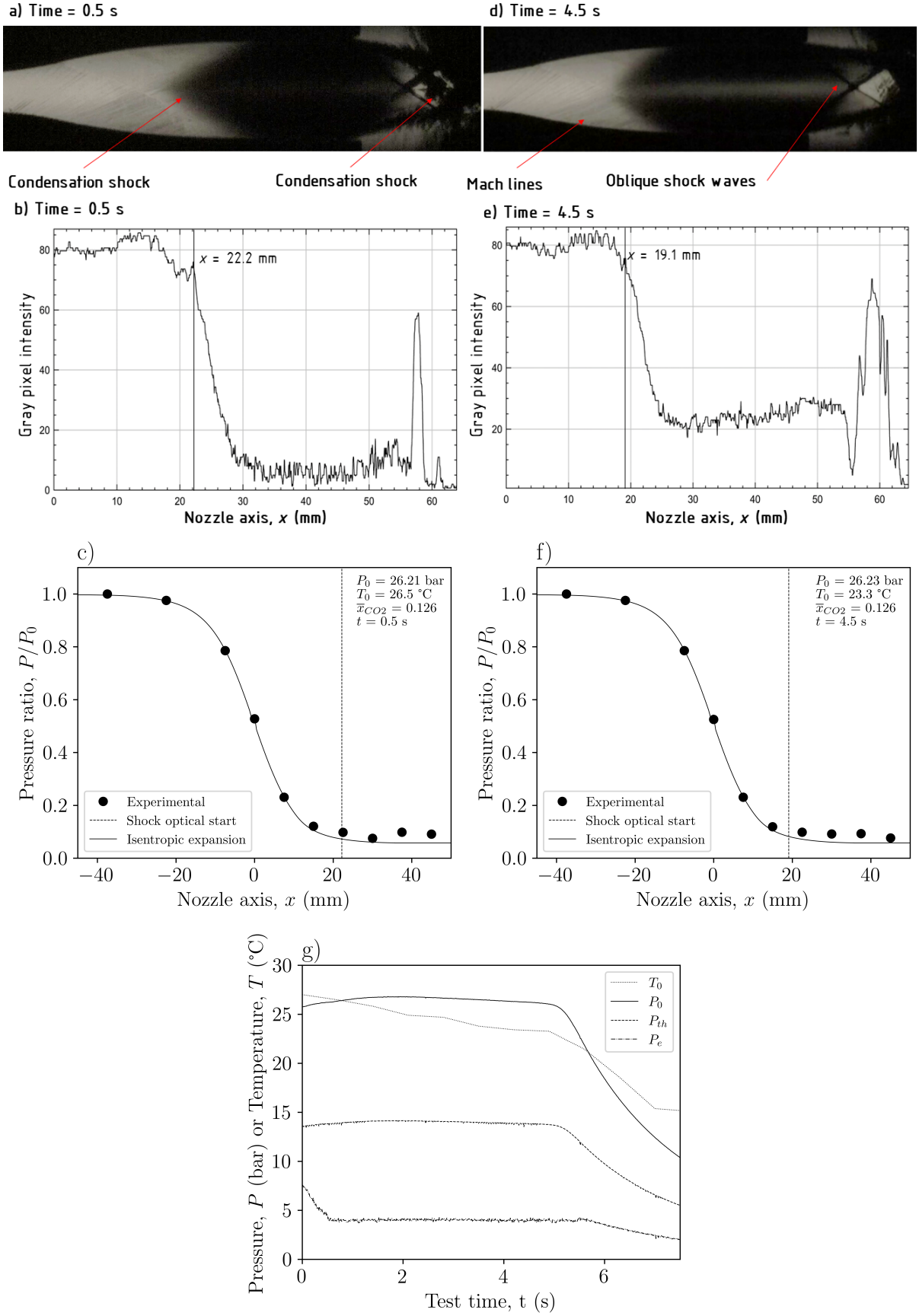

Figure I.4 – Test 24 results, left $t = 0.5$ s and right $t = 4.5$ s. a and b) Supersonic channel schlieren still picture, c and d) Nozzle centreline grey pixel intensity, e and f) Nozzle pressure profile and g) Stagnation P_0, throat P_{th}, exit pressure P_e and stagnation temperature T_0 test evolution.

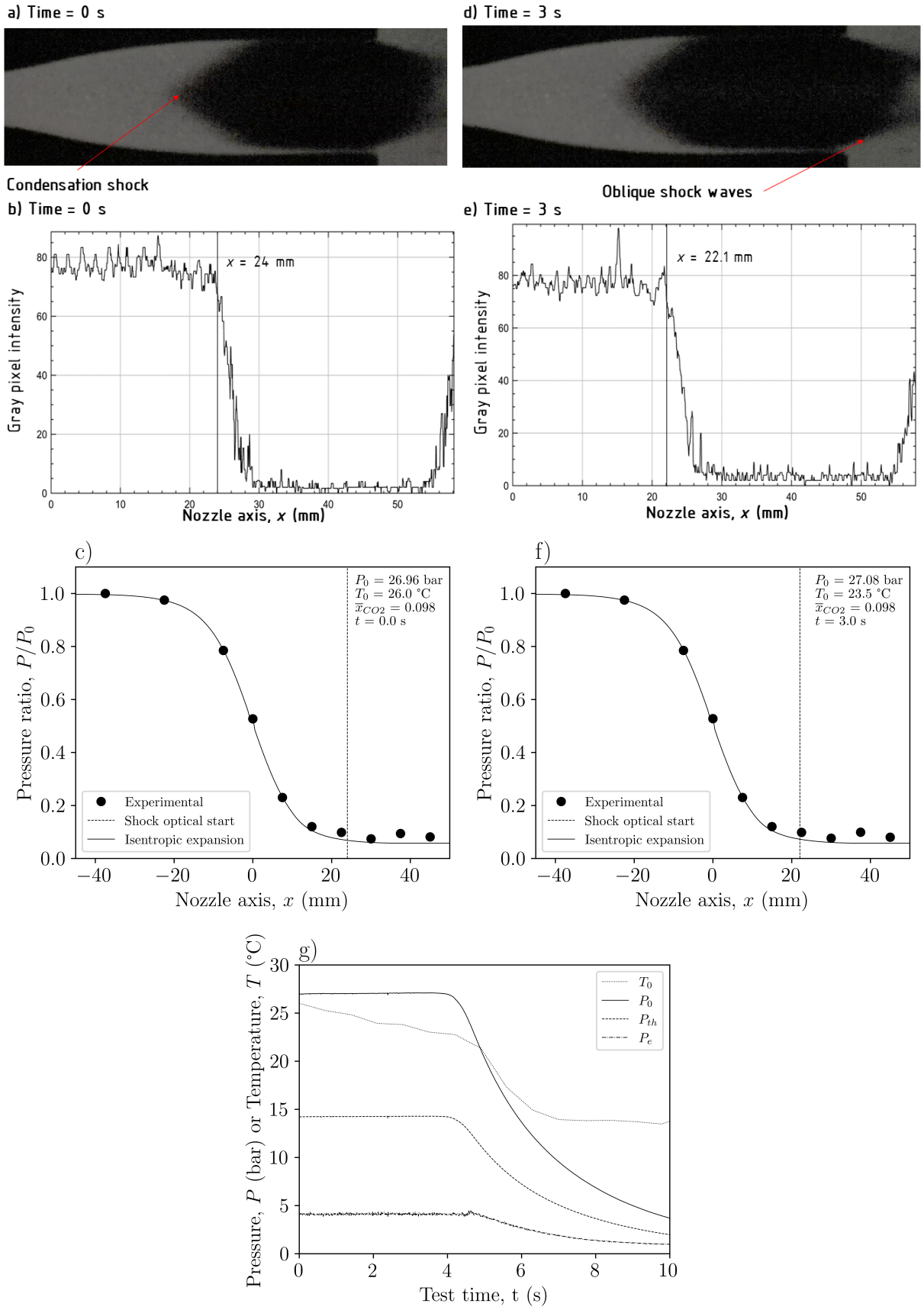

Figure I.5 – Test 25 results, left $t = 0$ s and right $t = 3$ s. a and b) Supersonic channel direct still picture, c and d) Nozzle centreline grey pixel intensity, e and f) Nozzle pressure profile and g) Stagnation P_0, throat P_{th}, exit pressure P_e and stagnation temperature T_0 test evolution.

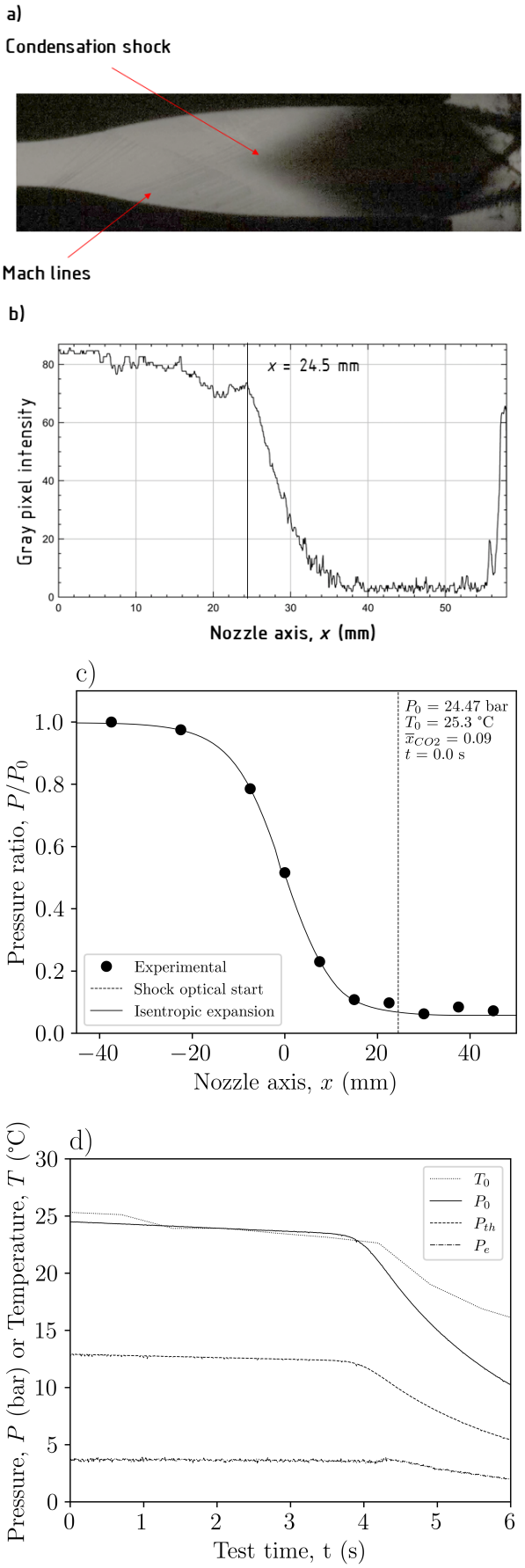

Figure I.6 – Test 26 results, a) Supersonic channel schlieren still picture b) Nozzle centreline grey pixel intensity, c) Nozzle pressure profile for a $t = 0$ s, d) Stagnation P_0, throat P_{th}, exit pressure P_e and stagnation temperature T_0 test evolution.

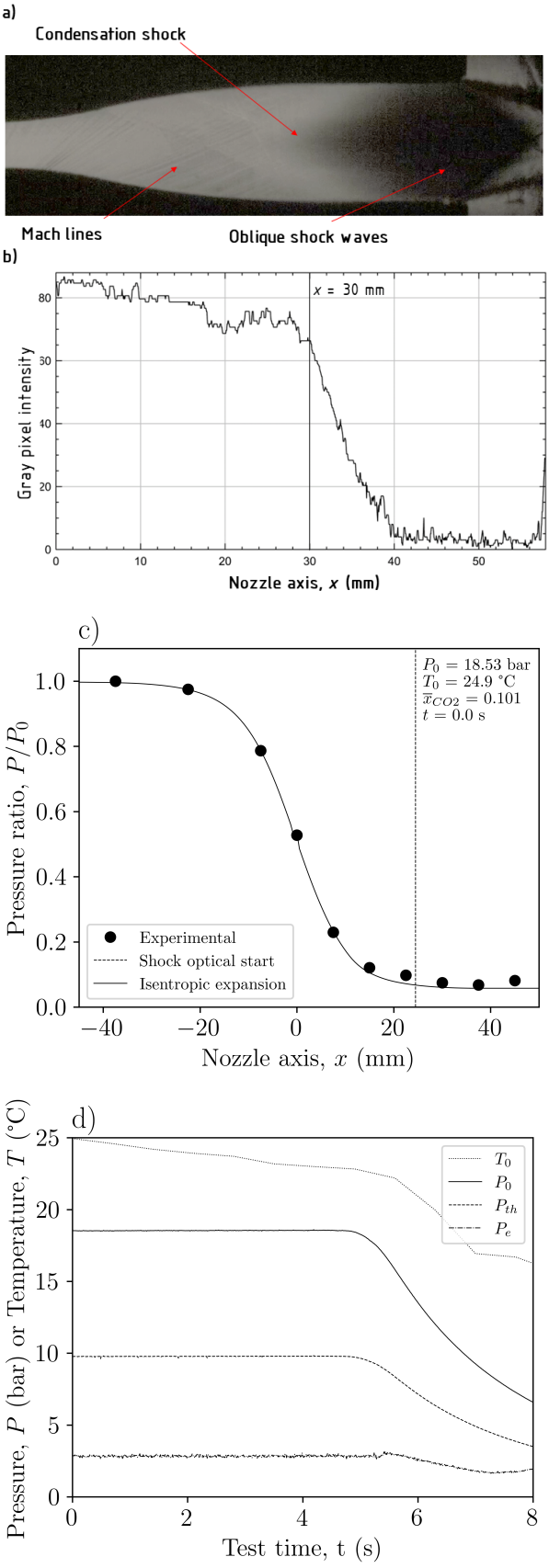

Figure I.7 – Test 27 results, a) Supersonic channel schlieren still picture b) Nozzle centreline grey pixel intensity, c) Nozzle pressure profile for a $t = 0$ s, d) Stagnation P_0, throat P_{th}, exit pressure P_e and stagnation temperature T_0 test evolution.

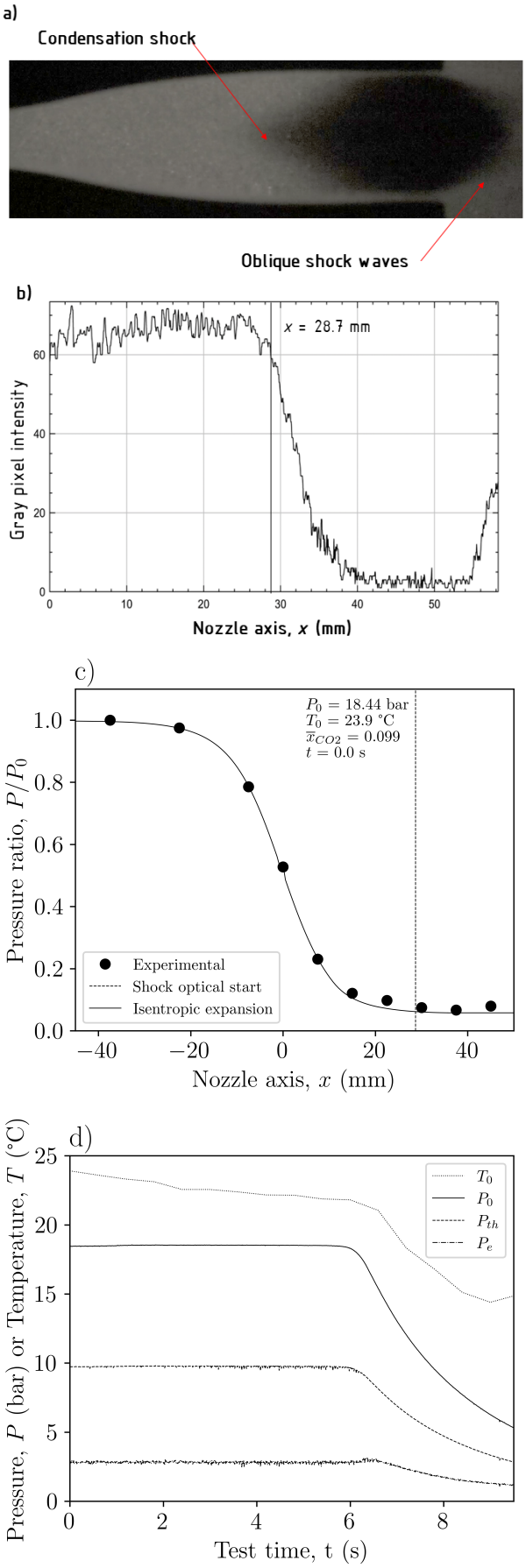

Figure I.8 – Test 28 results, a) Supersonic channel direct still picture b) Nozzle centreline grey pixel intensity, c) Nozzle pressure profile for a $t = 0$ s, d) Stagnation P_0, throat P_{th}, exit pressure P_e and stagnation temperature T_0 test evolution.

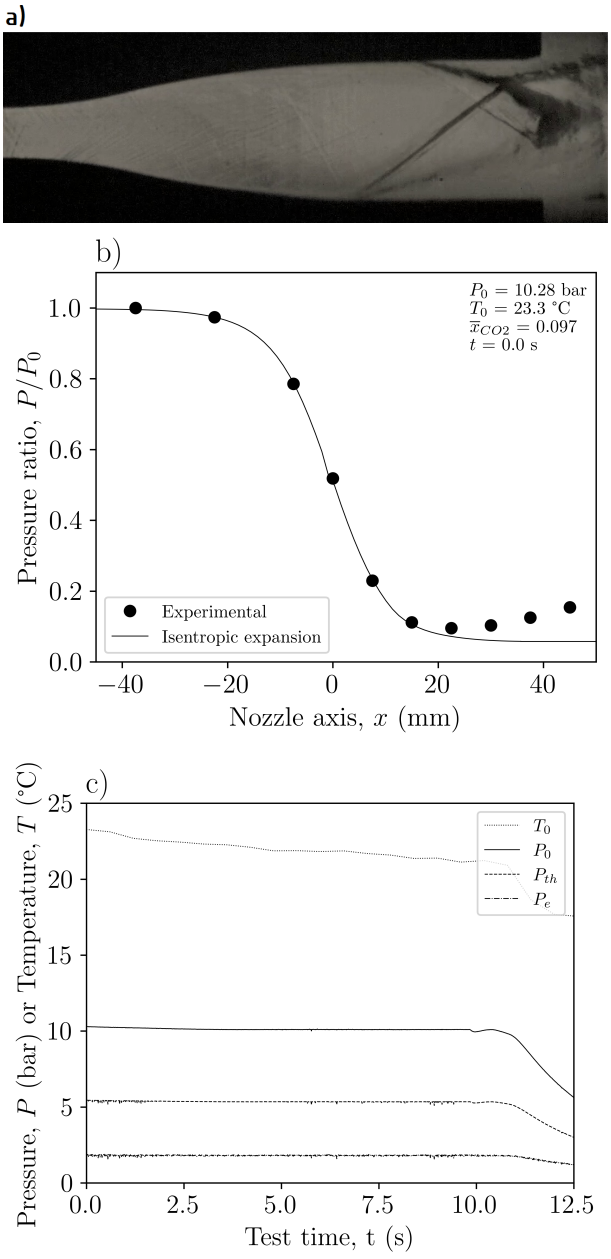

Figure I.9 – Test 30 results, a) Supersonic channel schlieren still picture, b) Nozzle pressure profile for a $t = 0$ s, c) Stagnation P_0, throat P_{th}, exit pressure P_e and stagnation temperature T_0 test evolution.

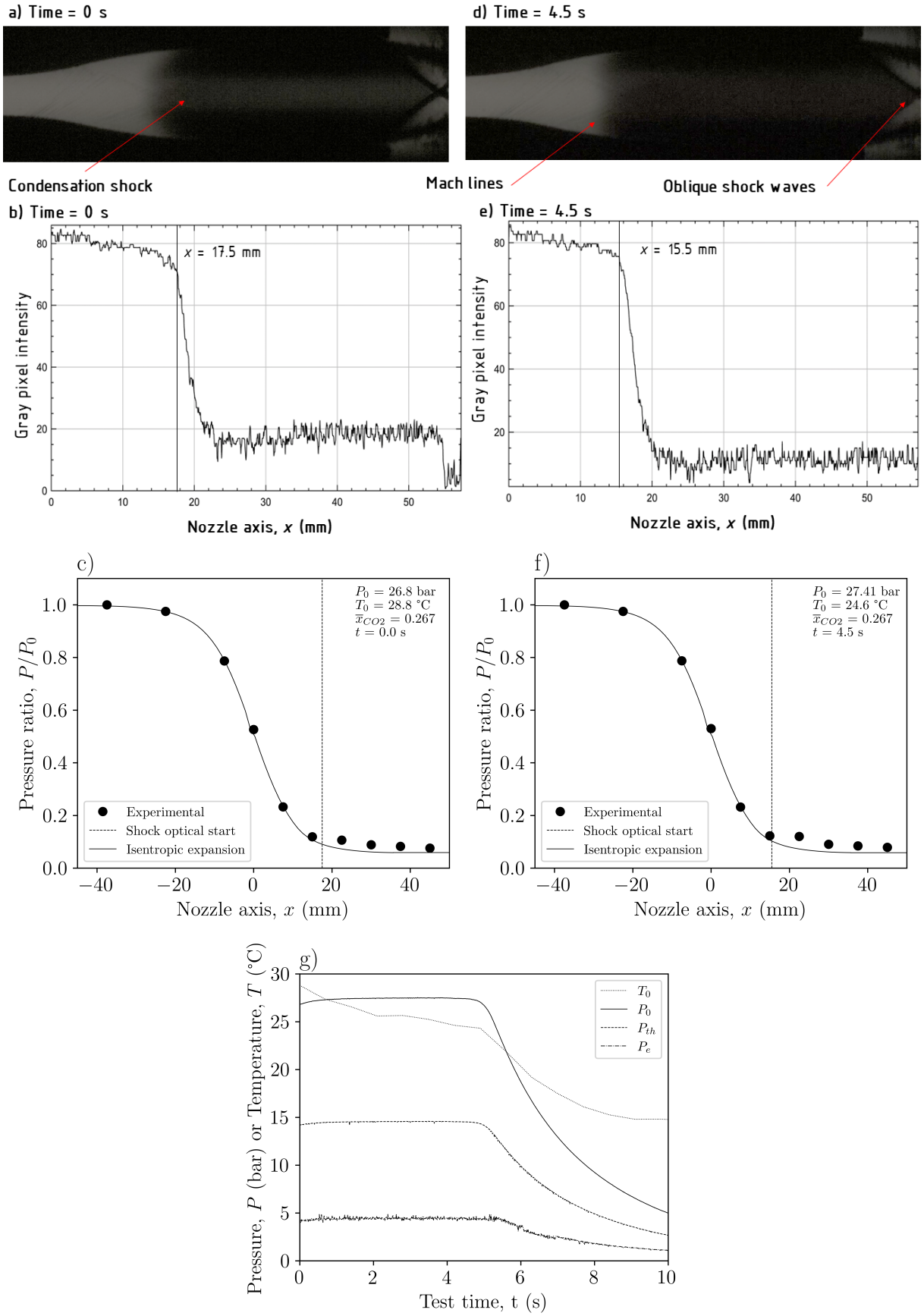

Figure I.10 – Test 31 results, left $t = 0$ s and right $t = 4.5$ s. a and b) Supersonic channel schlieren still picture, c and d) Nozzle centreline grey pixel intensity, e and f) Nozzle pressure profile and g) Stagnation P_0, throat P_{th}, exit pressure P_e and stagnation temperature T_0 test evolution.

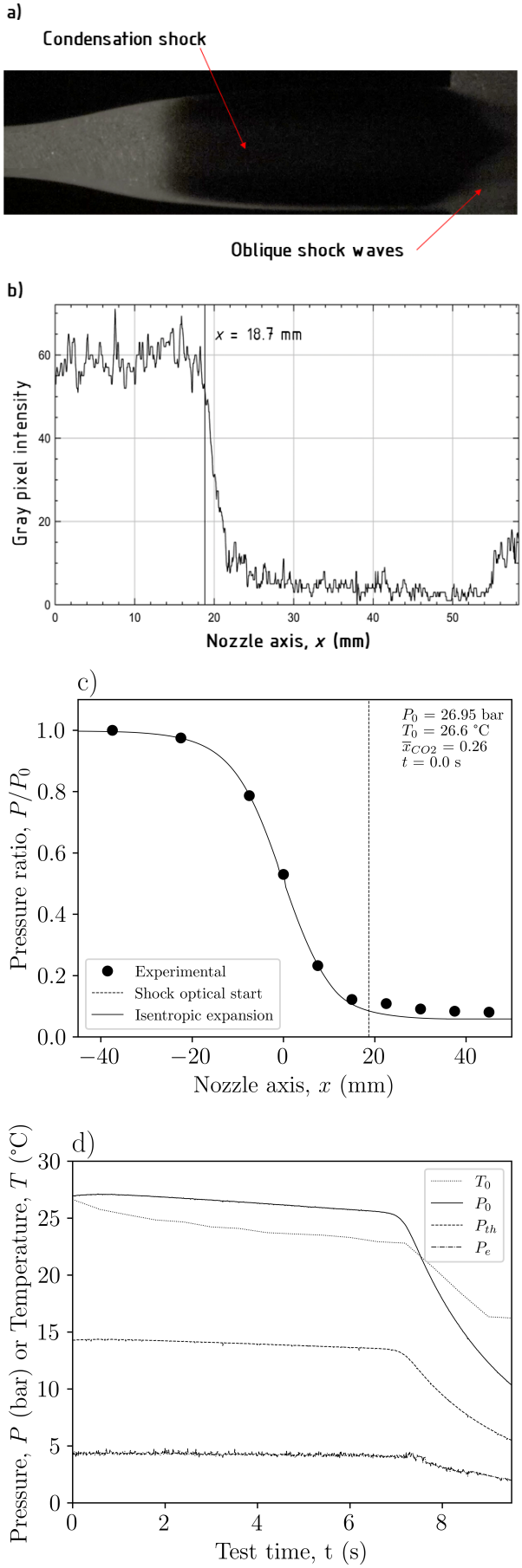

Figure I.11 – Test 32 results, a) Supersonic channel direct still picture, b) Nozzle pressure profile for a $t = 0$ s, c) Stagnation P_0, throat P_{th}, exit pressure P_e and stagnation temperature T_0 test evolution.

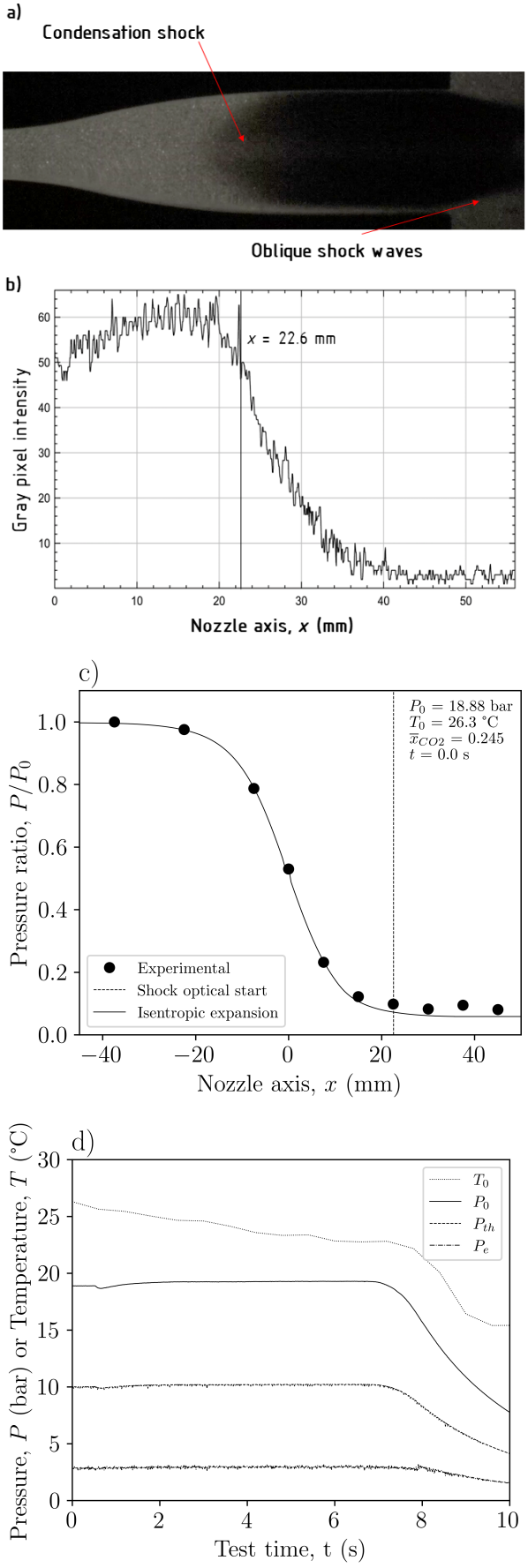

Figure I.12 – Test 33 results, a) Supersonic channel direct still picture, b) Nozzle pressure profile for a $t = 0$ s, c) Stagnation P_0, throat P_{th}, exit pressure P_e and stagnation temperature T_0 test evolution.

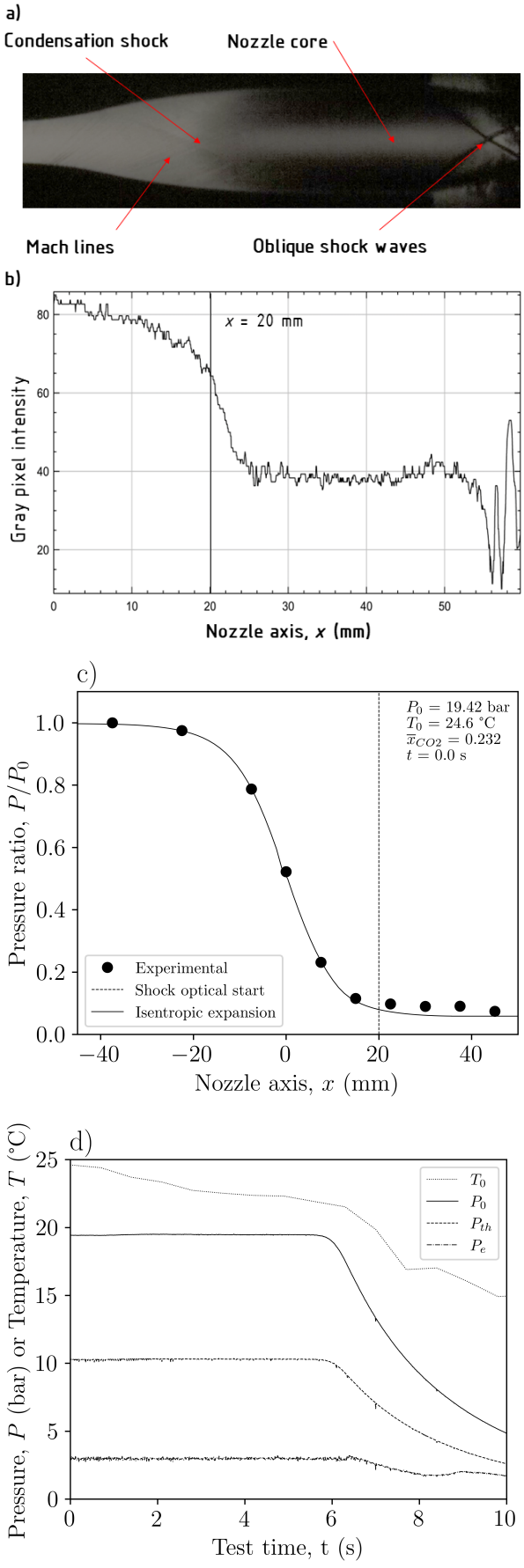

Figure I.13 – Test 34 results, a) Supersonic channel schlieren still picture, b) Nozzle pressure profile for a $t = 0$ s, c) Stagnation P_0, throat P_{th}, exit pressure P_e and stagnation temperature T_0 test evolution.

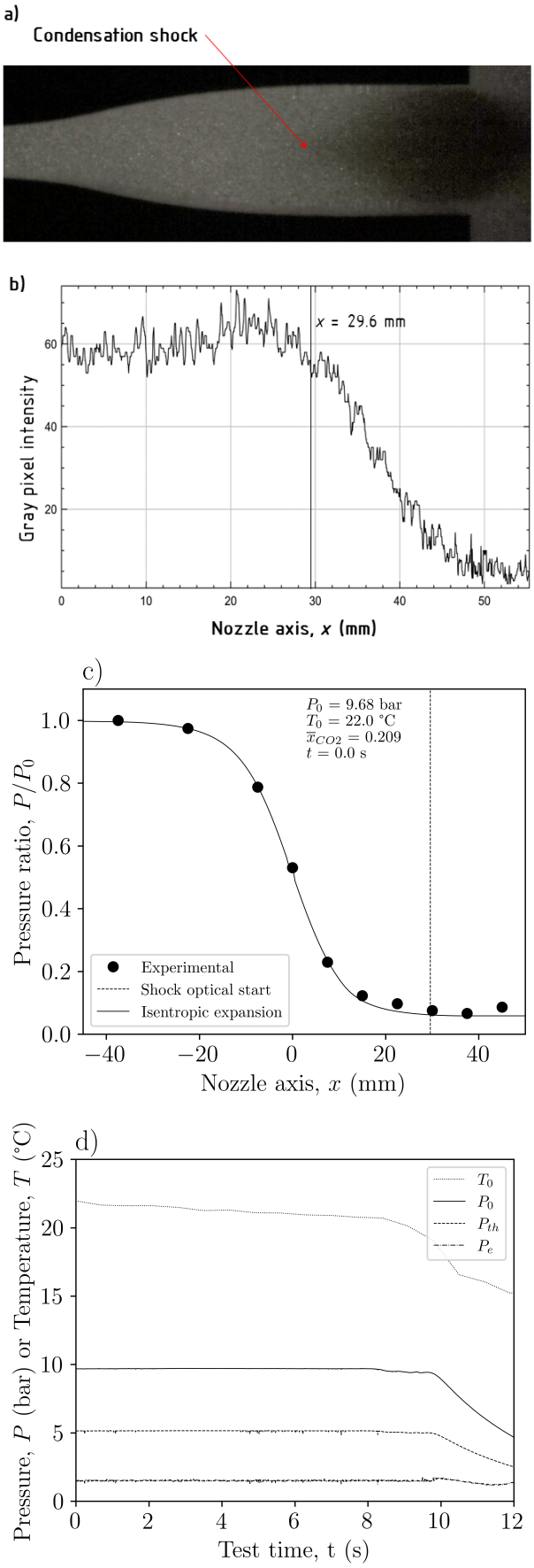

Figure I.14 – Test 36 results a) Supersonic channel direct still picture, b) Nozzle pressure profile for a $t = 0$ s, c) Stagnation P_0, throat P_{th}, exit pressure P_e and stagnation temperature T_0 test evolution.

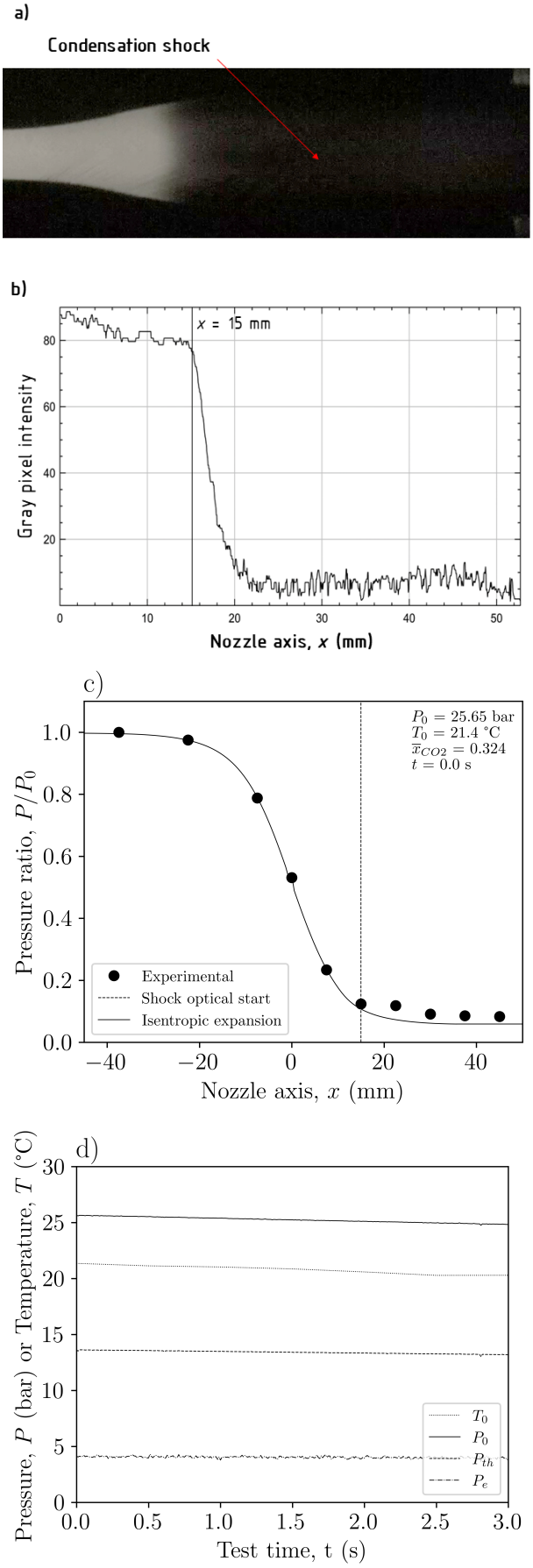

Figure I.15 – Test 38 results a) Supersonic channel schlieren still picture, b) Nozzle pressure profile for a $t = 0$ s, c) Stagnation P_0, throat P_{th}, exit pressure P_e and stagnation temperature T_0 test evolution.